DISS. ETH NO. 27886

Epoxy Composites Enabled by Graphene-Related Materials: Properties and Hazard Assessment of the Aerosols Released by Abrasion and Combustion

A thesis submitted to attain the degree of
DOCTOR OF SCIENCES of ETH ZURICH
(Dr. sc. ETH Zurich)

presented by
WORANAN NETKUEAKUL
MSc, ETH Zurich

born on *21.11.1988*
citizen of Thailand

accepted on the recommendation of
Prof. Dr. Jing Wang, examiner
Dr. Peter Wick, co-examiner
Dr. Tina Buerki-Thurnherr, co-examiner
Dr. Savvina Chortarea, co-examiner
Prof. Dr. Maosheng Yao, co-examiner

2021

To my family

Acknowledgements

I would like to express my sincere gratitude to Prof. Jing Wang, my supervisor, for giving me the opportunity to pursue my PhD. I really appreciate his support and valuable guidance that he has been provided throughout my time at Empa. I learned a lot from him in many ways and I wish I can be as kind and successful as him one day.

I would like to pay my regards to Thailand National Nanotechnology Center for the financial support throughout my master and PhD study.

I would like to show my gratitude to Prof. Maosheng Yao for agreeing to be my PhD committee and to Dr. Peter Molnar for chairing my defense.

I would like to thank Dr. Peter Wick and Dr. Tina Buerki-Thurnherr for their advices, and insightful discussions for the projects we have collaborated. This thesis could not be carried out without their supports. I am grateful to Dr. Savvina Chortarea for her patience and supports in scientific works as well as her advice professionally and personally. I enjoy chatting during our train ride to work. I would also like to thank them for accepting to be my PhD committees.

I wish to acknowledge all of my collaborators for their efforts and great works. Special thanks to Marcel Rees and Marcos for their supports during the fabrication of epoxy at the beginning of my study as well as Daria for her efforts to finish the paper together. I wish to thank all the colleagues at Laboratory of Advance Technologies Empa. I would like to recognize the invaluable discussions with Norbert for his insightful comments.

I would like to thank all past and present members of Jing's group for their fruitful discussions during our weekly group meetings. My time in Switzerland would not be pleasant without friends who I met in this group. Special thanks to Sarka, Marianna, Tobias, Hanchao, Jean, and Yeon Kyoung who have made my stay in Switzerland worth memorable. Thanks to Xing and Hao for great badminton games. I also wish to thank Ranxue, Yinghe and Weidong for their kindness and delicious foods.

Many thanks to all my Thai friends in Switzerland for their emotional supports. I enjoy our badminton games, dinner parties, and travelling. Special thanks to Nes for her kindness and fantastic meals over the past seven years. I also wish to thank Mai, Namhom, and J, my very best friends for sending love and encouragement throughout my time away from home.

I am forever indebted to my partner, Kittiphon, and my family, mom, dad, brothers, aunt and uncle, who are always by my side. Their endless support and unconditional love kept me going and this thesis would not have been possible without their inputs.

Abstract

Graphene-related nanomaterials, GRMs, such as graphene nanoplatelet (GNP), graphene oxide (GO), reduced GO (rGO), *etc.* have a number of applications in various fields such as composite materials, filtration, catalysis, and electronics. Due to the reinforcement, flame retardancy and electrical conductivity properties, GRMs have been explored as nanofillers in polymer composites. An increasing production volume of the GRMs and the GRM-containing composites in the market has brought attentions to their potential risks to humans and the environment. The exposure of GRMs or particles released from GRM-containing composites is possible during the production, the use phase, or the end-of-life of the GRMs and the GRM-containing composites. However, there are still a number of polymer systems that have not been investigated. Moreover, there are limited data about the toxicity of the aerosols released from GRMs-containing composites. Therefore, this thesis focused on three main goals. First, to manufacture the GRM-containing epoxy composites and characterize their mechanical reinforcement and the flame retardancy properties. Second, to analyze the physical and chemical properties, the released fraction of GRMs from the composites, and the *in vitro* toxicity of the released particles from the GRM-containing epoxy composites induced by an abrasion process, which resembled one of the release scenarios by mechanical force during the use phase of the composites. Finally, to investigate the released aerosols from the combustion, which was one of the scenarios that can take place at the end-of-life of the materials, of the GNP-reinforced epoxy composite (EP-GNP) as compared to pure epoxy (EP) in terms of the physicochemical properties and the potential adverse effects.

The mechanical reinforcement, flame retardancy, and electrical properties of the epoxy nanocomposites filled with GNP and phosphorous flame retardant, 9,10- dihydro-9-oxa-10-phosphaphenanthrene-10-oxide (DOPO) as fillers in epoxy composites (diglycidyl ether of bisphenol A and polyetheramine system) were investigated (Chapter 2). The homogeneous dispersion of GNP (0.1 – 5 wt %) was achieved by using high speed mixer followed by the three-roll milling process, while DOPO (3 – 30 wt %) was incorporated into the epoxy resin by heated stirring. The three-point bending test was carried out to evaluate the flexural modulus and flexural strength of the fabricated epoxy composites. The flame retardancy properties were tested using a cone calorimeter. The electrical properties were assessed based on corona discharge test and electrical resistance. Increasing the loading of GNP until 1 wt % and DOPO until 10 % could improve the mechanical properties of the epoxy composites, whereas higher loadings could reduce the flexural strengths of the composites. The combination of GNP and

DOPO could enhance the flame retardancy, based on flame retardancy index (FRI), of the epoxy composites compared to using GNP or DOPO alone. The formulation leading to an improvement in both mechanical properties and flame retardant efficiency of the nanocomposite was 0.5 wt % GNP and 10 wt % DOPO, which did not alter the insulating property of the epoxy resin since the percolation threshold was at 1.6 wt % GNP. The structure–property relationship of the additive-filled epoxy composites obtained from this study can be used as a property constraining guidance to manufacture the composites.

The characterization and the *in vitro* toxicity of the pristine GRMs and the released particles from abrasion of their epoxy composites were determined (Chapter 3). GRMs used in this study included GNP, GO and rGO. The lateral dimension, C/O ratio, thickness, and surface functionality of each GRM were thoroughly characterized. The particle size distributions of the released particles by abrasion measured by a scanning mobility particle sizer and an aerodynamic particle sizer revealed that the abraded particles were in a respirable size range. Since the GRMs that were embedded in the epoxy composite may be released by abrasion and may cause negative health impacts, the released fractions of GRMs were quantified using a lead-labelling method combined with an inductively coupled plasma-optical emission spectrometry. The released fractions of GRMs ranged from 52 % to 92%, depending on the type and size of the GRMs. Raman mapping spectroscopy revealed the defects on the graphitic layers on the GRMs in the abraded particle suggesting that GRMs may be transformed during the fabrication and abrasion process. For *in vitro* toxicity analysis, human macrophages exposed to the suspensions (5 to 40 µg/mL) of GRMs and particles released from abrasion of GRM-epoxy composites were assessed for several toxicity endpoints including the change in cell morphology, cell viability, oxidative stress, and (pro-) inflammatory responses after 24 h and 48 h. The pristine GRMs could cause dose-dependent oxidative responses, while only large GNP could cause cell death. None of the abraded particles induced negative impacts on cells.

A combustion platform has been established to characterize the fire behavior, emissions from combustion and their potential hazards of the EP-GNP compared to EP (Chapter 4). The particle size distributions of the emissions were measured on-line using an aerodynamic particle sizer and a fast mobility analyzer. The emitted particles were collected for further characterization. Raman spectroscopy and X-ray diffraction analysis of both airborne fraction and char residue demonstrated that GNP was only present in the char residues, not in the airborne fraction. The airborne particulate emissions from EP-GNP revealed higher polycyclic aromatic hydrocarbon concentrations, analyzed by gas chromatography-mass spectrometry, as compared to those

from EP. The human alveolar epithelium cells were directly exposed to the emissions at air-liquid interface conditions and the biological effects were evaluated at 24 h and 96 h after exposure. The toxicity endpoints included the change in cell morphology, cell viability, (pro-) inflammatory responses, and the expression of oxidative stress genes (*SOD2* and *HMOX1*) and aryl hydrocarbon receptor (AhR) gene (*CYP1A1*), which is responsible for the polycyclic aromatic hydrocarbon metabolism. The emissions from EP combustion induced the pro- inflammatory response (MCP-1 and GM-CSF) and the activation of AhR, but did not cause any effects on cell morphology, cell viability nor oxidative stress genes. Despite a transient decrease in mitochondrial activity at 24 h caused by EP-GNP, but not EP, the emissions from EP-GNP did not induce any additional adverse cell effects in comparison to those from EP.

In conclusions, the results from these studies improve the understanding about the role of GRMs to enhance the mechanical strength and the flame retardancy properties of epoxy composites and the physicochemical characteristics and potential hazards of aerosols released from the abrasion and combustion of the GRM-reinforced epoxy composites. These results revealed that the GRMs can be used as nanofillers in epoxy composites mainly due to their beneficial effects, and the limited *in vitro* toxicity is auxiliary.

Zusammenfassung

Graphenähnliche Materialien, GRMs, wie Graphen-Nanoplättchen (GNP), Graphenoxid (GO), reduziertes GO (rGO) usw. werden in verschiedenen Bereichen wie z.B. in Verbundmaterialien, zur Filtration, Katalyse und in der Elektronik eingesetzt. Aufgrund ihrer materialverstärkenden Eigenschaften, ihrer guten elektrischen Leitfähigkeit, sowie ihrer flammhemmenden Wirkung wurden GRMs als Nanofüllstoffe in Polymerverbundwerkstoffen erforscht und teils bereits verwendet. Das steigende Produktionsvolumen der GRMs und der GRM-haltigen Verbundwerkstoffe hat auf ihre potentiellen Risiken für Mensch und Umwelt aufmerksam gemacht. Eine Exposition zu GRMs oder aus GRM-haltigen Verbundwerkstoffen freigesetzten Partikeln ist sowohl während der Herstellung, der Nutzungsphase als auch am Lebensende der GRMs oder der GRM-haltigen Verbundwerkstoffe möglich. Es gibt jedoch noch eine Reihe von Polymersystemen, die diesbezüglich noch nicht untersucht wurden. Darüber hinaus gibt es nur wenig Daten hinsichtlich der Toxizität von aus GRM-haltigen Verbundstoffen freigesetzten Aerosolen. Daher konzentrierte sich diese Arbeit auf drei Hauptziele. Erstens, auf die Herstellung von GRM-haltigen Epoxidverbundstoffen, ihre mechanische Verstärkung und die Charakterisierung ihrer flammhemmenden Wirkung. Zweitens, auf die physikalischen und chemischen Eigenschaften der Komposite, den durch Abrieb aus den GRM-Epoxidverbundwerkstoffen freigesetzten GRM-Anteil und die damit verbundene *In-vitro*-Toxizität der freigesetzten Partikel. Es wurde speziell der Abriebprozess untersucht, da er durch die mechanische Krafteinwirkung einen normalen Gebrauch der Verbundwerkstoffe während der Nutzungsphase symbolisiert.

Schließlich, wurden die freigesetzten Aerosole die bei der Verbrennung (ein Freisetzungsszenario am Ende der Lebensdauer der Materialien), der GNP-Epoxidverbundmaterialien (EP-GNP) im Vergleich zu reinem Epoxid (EP) hinsichtlich der physikalisch-chemischen Eigenschaften und einer möglichen schädlichen Wirkung erforscht.

Die mechanische Verstärkung, die flammhemmenden und die elektrischen Eigenschaften der mit GNP gefüllten Epoxid-Nanokomposite und der Effekt des phosphorhaltige Flammschutzmittel 9,10-Dihydro-9-oxa-10-phosphaphenanthren-10-oxid (DOPO) als Füllstoff in Epoxid-Kompositen (DGEBA und Polyetheraminsystem) wurde untersucht (Kapitel 2). Die homogene Verteilung von GNP (0,1 – 5 Gew.-%) wurde mit einem Hochgeschwindigkeitsmischer und anschließendem Drei-Walzen-Mahlprozess erreicht, während DOPO (3 – 30 Gew.-%) durch Rühren und gleichzeitiges Erwärmen in das Epoxidharz

eingearbeitet wurde. Dreipunkt-Biegetests wurden durchgeführt, um das Biegemodul und die Biegefestigkeit der hergestellten Epoxidverbundstoffe einschätzen zu können. Die Flammschutzeigenschaften wurden mit einem Kegelkalorimeter getestet. Die elektrischen Eigenschaften wurden basierend auf dem Koronaentladungstest und dem elektrischen Widerstand bewertet. Eine Erhöhung des GNP-Anteils im Komposit auf 1 Gew.-% und von DOPO auf 10 % könnte sich positiv auf die mechanischen Eigenschaften der Epoxid-Komposite auswirken, während höhere Beladungen die Biegefestigkeiten der Komposite verringern könnten. Die Kombination von GNP und DOPO verbesserte die flammhemmende Wirkung, basierend auf dem Flammhemmungsindex (FRI), der Epoxidverbundstoffe im Vergleich zur alleinigen Verwendung von GNP oder DOPO. Die Formulierung, die zu einer Verbesserung sowohl der mechanischen Eigenschaften als auch der Flammschutzwirkung des Nanokomposits führte, betrug 0,5 Gew.-% GNP und 10 Gew.-% DOPO. Dies veränderte die Isoliereigenschaft des Epoxidharzes nicht, da die Perkolationsschwelle bei 1,6 Gew.-% lag. Die Struktur-Eigenschafts-Beziehung der additivgefüllten Epoxidverbundstoffe, die aus dieser Studie gewonnen wurden, kann als eigenschaftenbeschränkende Anleitung zur Herstellung der Verbundwerkstoffe verwendet werden.

Die Charakterisierung und die *In-vitro*-Toxizität der originalen GRMs und der freigesetzten Partikel aus dem Abrieb der GRM-Epoxid-Komposite wurden bestimmt (Kapitel 3). Zu den in dieser Studie verwendeten GRMs gehörten GNP, GO und rGO. Die laterale Dimension, das C/O-Verhältnis, die Dicke und die Oberflächenfunktionalität jedes GRM wurden gründlich charakterisiert. Die Partikelgrößenverteilungen der durch Abrieb freigesetzten Partikel, die mit einem Scanning Mobility Particle Sizer und einem aerodynamischen Partikelsizer gemessen wurden, zeigten, dass die abgeriebenen Partikel in einem lungengängigen Größenbereich lagen. Da die in den Epoxidverbund eingebetteten GRMs durch Abrieb freigesetzt werden und negative gesundheitliche Auswirkungen haben können, wurden die freigesetzten GRM-Anteile mittels einer Bleimarkierungsmethode in Kombination mit einer induktiv gekoppelten plasmaoptischen Emissionsspektrometrie quantifiziert und bewertet. Die freigesetzten Anteile an GRMs lagen je nach Art und Größe der GRMs zwischen 52 % und 92 %. Raman-Mapping-Spektroskopie zeigte die Defekte auf den Graphitschichten auf den GRMs in den abgeschliffenen Partikeln, was darauf hindeutet, dass GRMs während des Herstellungs- und Abriebprozesses umgewandelt werden können. Für die In-vitro-Toxizitätsanalyse wurden menschliche Makrophagen, die den Suspensionen (5 bis 40 µg/ml) mit GRMs und Partikeln, die durch Abrieb von GRM-Epoxid-Kompositen freigesetzt wurden ausgesetzt, auf verschiedene Toxizitätsendpunkte untersucht; einschließlich der Veränderung der

Zellmorphologie, Zelllebensfähigkeit, oxidativem Stress und (Pro-) Entzündungsreaktionen nach 24 h und 48 h. Die originalen, unbehandelten GRMs riefen dosisabhängige oxidative Reaktionen hervor, während nur große GNP zum Zelltod führten. Keines der abgeriebenen Partikel induzierte negative Auswirkungen auf die Zellen.

Eine Verbrennungsplattform wurde eingerichtet, um das Brandverhalten, die Emissionen aus der Verbrennung und damit verbundene potenzielle Gefahren des EP-GNP im Vergleich zu EP zu charakterisieren (Kapitel 4). Die Partikelgrößenverteilungen der Emissionen wurden online mit einem aerodynamischen Partikelgrößenmessgerät und einem schnellen Mobilitätsanalysator gemessen. Die emittierten Partikel wurden für weiteren Charakterisierungen gesammelt. Raman-Spektroskopie und Röntgenbeugungsanalyse sowohl der luftgetragenen Fraktion, als auch der Kohlerückstände, zeigten, dass GNP nur in den Kohlerückständen vorhanden war und nicht in der luftgetragenen Fraktion. Die luftgetragenen Partikelemissionen von EP-GNP zeigten höhere Konzentrationen polyzyklischer aromatischer Kohlenwasserstoffe (analysiert durch Gaschromatographie-Massenspektrometrie) im Vergleich zu EP. Die humanen Alveolarepithelzellen wurden den Emissionen unter Luft-Flüssigkeits-Grenzflächenbedingungen direkt ausgesetzt und die biologischen Wirkungen nach 24 h und 96 h Expositionszeit bewertet. Zu den Toxizitätsendpunkten gehörten die Veränderung der Zellmorphologie und der Zelllebensfähigkeit, (pro-) inflammatorische Reaktionen und die Expression von Genen für oxidativen Stress (*SOD2* und *HMOX1*) und dem Aryl-Hydrocarbon-Rezeptor-Gen (*CYP1A1*), das Ausdruck für den Stoffwechsel mit polyzyklischen aromatischer Kohlenwasserstoffen ist. Trotz einer vorübergehenden Abnahme der mitochondrialen Aktivität nach 24 h, die durch EP-GNP, aber nicht durch EP, hervorgerufen wurde, induzierten die Emissionen von EP-GNP keine zusätzlichen schädlichen Zellwirkungen im Vergleich zu denen von EP.

Zusammenfassend lässt sich sagen, dass die Ergebnisse dieser Studien das Verständnis von GRM hinsichtlich der Verbesserung der mechanischen Festigkeit und der Flammhemmungseigenschaften von Epoxidverbundstoffe, sowie der physikalisch-chemischen Eigenschaften und potenziellen Gefahren von Aerosolen, die durch Abrieb oder Verbrennung von GRM-Epoxid-Kompositen entstehen, verbessert. Die Ergebnisse zeigten, dass die GRMs hauptsächlich aufgrund ihrer vorteilhaften Wirkungen als Nanofüllstoffe in Epoxid-Kompositen verwendet werden können, und die begrenzte In-vitro-Toxizität ist dabei hilfreich.

Table of Contents

List of Abbreviations and Symbols

Abbreviations

A549	adenocarcinoma alveolar epithelial type II cells
ABS	acrylonitrile butadiene styrene
Ace	acenaphthene
Acy	acenaphthylene
AHEW	amine hydrogen equivalent weight
AhR	aryl hydrocarbon receptor
ALI	air-liquid interface
ANOVA	analysis of variance
Ant	anthracene
APS	aerodynamic particle sizer
ATR-FTIR	attenuated total reflection-Fourier transform infrared spectrometer
B35	rat neuroblastoma cells
BaA	benzo(a)anthracene
BaP	benzo(a)pyrene
BbF	benzo(b)fluoranthene
BEAS-2B	bronchial epithelial cells
BgP	benzo(g,h,i)perylene
BHBSS	Hank's balanced salt solution
BkF	benzo(k)fluoranthene
BSA	bovine serum albumin
BSO	L-buthionine-sulfoximine
cDNA	complementary DNA
Chr	chrysene
CLSM	confocal laser scanning microscope
CMD	count median diameter
CNT	carbon nanotube

COPD	chronic obstructive pulmonary disease
CPC	condensation particle counter
CVD	chemical vapor deposition
CYP1A1	cytochrome P450 1A1
DaA	dibenzo(a,h)anthracene
DAPI	4',6-diamidino-2-phenylindole
DDM	4,4'-diamino diphenyl methane
DDS	4,4'-diaminodiphenyl sulfone
DGEBA	diglycidyl ether of bisphenol A
DLS	dynamic light scattering
DMS500	fast mobility analyzer model DMS500 from Cambustion
DMTA	dynamic mechanical thermal analysis
DNA	deoxyribonucleic acid
DOPO	9,10- dihydro-9-oxa-10-phosphaphenanthrene-10-oxide
DRIFTS	diffuse reflectance Fourier transform spectroscopy
DSC	differential scanning calorimeter
DTG	derivative thermogravimetric
EDX	energy-dispersive x-ray spectroscopy
EEW	epoxy equivalent weight
EHC	effective heat of combustion
ELISA	enzyme-linked immunosorbent assay
EP	epoxy, pure epoxy, epoxy resin
EP-GNP	GNP-reinforced epoxy composite
EPN	epoxy novolac resin
FCS	fetal calf serum
Fla	fluoranthene
Flu	fluorene
FRI	flame retardancy index
FTIR	Fourier transform infrared spectrometer

GC-MS	gas chromatogrpahy-mass spectrometry
GM-CSF	granulocyte macrophage-colony stimulating factor
GNP	graphene nanoplatelet
GO	graphene oxide
GRM	graphene-related material
GSH	glutathione
H_2DCF	2′,7′-dichlorofluorescein
H_2DCF-DA	2′,7′-dichlorodihydrofluorescein-diacetate
HEK 293T	human embryonic kidney 293 cells
HMOX	heme-oxygenase
HRR	heat release rate
ICP-OES	inductively coupled plasma - optical emission spectrometry
IFN-γ	interferon gamma
IL-10	interleukin-10
IL-12(p40)	interleukin-12(p40)
IL-12(p70)	interleukin-12(p70)
IL-13	interleukin-13
IL-1ra	interleukin-1ra
IL-1β	interleukin-1beta
IL-2	interleukin-2
IL-4	interleukin-4
IL-5	interleukin-5
IL-6	interleukin-6
IL-8	interleukin-8
InP	indeno(1,2,3-c,d)pyrene
LDH	lactate dehydrogenase
LDPE	low-density polyethylene
LPE	liquid phase exfoliation
LPS	lipopolysaccharide

MCP-1	monocyte chemoattractant protein-1
MES	2-(N-morpholino)ethanesulphonic acid
MPA	metaphosphoric acid
mRNA	messenger ribonucleic acid
MTS	3-(4,5-dimethylthiazol-2-yl)-5-(3-cyrboxymethoxy-phenyl)-2-(4-sulfophenyl)-2H-tetrazolium, inner salt
MW	molecular weight
MWCNT	multi-walled carbon nanotube
Nap	naphthalene
NOAEL	no observed adverse effect level
NPs	nanoparticles
OEL	occupational exposure limit
PA-6	polyamide 6
PAH	polycyclic aromatic hydrocarbon
PBS	phosphate buffered saline
PC	Polycarbonate
PC12	rat dopaminergic pheochromocytoma cells
PEG	polyethylene glycol
PET	polyethylene terephthalate
PFA	paraformaldehyde
PFRs	phosphorous flame retardants
Phe	phenanthrene
pHRR	peak heat release rate
PLA	polylactic acid
PMA	phorbol 12-myristate 13-acetate
PMMA	polymethyl methacrylate
PN	phenol novolac
PP	Polypropylene
PR3D-HPEK-50	3D epidermal model constituted of human primary keratinocytes
PSDs	particle size distributions

PSL	polystyrene latex
PSN	penicillin–streptomycin–neomycin
PU	polyurethane
Pyr	pyrene
QCM	quartz crystal microbalance
rGO	reduced graphene oxide
RNA	ribonucleic acid
ROS	reactive oxygen species
RPMI-1640	Roswell Park Memorial Institute 1640
RT-PCR	real time-polymerase chain reaction
SOD	superoxide dismutase
THP-1	human monocytic cell line derived from an acute monocytic leukemia patient.

Symbols

μ_i	mean of the fitted mode
A_i	area under the graph of each fitted mode
C_c	slip correction factor
D	diffusion coefficient
d_a	aerodynamic diameter
d_c	diameter of the cylinder
d_e	electrical mobility
d_p	particle diameter
D_p	diameter of the platelet
d_{proj}	projected diameter
E'	storage elastic modulus (Pa)
f(d)	normalized fraction of the measured particle size distributions as a function of particle size (d)
g	acceleration of gravity
IPD	interparticle distance

k	Boltzmann's constant
n	number of the fitted modes
R	gas constant (8.3145 $m^3 \cdot Pa \cdot mol^{-1} \cdot K^{-1}$)
Re	Reynolds number
S	stopping distance
Stk	Stokes number
t	residence time
T	temperature (K)
$T_{-50\%}$	mid-point temperature
t_c	critical exponent
T_d	onset temperature or initial decomposition temperature
T_{max}	decomposition temperature at the maximum mass loss rate
t_p	thickness of the platelet
U	undisturbed air velocity
V_{TS}	terminal settling velocity
w_i	standard deviation of each fitted mode
x_{rms}	root-mean-square displacement
y_0	baseline of the lognormal distribution
η	air viscosity
ρ_0	unit density
$\rho_{E'}$	crosslinking density
ρ_p	particle density
σ_c	conductivity of the nanocomposite
σ_f	conductivity of the filler
σ_g	geometric standard deviation
τ	relaxation time
ϕ	filler concentration
ϕ_c	percolation threshold

Table of Figures and Tables

Figures

Tables

References

Bierkandt, F.S.; Leibrock, L.; Wagener, S.; Laux, P.; Luch, A. The impact of nanomaterial characteristics on inhalation toxicity. *Toxicol. Res. (Camb).* **2018**, *7*, 321–346, doi:10.1039/c7tx00242d.

Kong, W.; Kum, H.; Bae, S.-H.; Shim, J.; Kim, H.; Kong, L.; Meng, Y.; Wang, K.; Kim, C.; Kim, J. Path towards graphene commercialization from lab to market. *Nat. Nanotechnol.* **2019**, *14*, 927–938, doi:10.1038/s41565-019-0555-2.

Sanchez, V.C.; Jachak, A.; Hurt, R.H.; Kane, A.B. Biological Interactions of Graphene-Family Nanomaterials: An Interdisciplinary Review. *Chem. Res. Toxicol.* **2012**, *25*, 15–34, doi:10.1021/tx200339h.

Wick, P.; Louw-Gaume, A.E.; Kucki, M.; Krug, H.F.; Kostarelos, K.; Fadeel, B.; Dawson, K.A.; Salvati, A.; Vázquez, E.; Ballerini, L.; et al. Classification Framework for Graphene-Based Materials. *Angew. Chemie Int. Ed.* **2014**, *53*, 7714–7718, doi:10.1002/anie.201403335.

Escribano, R.; Sloan, J.J.; Siddique, N.; Sze, N.; Dudev, T. Raman spectroscopy of carbon-containing particles. *Vib. Spectrosc.* **2001**, *26*, 179–186, doi:10.1016/S0924-2031(01)00106-0.

Chapter 1

Introduction

1.1 Graphene-Related Materials (GRMs)

Graphene-related materials (GRMs) are a group of materials consisting of a single to several layers of graphene, a monolayer of two-dimensional (2D) carbon atoms bonded hexagonally, which is a basic elementary unit of all GRMs. In terms of electronic properties, graphene layers of 2 to <10 are still considered as 2D material [1]. GRMs can exist in numerous forms such as graphene nanoplatelet (GNP), graphene oxide (GO), or reduced GO (rGO) as shown in Figure 1.1. The classification of GRMs is necessary in order to avoid the misunderstanding about their properties and their safety to humans and the environment. GRMs can be classified according to three major physicochemical properties e.g. number of layers, average lateral dimension and carbon/oxygen (C/O) ratio as illustrated in Figure 1.1 [2].

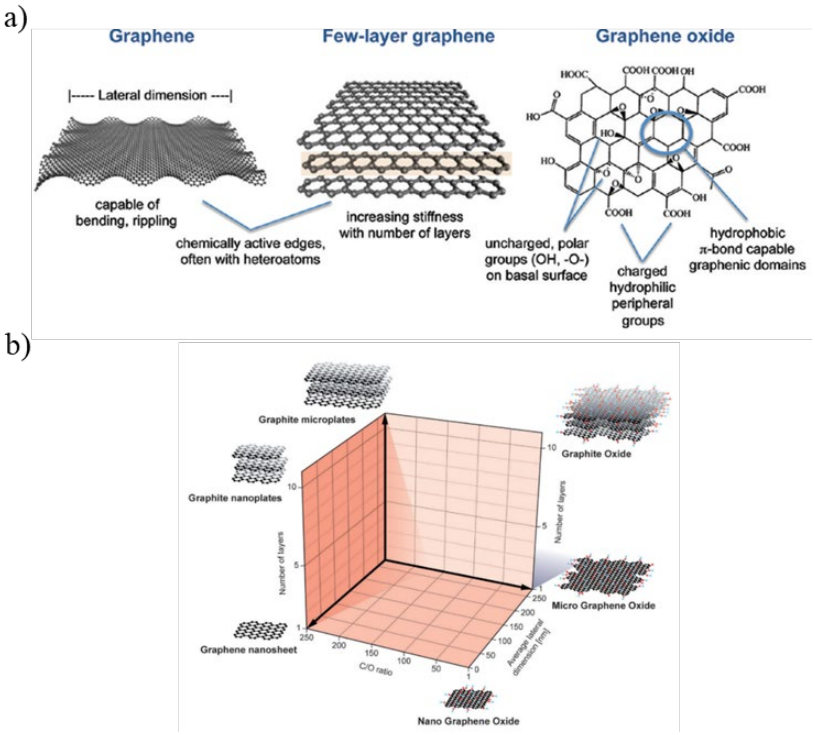

Figure 1.1 a) Examples of graphene-related materials (GRMs) and their properties (Extracted from [3]) and b) Proposed classification of the GRMs based on the number of layers, average lateral dimension and carbon to oxygen (C/O) ratio (Extracted from [2])

GRMs can be manufactured by different approaches, which can distinctively influence their quality and physicochemical properties. The most commonly used method for mass production is the top-down approach known as exfoliation using graphite as a starting material [4]. High-quality pristine nanoplatelets can be achieved by liquid phase exfoliation (LPE) or intercalation-exfoliation, which is done by weakening the interaction between graphene layers by inserting chemical species i.e. organic solvent or water/surfactant solution using ultrasonication for a number of hours. Solid-state exfoliation of graphite by edge functionalization can generate GNP with some defects on the graphene sheets. The oxidation of graphite followed by exfoliation can produce graphene oxide or functionalized graphene sheets. Graphene oxide can be reduced to reduced graphene oxide by means of thermal annealing, hydrothermal reaction or chemical reaction [4]. So far, it is challenging to manufacture GRMs using the LPE method to achieve GRMs with large lateral dimension, but still maintained monolayer and structural integrity [5]. The chemical vapor deposition (CVD) and sublimation of SiC are the bottom-up method that can be used to fabricate continuous monolayer graphene. The former can directly grow epitaxial graphene on the SiC substrate for microelectronic application, while the latter is a promising candidate for up-scaling production of electronic-grade graphene [5].

Depending on particular properties of each species, GRMs have been investigated for a board range of applications ranging from composites, electronics to nanomedicine [5–7]. GNP has been studied as nanofillers to establish specific properties of polymer nanocomposites such as antistatic and anticorrosion due to high electrical conductivity and impermeability [4], thermal interfacial or heat-spreading in electronic materials due to high thermal conductivity [4] or toughness of polymer due to good mechanical properties. GO and rGO have been extensively explored for sensor applications such as gas sensor and biosensor due to their high specific surface area, electrical conductivity, electron transfer rate, optical transmittance, and excellent mechanical flexibility [8–10].

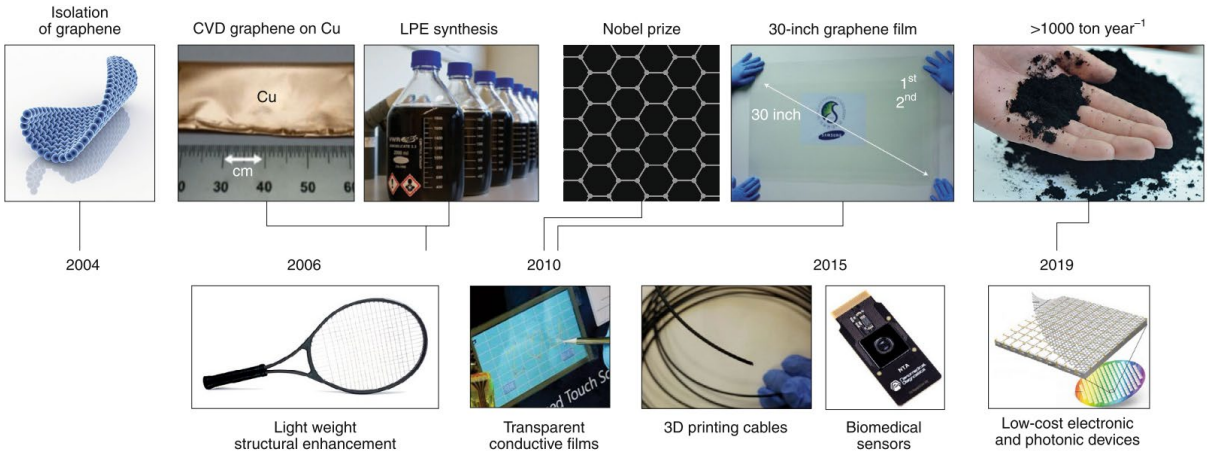

Figure 1.2 Important events related to GRMs production and applications since the successful isolation of graphene in 2004 (Extracted from [5])

Since the successful isolation of single-layer graphene in 2004, the continuous research about GRMs manufacturing has led to the mass production and commercialization of GRMs as well as GRM-based products as depicted in Figure 1.2. Spike in the number of patent related to GRMs in 2009 is considered as time-zero for GRMs commercialization [11]. Then in 2010, Geim and Novoselov has been awarded Nobel Prize for the discovery of free-standing graphene. With a board range of applications and an increasing market value, GRMs have a foreseen increase in production [12]. The lack of toxicological information on GRMs is one of several reasons that could slow down the production and innovation of GRMs and GRM-containing products. In order to support the safe and sustainable way to produce and to use GRMs and GRM-based products, toxicity and hazard assessment of GRMs from cradle-to-grave should be evaluated.

1.2 GRM/Polymer Composites

One of the GRM applications is the use as fillers in polymer composites. The GRM-based polymer composites showed the enhancement in mechanical reinforcement, electrical conductivity, thermal conductivity, and flame retardancy properties of different polymers such as epoxy, polypropylene (PP) polycarbonate (PC), and polyurethane (PU) [6,13,14]; therefore, they have been investigated for mechanical enhancement [15], electronic [16–19], anticorrosion [20,21], sensing [22,23], and electromagnetic shielding [24] applications. These research works show the promising applications of GRM/polymer composites in the industrial section. So far, there have been several GRM-based polymer products in the market such as tennis racket and skis developed by HEAD, cycling helmet and cycling shoes from Spanish company called Catlike, and earphones from FiiO Electronics and Anker's audio [25]. Some products are still under

development, for example, Haydale and Airbus have filed a joint patent about the composite materials filled with functionalized 2D graphene to improve lightning strike protection for aerospace application [26].

The GRM/polymer composite can be further developed by combining GRM with other fillers or additives, which can offer novel properties or synergistic effects. The synergy of CNT and GNP on mechanical reinforcement of epoxy composite has been reported [27,28]. For example, Yang *et al*. demonstrated that the hybrid of 0.1 wt % MWCNT and 0.9 wt % GNP fillers showed better dispersion and compatibility in epoxy matrix than the composite filled with 1 wt % MWCNT or 1 wt % GNP alone and resulted in significant enhancement in tensile strength and thermal conductivity [27]. To achieve a significant improvement in flame retardancy efficiency of the polymer composite, high concentration of GRMs were needed. Therefore, the synergistic flame retardancy effects by combining GRM with the traditional flame retardants have been largely investigated [29–34]. For example, Liu *et al*. showed that the combination of 0.5 wt % layered double hydroxide and 0.5 wt % graphene nanosheet resulted in synergistic effects by increasing the oxygen index and retarding the flame propagation of epoxy composite. By increasing the loading of each filler to 2.5 wt%, the total heat release was reduced by 26% [35]. The combination of 2.5 wt% graphene nanaosheet and 2.5 wt % DOPO (9,10-dihydro-9-oxa-10-phosphaphenanthrene-10-oxide) in epoxy matrix showed a synergistic flame retardancy by decreasing the peak heat release rate and the total heat release and forming a char with denser structure and more thermal stability [29,35].

The current challenges lie on the fabrication process that enables high GRM loading with good dispersion and strong adhesion between epoxy and surface of GRM, which can result in the notorious enhancement in materials' properties. Agglomeration of GRM in the polymer matrix can occur at higher GRM concentration. Surface coating or functionalization can improve the dispersion and can even form the covalent bond with the polymer matrix, but the electrical conductivity may be compromised. The optimization of the amount of GRM and/or other fillers in polymer matrix to achieve the desired properties of the materials still needs more experimental and computational modelling data to improve the understanding about the structure-property relationship.

1.3 Flame Retardants for Polymer

Flame retardants are a group of chemicals added to the polymer to prevent the start or to slow down the growth of the fire. Examples of flame retardants are mineral fillers, halogenated compounds, phosphorous-based compounds, nitrogen-based compounds, and silicon-based compounds. They can be classified into two main categories including the additive (non-reactive) flame retardants and the reactive flame retardants. The additive flame retardants do not react with the polymer during the manufacturing process such as mineral fillers, whereas the reactive type chemically bond with the polymer molecule and is integrated in the polymer chains.

Flame retardants can act via two major modes including the physical and chemical mechanism. Physical mechanism involves the cooling effect by endothermic decomposition of the flame retardants, the dilution of the combustible volatile gases by releasing non-combustible gases such as H_2O, CO_2, and NH_3 during the combustion and the formation of the physical barriers to obstruct the diffusion of combustible gases to the flame and insulate the polymer's surface from air and heat. The chemical mechanism can take place in both gas phase and condensed phase. The reaction in gas phase involves the release of free-radicals that can scavenge the highly reactive radical species such as H• and OH• that are formed during the combustion, which result in the less reactive or inert molecules. The reaction in condensed phase invoked by the flame retardant can occur either via an acceleration of degradation of polymer chain, which results in polymer dripping from the flame, or a catalytic formation of the char, which acts as physical barriers between the gas phase and the condensed phase [36,37].

An increasing in the restrictions of the use of some brominated and chlorinated flame retardants has been introduced since the 1970s because of their environmental persistence and toxicity, which has led to concerns about the adverse effects to humans and the environment. Therefore, novel classes of flame retardants have gained more interests. DOPO (9,10-dihydro-9-oxa-10-phosphaphenanthrene-10-oxide) is a widely used organophosphorous flame retardant (OPFR) because of its exceptional thermal stability. DOPO and its derivatives have been studied as flame retardants in several polymer systems [38–40]. The flame retarding mechanism of DOPO involves the chemical mode in both gas phase by producing HPO•, PO• and PO_2• species that can interact with H• and OH• and condensed phase by promoting the polymer charring [29,41].

The toxicity of DOPO has been reported as low cytotoxicity and low neurotoxicity compared to halogenated flame retardants [42,43], some of which are cytotoxic and neurotoxic [44]. Hen-

driks *et al*. demonstrated that rat dopaminergic pheochromocytoma (PC12) and rat neuroblastoma (B35) cells treated with DOPO (>100 μM) for 24 h did not show cytotoxicity, ROS formation, nor change in intracellular Ca^{2+} level [42]. Similarly, Hirsch *et al*. revealed that DOPO did not induce any biological effects at the maximal concentration of 100 μM on different *in vitro* biological models including human alveolar epithelial cells (A549), human macrophages (THP-1), 3D epidermal model (human primary keratinocytes (PR3D-HPEK-50), central nervous system neurons (LUHMES cells), and peripheral nervous system neurons (human pluripotent stem cells) [43]. Moreover, during the combustion of epoxy composite, DOPO could suppress the smoke formation and reduce the toxic gas release [29]. Data on the thermal degradation products of DOPO are still needed to ensure the safe use of DOPO.

1.4 Toxicity of GRMs

A number of review studies suggested that the toxicity of GRMs was influenced by several factors such as concentration, lateral dimension, surface chemistry, functionalization, charge, impurities, aggregations, and protein corona effect [3,45–51]. This section shows examples of some studies highlighting the effects of lateral dimension and surface chemistry, which are the properties often reported in the toxicity studies.

The cellular internalization of GRMs could be influenced by their shape and size [52–54]. Studies showed that small-sized GRMs could be internalized by cells, whereas larger GRMs that could not be completely internalized could have interaction with the cell membrane and may cause negative effects [55,56]. Schinwald *et al*. demonstrated that GNP with large lateral sizes up to 25 μm can have smaller aerodynamic diameters, which are in the respirable range owing to its platelet structure and thin nature [53]. The respirable fraction of GNP could reach beyond the ciliated airways, where the only clearance mechanism is via macrophages. Then, they assessed the toxicity of GNP *in vitro* using THP-1 macrophages and *in vivo* using mice. They reported that GNP having a lateral size of 5 μm could induce frustrated phagocytosis of macrophages and inflammogenicity *in vitro* and *in vivo* [53]. Li *et al*. showed that few-layer graphene with lateral dimension ranging from 0.5 to 10 μm can enter the cells by edge-first uptake followed by a complete internalization, which is spontaneous membrane penetration process [57]. Ma *et al*. demonstrated that larger GO sheets (lateral size of 750 to 1300 nm) could be strongly adsorbed on the cell membrane and induced M1 polarization of macrophages, which led to inflammatory responses. Smaller GO sheets (lateral size of 50 to 250 nm) were more likely taken up by macrophages and could induce negative biological responses such as oxidative stress inside cells [56]. Jia *et al*. found that among three different lateral sizes of graphene

and GO including small (~30 nm), medium (~300 nm) and large (~2 μm) sizes, the small graphene and GO induced more cytotoxicity, DNA damage, and reactive oxygen species production in human embryonic kidney 293 (HEK 293T) cells compared to medium and large sizes [55]. On the contrary, Yue *et al*. reported that the larger GO (lateral size of 2 μm) induced higher level of the inflammatory responses of the murine peritoneal macrophages compared to the smaller GO (lateral size of 350 nm), even though they showed similar uptake amount by the macrophages [58]. Roberts *et al*. performed *in vivo* study in mice exposed to graphite nanoplatelet via pharyngeal aspiration. They reported that graphite nanoplatelet with lateral size of 5 and 20 μm at a dose of 40 μg/mouse induced more lung inflammation, injury in lavage fluid, and an increase tissue gene expression than 1 μm graphite nanoplatelet, whereas no toxicity effects were observed at a low dose of 4 μg/mouse [59].

Surface chemistry of GRMs such as C/O ratio and functionaltization is linked to the hydrophilicity of the materials and can affect the aggregation and dispersion of the GRMs in different media as well as the interaction between GRMs and cells. A study reported that GO induced higher oxidative and genotoxic stress in HEK 293T cells than graphene because GO has higher oxygen content leading to higher surface activity and better adherent to biomolecules [55]. Duch *et al*. compared the biocompatibility of graphene flakes (produced by ultrasonication of natural graphite) and GO in the lung *in vivo* and *in vitro*. The *in vivo* results in mice revealed that GO caused acute lung injury and inflammation, while graphene induced minimal inflammation in lung. For *in vitro* study, GO induced more toxic effects to mouse alveolar macrophages and epithelial cells compared to graphene flakes such as an increase in mitochondrial respiration rate, reactive oxygen species (ROS) generation, and an activation of inflammatory and apoptotic pathways [60]. Similarly, *in vivo* inhalation study showed that Sprague-Dawley rats exposed to GNP up to 1.88 mg/m^3 did not show any dose-dependent effects for body and organ weights, inflammatory responses in bronchoalveolar lavage fluid, and blood biochemical parameters at 1 and 28 days after exposure [61]. However, some studies reported that GO showed no obvious cytotoxic effects towards human alveolar epithelial cells (A549), which was probably due to the oxygen-containing groups on GO surface such as carboxyl, epoxy, and hydroxyl that could lessen the cytotoxic effects [62,63].

The functionalization on the surface of GRMs were studied to improve the solubility and biocompatibility of the GRMs in various biological systems [64,65]. For instance, Sasidharan *et al*. revealed that pristine GNP above 50 μg/mL induced a decrease in metabolic activity of

murine RAW 264.7 macrophages at 48 h time point, whereas GNP covalently bound to polyethylene glycol (PEG) did not show any reduction in metabolic activity up to a maximum tested concentration of 75 μg/mL. Moreover, the intracellular ROS formation was increased for cells treated with pristine GNP at 24 h, while PEG-functionalized GNP showed insignificant amount of ROS formation. The authors suggested that the negative cellular impact was due to the hydrophobicity of pristine GNP that may favor the interaction with the cellular plasma membrane. The accumulation of the pristine GNP bound to plasma membrane could block the transportation of nutrients and ions into the cells, which triggered the ROS formation [64].

1.5 Exposure to GRMs and Nanoparticles (NPs) Released from GRM-Containing Polymers

With an increasing demand of GRMs and the GRM-containing products, occupational exposure during the manufacturing of the GRMs and the products containing GRMs is unavoidable. Knowledge about the toxicity of GRMs is necessary for the regulations of the occupational exposure limit (OEL) to prevent the adverse health effects on the workers. Up to now, there is no legally binding OEL for GRMs due to limited number of *in vivo* toxicity data on GRMs. Nevertheless, researchers have reported the estimated OEL for some GRMs. The estimated OEL for GO was 18 μg/m^3, which was derived from a multi-path particle dosimetry (MPPD) model based on no observed adverse effect level (NOAEL) from a sub-chronic inhalation study in rats [66]. Limited number of studies reported the estimated occupational exposure to GRMs. For example, the occupational inhalation exposure to GNP was estimated at 212 μg/m^3 based on data reported in inhalation exposure studies [67]. Lovén *et al*. measured the concentration of GNP and GO using optical-thermal analysis in personal breathing zone of the workers in workplaces dealing with ink formulations and surface coating. The highest occupational exposure to GNP and GO was 5.6 μg/m^3, which corresponded to an 8-h average of 1.2 μg/m^3 [68].

Not only the occupational exposure to GRMs in the manufacturing phase, but also the exposure to consumers during the use phase and end-of-life of the products is inevitable. During the use phase of the nanomaterial-containing products, nanomaterials embedded in the matrix may be unintentionally released as free-standing nanomaterials or matrix-bound nanomaterials by chemical degradation (weathering) and/or mechanical process [69,70]. At the end of life of the products, one of the possible scenarios that can occur is combustion, which can take place by an accidental fire or a waste incineration. However, little is known about the release of GRMs from the GRM-containing materials. For example, Bernard *et al*. investigated the fate of GO in

the polyurethane (PU) composites when exposed to UV. They reported the considerable accumulation of GO on the surface of the composite due to the degradation of the PU matrix [71]. The release of GNP from the polylactic acid/GNP/MWCNT film was induced by the swelling and dissolution of the polylactic acid in food simulants, ethanol and acetic acid, at 90 °C for 4 h [72]. Kotsilkov *et al*. found that GNP could be released from the biodegradable polymer during the combustion [73].

1.6 Particle Deposition and Clearance Mechanism in the Lung

Inhalation is one of the major human exposure routes to airborne particles. Figure 1.3 illustrates the human respiratory airway and the related deposition mechanism in each region. The respiratory system consists of three regions including head airways region, lung airways region, and pulmonary or alveolar region [74]. The head airways region consists of nose, mouth, pharynx and larynx and functions to warm and humidify the inhaled air. The lung airways, also called tracheobronchial region, starts from the trachea until the terminal bronchioles. The deepest region of the lung is the alveolar region consisting of a number of small thin sacs called alveoli, whose function is to exchange oxygen and carbon dioxide to the adjacent bloodstream in capillary network. There are three major types of alveolar cells. The first is an alveolar epithelium type I, which has squamous shape covering 95% of the alveolar surface [75]. The second is a cuboidal-shaped alveolar epithelium type II, which can secrete the surfactant to reduce the surface tension in the lung and can renew and repair the epithelium type I and II cells. Both alveolar epithelium type I and II are components of alveolar wall. The ratio of the amount of epithelium type I to type II is approximately 1:2 [75]. Finally, alveolar macrophages, the phagocytic cells, are responsible for removing foreign particles from the respiratory tract.

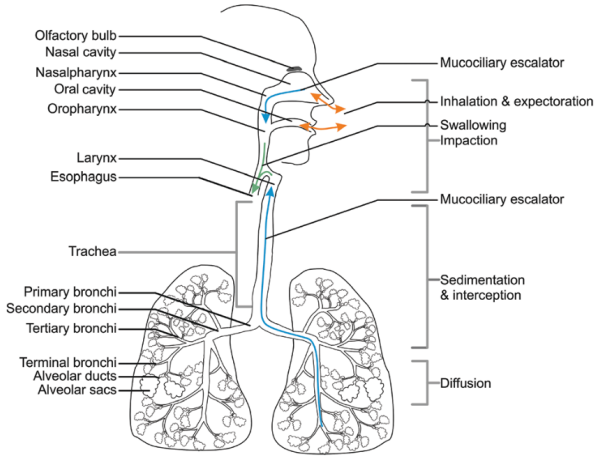

Figure 1.3 Human respiratory tract and the deposition mechanisms of the inhaled airborne particles in each part of the airways (Extracted from [76])

When aerosols enter the respiratory tract, they may deposit in each region via three major mechanisms including inertial impaction, gravitational sedimentation, and Brownian diffusion, while turbulence mixing, interception, and electrostatic precipitation are of less importance [77], or they may be exhaled. The degree and region of particle deposition mechanism in the respiratory airway is driven by particle characteristics such as size and density, airway geometry such as airway radius and branching angle, and breathing pattern such as residual time and particle velocity [74,76]. This section focuses on three main particle deposition mechanisms (impaction, sedimentation, and Brownian diffusion) in the respiratory tract.

Impaction mechanism depends on inertia of particles, which is a property to withstand the change of their existing status of motion. When the inhaled air flows through the respiratory tract, it must pass a sequence of direction changes. When the air changes direction, due to their inertia, particles continue to follow their original direction for a short distance resulting in the deposition of some particles that are near the airway wall. The probability of inertial impaction in the respiratory airway depends on Stokes number (Stk), which is the ratio of the stopping distance of a particle to airway dimensions (Equation 1.1). Since small particles can follow the air streamline, the impaction mechanism mostly affects larger particles, typically at the large airways i.e. dividing points from the trachea to the bronchi and to a less extent other bifurcations [74].

$$Stk = \frac{S}{d_c} = \frac{\tau U}{d_c} = \frac{\rho_p d_p^2 C_c U}{18\eta d_c} \qquad \text{Equation 1.1}$$

Sedimentation is an important deposition mechanism in smaller airways and alveolar region. The probability of the sedimentation is associated with the ratio of the settling distance ($terminal\ settling\ velocity\ (V_{TS}) \times residence\ time$) to the airway diameter. Equation 1.2 is the terminal settling velocity, V_{TS}, in a laminar regime (Re < 1). It is important to note that under the normal breathing condition, the airflow in the trachea and bronchi can be turbulent at the highest flow rates, while the airflow in other parts of airways is laminar. However, the laminar flow in smaller airways is not fully developed due to their relatively short length compared to dimeter [74].

$$V_{TS} = \frac{\rho_p d_p^2 g C_c}{18\eta} \; for\ Re < 1 \qquad \text{Equation 1.2}$$

Diffusion mechanism prevails for the deposition of particles smaller than 0.5 μm in the small airways and alveoli. The movement of submicron-sized particles is governed by Brownian motion, which is a random motion caused by the impact of gas molecules on these particles. The

likelihood of the diffusion deposition is determined by the ratio between root-mean-square displacement, x_{rms}, to the airway diameter. As shown in Equation 1.3, x_{rms} depends on diffusion coefficient, D (Equation 1.4), and the residence time, t, of the particles in the airways [74].

$$x_{rms} = \sqrt{2Dt} \qquad \text{Equation 1.3}$$

$$D = \frac{kTC_c}{3\pi\eta d_p} \qquad \text{Equation 1.4}$$

When the particles deposit in the lung, their fates depend on their physicochemical properties and the region of the lung they deposit. The surfaces of the head and lung airways (upper airway) are lined with mucus, which is transported to the pharynx by ciliary activity and then swallowed to the gastrointestinal tract [74]. The mucociliary clearance can transport the particles in the upper airway out of the respiratory system within hours. Particles deposited in the alveolar region of the lung have different fates from the ones deposited in the upper airway and take considerably longer time over months or years to be removed from the respiratory tract. Alveolar macrophage internalizes insoluble particles that deposit in alveolar region and dissolves them or transports them to the lymph nodes or to the upper airway where they can be removed by mucociliary clearance. The soluble particles can cross alveolar membrane to the bloodstream and translocate to other organs [74].

1.7 Research Objectives and Outline of the Thesis

Even though GRM-reinforced polymer composites have been widely studied in terms of their mechanical properties, flame retardancy, and electrical properties, there are still plenty of combinations of GRMs and epoxy/hardener system to be investigated. Moreover, an increasing number of the production of GRMs and GRM-based products led to the requirement to understand their potential health risks related to their life time *i.e.* production, use, and end-of-life, for prompting the safety regulations. However, the available information about the potential release of particles from the GRM-based composite and their associated hazards is still limited.

This thesis aims to support the hypotheses that the structure of hardener and fillers including GNP and DOPO in epoxy composites can affect the composite's properties, and the physicochemical properties of GRMs including their shape, lateral dimension, and C/O ratio can affect their toxicity. Moreover, when GRMs are used as nanofillers in epoxy composites, their physicochemical properties can affect the interaction between epoxy and GRM surface, which play an important role on the release mechanisms of aerosols from the epoxy composites.

Therefore, the main objectives of this thesis are three-fold and three main studies have been conducted according to each objective. Firstly, to investigate the effects of GNP combined with DOPO as additives in epoxy composite (DGEBA and polyetheramine) in terms of mechanical reinforcement, flame retardancy, and electrical properties (Chapter 2). Secondly, to study the characteristics and the potential hazard of the pristine GRMs and the particles released from the GRM-containing epoxy composites by abrasion, which is a process that could induce the release of nanoparticles from the composites during the use phase (Chapter 3). Finally, to determine the characteristics and the potential biological impacts of the emissions from the combustion of GNP-reinforced epoxy composite and pure epoxy, which is a process that can occur at the end-of-life of the composites (Chapter 4).

Chapter 2 presents the fabrication and the characterization of mechanical reinforcement, flame retardancy, and electrical conductivity of epoxy resin filled with GNP and phosphorous flame retardant namely 9,10- dihydro-9-oxa-10-phosphaphenanthrene-10-oxide (DOPO). The epoxy resin (diglycidyl ether of bisphenol A), the linear structure hardener (polyetheramine), and the fabrication process used in this chapter were also applied to the following studies in Chapter 3 and 4. Moreover, the information about the properties of the GNP-reinforced epoxy nanocomposites, especially the mechanical properties and the flame retardancy property, was useful to help understanding the release mechanisms of airborne particles from the epoxy nanocomposites. This study has been published as

Netkueakul, W.; Fischer, B.; Walder, C.; Nüesch, F.; Rees, M.; Jovic, M.; Gaan, S.; Jacob, P.; Wang, J. Effects of Combining Graphene Nanoplatelet and Phosphorous Flame Retardant as Additives on Mechanical Properties and Flame Retardancy of Epoxy Nanocomposite. *Polymers (Basel).* **2020**, *12* (10), 2349. https://doi.org/10.3390/polym12102349.

In Chapter 3 and 4, the hazard assessments of the particles released from abrasion and combustion of GRM-reinforced epoxy composites are reported, respectively. Since the GRMs and the released particles could be small enough to reach alveolar region of the respiratory system, where the clearance of the nanomaterials is only via macrophages, the *in vitro* toxicity evaluations were performed on human macrophages (Chapter 3) and alveolar epithelial (Type II) cells (Chapter 4).

Chapter 3 involves the characterization and hazard assessment of pristine GRMs and the particles released from abrasion of GRM-epoxy composites using the human macrophages differentiated from THP-1 cells. This study has been published as

Netkueakul, W.; Korejwo, D.; Hammer, T.; Chortarea, S.; Rupper, P.; Braun, O.; Calame, M.; Rothen-Rutishauser, B.; Buerki-Thurnherr, T.; Wick, P.; Wang, J. Release of Graphene-Related Materials from Epoxy-Based Composites: Characterization, Quantification and Hazard Assessment in Vitro. *Nanoscale* **2020**, *12* (19), 10703–10722. https://doi.org/10.1039/C9NR10245K.

Chapter 4 shows the establishment of the system to investigate the physicochemical properties and the *in vitro* toxicity of the emissions from the combustion of GNP-reinforced epoxy compared to pure epoxy. The manuscript of this study has been submitted to *Environmental Science and Technology*.

In Chapter 5, the results obtained from the three studies are briefly summarized. In addition, the potential outlooks are proposed.

1.8 References

1. Geim, A.K..; Novoselov, K.S. The rise of graphene. *Nat. Mater.* **2007**, *6*, 183–191, doi:https://doi.org/10.1038/nmat1849.
2. Wick, P.; Louw-Gaume, A.E.; Kucki, M.; Krug, H.F.; Kostarelos, K.; Fadeel, B.; Dawson, K.A.; Salvati, A.; Vázquez, E.; Ballerini, L.; et al. Classification Framework for Graphene-Based Materials. *Angew. Chemie Int. Ed.* **2014**, *53*, 7714–7718, doi:10.1002/anie.201403335.
3. Sanchez, V.C.; Jachak, A.; Hurt, R.H.; Kane, A.B. Biological Interactions of Graphene-Family Nanomaterials: An Interdisciplinary Review. *Chem. Res. Toxicol.* **2012**, *25*, 15–34, doi:10.1021/tx200339h.
4. Ren, W.; Cheng, H.-M. The global growth of graphene. *Nat. Nanotechnol.* **2014**, *9*, 726–730, doi:10.1038/nnano.2014.229.
5. Kong, W.; Kum, H.; Bae, S.-H.; Shim, J.; Kim, H.; Kong, L.; Meng, Y.; Wang, K.; Kim, C.; Kim, J. Path towards graphene commercialization from lab to market. *Nat. Nanotechnol.* **2019**, *14*, 927–938, doi:10.1038/s41565-019-0555-2.
6. Mohan, V.B.; Lau, K.; Hui, D.; Bhattacharyya, D. Graphene-based materials and their composites: A review on production, applications and product limitations. *Compos. Part B Eng.* **2018**, *142*, 200–220, doi:10.1016/j.compositesb.2018.01.013.
7. Cataldi, P.; Athanassiou, A.; Bayer, I. Graphene Nanoplatelets-Based Advanced Materials and Recent Progress in Sustainable Applications. *Appl. Sci.* **2018**, *8*, 1438, doi:10.3390/app8091438.
8. Huang, H.; Su, S.; Wu, N.; Wan, H.; Wan, S.; Bi, H.; Sun, L. Graphene-Based Sensors for Human Health Monitoring. *Front. Chem.* **2019**, *7*, 1–26, doi:10.3389/fchem.2019.00399.
9. Peña-Bahamonde, J.; Nguyen, H.N.; Fanourakis, S.K.; Rodrigues, D.F. Recent advances in graphene-based biosensor technology with applications in life sciences. *J. Nanobiotechnology* **2018**, *16*, 75, doi:10.1186/s12951-018-0400-z.
10. Suvarnaphaet, P.; Pechprasarn, S. Graphene-Based Materials for Biosensors: A Review. *Sensors* **2017**, *17*, 2161, doi:10.3390/s17102161.

11. Zurutuza, A.; Marinelli, C. Challenges and opportunities in graphene commercialization. *Nat. Nanotechnol.* **2014**, *9*, 730–734, doi:10.1038/nnano.2014.225.
12. Garrington, A. The Graphene Market Will Reach $700m by 2031 Available online: https://www.idtechex.com/en/research-article/idtechex-the-graphene-market-will-reach-700m-by-2031/22414.
13. Szeluga, U.; Pusz, S.; Kumanek, B.; Olszowska, K.; Kobyliukh, A.; Trzebicka, B. Effect of graphene filler structure on electrical, thermal, mechanical, and fire retardant properties of epoxy-graphene nanocomposites - a review. *Crit. Rev. Solid State Mater. Sci.* **2021**, *46*, 152–187, doi:10.1080/10408436.2019.1708702.
14. Kim, H.; Abdala, A.A.; Macosko, C.W. Graphene/Polymer Nanocomposites. *Macromolecules* **2010**, *43*, 6515–6530, doi:10.1021/ma100572e.
15. Papageorgiou, D.G.; Kinloch, I.A.; Young, R.J. Mechanical properties of graphene and graphene-based nanocomposites. *Prog. Mater. Sci.* **2017**, *90*, 75–127, doi:10.1016/j.pmatsci.2017.07.004.
16. Meng, Q.; Wu, H.; Zhao, Z.; Araby, S.; Lu, S.; Ma, J. Free-standing, flexible, electrically conductive epoxy/graphene composite films. *Compos. Part A Appl. Sci. Manuf.* **2017**, *92*, 42–50, doi:10.1016/j.compositesa.2016.10.028.
17. Meng, Q.; Zhao, Y.; Liu, Z.; Han, S.; Lu, S.; Liu, T. Flexible strain sensors based on epoxy/graphene composite film with long molecular weight curing agents. *J. Appl. Polym. Sci.* **2019**, *136*, 1–10, doi:10.1002/app.47906.
18. Shi, G.; Zhao, Z.; Pai, J.H.; Lee, I.; Zhang, L.; Stevenson, C.; Ishara, K.; Zhang, R.; Zhu, H.; Ma, J. Highly Sensitive, Wearable, Durable Strain Sensors and Stretchable Conductors Using Graphene/Silicon Rubber Composites. *Adv. Funct. Mater.* **2016**, *26*, 7614–7625, doi:10.1002/adfm.201602619.
19. Zhang, B.X.; Hou, Z.L.; Yan, W.; Zhao, Q.L.; Zhan, K.T. Multi-dimensional flexible reduced graphene oxide/polymer sponges for multiple forms of strain sensors. *Carbon N. Y.* **2017**, *125*, 199–206, doi:10.1016/j.carbon.2017.09.055.
20. Li, Z.J.; Wang, F.S.; Lai, Y.C.; Shi, Z.E.; Yu, Y.H. Flexible epoxy graphene thermoset with excellent weather and corrosion resistance. *Prog. Org. Coatings* **2021**, *151*, 106052, doi:10.1016/j.porgcoat.2020.106052.
21. Wu, H.; Cheng, L.; Liu, C.; Lan, X.; Zhao, H. Engineering the interface in graphene oxide/epoxy composites using bio-based epoxy-graphene oxide nanomaterial to achieve superior anticorrosion performance. *J. Colloid Interface Sci.* **2021**, *587*, 755–766, doi:10.1016/j.jcis.2020.11.035.
22. Han, S.; Meng, Q.; Xing, K.; Araby, S.; Yu, Y.; Mouritz, A.; Ma, J. Epoxy/graphene film for lifecycle self-sensing and multifunctional applications. *Compos. Sci. Technol.* **2020**, *198*, 108312, doi:10.1016/j.compscitech.2020.108312.
23. Han, S.; Chand, A.; Araby, S.; Cai, R.; Chen, S.; Kang, H.; Cheng, R.; Meng, Q. Thermally and electrically conductive multifunctional sensor based on epoxy/graphene composite. *Nanotechnology* **2020**, *31*, doi:10.1088/1361-6528/ab5042.
24. Wan, Y.-J.; Yu, S.-H.; Yang, W.-H.; Zhu, P.-L.; Sun, R.; Wong, C.-P.; Liao, W.-H. Tuneable cellular-structured 3D graphene aerogel and its effect on electromagnetic interference shielding performance and mechanical properties of epoxy composites. *RSC Adv.* **2016**, *6*, 56589–56598, doi:10.1039/C6RA09459G.
25. Graphene products: introduction and market status Available online: https://www.graphene-

info.com/graphene-products.

26. Peleg, R. Haydale files joint patent with Airbus as part of GraCELS-2 project Available online: https://www.graphene-info.com/haydale-files-joint-patent-airbus-part-gracels-2-project.
27. Yang, S.Y.; Lin, W.N.; Huang, Y.L.; Tien, H.W.; Wang, J.Y.; Ma, C.C.M.; Li, S.M.; Wang, Y.S. Synergetic effects of graphene platelets and carbon nanotubes on the mechanical and thermal properties of epoxy composites. *Carbon N. Y.* **2011**, *49*, 793–803, doi:10.1016/j.carbon.2010.10.014.
28. Chatterjee, S.; Nafezarefi, F.; Tai, N.H.; Schlagenhauf, L.; N??esch, F.A.; Chu, B.T.T. Size and synergy effects of nanofiller hybrids including graphene nanoplatelets and carbon nanotubes in mechanical properties of epoxy composites. *Carbon N. Y.* **2012**, *50*, 5380–5386, doi:10.1016/j.carbon.2012.07.021.
29. Liu, S.; Fang, Z.; Yan, H.; Wang, H. Superior flame retardancy of epoxy resin by the combined addition of graphene nanosheets and DOPO. *RSC Adv.* **2016**, *6*, 5288–5295, doi:10.1039/C5RA25988F.
30. Yan, W.; Zhang, M.Q.; Yu, J.; Nie, S.Q.; Zhang, D.Q.; Qin, S.H. Synergistic Flame-retardant Effect of Epoxy Resin Combined with Phenethyl-bridged DOPO Derivative and Graphene Nanosheets. *Chinese J. Polym. Sci. (English Ed.* **2019**, *37*, 79–88, doi:10.1007/s10118-019-2175-6.
31. Shi, Y.; Yu, B.; Zheng, Y.; Yang, J.; Duan, Z.; Hu, Y. Design of reduced graphene oxide decorated with DOPO-phosphanomidate for enhanced fire safety of epoxy resin. *J. Colloid Interface Sci.* **2018**, *521*, 160–171, doi:10.1016/j.jcis.2018.02.054.
32. Qian, X.; Song, L.; Yu, B.; Wang, B.; Yuan, B.; Shi, Y.; Hu, Y.; Yuen, R.K.K. Novel organic–inorganic flame retardants containing exfoliated graphene: preparation and their performance on the flame retardancy of epoxy resins. *J. Mater. Chem. A* **2013**, *1*, 6822, doi:10.1039/c3ta10416h.
33. Liao, S.H.; Liu, P.L.; Hsiao, M.C.; Teng, C.C.; Wang, C.A.; Ger, M. Der; Chiang, C.L. One-step reduction and functionalization of graphene oxide with phosphorus-based compound to produce flame-retardant epoxy nanocomposite. *Ind. Eng. Chem. Res.* **2012**, *51*, 4573–4581, doi:10.1021/ie2026647.
34. Guo, W.; Yu, B.; Yuan, Y.; Song, L.; Hu, Y. In situ preparation of reduced graphene oxide/DOPO-based phosphonamidate hybrids towards high-performance epoxy nanocomposites. *Compos. Part B Eng.* **2017**, *123*, 154–164, doi:10.1016/j.compositesb.2017.05.024.
35. Liu, S.; Fang, Z.; Yan, H.; Chevali, V.S.; Wang, H. Synergistic flame retardancy effect of graphene nanosheets and traditional retardants on epoxy resin. *Compos. Part A Appl. Sci. Manuf.* **2016**, *89*, 26–32, doi:10.1016/j.compositesa.2016.03.012.
36. Laoutid, F.; Bonnaud, L.; Alexandre, M.; Lopez-Cuesta, J.M.; Dubois, P. New prospects in flame retardant polymer materials: From fundamentals to nanocomposites. *Mater. Sci. Eng. R Reports* **2009**, *63*, 100–125, doi:10.1016/j.mser.2008.09.002.
37. Lu, S.-Y.; Hamerton, I. Recent developments in the chemistry of halogen-free flame retardant polymers. *Prog. Polym. Sci.* **2002**, *27*, 1661–1712, doi:10.1016/S0079-6700(02)00018-7.
38. Salmeia, K.A.; Gooneie, A.; Simonetti, P.; Nazir, R.; Kaiser, J.P.; Rippl, A.; Hirsch, C.; Lehner, S.; Rupper, P.; Hufenus, R.; et al. Comprehensive study on flame retardant polyesters from phosphorus additives. *Polym. Degrad. Stab.* **2018**, *155*, 22–34, doi:10.1016/j.polymdegradstab.2018.07.006.
39. Gaan, S.; Liang, S.; Mispreuve, H.; Perler, H.; Naescher, R.; Neisius, M. Flame retardant flexible polyurethane foams from novel DOPO-phosphonamidate additives. *Polym. Degrad. Stab.* **2015**, *113*, 180–188, doi:10.1016/j.polymdegradstab.2015.01.007.
40. Wendels, S.; Chavez, T.; Bonnet, M.; Salmeia, K.A.; Gaan, S. Recent developments in organophosphorus

flame retardants containing P-C bond and their applications. *Materials (Basel).* **2017**, *10*, doi:10.3390/ma10070784.

41. He, M.; Zhang, D.; Zhao, W.; Qin, S.; Yu, J. Flame retardant and thermal decomposition mechanism of poly(butylene terephthalate)/DOPO-HQ composites. *Polym. Compos.* **2019**, *40*, 974–985, doi:10.1002/pc.24772.
42. Hendriks, H.S.; Meijer, M.; Muilwijk, M.; Van Den Berg, M.; Westerink, R.H.S. A comparison of the in vitro cyto- and neurotoxicity of brominated and halogen-free flame retardants: Prioritization in search for safe(r) alternatives. *Arch. Toxicol.* **2014**, *88*, 857–869, doi:10.1007/s00204-013-1187-1.
43. Hirsch, C.; Striegl, B.; Mathes, S.; Adlhart, C.; Edelmann, M.; Bono, E.; Gaan, S.; Salmeia, K.A.; Hoelting, L.; Krebs, A.; et al. Multiparameter toxicity assessment of novel DOPO-derived organophosphorus flame retardants. *Arch. Toxicol.* **2017**, *91*, 407–425, doi:10.1007/s00204-016-1680-4.
44. Costa, L.; Giordano, G. Developmental neurotoxicity of polybrominated diphenyl ether (PBDE) flame retardants. *Neurotoxicology* **2007**, *28*, 1047–1067, doi:10.1016/j.neuro.2007.08.007.
45. Ou, L.; Song, B.; Liang, H.; Liu, J.; Feng, X.; Deng, B.; Sun, T.; Shao, L. Toxicity of graphene-family nanoparticles: a general review of the origins and mechanisms. *Part. Fibre Toxicol.* **2016**, *13*, 57, doi:10.1186/s12989-016-0168-y.
46. Jarosz, A.; Skoda, M.; Dudek, I.; Szukiewicz, D. Oxidative Stress and Mitochondrial Activation as the Main Mechanisms Underlying Graphene Toxicity against Human Cancer Cells. *Oxid. Med. Cell. Longev.* **2016**, *2016*, 1–14, doi:10.1155/2016/5851035.
47. Seabra, A.B.; Paula, A.J.; de Lima, R.; Alves, O.L.; Duran, N. Nanotoxicity of graphene and graphene oxide. *Chem. Res. Toxicol.* **2014**, *27*, 159–168, doi:10.1021/tx400385x.
48. Yang, K.; Li, Y.; Tan, X.; Peng, R.; Liu, Z. Behavior and Toxicity of Graphene and Its Functionalized Derivatives in Biological Systems. *Small* **2013**, *9*, 1492–1503, doi:10.1002/smll.201201417.
49. Jastrzębska, A.M.; Kurtycz, P.; Olszyna, A.R. Recent advances in graphene family materials toxicity investigations. *J. Nanoparticle Res.* **2012**, *14*, doi:10.1007/s11051-012-1320-8.
50. Ema, M.; Gamo, M.; Honda, K. A review of toxicity studies on graphene-based nanomaterials in laboratory animals. *Regul. Toxicol. Pharmacol.* **2017**, *85*, 7–24, doi:10.1016/j.yrtph.2017.01.011.
51. Zhang, B.; Wei, P.; Zhou, Z.; Wei, T. Interactions of graphene with mammalian cells: Molecular mechanisms and biomedical insights. *Adv. Drug Deliv. Rev.* **2016**, *105*, 145–162, doi:10.1016/j.addr.2016.08.009.
52. Guo, R.; Mao, J.; Yan, L.T. Computer simulation of cell entry of graphene nanosheet. *Biomaterials* **2013**, *34*, 4296–4301, doi:10.1016/j.biomaterials.2013.02.047.
53. Schinwald, A.; Murphy, F.A.; Jones, A.; MacNee, W.; Donaldson, K. Graphene-Based Nanoplatelets: A New Risk to the Respiratory System as a Consequence of Their Unusual Aerodynamic Properties. *ACS Nano* **2012**, *6*, 736–746, doi:10.1021/nn204229f.
54. Bussy, C.; Ali-Boucetta, H.; Kostarelos, K. Safety Considerations for Graphene: Lessons Learnt from Carbon Nanotubes. *Acc. Chem. Res.* **2013**, *46*, 692–701, doi:10.1021/ar300199e.
55. Jia, P.-P.; Sun, T.; Junaid, M.; Yang, L.; Ma, Y.-B.; Cui, Z.-S.; Wei, D.-P.; Shi, H.-F.; Pei, D.-S. Nanotoxicity of different sizes of graphene (G) and graphene oxide (GO) in vitro and in vivo. *Environ. Pollut.* **2019**, *247*, 595–606, doi:10.1016/j.envpol.2019.01.072.
56. Ma, J.; Liu, R.; Wang, X.; Liu, Q.; Chen, Y.; Valle, R.P.; Zuo, Y.Y.; Xia, T.; Liu, S. Crucial role of lateral

size for graphene oxide in activating macrophages and stimulating pro-inflammatory responses in cells and animals. *ACS Nano* **2015**, *9*, 10498–10515, doi:10.1021/acsnano.5b04751.

57. Li, Y.; Yuan, H.; von dem Bussche, A.; Creighton, M.; Hurt, R.H.; Kane, A.B.; Gao, H. Graphene microsheets enter cells through spontaneous membrane penetration at edge asperities and corner sites. *Proc. Natl. Acad. Sci.* **2013**, *110*, 12295–12300, doi:10.1073/pnas.1222276110.
58. Yue, H.; Wei, W.; Yue, Z.; Wang, B.; Luo, N.; Gao, Y.; Ma, D.; Ma, G.; Su, Z. The role of the lateral dimension of graphene oxide in the regulation of cellular responses. *Biomaterials* **2012**, *33*, 4013–4021, doi:10.1016/j.biomaterials.2012.02.021.
59. Roberts, J.R.; Mercer, R.R.; Stefaniak, A.B.; Seehra, M.S.; Geddam, U.K.; Chaudhuri, I.S.; Kyrlidis, A.; Kodali, V.K.; Sager, T.; Kenyon, A.; et al. Evaluation of pulmonary and systemic toxicity following lung exposure to graphite nanoplates: a member of the graphene-based nanomaterial family. *Part. Fibre Toxicol.* **2015**, *13*, 34, doi:10.1186/s12989-016-0145-5.
60. Duch, M.C.; Budinger, G.R.S.; Liang, Y.T.; Soberanes, S.; Urich, D.; Chiarella, S.E.; Campochiaro, L.A.; Gonzalez, A.; Chandel, N.S.; Hersam, M.C.; et al. Minimizing oxidation and stable nanoscale dispersion improves the biocompatibility of graphene in the lung. *Nano Lett.* **2011**, *11*, 5201–5207, doi:10.1021/nl202515a.
61. Kim, J.K.; Shin, J.H.; Lee, J.S.; Hwang, J.H.; Lee, J.H.; Baek, J.E.; Kim, T.G.; Kim, B.W.; Kim, J.S.; Lee, G.H.; et al. 28-Day inhalation toxicity of graphene nanoplatelets in Sprague-Dawley rats. *Nanotoxicology* **2016**, *10*, 891–901, doi:10.3109/17435390.2015.1133865.
62. Chang, Y.; Yang, S.T.; Liu, J.H.; Dong, E.; Wang, Y.; Cao, A.; Liu, Y.; Wang, H. In vitro toxicity evaluation of graphene oxide on A549 cells. *Toxicol. Lett.* **2011**, *200*, 201–210, doi:10.1016/j.toxlet.2010.11.016.
63. Jin, C.; Wang, F.; Tang, Y.; Zhang, X.; Wang, J.; Yang, Y. Distribution of Graphene Oxide and TiO2-Graphene Oxide Composite in A549 Cells. *Biol. Trace Elem. Res.* **2014**, *159*, 393–398, doi:10.1007/s12011-014-0027-3.
64. Sasidharan, A.; Panchakarla, L.S.; Sadanandan, A.R.; Ashokan, A.; Chandran, P.; Girish, C.M.; Menon, D.; Nair, S. V.; Rao, C.N.R.; Koyakutty, M. Hemocompatibility and macrophage response of pristine and functionalized graphene. *Small* **2012**, *8*, 1251–1263, doi:10.1002/smll.201102393.
65. Sasidharan, A.; Panchakarla, L.S.; Chandran, P.; Menon, D.; Nair, S.; Rao, C.N.R.; Koyakutty, M. Differential nano-bio interactions and toxicity effects of pristine versus functionalized graphene. *Nanoscale* **2011**, *3*, 2461, doi:10.1039/c1nr10172b.
66. Lee, Y.-S.; Sung, J.-H.; Song, K.-S.; Kim, J.-K.; Choi, B.-S.; Yu, I.-J.; Park, J.-D. Derivation of occupational exposure limits for multi-walled carbon nanotubes and graphene using subchronic inhalation toxicity data and a multi-path particle dosimetry model. *Toxicol. Res. (Camb).* **2019**, *8*, 580–586, doi:10.1039/C9TX00026G.
67. Spinazzè, A.; Cattaneo, A.; Borghi, F.; Del Buono, L.; Campagnolo, D.; Rovelli, S.; Cavallo, D.M. Probabilistic approach for the risk assessment of nanomaterials: A case study for graphene nanoplatelets. *Int. J. Hyg. Environ. Health* **2019**, *222*, 76–83, doi:10.1016/j.ijheh.2018.08.011.
68. Lovén, K.; Franzén, S.M.; Isaxon, C.; Messing, M.E.; Martinsson, J.; Gudmundsson, A.; Pagels, J.; Hedmer, M.; Lovén, K.; Franzén, S.M.; et al. Emissions and exposures of graphene nanomaterials, titanium dioxide nanofibers, and nanoparticles during down-stream industrial handling. *J. Expo. Sci.*

Environ. Epidemiol. **2021**, *31*, 736–752, doi:10.1038/s41370-020-0241-3.

69. Hirth, S.; Cena, L.; Cox, G.; Tomović, Ž.; Peters, T.; Wohlleben, W. Scenarios and methods that induce protruding or released CNTs after degradation of nanocomposite materials Technology Transfer and Commercialization of Nanotechnology. *J. Nanoparticle Res.* **2013**, *15*, doi:10.1007/s11051-013-1504-x.
70. Vílchez, A.; Fernández-Rosas, E.; González-Gálvez, D.; Vázquez-Campos, S. Nanomaterials Release from Nano-Enabled Products. In *Indoor and Outdoor Nanoparticles: Determinants of Release and Exposure Scenarios*; Viana, M., Ed.; Springer International Publishing Switzerland, 2015; pp. 127–158 ISBN 1433-6863r978-3-642-03970-6.
71. Bernard, C.; Nguyen, T.; Pellegrin, B.; Holbrook, R.D.; Zhao, M.; Chin, J. Fate of graphene in polymer nanocomposite exposed to UV radiation. *J. Phys. Conf. Ser.* **2011**, *304*, 012063, doi:10.1088/1742-6596/304/1/012063.
72. Velichkova, H.; Petrova, I.; Kotsilkov, S.; Ivanov, E.; Vitanov, N.K.; Kotsilkova, R. Influence of polymer swelling and dissolution into food simulants on the release of graphene nanoplates and carbon nanotubes from poly(lactic) acid and polypropylene composite films. *J. Appl. Polym. Sci.* **2017**, *134*, 45469, doi:10.1002/app.45469.
73. Kotsilkov, S.; Ivanov, E.; Vitanov, N. Release of Graphene and Carbon Nanotubes from Biodegradable Poly(Lactic Acid) Films during Degradation and Combustion: Risk Associated with the End-of-Life of Nanocomposite Food Packaging Materials. *Materials (Basel).* **2018**, *11*, 2346, doi:10.3390/ma11122346.
74. Hinds, W.C. *Aerosol Technology: Properties, Behavior, and Measurement of Airborne Particles*; 2nd ed.; Wiley-Interscience: New York, 1999; ISBN 0-471-19410-7.
75. Knudsen, L.; Ochs, M. The micromechanics of lung alveoli: structure and function of surfactant and tissue components. *Histochem. Cell Biol.* **2018**, *150*, 661–676, doi:10.1007/s00418-018-1747-9.
76. Bierkandt, F.S.; Leibrock, L.; Wagener, S.; Laux, P.; Luch, A. The impact of nanomaterial characteristics on inhalation toxicity. *Toxicol. Res. (Camb).* **2018**, *7*, 321–346, doi:10.1039/c7tx00242d.
77. Darquenne, C. Aerosol Deposition in Health and Disease. *J. Aerosol Med. Pulm. Drug Deliv.* **2012**, *25*, 140–147, doi:10.1089/jamp.2011.0916.

Chapter 2

Effects of Combining Graphene Nanoplatelet and Phosphorous Flame Retardant as Additives on Mechanical Properties and Flame Retardancy of Epoxy Nanocomposite

Woranan Netkueakul [1,2], Beatrice Fischer [3], Christian Walder [3], Frank Nüesch [3], Marcel Rees [4], Milijana Jovic [5], Sabyasachi Gaan [5], Peter Jacob [6] and Jing Wang [1,2,*]

[1] Institute of Environmental Engineering, ETH Zurich (Swiss Federal Institute of Technology Zurich), Zurich 8093, Switzerland

[2] Laboratory for Advanced Analytical Technologies, Empa – Swiss Federal Laboratories for Materials Science and Technology, Dübendorf 8600, Switzerland

[3] Laboratory for Functional Polymers, Empa – Swiss Federal Laboratories for Materials Science and Technology, Dübendorf 8600, Switzerland

[4] Laboratory for Mechanical Systems Engineering, Empa – Swiss Federal Laboratories for Materials Science and Technology, Dübendorf 8600, Switzerland

[5] Additives and Chemistry Group, Advanced Fibers, Empa – Swiss Federal Laboratories for Materials Science and Technology, St. Gallen 9014, Switzerland

[6] Electronics and Reliability Center, Empa – Swiss Federal Laboratories for Materials Science and Technology, Dübendorf 8600, Switzerland

* Correspondence: jing.wang@ifu.baug.ethz.ch

Author contributions

W.N. fabricated the nanocomposites, performed all experiment except TGA, DSC and electrical discharge, analyzed all data, and wrote the manuscript. B.F. performed TGA and DSC analysis and supported the mechanical property measurement. C.W. performed DMTA analysis. F.N. advised and supported the measurement and analysis of TGA and mechanical property. M.R. supported the fabrication of the nanocomposites. M.J. and S.G. supported the experiments and analysis related to cone calorimetry. J.W. acquired the funding and supervised the study. All authors have read, reviewed, and agreed to the published version of the manuscript.

This work has been published in *Polymers (Basel).* **2020**, *12* (10), 2349. DOI: 10.3390/polym12102349. This is a post-print version, differing from the published paper only in in terms of layout and formatting. The name convention of the epoxy composites filled with DOPO and/or GNP is EP/xDOPO/yGNP, where x and y are percentages by weight of DOPO and/or GNP added into epoxy resin.

Abstract

The effects of combining 0.1–5 wt % graphene nanoplatelet (GNP) and 3–30 wt % phosphorous flame retardant, 9,10- dihydro-9-oxa-10-phosphaphenanthrene-10-oxide (DOPO) as fillers in epoxy polymer on the mechanical, flame retardancy, and electrical properties of the epoxy nanocomposites was investigated. GNP was homogeneously dispersed into the epoxy matrix using a solvent-free three-roll milling process, while DOPO was incorporated into the epoxy resin by mechanical stirring at elevated temperature. The incorporation of DOPO reduced the crosslinking density of the epoxy resin. When using polyetheramine as a hardener, the structural rigidity effect of DOPO overshadowed the crosslinking effect and governed the flexural moduli of epoxy/DOPO resins. The flexural moduli of the nanocomposites were improved by adding GNP up to 5 wt % and DOPO up to 30 wt %, whereas the flexural strengths deteriorated when the GNP and DOPO loading were higher than 1 wt % and 10 wt %, respectively. Limited by the adverse effects on mechanical property, the loading combinations of GNP and DOPO within the range of 0-1 wt % and 0-10 wt %, respectively, in epoxy resin were further studied. Flame retardancy index (FRI), which depended on three parameters obtained from cone calorimetry, was considered to evaluate the flame retardancy of the epoxy composites. DOPO showed better performance than GNP as the flame retardant additive, while combining DOPO and GNP could further improve FRI to some extent. With the combination of 0.5 wt % GNP and 10 wt % DOPO, improvement in both mechanical properties and flame retardant efficiency of the nanocomposite was observed. Such a combination did not affect the electrical conductivity of the nanocomposites since the percolation threshold was at 1.6 wt % GNP. Our results enhance the understanding of the structure–property relationship of additive-filled epoxy resin composites and serve as a property constraining guidance for the composite manufacturing.

Keywords: nanocomposites; graphene nanoplatelets; mechanical properties; flame retardancy

2.1 Introduction

Epoxy resin (denoted as EP) is a thermoset polymer that has been extensively used for composite manufacturing due to its chemical and thermal resistance, excellent adhesion, and ease of processing [1]. Despite its attractive properties, the main disadvantages of epoxy resin are flammability [2], poor thermal conductivity, and brittleness. To manufacture epoxy thermosets, hardeners or curing agents can be employed for curing epoxy resin by crosslinking epoxy molecules forming the three-dimensional network. Among numerous kinds of hardeners

such as amines, anhydrides, phenols, and thiols, amines have been the most widely used hardeners. The chemical structure of amines, i.e. aliphatic, cycloaliphatic and aromatic play important roles in the mechanical properties and thermal properties of the cured epoxy resin [3,4]. For example, due to the more rigid structure of 4,4'-diamino diphenyl methane (DDM), which is an aromatic amine, the epoxy thermoset cured with DDM showed higher glass transition temperature as compared to the epoxy thermoset cured with polyetheramine, which is an aliphatic amine [3]. Moreover, the type of hardener was chosen according to the desired properties and the applications of the resulting thermoset. For example, polyetheramine, an aliphatic amine, has been used for surface coatings, adhesives and castings for artistic purposes since aliphatic amines usually are colorless after curing. Aromatic amines such as 4,4'-diaminodiphenyl sulfone (DDS) provide excellent heat and chemical resistance, so it has been applied in the aerospace industry.

Various flame retardants and reinforcing nanomaterials have been investigated as epoxy resin fillers to overcome the flammability of epoxy thermosets. 9,10- dihydro-9-oxa-10-phosphaphenanthrene-10-oxide (DOPO) is one of the phosphorous flame retardants (PFRs), which were proposed as an alternative to halogenated flame retardants due to concerns about the latter's toxic effects and environmental impacts [5,6]. Owing to its promising flame retardant efficiency, a number of studies have reported the effect of DOPO and its derivatives to enhance flame retardancy of epoxy composites [7–11]. The DOPO-incorporated epoxy resin cured with DDS and 2,4,6-tri (phenol-methylene-amide)-triazine with a phosphorous content of 3 wt % showed enhanced thermal stability as compared to the epoxy resin, but the glass transition temperature, flexural strength, and impact strength were decreased with increasing phosphorous content [7]. The flame inhibition mechanism of DOPO was proposed through a gas-phase reaction involving phosphorous oxide radical, PO, and H–PO fragment as reactive gas species [12]. However, incorporation of DOPO into epoxy resin is still a critical task because DOPO reacts with the epoxide group and thus can deteriorate the crosslinking density of epoxy resin, which is strongly dependent on the amount of epoxide groups, and might adversely affect the mechanical properties of the composites [7,10,13].

Graphene nanoplatelets (GNP) have been investigated as a filler in epoxy resin to enhance mechanical properties, thermal conductivity, electrical conductivity, and flame retardancy. Improved mechanical properties when adding GNP to epoxy resin have been reported, such as an increase in fracture toughness, flexural modulus, and hardness of the nanocomposites [14–

18]. Wang and colleagues found a significant improvement in electrical conductivity of the epoxy/GNP nanocomposite by six orders of magnitude with 3 wt % GNP as compared to neat epoxy resin [19]. Previous studies revealed that GNP can delay the combustion process by retarding the formation of volatile gases and forming continuous and compact char that can block the radiation and decrease the combustion temperature, which can lead to an enhanced flame retardant effectiveness of polymer/GNP nanocomposites [20–22]. However, using GNP as a flame retardant is challenging due to poor dispersion of GNP in the polymer matrix, weak interaction between graphene surface and polymer, and strong tendency to agglomerate at high concentrations [23].

The combination of GNP with other flame retardants has gained attention to further enhance the properties of the nanocomposites in terms of mechanical performance as well as flame retarding efficiency. Recent studies reported that the combination of DOPO and GNP could improve flame retardancy of epoxy thermosets [24,25]. For example, the combination of DOPO and GNP showed a synergistic effect on flame retardancy properties of epoxy nanocomposites, i.e., by adding 2.5 wt % DOPO and 2.5 wt % GNP, the peak heat release rate was significantly reduced from 1194 to 396 kW/m^2 [24]. Although studies have focused on the effects of combining GNP and DOPO on the flame retardancy property, there has not yet been an elaborate investigation on the effect of combining GNP and DOPO on mechanical properties of the composite. Especially, the role of DOPO in mechanical properties of the epoxy composites is still unclear. The incorporation of DOPO could cause negative effects on the mechanical properties of epoxy resin due to the decrease in crosslinking density by the reaction between DOPO and epoxy resin, which consumes epoxide groups [7,13]. However, some studies demonstrated that the incorporation of DOPO did not deteriorate the mechanical properties of the epoxy resin [26,27]. Wang and colleagues suggested that the mechanical properties of the epoxy/DOPO composites was not adversely affected because the constraining effect of the bulky DOPO group for the epoxy chain rotation could counteract the effect of the loss in crosslinking density [26]. In addition, too high concentration of GNP can lead to GNP agglomeration and worsen mechanical properties [23]. To our best knowledge, the effect of incorporation of DOPO as well as the combination of DOPO and GNP on the mechanical properties of the epoxy resin is still ambiguous and needs to be further studied.

Based on structural classification, the above-mentioned studies [7,26,27] employed the aromatic hardeners resulting in deteriorating mechanical properties when the DOPO amounts

exceeded certain thresholds. In our study, we aim to study the influence of DOPO on the mechanical properties of epoxy nanocomposite with another type of hardener as compared to previous studies. Therefore, we used an aliphatic amine, polyetheramine Jeffamine D-230, as a curing agent for epoxy resin (diglycidyl ether of bisphenol A). The solvent-free three-roll milling process was employed to disperse the GNP in the epoxy resin matrix. The influence of DOPO on the three-dimensional network structure of the epoxy resin was studied by assessing the crosslinking density. The flexural moduli of the epoxy nanocomposites with different loadings of DOPO and GNP were determined. Based on the mechanical properties, the maximum loading amounts of DOPO and GNP and their combination were chosen for further investigations. Flame retardancy of the composites was studied using cone calorimetry and the flame retardancy index (FRI) was applied to compare the flame retardancy efficiency among different samples. The results from this study revealed the appropriate formulation of DOPO-modified epoxy resin filled with GNP to achieve better overall performance especially the mechanical properties and flame retardancy. This study provides better understanding of the relationship between the structure of epoxy resin composites filled with two types of additives (DOPO and GNP) and their properties and facilitates the design of epoxy resin composites with desired properties.

2.2 Material and Methods

2.2.1 Materials

The epoxy resin used in this study was diglycidyl ether of bisphenol A (DGEBA, Araldite GY 250, Huntsman, Montgomery and Harris, TX, USA), which has an epoxy equivalent of 183–189 $g \cdot eq^{-1}$. The curing agent was polyetheramine Jeffamine D-230 (Huntsman, Montgomery and Harris, TX, USA), which has molecular weight (MW) of 230 $g \cdot mol^{-1}$ and amine hydrogen equivalent weight (AHEW) of 60 $g \cdot eq^{-1}$. The phosphorous-containing flame retardant 9,10-dihydro-9-oxa-10-phosphaphenanthrene-10-oxide (DOPO, MW = 216 $g \cdot mol^{-1}$) was purchased from Tokyo Chemical Industry (Tokyo, Japan). Graphene nanoplatelet xGNP M25 (carbon content > 99.5%, average particle diameters = 25 μm, thickness = 6–8 nm, typical surface area = 120–150 $m^2 \cdot g^{-1}$ and density = 2.2 $g \cdot cm^{-3}$) was purchased from XG Sciences, St. Louis, MO, USA.

2.2.2 Incorporation of DOPO into Epoxy Resin

The desired amount of DOPO was added into the epoxy resin. The mixture was then heated with continuous stirring until the temperature reached 160 °C and kept constant with continuous stirring for 5 h for complete reaction between DOPO and epoxy resin [26]. The amount of DOPO was 3 wt %, 10wt %, 20 wt % and 30 wt % of the epoxy resin matrix, which corresponded to the phosphorous content of 0.3, 1.0, 2.0 and 2.9 wt %, respectively.

2.2.3 Dispersion of GNP in Epoxy Resin

The dispersion method and manufacturing process of the composites was adapted from a previous study [28]. The desired amounts of GNP were added to epoxy resin or DOPO-incorporated epoxy resin (EP/DOPO). The components were mechanically mixed at 2000 rpm using an overhead mixer for 5 min. A three-roll mill machine (SDY200, Bühler AG, Uzwil, Switzerland) was employed to improve the dispersion of GNP in the polymer matrix. The mixture was passed through the three-roll mill for at least three times. Neat epoxy polymer was also prepared with the same method without any fillers.

2.2.4 Processing of Epoxy Resin

The ratio of resin/hardener was 100:32 for the composites without DOPO. For the EP/DOPO mixtures, since DOPO reacted with the epoxy groups, the amount of hardener added was adjusted according to the available epoxy groups obtained from the theoretical value as shown in the Appendix A. The mixture was mixed at 2000 rpm for 5 min. Afterward, the mixture was degassed at 80 °C for 2 min under vacuum. The formulation was transferred to a metal mold and cured at 80 °C for 12 h, and post-cured at 120 °C for 4 h. The mold was preheated at 80 °C for samples containing DOPO. All samples were allowed to cool down slowly to room temperature.

2.2.5 Characterization of GNP and EP/GNP/DOPO Composites and Measurement Procedures

Attenuated total reflection-Fourier transform infrared spectrometer (Agilent 640 FTIR spectrometer, Agilent technologies, Santa Clara, CA, USA) was used to characterize the functional groups of DOPO, epoxy resin, cured epoxy resins and cured EP/DOPO. The dispersion state of GNPs in the epoxy matrix was determined using an optical microscope (Zeiss, Oberkochen, Germany).

A discharge test was performed using an electrostatic Wimshurst machine as a high voltage source and the samples were placed adjacent to the spark gap formed by two metal spheres. The surface resistance was measured using a Keithley multimeter (model DMM7510, Keithley Instruments, Cleveland, OH, USA) with two-point electrodes. The samples had dimensions of 10 cm × 10 cm and 4 mm thickness.

The flexural modulus was evaluated by the three-point bending test according to ISO 178:2001 [29] using the Zwick Roell Z010 testing machine (ZwickRoell, Ulm, Germany) with a constant loading speed of 1 mm·min^{-1}. Five specimens from each sample were tested. The dimensions of the specimen were 1 cm × 8 cm × 4 cm (width × length × thickness). Scanning electron microscope (Nova NanoSEM 230, FEI company, Hillsboro, OR, USA) was employed to analyze the fracture surface of the samples after a three-point bending test.

In order to determine the crosslinking density, dynamic mechanical thermal analysis (DMTA) was performed using an advanced rheometric expansion system (Rheometric Scientific, Piscataway, NJ, USA) to obtain the storage elastic modulus and tan δ of the cured resins, which were important parameters for an estimation of the crosslinking density. The samples tested were neat epoxy and EP/10DOPO. Samples were analyzed with applying constant static force at 1 Hz and a strain of 0.05%. The scanning temperature was from −150 to 180 °C at a heating rate of 3 °C·min^{-1}. The sample dimensions were 10 mm × 50 mm and 4 mm thickness. The crosslinking density ($\rho(E')$) in mol·m^{-3} was evaluated using the kinetic theory of rubber elasticity as follows:

$$\boldsymbol{\rho(E') = \frac{E'}{3RT}} \qquad \text{Equation 2.1,}$$

where E' is storage elastic modulus (Pa) of cured resin at the peak temperature of tan δ + 40 °C to ensure the rubbery stage of the sample. R is the gas constant (8.3145 m^3·Pa·mol^{-1}·K^{-1}) and T is the absolute temperature (K) at which E' is determined, in this case at the peak temperature of tan δ + 40 °C.

The glass transition temperature (T_g) was analyzed using a differential scanning calorimeter (DSC 8000, Perkin Elmer, Waltham, Massachusetts, USA) with a heating rate of 20 °C·min^{-1}. The scanned temperature ranged from 20 to 200 °C. Thermal stability was measured by a thermogravimetric analysis using Thermobalance Netzsch TG209 F1 (NETZSCH-Gerätebau GmbH, Selb, Germany) under a nitrogen environment at the heating rate of 20 °C·min^{-1} from

28 to 1008 °C. Several parameters were obtained to describe the thermal stability of cured epoxy resins. The onset temperature or initial decomposition temperature (T_d) is the temperature at which the sample starts to decompose. The mid-point temperature ($T_{-50\%}$) is the temperature at which 50% of the weight loss occurred. T_{max} stands for the decomposition temperature at the maximum mass loss rate. The amount of final residue presented by % char is the percentage of final residual weight at 1008 °C with relative to the initial sample weight.

The FTT Cone calorimeter (Fire Testing Technology, West Sussex, UK) was employed to analyze the flammability of the composites according to ISO 5660-1 with the heat flux of 50 $kW \cdot m^{-2}$. The experiments were terminated after the flame stopped for 100 s. The sample size was 10 cm × 10 cm × 4 mm (length × width × thickness).

2.3 Results and Discussion

2.3.1 Verification of the Incorporation of DOPO into Epoxy Resin using ATR-FTIR

The successful incorporation of DOPO into the epoxy resin, whose reaction is presented in Fig. A1, was confirmed by FTIR spectroscopy (Fig. A2). The P–H stretching vibration peak of DOPO appeared at 2384 cm^{-1}. The disappearance of this peak confirmed the bonding of DGEBA and DOPO [10]. The reaction between DGEBA and DOPO led to the epoxide ring opening that resulted in the formation of hydroxyl group on the sp^3 carbon [26]. The formed hydroxyl group could further react with another epoxide ring via the etherification reaction, which subsequently formed the C–O–C (alkoxy) bond and a hydroxyl group (O–H) [26]. The occurrence of this reaction could be evidenced in the EP/DOPO sample from the presence of the alkoxy C–O bond at 1117 cm^{-1} and the existence of hydroxyl groups as a broad peak between 3200 and 3600 cm^{-1}, which was broader and more intense as compared to the O–H peak of the neat epoxy resin, which appeared between 3400 and 3600 cm^{-1}. Moreover, the shift of the P–C stretching vibration from 682 cm^{-1} in DOPO to 686 cm^{-1} in EP/DOPO could also be a sign of the bonding between the phosphorus atom of DOPO and a carbon atom of epoxide ring.

2.3.2 Dispersion of GNP in the Epoxy Resin

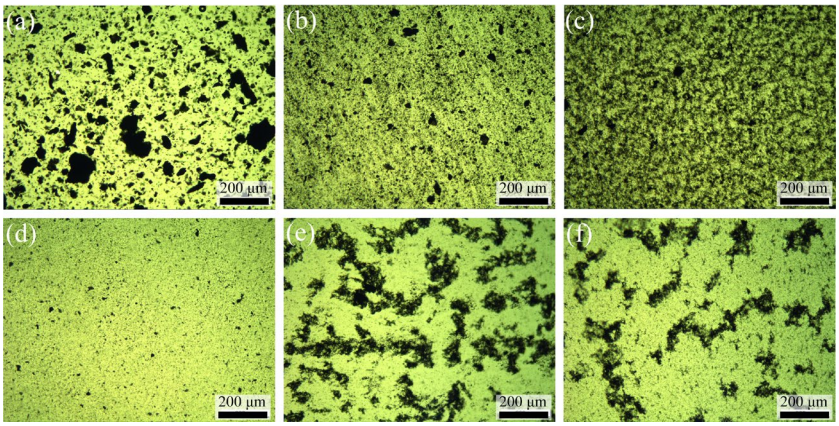

Figure 2.1 Light micrographs illustrating the dispersion degree of GNP in the epoxy resin (a) after mixing the epoxy resin with 0.5 wt % GNP using a high speed mixer, (b) and (c) after one and three runs of three-roll milling, (d) after adding the hardener, and (e) and (f) after curing at room temperature and at 80 °C, respectively.

Fig. 2.1 shows the dispersion state of GNP in the epoxy resin matrix. Heterogeneity in lateral size and dispersion state of GNPs was observed after mixing GNP and epoxy resin with a high-speed mixer for 5 min. The lateral dimension of GNPs substantially reduced and the dispersion of GNPs was more homogeneous after one and three runs of three-roll milling. After adding the hardener, the GNP concentration decreased due to the dilution by the added hardener. Reagglomeration of GNPs was observed for the samples cured at both room temperature and 80 °C. The reagglomeration during the curing process was expected and previously reported for reduced graphene oxide [30] and carbon nanotube [31,32]. Since the curing rate is faster at higher temperature, the diffusion of GNP could be more limited by a sharp increase in viscosity of the resin during the curing process at higher temperature [31]. Therefore, we assumed that curing the epoxy resin at 80 °C yielded better GNP dispersion.

2.3.3 Electrical Property

The discharge measurement (Table A3) revealed that the nanocomposites with GNP content higher than 1 wt % showed an electrical discharge from the metal spheres to the samples, implying that the nanocomposites contained conductive networks. Corona discharge appeared for the nanocomposites with 2-3 wt % GNP, indicating the suitability for antistatic packaging purpose [33]. The nanocomposites containing less than 1 wt % GNP were completely insulating as the line spark appeared between two metal spheres.

Percolation theory can be applied to predict the critical amount of the filler that can form the connected network and affect the behaviors of the nanocomposite. The electrical percolation threshold, ϕ_c, and critical exponent, t_c, obtained from fitting the experimental data with the power law $\sigma_c = \sigma_f(\Phi - \Phi_c)^{t_c}$ were 0.006 and 3, respectively as demonstrated in Fig. 2.2a. This corresponds to a volume fraction ϕ_c of 0.006 or 1.6 wt % GNP. σ_c and σ_f are the conductivity of the nanocomposite and the filler, respectively, and ϕ is the filler concentration.

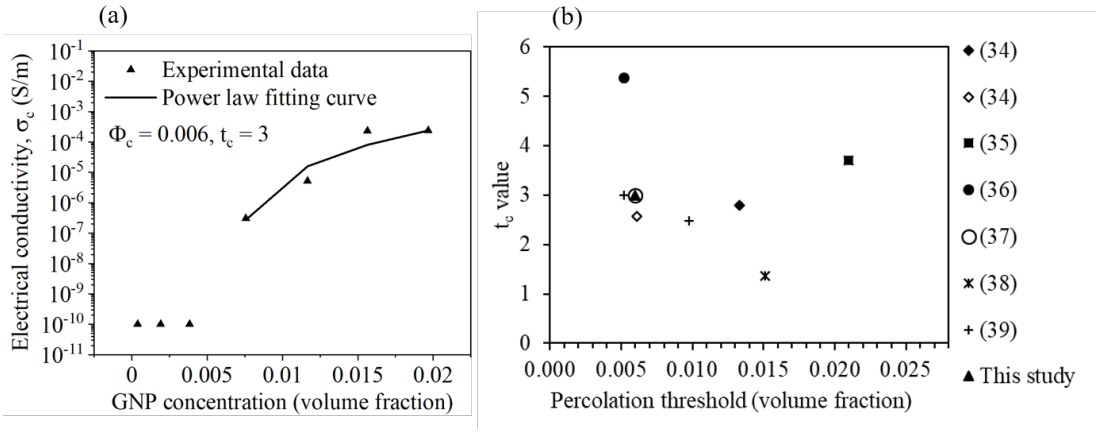

Figure 2.2 (a) Percolation threshold of the EP/GNP nanocomposites in this study and (b) comparison of percolation threshold and t_c values among EP/GNP nanocomposites from different studies.

The percolation threshold values published earlier ranged from 0.0052 to 0.021 volume fraction, while the corresponding t_c values were in the range of 1.36–5.37 as summarized in Fig. 2.2b [34–39]. Higher t_c value than the universal value (1.65 – 2) indicates the nonuniversal transport behavior, which can happen when the fillers have exceptional geometries such as a high aspect ratio like GNP [40]. An analytical model $\sigma_c = \frac{27\pi D_p^2 t_p}{4(D+IPD)^3}$ was also proposed to predict the percolation threshold of nanocomposites containing three-dimensional randomly dispersed disc-shaped or platelet-like nanoparticles based on average interparticle distance (IPD) and aspect ratio of the particles, where D_p is the diameter of the platelet and t_p is the thickness of the platelet [41]. The suggested IPD value was 10 nm [41], at which the electron hopping can occur, according to the quantum mechanical tunneling mechanism. Regarding GNP with the diameter and thickness of 25 μm and 6 – 8 nm, respectively, the estimated percolation threshold was between 0.0051 and 0.0068 volume fraction, which is in good agreement with the calculated percolation threshold from the power law fitting of our experimental data.

2.3.4 Crosslinking Density of Epoxy Resins

Properties of the epoxy resins were influenced by the chemical network structure, which could be explained by the crosslinking state of the cured epoxy resins [42]. In order to assess the effect of DOPO on the network structure of the cured resin, the crosslinking density of EP/10DOPO was estimated (Equation 2.1) and compared to that of neat epoxy using the rubbery storage modulus (E'), which was E' at the peak temperature of tan δ + 40 °C, obtained from DMTA results (Fig. A3). The peak temperature of tan δ + 40 °C was 136 °C. The results involved in the determination of the crosslinking density are presented in Table 2.1.

Table 2.1 Storage modulus (E') in rubbery region and crosslinking density of neat epoxy resin and EP/10DOPO.

Samples	E' at Peak Temperature of tan δ + 40 °C (MPa)	ρ (mol·m^{-3})
Neat epoxy	7.67	751.5
EP/10DOPO	6.36	623.2

As shown in **Table 2.1**, the crosslinking density of the EP/10DOPO was lower than that of neat epoxy. This was a result of the reaction of epoxide groups with DOPO, causing the depletion of available epoxide groups and less crosslinking reaction between epoxide groups and amine groups of the hardener.

2.3.5. Mechanical Properties

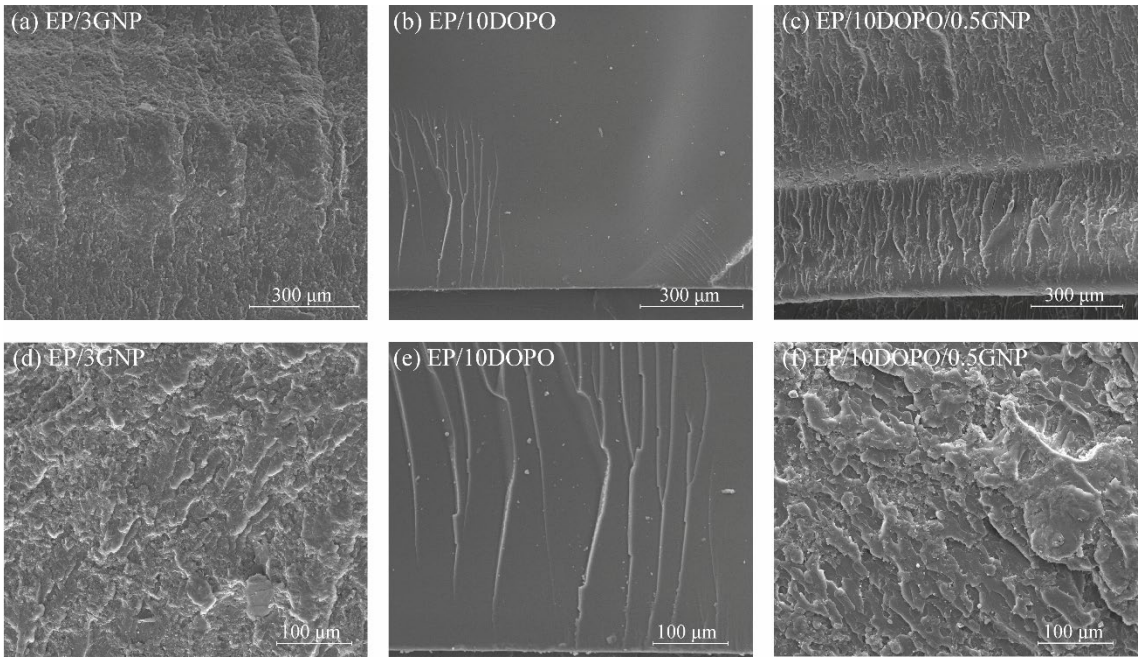

Figure 2.3 Scanning electron microscopy (SEM) images of fracture surface after three-point bending test of (a), (d) EP/3GNP, (b), (e) EP/10DOPO, and (c), (f) EP/10DOPO/0.5GNP.

The flexural fracture surface of the epoxy composites was determined using SEM as shown in Fig. 2.3. The fracture surface of the formulation containing GNP showed a rough feature. The roughness on the EP/GNP nanocomposites was caused by GNP acting as an obstruction of the crack propagation, which resulted in an alteration of the crack path as seen in Fig. 2.3a,c. Moreover, the rough surface included holes and GNP agglomerates on the fracture surface (Fig. 2.3d,f) suggesting adhesive failure of the composite. The fracture surface of EP/10DOPO (Fig. 2.3b,e) revealed mirror-like feature with some cracks, which was similar to that of neat epoxy resin.

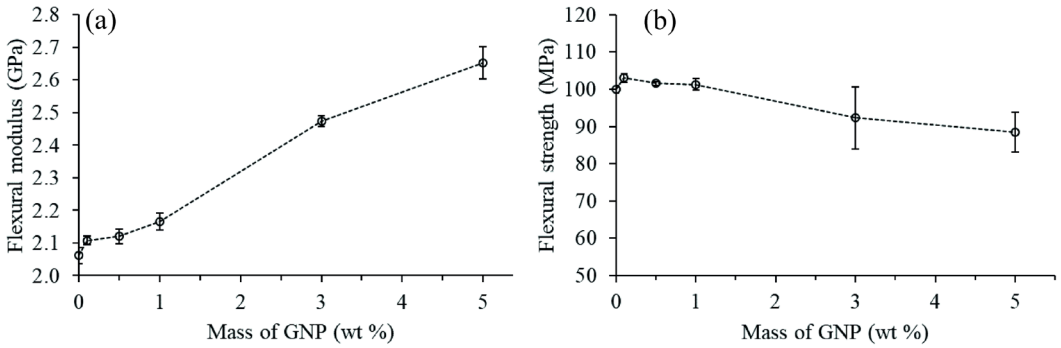

Figure 2.4 Effect of GNP on the (a) flexural modulus and (b) flexural strength of EP/GNP nanocomposites.

Flexural modulus and flexural strength were investigated to describe the mechanical performance of the EP/GNP nanocomposites as displayed in Fig. 2.4. We found an increase in flexural modulus by 20% and 29% compared to neat epoxy resin when the amount of GNP increased to 3 wt % and 5 wt. %, respectively. The flexural strength of the nanocomposite slightly increased as GNP content increased up to 1 wt %. When GNP content increased to 3 wt % and 5 wt %, a decreasing trend of flexural strength of the nanocomposites was observed due to the weak adherence between the surface of epoxy resin matrix and non-functionalized GNP used in this study, which prevent the load transfer from matrix to GNP. Therefore, GNP could act as a stress concentrator and deteriorate the mechanical properties of the nanocomposites [18,43]. This could be confirmed by the fracture surface analyzed by SEM (Fig. 2.3) revealing rough surface with voids and GNP agglomerates, which indicated the adhesion failure between the matrix and GNP.

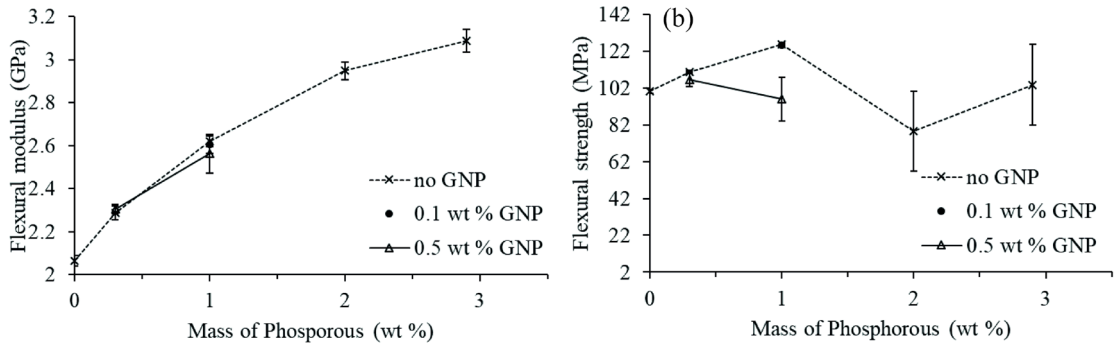

Figure 2.5 Effect of DOPO on the (a) flexural modulus and (b) flexural strength of DOPO-incorporated epoxy nanocomposites.

Fig. 2.5 shows the effect of incorporating DOPO into epoxy resin on the flexural modulus and flexural strength. The addition of DOPO led to a significant increase in the flexural modulus.

In the presence of DOPO, the addition of GNP did not significantly alter the flexural modulus and strength of the nanocomposite as compared to the EP/DOPO composites. The incorporation of DOPO up to 10 wt % (or 1 wt % of phosphorus) showed an improvement in flexural strength of the nanocomposites, whereas adding a higher amount of DOPO adversely affected the flexural strength. The mechanical effect of DOPO in the epoxy thermoset is still unclear due to a lack of data and the inconsistent results among different studies [7,13,26,27]. The incorporation of DOPO was reported to cause a negative impact on the flexural modulus and strength of the cured epoxy resins [7,13] because of the reaction of DOPO with the epoxide group, which reduced the functionality of the epoxy resin and thus diminished the degree of crosslinking in the resulting thermosets [26]. On the other hand, the rigidifying effect of DOPO once linked to the epoxy chain might compensate the crosslinking effect; therefore, the addition of DOPO to a certain concentration level led to an increase in the flexural modulus of the epoxy thermosets [26,27].

The flexural moduli and strengths of the nanocomposites measured in this study were compared with the values from other studies as shown in Fig. 2.6 [15,18,39,43]. Since we are interested in the effects of DOPO and GNP incorporation, the flexural moduli and strengths were normalized to the cured neat epoxy resin so that the values from different studies could be compared. Regarding GNP addition, the improvement in flexural modulus could be mainly attributed to the good dispersion of GNP in the epoxy resin by three-roll milling as shown in Fig. 2.1. Several previous studies also used three-roll milling [15,18,39,43,44] for GNP dispersion and showed improvement of the mechanical properties of the nanocomposites.

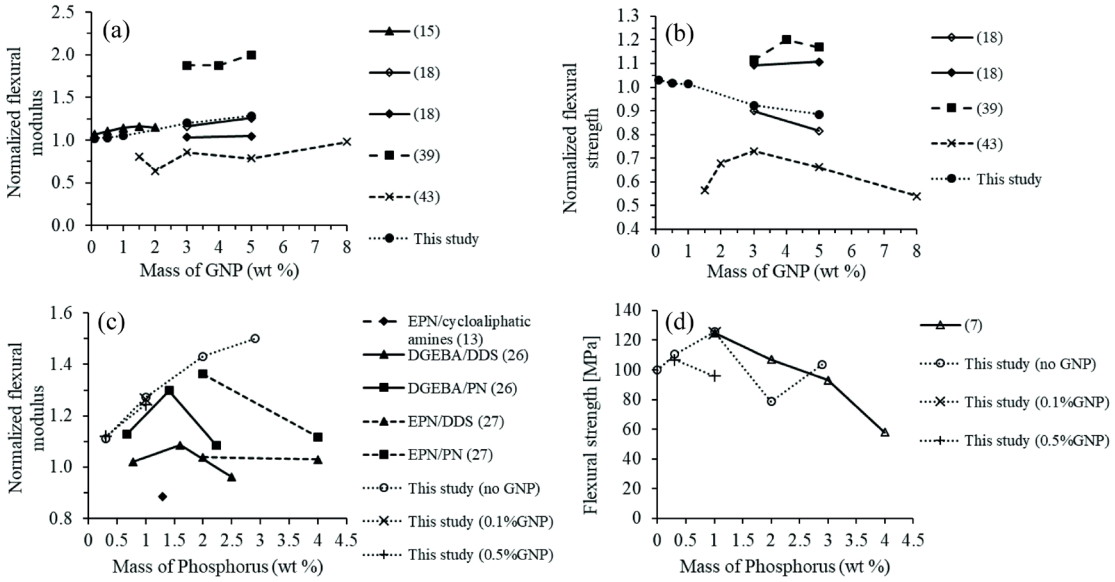

Figure 2.6 Comparison among different studies of the effect of GNP on the (a) flexural modulus and (b) flexural strength of epoxy nanocomposites normalized to neat epoxy resin and the effect of DOPO on the (c) flexural modulus normalized to neat epoxy resin and (d) flexural strength in MPa.

With an increasing amount of DOPO, our study showed a continuous improvement in the flexural modulus of the EP/DOPO thermosets, which does not completely agree with other studies, as shown in Fig. 2.6c. Our study presents an increasing trend in the flexural modulus when phosphorous content in DOPO-incorporated epoxy resin rose up to 3 wt %. Other studies found a decrease in terms of the flexural modulus of the DOPO-incorporated epoxy resin as the phosphorous content increased to some extent. For example, Wang and Lin [26] reported an improvement in flexural modulus of the DOPO-incorporated resin (DGEBA) cured with 4,4′-diaminodiphenyl sulfone (DDS) and phenol novolac (PN) when the phosphorous content increased to 1.6 wt % and 1.4 wt %, respectively. When the phosphorous content exceeded these values, the flexural modulus decreased. Wang et al. [13] examined the flexural modulus of the DOPO-incorporated epoxy novolac resin (EPN) with 1.3 wt % phosphorous cured with modified cycloaliphatic amines. They found that the flexural modulus of the DOPO-modified epoxy resin was worsened by 11% as compared to neat resin, but it could be improved by adding 0.5 wt % of graphene into the formulation.

Such a discrepancy in the DOPO effect on the flexural modulus of the cured DOPO-modified epoxy resin could result from different types of hardeners used in various studies since the structure of the hardeners could also play an important role on the mechanical properties of the epoxy thermosets [3,45,46]. Hardeners containing aromatic rings such as phenol novolac (PN) and 4,4′-diaminodiphenyl sulfone (DDS) [26,27] or cycloaliphatic structure [13] could also enhance the flexural modulus or rigidity of the epoxy thermoset. Considering the molecular structure of the involved compounds, the rigidity of DOPO and aromatic hardeners could contribute to an improvement in flexural modulus of the cured DOPO-incorporated resin. When the load of DOPO increased, the available epoxide groups decreased due to the reaction of DOPO with some of the epoxide groups and thus less of an amount of hardener was required to crosslink DOPO-incorporated epoxy resin. Therefore, the flexural modulus could be strengthened by the rigidity of DOPO; meanwhile, it could be weakened by both the loss of crosslinking density and reduction in aromatic structures caused by less of an amount of hardener required. On the other hand, hardeners with a linear molecular structure did not

contribute strongly to the mechanical properties of the epoxy thermoset; therefore, the rigidifying effect of DOPO was the dominant factor on the flexural modulus and the flexural modulus increased continuously when phosphorus content increased. The competition of the above strengthening and weakening effects was the reason for the different slopes of flexural modulus versus phosphorus content curves from previous studies [26,27] in Fig. 2.6c.

2.3.6 Thermal Properties

TGA curves and their derivatives (derivative thermogravimetric, DTG), which represent the thermal stability of the samples are demonstrated in Fig. 2.7. EP/GNP samples had similar TGA profile as compared to neat epoxy resin, which showed T_d around 369 °C and the maximum mass loss rate around 387 °C. However, GNP significantly increased the char residues of the epoxy. The addition of GNP up to 1 wt % loading can increase the char content up to 50% by forming the structure containing smaller pores as compared to the char of neat epoxy, which led to a compact and continuous char structure [20]. DOPO underwent the mass loss in two steps from 200 to 370 °C and from 370 to 480 °C, respectively, which was earlier than the T_d of neat epoxy resin at 369 °C. After 480 °C, DOPO completely decomposed, as there was almost no residue left. Regarding EP/DOPO samples, when the DOPO loading increased, T_d and T_{max} of the EP/DOPO decreased. Our results clearly showed significant improvement in char yields as the amount of DOPO increased. This could be due to the fact that the decomposition products of DOPO could catalyze the formation of char, which can insulate the underneath layer from burning [13,24,47]. Adding GNP to the EP/DOPO composite did not affect T_d and T_{max} of the epoxy resin as compared to EP/DOPO, but it could further improve the char residues.

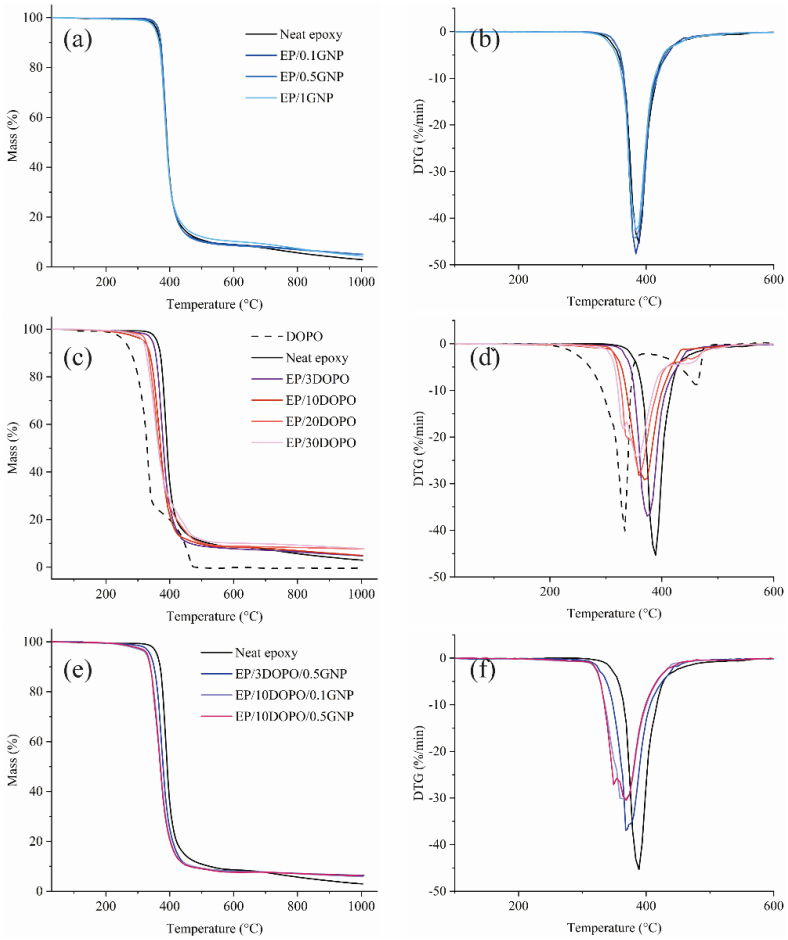

Figure 2.7 TGA and DTG curves from thermogravimetric analysis under the nitrogen environment of DOPO, GNP, cured neat epoxy resin, EP/GNP, EP/DOPO, and EP/DOPO/GNP.

Table 2.2 Glass transition temperatures (T_g) and thermogravimetric analysis data of DOPO, neat epoxy, EP/GNP, EP/DOPO, and EP/DOPO/GNP nanocomposites.

Samples	**T_g (°C)**	**T_d (°C)**	**$T_{-50\%}$ (°C)**	**T_{max} (°C)**	**% Char**
DOPO	N.A.	279	329	333	0
Neat epoxy	98.0	369	389	387	2.88
EP/0.1GNP	91.8	370	389	386	5.07
EP/0.5GNP	95.1	368	389	381	5.06

EP/1GNP	95.8	366	389	385	4.31
EP/3DOPO	94.3	355	379	374	4.76
EP/10DOPO	87.4	339	369	370	4.92
EP/20DOPO	83.3	325	366	360	7.69
EP/30DOPO	72.8	319	363	357	7.80
EP/3DOPO/0.5GNP	94.1	353	378	369	6.32
EP/10DOPO/0.1GNP	88.1	340	369	362	5.81
EP/10DOPO/0.5GNP	84.9	338	369	368	6.14

Table 2.2 summarizes the glass transition temperatures (T_g) of epoxy nanocomposites determined by DSC and the important parameters obtained from thermal stability investigation by TGA. GNP slightly reduced T_g of the cured epoxy resin as compared to the neat epoxy resin. The reduction in T_g could be the result of GNP acting as a heat flow barrier in the polymer matrix [48]. Moreover, non-functionalized GNP had free surface and formed repulsive interface with the polymer, which could result in a decrease in T_g because polymer chain mobility was more enhanced with respect to the neat epoxy resin [49,50].

An increase in the DOPO content resulted in a decrease in T_g due to the reaction of epoxide groups and DOPO, which depleted the available crosslinking sites between epoxy resin and hardener and resulted in less crosslinking network of the cured DOPO-incorporated epoxy resin. The addition of GNP to EP/DOPO did not make a notable difference in T_g and T_d of the resulting nanocomposites as compared to EP/DOPO samples; however, the significant improvement in char yield was observed in samples containing GNP.

2.3.7 Flame Retardancy

The important parameters for flame retardancy including time to ignition (TTI), peak heat release rate (pHRR), average heat release rate (ave-HRR), average effective heat of combustion (ave-EHC), total heat release (THR), total smoke production (TSP), average CO formation (ave-CO yield), and average CO_2 formation (ave-CO_2 yield) were obtained from cone calorimetry. Fig. 2.8 shows plots of HRR and THR as a function of burning time from cone calorimetry analysis. HRR profile of neat epoxy resin showed pHRR of 1246 $kW \cdot m^{-2}$ at 140 s. GNP did not significantly influence pHRR, but another HRR peak around 200–300 s was more pronounced as compared to that of the neat epoxy. The development of the second peak in the HRR profile of EP/GNP could be an effect of the breakage of the char layer formed by GNP. When the char layer broke, the combustible gases were released, which enhanced the combustion. As a result, THR of the EP/GNP was higher than that of neat epoxy. Liu et al. reported a similar effect of GNP on the development of small HRR peaks with the addition of 5 wt % of GNP; however, they showed substantial reduction of pHRR by 57% as compared to the epoxy resin without a filler [24], while our EP/GNP did not reveal an obvious reduction in pHRR. This might be explained by the fact that the concentration of GNP in our study was lower and thus the protective char layer formed was weaker and easier to break.

The incorporation of DOPO could decrease the pHRR and THR in relation to the epoxy resin because DOPO could act in both the condensed phase by forming the protective char layer and gas phase by scavenging the reactive combustible species [12]. By adding GNP into EP/DOPO, the pHRR and THR were further reduced as compared to EP/DOPO.

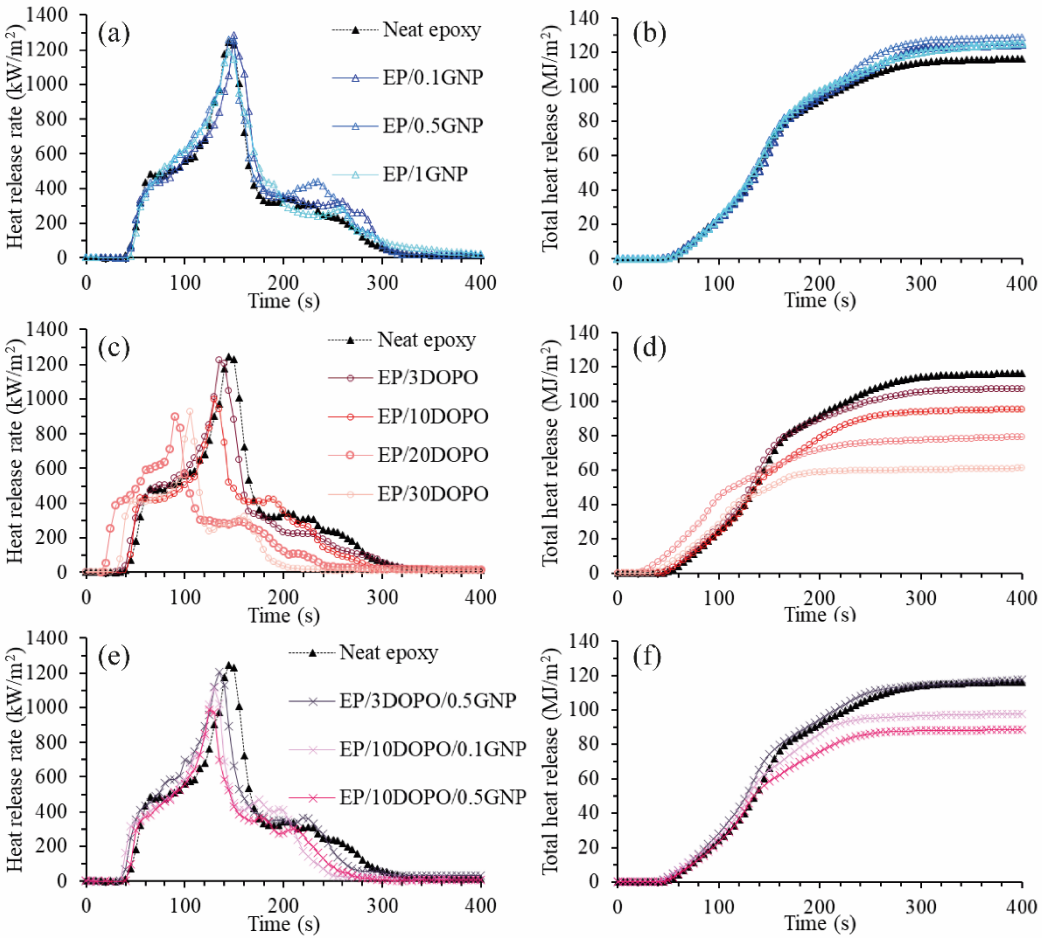

Figure 2.8 Heat release rate plots from cone calorimetry of neat epoxy resin compared to (a) EP/GNP nanocomposites, (b) EP/DOPO, and (c) EP/DOPO/GNP nanocomposites and total heat release plots from cone calorimetry of neat epoxy resin compared to (d) EP/GNP nanocomposites, (e) EP/DOPO, and (f) EP/DOPO/GNP nanocomposites.

Table 2.3 summarizes some important parameters from cone calorimetry. Moreover, based on TTI, pHRR, and THR, the flame retardancy index (FRI), which is a dimensionless value defined as $FRI = \frac{\left(THR \times \frac{pHRR}{TTI}\right)_{neat\ epoxy}}{\left(THR \times \frac{pHRR}{TTI}\right)_{composite}}$ [51], was calculated in order to compare the effect of adding GNP, DOPO, and the combination of both additives on the flame retardancy efficiency of the epoxy resins. The addition of GNP could increase the TTI, which could be an effect of GNP changing the gas pathway in the condensed phase and retarding the gas transfer to the gas phase. The high thermal diffusivity of GNP could also contribute to the delay of TTI as GNP could transfer the heat from the surface of the composite to the bulk [52]. On the other hand, when the loading amounts of DOPO increased, the TTI did not show an increasing trend. This might be due to the relatively low T_d of DOPO as compared to the neat epoxy resin as shown in TGA

results. TSP, ave-CO yield, and ave-CO_2 yield are indicators of the completeness of the combustion. The products of complete combustion are water and CO_2, while incomplete combustion produces smoke and CO [53]. Addition of DOPO resulted in higher TSP, greater development of CO, and lower CO_2 production, which indicated more incomplete combustion as compared to the neat epoxy resin. The incorporation of DOPO reduced pHRR, ave-HRR, ave-EHC, and THR of the composites as compared to the cured neat epoxy resin. According to our finding, GNP up to 1 wt % did not significantly promote the flame retarding efficiency of the epoxy resin in terms of pHRR and THR. However, the combination of DOPO and GNP could further reduce pHRR, ave-HRR, and THR of the nanocomposites as compared to the EP/DOPO or EP/GNP alone.

The flame retarding mechanism of combining DOPO and GNP has been proposed as GNP is acting in the condensed phase, while DOPO is acting in both the condensed phase and gas phase [24,47]. Ave-EHC reflects the combustion rate of volatile compounds in the gas phase during combustion [24,47]. A significant decrease in ave-EHC was observed for EP/DOPO composites, implying that DOPO reacts in the gas phase by scavenging the volatile compounds and thus resulted in the reduction of the burning rate. On the other hand, GNP did not reduce the ave-EHC when added to the composite, which suggests that GNP did not contribute to the gas phase reaction.

The change in TTI, pHRR, and THR with respect to the neat epoxy resin was reflected in FRI values of the composites. Three performance categories were proposed including poor, good, and excellent, corresponding to FRI < 1, 1 < FRI < 10, and FRI > 10, respectively [51]. The results revealed that adding GNP slightly improved FRI due to the effect of GNP on delaying the TTI of the EP/GNP nanocomposites, although it caused an increase in pHRR and THR. In case of DOPO, when DOPO loading increased, the pHRR and THR reduced, which resulted in an increase in FRI, even though the TTI was not delayed. It can be seen that all samples except for EP/0.5GNP, EP/3DOPO, and EP/3DOPO/0.5GNP showed good flame retardancy performance, whereas EP/0.5GNP, EP/3DOPO, and EP/3DOPO/0.5GNP showed poor FRI quantities. Regarding EP/0.5GNP, as mentioned earlier, the formed char layer was not strong enough, resulting in the breakage of the char layer, which caused a release of combustible gases and an increase of THR. Moreover, pHRR was not decreased by adding GNP. These were major contributions to poor FRI. Since ave-EHC, CO, and CO_2 production, which reflected the chemical reaction process [20], of EP/0.5DOPO were similar to those of the neat epoxy resin,

this indicated that GNP did not interfere with the gas phase reaction. For EP/3DOPO, the poor FRI was mainly due to low TTI, which could be a result of relatively low T_d of DOPO as compared to the neat epoxy resin, meaning that EP/3DOPO decomposed earlier than neat epoxy resin, as evidenced in the TGA results. Combining 0.5 wt % GNP with 3 wt % DOPO could delay TTI of the epoxy composite, but THR was increased, which was a major contribution to the poor FRI. In both cases, avg-EHC did not decrease, indicating that no gas phase reaction occurred. Since DOPO was responsible for the effect on the gas phase reaction, we concluded that the loading of 3 wt % DOPO in our epoxy system was not enough for DOPO to affect the gas phase reaction. The combination of 10 wt % DOPO and 0.5 wt % GNP could additionally promote the FRI to 1.9 as compared to the epoxy resin loaded with 10 wt % DOPO, which showed FRI at 1.7.

Since FRI is a relative value indicating the flame retardancy efficiency of the composites with respect to the neat epoxy resin, this allows us to compare the influence of additives on the flame retardancy efficiency of different epoxy resin systems. Our results demonstrated that, in terms of the FRI values, DOPO showed better flame retardancy performance as compared to GNP. Our finding was consistent with the previous review work, which extracted the information regarding flame retardancy efficiency from a number of literature [54]. They reported that generally phosphorous-containing flame retardants were more effective in terms of flame retardancy in epoxy resin as compared to nanoparticle fillers [54]. Specifically, they showed that DOPO-incorporated epoxy resins with the DOPO loading ranging from 1.3 to 13 wt % had an FRI in the range of 0.8 to 3.94. Regarding graphene-related materials including GNP, expanded graphite, graphene oxide and reduced graphene oxide, with the nanoparticle loadings ranged from 1 to 30 wt %, the FRI of the epoxy nanocomposites were in the range of 0.98 to 2.34. It can be seen that epoxy filled with DOPO could achieve better FRI than epoxy filled with graphene-related materials, while loadings of DOPO (1.3 – 13 wt %) were less than loadings of graphene-related materials (1 – 30 wt %).

Table 2.3 Parameters from cone calorimetry analysis including TTI, pHRR, ave-HRR, ave-EHC THR, TSP, ave-CO yield and ave-CO_2 yield.

Samples	TTI (s)	pHRR ($kW \cdot m^{-2}$)	Ave-HRR (300s) ($kW \cdot m^{-2}$)	Ave-EHC (300 s) ($MJ \cdot kg$)	THR ($MJ \cdot m^{-2}$)	TSP (m^2)	Ave- CO yield ($kg \cdot kg^{-1}$)	Ave- CO_2 yield ($kg \cdot kg^{-1}$)	FRI (-)
Neat epoxy	34	1246	384	21.3	117	30.3	0.05	1.6	-
EP/0.1GNP	40	1285	411	23.9	125	34.0	0.06	1.7	1.1
EP/0.5GNP	38	1263	425	24.8	130	33.7	0.06	1.8	1.0
EP/1GNP	42	1189	410	24.0	126	33.4	0.06	1.7	1.2
EP/3DOPO	28	1226	355	22.0	108	37.1	0.08	1.5	0.9
EP/10DOPO	37	996	315	19.5	96	36.4	0.11	1.3	1.7
EP/20DOPO	18	902	259	13.6	81	39.2	0.10	0.7	1.1
EP/30DOPO	29	927	201.1	13.9	60.1	35.7	0.10	0.8	2.3
EP/3DOPO/0.5GNP	34	1208	385.4	23.2	118	49.4	0.12	1.7	1.0
EP/10DOPO/0.1GNP	31	1116	323.7	20.9	98.4	38.5	0.12	1.3	1.2
EP/10DOPO/0.5GNP	38	989	294.2	19.1	89.3	35.5	0.11	1.3	1.9

Studies have reported enhanced flame retardancy property by adding graphene-related materials. For example, when 5 wt % of multilayer graphene was added to polypropylene and 5 wt % of graphene nanosheets were added to epoxy resin, they could achieve FRI of 2.9 [21] and 4.4 [24], respectively, which were considered good performance in terms of FRI [51]. However, the amounts of graphene-related materials used in those studies were at least 5 wt %,

which could adversely affect the mechanical properties of the epoxy composite according to our findings. By combining DOPO and GNP, the loading amount of GNP could be reduced and the flame retardancy property could be improved without worsening the mechanical properties of the nanocomposites, which was demonstrated in this work.

As shown in our study, the flame retardancy efficiency of epoxy resins could be enhanced by the incorporation of DOPO since DOPO could act in both the condensed phase and gas phase to retard the flame. By combining DOPO and GNP, the flame retardancy efficiency could be further improved to some extent as compared to the EP/DOPO composite due to the effect of GNP on delaying the ignition time and improving char formation. One might consider increasing the GNP loading to achieve better flame retardancy performance; however, a balance must be considered due to the adverse effect on the mechanical properties of the composites resulting from agglomeration of GNP at high loading.

2.4 Conclusions

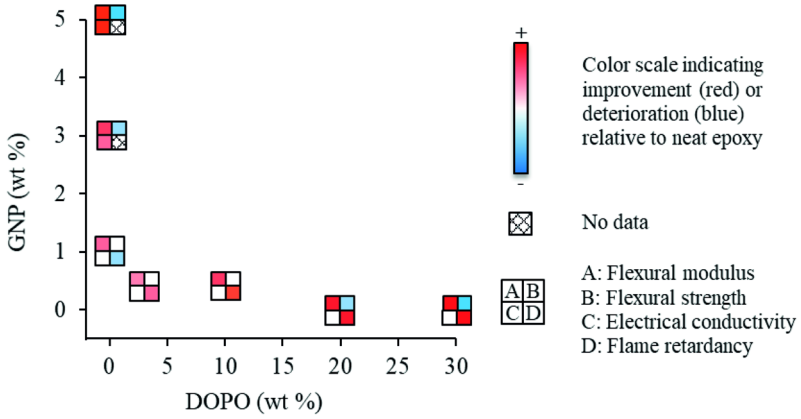

Figure 2.9 Comparison, with respect to neat epoxy resin, of the mechanical, electrical, and flame retarding properties of epoxy composites with different loading amounts of GNP and DOPO.

Epoxy-based composites with homogeneously dispersed GNP were produced using a three-roll milling process. DOPO was also successfully incorporated into the epoxy resin. The electrical percolation threshold was detected at 0.006 volume fraction of GNP or 1.6 wt % GNP. Both DOPO and GNP could enhance the flexural modulus and flexural strength of the epoxy composites. Unlike aromatic hardeners, the linear structure of polyetheramine, which was the hardener used in this study, allowed the rigidity of grafted DOPO to dominate the flexural modulus of the composites; therefore, the flexural modulus increased continuously as the

DOPO loading increased, although the crosslinking density decreased when DOPO was incorporated. However, higher DOPO and GNP contents (more than 10 wt % DOPO and 1 wt % GNP) could cause difficulty in composite manufacturing due to an increase in viscosity, which resulted in poorer dispersion of GNP and poorer flexural strength of the composites. Since incorporation of DOPO depleted the crosslinking density of the epoxy thermoset, the glass transition temperature decreased as DOPO loading increased. Thermogravimetric analysis showed that both GNP and DOPO could enhance the char residues. Incorporating 10 wt % DOPO could reduce the peak heat release rate (pHRR) and the total heat release (THR) of epoxy composites by 20% and 18%, respectively, compared to the neat epoxy resin. Increasing GNP loading up to 1 wt % did not significantly affect the pHRR of epoxy composites, but increased the THR by 8% and delayed TTI. These three parameters, pHRR, THR, and TTI could be converted to FRI. The results revealed that EP/DOPO had better FRI than EP/GNP. Using DOPO and GNP together could further improve FRI to some extent and achieve good performance regarding the FRI criterion.

The effects of GNP and DOPO loading on the composites' properties are illustrated in Fig. 2.9. Here, based on a DGEBA/polyetheramine system, we proposed the combination of 10 wt % DOPO and 0.5 wt % GNP as an optimal formulation providing enhanced flexural modulus and strength, an improvement in flame retarding efficiency of the composite by lowering the pHRR and THR by 21% and 24%, respectively, and maintained electrical insulating properties of the epoxy resin.

Supplementary Materials: The supplementary information is available online at http://www.mdpi.com/2073-4360/12/10/2349/s1 and in Appendix A in this thesis. Figure A1: Reaction between epoxy resin (DGEBA) and DOPO, Figure A2: ATR-FTIR spectra indicating the functional groups of DOPO, neat epoxy and epoxy/DOPO mixture, Figure A3: Storage modulus (E') and tan δ of neat epoxy resin and EP/10DOPO obtained from DMTA, Table A1: Formulations of epoxy resin and DOPO-incorporated epoxy resin cured with polyetheramine (Jeffamine D-230), Table A2: Identification of observed peaks from FTIR spectra of DOPO, neat epoxy and epoxy/DOPO mixtures, Table A3: Electrical properties of the epoxy/GNP composites

Funding: This research was funded by Swiss National Science Foundation (SNF) (grant number 310030_169207).

Acknowledgments: This work was supported by Swiss National Science Foundation (SNF) (grant number 310030_169207).

Conflicts of Interest: The authors declare no conflict of interest.

2.5 References

1. Pascault, J.-P., Williams, R.J.J. *Epoxy Polymers : New Materials and Innovations*, 1st ed.; Wiley: Weinheim, Germany, 2010; pp. 1–12.
2. Saba, N.; Jawaid, M.; Paridah, M.T.; Al-othman, O.Y. A review on flammability of epoxy polymer, cellulosic and non-cellulosic fiber reinforced epoxy composites. *Polym. Adv. Technol.* **2016**, *27*, 577–590, doi:10.1002/pat.3739.
3. De Nograro, F.F.; Guerrero, P.; Corcuera, M.A.; Mondragon, I. Effects of chemical structure of hardener on curing evolution and on the dynamic mechanical behavior of epoxy resins. *J. Appl. Polym. Sci.* **1995**, *56*, 177–192, doi:10.1002/app.1995.070560208.
4. Teh, P.L.; Mariatti, M.; Wagiman, A.N.R.; Beh, K.S. Effect of curing agent on the properties of mineral silica filled epoxy composites. *Polym. Compos.* **2008**, *29*, 27–36, doi:10.1002/pc.20345.
5. van der Veen, I.; de Boer, J. Phosphorus flame retardants: Properties, production, environmental occurrence, toxicity and analysis. *Chemosphere* **2012**, *88*, 1119–1153, doi:10.1016/j.chemosphere.2012.03.067.
6. Birnbaum, L.S.; Staskal, D.F. Brominated flame retardants: Cause for concern? *Environ. Health Perspect.* **2004**, *112*, 9–17, doi:10.1289/ehp.6559.
7. Gu, J.; Dang, J.; Wu, Y.; Xie, C.; Han, Y. Flame-Retardant, Thermal, Mechanical and Dielectric Properties of Structural Non-Halogenated Epoxy Resin Composites. *Polym. Plast. Technol. Eng.* **2012**, *51*, 1198–1203, doi:10.1080/03602559.2012.694951.
8. Schäfer, A.; Seibold, S.; Lohstroh, W.; Walter, O.; Döring, M. Synthesis and properties of flame-retardant epoxy resins based on DOPO and one of its analog DPPO. *J. Appl. Polym. Sci.* **2007**, *105*, 685–696, doi:10.1002/app.26073.
9. Schartel, B.; Balabanovich, A.I.; Braun, U.; Knoll, U.; Artner, J.; Ciesielski, M.; Döring, M.; Perez, R.; Sandler, J.K.W.; Altstädt, V.; et al. Pyrolysis of epoxy resins and fire behavior of epoxy resin composites flame-retarded with 9,10-dihydro-9-oxa-10-phosphaphenanthrene-10-oxide additives. *J. Appl. Polym. Sci.* **2007**, *104*, 2260–2269, doi:10.1002/app.25660.
10. Hussain, M.; Varley, R.J.; Zenka, M.; Simon, G.P. Synthesis, Thermal Behavior, and Cone Calorimetry of Organophosphorus Epoxy Materials. *J. Appl. Polym. Sci.* **2003**, *90*, 3696–3707, doi:10.1002/app.12983.
11. Ciesielski, M.; Burk, B.; Heinzmann, C.; Döring, M. Fire-retardant high-performance epoxy-based materials. In *Novel Fire Retardant Polymers and Composite Materials*, 1st ed.; Wang, D.-Y.; Elsevier: Amsterdam, Netherlands, **2017**, pp. 3–51.
12. Ciesielski, M.; Diederichs, J.; Döring, M.; Schäfer, A. Advanced Flame-Retardant Epoxy Resins for Composite Materials. In *Fire and Polymers V: Materials and Concepts for Fire Retardancy,* 1st ed.; Wilkie, C.A.; Nelson, G.L., Eds.; American Chemical Society: Washington D.C., USA, 2009; Volume 1013, pp. 174–190.

13. Wang, X.; Song, L.; Pornwannchai, W.; Hu, Y.; Kandola, B. The effect of graphene presence in flame retarded epoxy resin matrix on the mechanical and flammability properties of glass fiber-reinforced composites. *Compos. Part A Appl. Sci. Manuf.* **2013**, *53*, 88–96, doi:10.1016/j.compositesa.2013.05.017.
14. Chandrasekaran, S.; Seidel, C.; Schulte, K. Preparation and characterization of graphite nano-platelet (GNP)/epoxy nano-composite: Mechanical, electrical and thermal properties. *Eur. Polym. J.* **2013**, *49*, 3878–3888, doi:10.1016/j.eurpolymj.2013.10.008.
15. Chatterjee, S.; Wang, J.W.; Kuo, W.S.; Tai, N.H.; Salzmann, C.; Li, W.L.; Hollertz, R.; Nüesch, F.A.; Chu, B.T.T. Mechanical reinforcement and thermal conductivity in expanded graphene nanoplatelets reinforced epoxy composites. *Chem. Phys. Lett.* **2012**, *531*, 6–10, doi:10.1016/j.cplett.2012.02.006.
16. Wajid, A.S.; Ahmed, H.S.T.; Das, S.; Irin, F.; Jankowski, A.F.; Green, M.J. High-Performance Pristine Graphene/Epoxy Composites With Enhanced Mechanical and Electrical Properties. *Macromol. Mater. Eng.* **2013**, *298*, 339–347, doi:10.1002/mame.201200043.
17. Ma, J.; Meng, Q.; Zaman, I.; Zhu, S.; Michelmore, A.; Kawashima, N.; Wang, C.H.; Kuan, H.-C. Development of polymer composites using modified, high-structural integrity graphene platelets. *Compos. Sci. Technol.* **2014**, *91*, 82–90, doi:10.1016/j.compscitech.2013.11.017.
18. Wang, F.; Drzal, L.T.; Qin, Y.; Huang, Z. Mechanical properties and thermal conductivity of graphene nanoplatelet/epoxy composites. *J. Mater. Sci.* **2015**, *50*, 1082–1093, doi:10.1007/s10853-014-8665-6.
19. Wang, Y.; Yu, J.; Dai, W.; Song, Y.; Wang, D.; Zeng, L.; Jiang, N. Enhanced thermal and electrical properties of epoxy composites reinforced with graphene nanoplatelets. *Polym. Compos.* **2015**, *36*, 556–565, doi:10.1002/pc.22972.
20. Zhang, Q.; Wang, Y.C.; Bailey, C.G.; Yuen, R.K.K.; Parkin, J.; Yang, W.; Valles, C. Quantifying effects of graphene nanoplatelets on slowing down combustion of epoxy composites. *Compos. Part B Eng.* **2018**, *146*, 76–87, doi:10.1016/j.compositesb.2018.03.049.
21. Dittrich, B.; Wartig, K.-A.; Hofmann, D.; Mülhaupt, R.; Schartel, B. Flame retardancy through carbon nanomaterials: Carbon black, multiwall nanotubes, expanded graphite, multi-layer graphene and graphene in polypropylene. *Polym. Degrad. Stab.* **2013**, *98*, 1495–1505, doi:10.1016/j.polymdegradstab.2013.04.009.
22. Liu, S.; Yan, H.; Fang, Z.; Wang, H. Effect of graphene nanosheets on morphology, thermal stability and flame retardancy of epoxy resin. *Compos. Sci. Technol.* **2014**, *90*, 40–47, doi:10.1016/j.compscitech.2013.10.012.
23. Sang, B.; Li, Z.; Li, X.; Yu, L.; Zhang, Z. Graphene-based flame retardants: A review. *J. Mater. Sci.* **2016**, *51*, 8271–8295, doi:10.1007/s10853-016-0124-0.
24. Liu, S.; Fang, Z.; Yan, H.; Wang, H. Superior flame retardancy of epoxy resin by the combined addition of graphene nanosheets and DOPO. *RSC Adv.* **2016**, *6*, 5288–5295, doi:10.1039/C5RA25988F.
25. Liu, S.; Fang, Z.; Yan, H.; Chevali, V.S.; Wang, H. Synergistic flame retardancy effect of graphene nanosheets and traditional retardants on epoxy resin. *Compos. Part A Appl. Sci. Manuf.* **2016**, *89*, 26–32, doi:10.1016/j.compositesa.2016.03.012.

26. Wang, C.S.; Lin, C.H. Synthesis and Properties of Phosphorus-Containing Epoxy. *J. Polym. Sci. Part A Polym. Chem.* **1999**, *37,* 3903–3909.
27. Lin, C.H.; Wang, C.S. Novel phosphorus-containing epoxy resins Part I. Synthesis and properties. *Polymer (Guildf).* **2001**, *42*, 1869–1878, doi:10.1016/S0032-3861(00)00447-X.
28. Schlagenhauf, L.; Chu, B.T.T.; Buha, J.; Nüesch, F.; Wang, J. Release of Carbon Nanotubes from an Epoxy-Based Nanocomposite during an Abrasion Process. *Environ. Sci. Technol.* **2012**, *46*, 7366–7372, doi:10.1021/es300320y.
29. International Organization for Standardization (ISO). ISO 178 : 2001 Plastics - Determination of flexural properties. In *ISO Standards;* ISO Central Secretariat: Geneva, Switzerland, 2003.
30. Tang, L.C.; Wan, Y.J.; Yan, D.; Pei, Y.B.; Zhao, L.; Li, Y.B.; Wu, L. Bin; Jiang, J.X.; Lai, G.Q. The effect of graphene dispersion on the mechanical properties of graphene/epoxy composites. *Carbon* **2013**, *60*, 16–27, doi:10.1016/j.carbon.2013.03.050.
31. Hollertz, R.; Chatterjee, S.; Gutmann, H.; Geiger, T.; Nüesch, F. a; Chu, B.T.T. Improvement of toughness and electrical properties of epoxy composites with carbon nanotubes prepared by industrially relevant processes. *Nanotechnology* **2011**, *22*, 125702, doi:10.1088/0957-4484/22/12/125702.
32. Ma, P.C.; Mo, S.Y.; Tang, B.Z.; Kim, J.K. Dispersion, interfacial interaction and re-agglomeration of functionalized carbon nanotubes in epoxy composites. *Carbon* **2010**, *48*, 1824–1834, doi:10.1016/j.carbon.2010.01.028.
33. International Electrotechnical Commission (IEC). IEC 61340-5-1:2016 Electrostatics - Part 5-1: Protection of electronic devices from electrostatic phenomena - General requirements. In *IEC standards;* IEC Central Office: Geneva, Switzerland, 2016.
34. Zaman, I.; Kuan, H.-C.; Dai, J.; Kawashima, N.; Michelmore, A.; Sovi, A.; Dong, S.; Luong, L.; Ma, J. From carbon nanotubes and silicate layers to graphene platelets for polymer nanocomposites. *Nanoscale* **2012**, *4*, 4578–4586, doi:10.1039/c2nr30837a.
35. Matzui, L.Y.; Vovchenko, L.L.; Perets, Y.S.; Lazarenko, O.A. Electrical conductivity of epoxy resin filled with graphite nanoplatelets and boron nitride. *Materwiss. Werksttech.* **2013**, *44*, 254–258, doi:10.1002/mawe.201300117.
36. Liang, J.; Wang, Y.; Huang, Y.; Ma, Y.; Liu, Z.; Cai, J.; Zhang, C.; Gao, H.; Chen, Y. Electromagnetic interference shielding of graphene/epoxy composites. *Carbon* **2009**, *47*, 922–925, doi:10.1016/j.carbon.2008.12.038.
37. Meng, Q.; Wu, H.; Zhao, Z.; Araby, S.; Lu, S.; Ma, J. Free-standing, flexible, electrically conductive epoxy/graphene composite films. *Compos. Part A Appl. Sci. Manuf.* **2017**, *92*, 42–50, doi:10.1016/j.compositesa.2016.10.028.
38. Min, C.; Yu, D.; Cao, J.; Wang, G.; Feng, L. A graphite nanoplatelet/epoxy composite with high dielectric constant and high thermal conductivity. *Carbon* **2013**, *55*, 116–125, doi:10.1016/j.carbon.2012.12.017.
39. Li, Y.; Zhang, H.; Porwal, H.; Huang, Z.; Bilotti, E.; Peijs, T. Mechanical, electrical and thermal properties of in-situ exfoliated graphene/epoxy nanocomposites. *Compos. Part A Appl. Sci. Manuf.* **2017**, *95*, 229–236, doi:10.1016/j.compositesa.2017.01.007.

40. Chen, G.; Weng, W.; Wu, D.; Wu, C. PMMA/graphite nanosheets composite and its conducting properties. *Eur. Polym. J.* **2003**, *39*, 2329–2335, doi:10.1016/j.eurpolymj.2003.08.005.
41. Li, J.; Kim, J.K. Percolation threshold of conducting polymer composites containing 3D randomly distributed graphite nanoplatelets. *Compos. Sci. Technol.* **2007**, *67*, 2114–2120, doi:10.1016/j.compscitech.2006.11.010.
42. Jouyandeh, M.; Paran, S.M.R.; Jannesari, A.; Saeb, M.R. 'Cure Index' for thermoset composites. *Prog. Org. Coat.***2019**, *127*, 429–434, doi:10.1016/j.porgcoat.2018.11.025.
43. Prolongo, S.G.; Moriche, R.; Jiménez-Suárez, A.; Sánchez, M.; Ureña, A. Advantages and disadvantages of the addition of graphene nanoplatelets to epoxy resins. *Eur. Polym. J.* **2014**, *61*, 206–214, doi:10.1016/j.eurpolymj.2014.09.022.
44. Atif, R.; Shyha, I.; Inam, F. Mechanical, Thermal, and Electrical Properties of Graphene-Epoxy Nanocomposites—A Review. *Polymers (Basel)* **2016**, *8*, 281, doi:10.3390/polym8080281.
45. Garcia, F.G.; Soares, B.G.; Pita, V.J.R.R.; Sánchez, R.; Rieumont, J. Mechanical properties of epoxy networks based on DGEBA and aliphatic amines. *J. Appl. Polym. Sci.* **2007**, *106*, 2047–2055, doi:10.1002/app.24895.
46. Matsumoto, A.; Hasegawa, K.; Fukuda, A.; Pae, J. -S Properties of epoxy resin cured by phenol novolac/4-hydroxyphenylmaleimide polymer blend hardeners. *Polym. Int.* **1993**, *31*, 275–282, doi:10.1002/pi.4990310310.
47. Yang, S.; Wang, J.; Huo, S.; Wang, M.; Wang, J.; Zhang, B. Synergistic flame-retardant effect of expandable graphite and phosphorus-containing compounds for epoxy resin: Strong bonding of different carbon residues. *Polym. Degrad. Stab.* **2016**, *128*, 89–98, doi:10.1016/j.polymdegradstab.2016.03.017.
48. Layek, R.K.; Samanta, S.; Chatterjee, D.P.; Nandi, A.K. Physical and mechanical properties of poly(methyl methacrylate) -functionalized graphene/poly(vinylidine fluoride) nanocomposites: Piezoelectric β polymorph formation. *Polymer (Guildf)* **2010**, *51*, 5846–5856, doi:10.1016/j.polymer.2010.09.067.
49. Potts, J.R.; Dreyer, D.R.; Bielawski, C.W.; Ruoff, R.S. Graphene-based polymer nanocomposites. *Polymer (Guildf)* **2011**, *52*, 5–25, doi:10.1016/j.polymer.2010.11.042.
50. Rittigstein, P.; Priestley, R.D.; Broadbelt, L.J.; Torkelson, J.M. Model polymer nanocomposites provide an understanding of confinement effects in real nanocomposites. *Nat. Mater.* **2007**, *6*, 278–282, doi:10.1038/nmat1870.
51. Vahabi, H.; Kandola, B.; Saeb, M. Flame Retardancy Index for Thermoplastic Composites. *Polymers (Basel)* **2019**, *11*, 407, doi:10.3390/polym11030407.
52. Laachachi, A.; Burger, N.; Apaydin, K.; Sonnier, R.; Ferriol, M. Is expanded graphite acting as flame retardant in epoxy resin? *Polym. Degrad. Stab.* **2015**, *117*, 22–29, doi:10.1016/j.polymdegradstab.2015.03.016.
53. Genovese, A.; Shanks, R.A. Fire performance of poly(dimethyl siloxane) composites evaluated by cone calorimetry. *Compos. Part A Appl. Sci. Manuf.* **2008**, *39*, 398–405, doi:10.1016/j.compositesa.2007.09.009.

54. Movahedifar; Vahabi; Saeb; Thomas Flame Retardant Epoxy Composites on the Road of Innovation: An Analysis with Flame Retardancy Index for Future Development. *Molecules* **2019**, *24*, 3964, doi:10.3390/molecules24213964.

Appendix A

Graphical Abstract

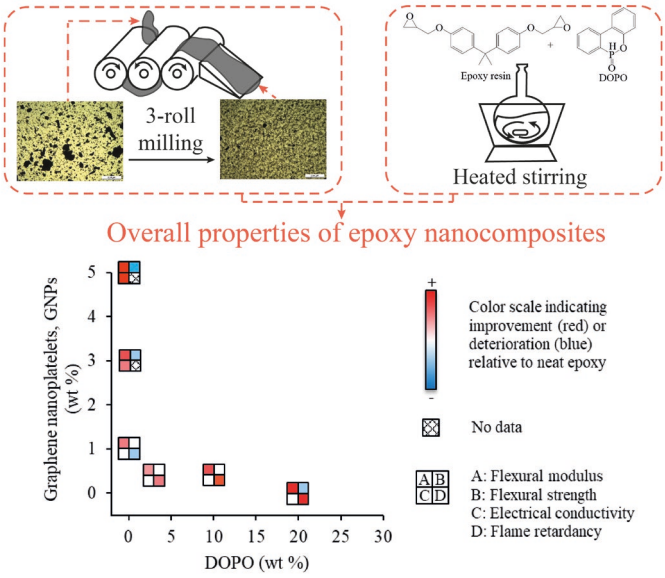

Calculation of Epoxy/Hardener Ratio and Epoxy Equivalent Weight (EEW)

The epoxy/hardener ratio was calculated according to the following equation:

$$\frac{Epoxy}{hardener} ratio = \frac{AHEW}{EEW} \times 100,$$

where amine hydrogen equivalent weight (AHEW) of Jeffamine D-230 is 59.52 g/eq;

EEW of neat epoxy= 186 g/eq (averaged value).

Therefore, the epoxy/hardener ratio is 32. For DOPO-incorporated epoxy resin, EEW value increased as the DOPO content increased due to the reaction between epoxide groups and DOPO molecules as displayed in Fig. A1. The EEW can be calculated as follows:

$$EEW = \frac{Mass\ of\ epoxy\ resin + mass\ of\ DOPO}{\left(\frac{mass\ of\ epoxy\ resin}{EEW\ of\ epoxy\ resin} - \frac{mass\ of\ DOPO}{MW\ of\ DOPO}\right)}.$$

Reaction between Epoxy and DOPO

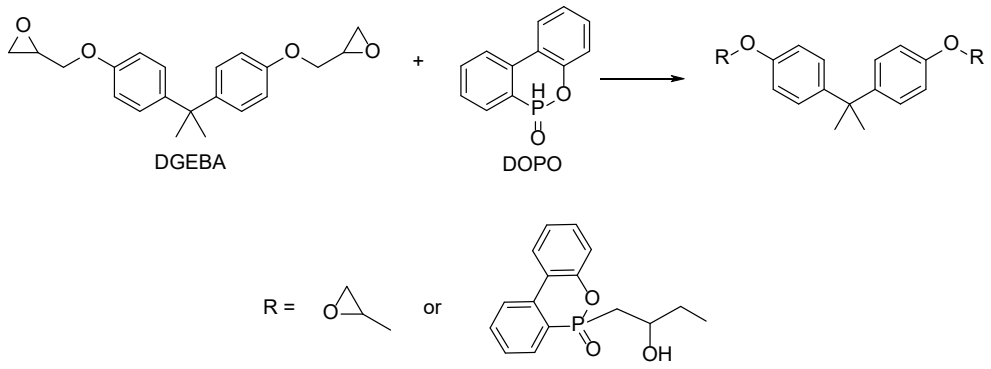

Figure A1 Reaction between epoxy resin (DGEBA) and DOPO

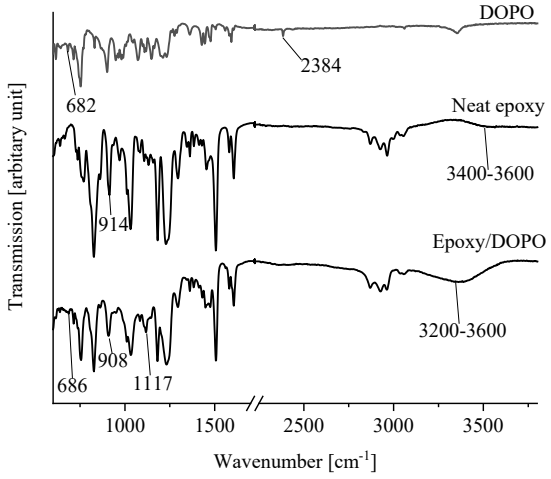

Figure A2 ATR-FTIR spectra indicating the functional groups of DOPO, neat epoxy and epoxy/DOPO mixture

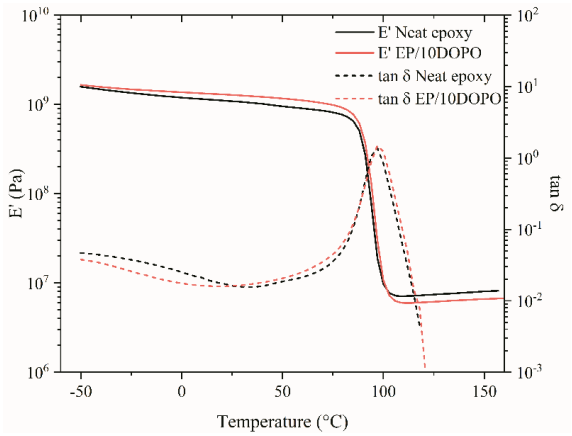

Figure A3 Storage modulus (E') and tan δ of neat epoxy resin and EP/10DOPO obtained from DMTA

Table A1 Formulations of epoxy resin and DOPO-incorporated epoxy resin cured with polyetheramine (Jeffamine D-230)

Epoxy resin mass (g)	DOPO mass (g)	Hardener mass (g)	Phosphorous content (wt.%)
100	0	32	0
100	3	30	0.3
100	10	27	1.0
100	20	22	2.0
100	30	18	2.9

Table A2 Identification of observed peaks from FTIR spectra of DOPO, neat epoxy and epoxy/DOPO mixtures

Compound	Region (cm^{-1})	Assignment
DOPO	3353	O-H stretching
	3060	aromatic C-H stretching
	2384	P-H stretching
	1593	aromatic C=C stretching
	1147	P=O stretching
	990	P-H bending
	753	aromatic C-H bending (ortho-substituted)
	682	P-C stretching
Neat epoxy	3200-3500	O-H stretching
	2964, 2926, 2871	C-H stretching of sp^3 CH
	1606, 1506, 1454	aromatic C=C stretching
	1581	aromatic C=C bending
	1361	sp^3 C-H bending
	1295	aromatic C-C stretching
	1182	C-C symmetrical stretching

	1031	C-O-C of ether
	914	C-O stretching of oxirane group
	827	aromatic C-H bending (para-substituted)
	770	C-H bending
EP/30DOPO	3200-3500	O-H stretching
	2962, 2927, 2869	C-H stretching of sp^3 CH
	1606, 1507, 1448	aromatic C=C stretching
	1581	aromatic C=C bending
	1361	sp^3 C-H bending
	1294	aromatic C-C stretching
	1181	C-C symmetrical stretching
	1117	alkoxy C-O from ring opening of epoxide group
	1033	C-O-C of ether
	908	C-O stretching of oxirane group
	826	aromatic C-H bending (para-substituted)
	755	aromatic C-H bending (ortho-substituted)
	686	P-C stretching

Electrical Properties of the Epoxy Nanocomposites

Table A3 Electrical properties of the epoxy/GNP composites

GNP content (wt.%)	**GNP content (volume fraction)**	**Discharge type**	**Measured electrical resistance (Ω)**	**Resistivity (Ohm-m)**	**Conductivity (S/m)**
0.1	0.0004	sphere to sphere line spark	1.00E+12[a]	1.00E+10[b]	1.00E-10
0.5	0.0019	sphere to sphere line spark	1.00E+12 [a]	1.00E+10 [b]	1.00E-10
1	0.0038	sphere to sphere line spark	1.00E+12 [a]	1.00E+10[b]	1.00E-10

2	0.0076	corona	7.33E+08	3.23E+06	3.10E-07
3	0.0117	corona	4.34E+07	1.91E+05	5.24E-06
4	0.0156	changing between corona and line	9.81E+05	4.32E+03	2.32E-04
5	0.0197	line	9.38E+05	4.13E+03	2.42E-04

[a] The values were measured in order of magnitude.

[b] The values were approximated using the relationship in Equation A1 and the order of magnitude of the electrode dimensions.

In order to interpret the results from the discharge test, three different phenomena can happen according to the electrical properties of each material. In case of insulating material, the hard spark can be observed between the two metal spheres. For conductive or low-resistant material, line spark originating from the metal spheres to the samples can be detected. If the sample is dissipative and has high resistance, a corona or smooth discharge can be observed between the metal spheres and the sample.

The resistance of the composites with the GNP content ranging from 0 wt.% to 1 wt.% was over the detection limit of the multimeter; therefore, the surface resistance meter (SR110, Wolfgang Warmbier GMBH & Co., Germany), which provided the measured results in orders of magnitude ranging from 10^3 Ω to 10^{12} Ω was employed. The results showed that the resistance of these composites were in the order of 10^{12} Ω. When the GNP content increased up to 5 wt.%, the resistance decreased by seven orders of magnitude as shown in Table A3. The relationship between resistance (Ω) and resistivity (Ω-m) is presented in Equation A1.

$$R = \rho \times \frac{L}{A} \qquad \text{Equation A1}$$

where R is resistance; ρ is resistivity; L is length between electrodes and A is the cross sectional area between electrodes.

The percolation threshold can be calculated according to scaling theory as shown in Equation A2, where σ_c and σ_f are the conductivity of the composite and the conductivity of the filler, respectively, Φ is the filler concentration, Φ_c is the volume fraction of filler at the percolation threshold, and t is the critical exponent that depends on the dimensionality of the GNP network. GNP conductivity used was 10^2 S/m, which was the lower bound of the conductivity reported by manufacturer (10^2 S/m when measured perpendicular to the sheet and 10^7 S/m when measured parallel to the sheet). Normally, t≈2 means GNPs form three-dimensional network [39]. This equation is only feasible when $\Phi > \Phi_c$. To calculate the volume fraction of GNP, the density of GNP, epoxy, and hardener used were 2.2 g/cm^3, 1.17 g/cm^3 and 9.47 g/cm^3, respectively.

$\sigma_c = \sigma_f(\Phi - \Phi_c)^t$ Equation A2

The electrical conductivity of the EP/GNP composites improved by three orders of magnitude when the GNP content increased from 1 wt.% to 2 wt.% corresponding to 0.0038 – 0.0076 volume fraction. The precipitous increase in conductivity suggested that the electrical percolation threshold should be between 1 wt.% and 2 wt.% GNP.

Chapter 3

Release of Graphene-Related Materials from Epoxy-Based Composites: Characterization, Quantification and Hazard Assessment *In Vitro*

Woranan Netkueakul [1,2,#], Daria Korejwo [3,4,#], Tobias Hammer [1,2], Savvina Chortarea [3], Patrick Rupper [5], Oliver Braun [6,7], Michel Calame [5,6,8], Barbara Rothen-Rutishauser [4], Tina Buerki-Thurnherr [3], Peter Wick [3,‡], Jing Wang [1,2,‡]

[1] Institute of Environmental Engineering, ETH Zurich, 8093, Zurich, Switzerland
[2] Laboratory for Advanced Analytical Technologies, Empa, Swiss Federal Laboratories for Materials Science and Technology, 8600, Dübendorf, Switzerland
[3] Particles-Biology Interactions Lab, Empa, Swiss Federal Laboratories for Materials Science and Technology, 9014, St. Gallen, Switzerland
[4] Adolphe Merkle Institute, University of Fribourg, 1700 Fribourg, Switzerland
[5] Laboratory for Advanced Fibers, Empa, Swiss Federal Laboratories for Materials Science and Technology, 9014, St. Gallen, Switzerland
[6] Transport at Nanoscale Interfaces Laboratory, Empa, Swiss Federal Laboratories for Materials Science and Technology, 8600, Dübendorf, Switzerland
[7] University of Basel, Department of Physics, Basel, 4056, Switzerland
[8] University of Basel, Swiss Nanoscience Institute, Basel, 4056, Switzerland

[#] shared first author contribution; [‡] shared corresponding author contribution

Author contributions

W.N. fabricated epoxy composites, performed abrasion tests, and characterized physicochemical properties of GRMs and abrade particles. D. K. performed *in vitro* toxicity assessments and evaluated the interferences of pristine GRMs as well as analyzed the toxicity data. W.N. and S.C performed the *in vitro* toxicity assessment of abraded particles. T.H. analyzed the exposed GRMs using lead-labeling method with ICP-OES. P.R. performed XPS analysis. O.B. performed Raman spectroscopy mapping of the abraded particles under supervision of M.C. T.B.T. supervised and helped with the *in-vitro* toxicity assessment. B.R.R. supervised the *in-vitro* toxicity part. P.W. and J.W. initiated the project and conceived the study. W.N. and D.K. wrote the manuscript. All of the authors have discussed the results and have given approval to the final version of the manuscript.

This work has been published in *Nanoscale* **2020**, 12 (19), 10703–10722. DOI: 10.1039/C9NR10245K. This is a post-print version, differing from the published paper only in in terms of layout and formatting.

Abstract

Due to their mechanical strength, thermal stability and electrical conductivity, graphene-related materials (GRMs) have been extensively explored for various applications. Moreover, GRMs

have been studied and applied as fillers in polymer composite manufacturing to enhance polymer performance. With the foreseen growth in GRMs production, occupational and consumer exposure is inevitable, thus raising concerns for potential health risks. Therefore, this study aims 1) to characterize aerosol particles released after mechanical abrasion on GRM-reinforced epoxy composites, 2) to quantify the amounts of protruding and free-standing GRMs in the abraded particles and 3) to assess potential effects of the pristine GRMs as well as the abraded particles on human macrophages differentiated from the THP-1 cell line in vitro. GRMs used in this study included graphene nanoplatelets (GNPs), graphene oxide (GO), and reduced graphene oxide (rGO). All types of pristine GRMs tested induced a dose-dependent increase in reactive oxygen species formation, but a decrease in cell viability was only detected for large GNPs at high concentrations (20 and 40 μg/mL). The particle modes measured by the scanning mobility particle sizer (SMPS) were 300-400 nm and by the aerodynamic particle sizer (APS) were between 2-3 μm, indicating the release of respirable particles. A significant fraction (51% to 92%) of the GRMs embedded in the epoxy composites were released in the form of free-standing or protruding GRMs in the abraded particles. The abraded particles did not induce any acute cytotoxic effects.

Keywords: Graphene-related materials, Nanocomposites, Release, Abrasion, In vitro toxicity, Lung

3.1 Introduction

Graphene is a two dimensional single atomic layer material consisting of hexagonally arranged sp^2 carbon. This allows graphene to possess exceptional properties such as high charge carrier mobility of 2.5×10^5 cm^2 V^{-1} s^{-1} at room temperature [1], superior elastic properties of 1 TPa [2], and excellent thermal conductivity with reported values up to 5300 W m^{-1} K^{-1} [3]. Despite graphene's unique characteristics, it is challenging in terms of costs and processing to produce high quality graphene in bulk. Graphene related materials (GRMs) such as graphene nanoplatelets (GNP), graphene oxide (GO), and reduced GO (rGO) are derivative species of graphene containing a few to multiple graphene layers. They can be classified according to their thickness, C/O ratio or lateral size [4].

GRMs are studied and applied as filler to enhance the properties of polymers. Epoxy is a widely used thermoset polymer with a variety of applications as structural, coating and adhesive materials in several fields such as automotive, aeronautics and electronics, due to its high chemical resistance, good adhesive strength, ease of processing, and reasonable price. However, it is brittle and has poor thermal and electrical conductivity [5,6]. The addition of GRMs can improve electrical properties [7,8], thermal conductivity [9,10], mechanical properties [11–13], and flame retardancy [14–18] of epoxy composites.

Due to an increased interest in possible applications of GRMs, concerns about their risk and potential adverse effects on human health have been raised, in particular upon inhalation that represents the most likely route of exposure. Several *in vitro* and *in vivo* studies, with different exposure conditions, doses and time points, have shown that some types of GRMs can either induce cell apoptosis, oxidative stress or DNA damage, while others did not induce any adverse effects [19–23]. The toxicity of GRMs is generally dependent on their physicochemical properties including lateral dimension, surface structure, and functionalization, as well as on their dispersion state and exposure doses [19,20,24–28]. For example, Mittal and colleagues revealed that both lateral dimension and functional groups play an important role on the internalization of graphene derivatives including GO, thermally reduced GO and chemically reduced GO by human lung cells [27]. Thermally reduced GO, having smaller lateral size than GO and sharp corners that promoted cellular uptake, showed increased adverse effects on cell viability, oxidative stress and genotoxicity as compared to GO and chemically reduced GO [27]. Surface properties such as the C/O ratio of GRMs also play an important role on their toxicity effects. GNPs are hydrophobic, while the GO is more hydrophilic due to oxygenated groups. The hydrophilicity of rGO is between that of GNP and GO. GO was reported to cause significantly less cytotoxicity to A549 human alveolar basal epithelial cells than rGO probably due to differences in hydrophilicity [29]. Moreover, because of higher oxygen content and higher hydrophilicity of GO, which facilitates the formation of a protein corona [30] and prevents particle agglomeration [31], GO showed less cytotoxicity to human erythrocytes and skin fibroblasts (CRL-2522) than GNP [31].

During the use phase of the GRM-containing composites, GRMs might be released from the composite due to degradation of the matrix by means of mechanical force, thermal degradation, hydrolysis or UV exposure [32,33]. The released particles might be in the form of free-standing GRMs, GRMs fully-embedded in polymer matrix, or GRMs partially protruding from polymer matrix. They might pose risks to human health depending on their size and shape. Particles with an aerodynamic diameter smaller than 100 μm can be inhaled, but only a certain percentage of the particles with an aerodynamic diameter smaller than 10 μm can penetrate to the alveolar region of the lung [34]. The 2D morphology of GNPs and other GRMs leads to a significant difference between the geometric dimensions (thickness and lateral size) and the aerodynamic size ($d_a = \sqrt{\frac{9\pi}{16}\frac{\rho}{\rho_0} d_{proj} t}$, where d_a is aerodynamic diameter, d_{proj} is projected diameter, t is platelet thickness and ρ and ρ_0 is particle density and unit density, respectively) [21]. This means that the aerodynamic size of such 2D materials can be much smaller than their lateral dimension, represented by the projected area diameter. Su and colleagues studied the deposition of graphene nanoparticles with a lateral size of 2 μm using human upper airway replicas including nasal and oral-to-lung airways. Only a small fraction (less than 4%) of the graphene nanoparticles were deposited on the studied airways with a deposition efficiency lower than 0.03,

implying that the inhalable fraction of graphene nanoparticles could penetrate and deposit into the lower lung compartments [35].

In contrast to pristine nanoparticles, hazard assessment of processed particles released from nanoparticle-containing products are scarce and there is, to the best of our knowledge, no study available on the biological impact of particles released from GRM-reinforced composites. For example, the toxicity of the particles generated in the workplace by machining process of six different epoxy/carbon fiber composites was investigated *in vitro* using rabbit alveolar macrophages and *in vivo* using direct intratracheal injection into rat lungs [36]. They found that *in vitro* and *in vivo* results showed similar ranking for all samples. The toxicity results showed that two of the composites were more toxic than the reference inert particle (Al_2O_3) for alveolar macrophages, while other four composites showed little toxicity. The inconsistent results among different composites suggested that the composition of the matrix material, i.e. types of epoxy and hardener, could play an important role for the different biological impacts [36–38]. For epoxy/carbon nanotube (CNT) composites, Schlagenhauf and co-workers found that abraded particles contained a low fraction of free-standing or protruding CNTs but they did not significantly induce reactive oxygen species (ROS) formation, DNA damage, release of inflammatory cytokines, or cytotoxicity in differentiated human THP-1 macrophages and A549 human alveolar epithelial cells [39]. Pang *et al.* investigated the *in vitro* toxicity of released particles from sanding process of nanoscale copper phthalocyanine (n-CuPc)-containing automobile coatings on mouse macrophages. They demonstrated that although n-CuPc itself induced the formation of ROS, the released particles did not induce the ROS formation because n-CuPc particles were embedded in the polymer matrix [40]. A recent study found that released nanoclay particles from low-density polyethylene (LDPE) composites by aging process using UV and ozone did not induce ROS formation nor a decrease in cell viability on A549 alveolar epithelial cells at both 24 h and 48 h time points [41].

Overall, there is inconsistency of the biological impacts of pristine GRMs and a lack of studies on the released particles from the GRM-containing composites, which is critical to the safe and sustainable design of novel GRM-reinforced composites. To fill this knowledge gap, we aim to perform a comprehensive analysis on the safety of GRMs along some stages of the life cycle of epoxy/GRM composites i.e. the occupational exposure to pristine GRMs and the exposure to released particles during the use phase simulated by an abrasion process. This includes investigations on acute toxicity of pristine GRMs (commercial GNP, GO and rGO) with distinct physicochemical properties on human macrophages differentiated from THP-1 cell line, particle size distributions (PSDs) of released particles from abrasion of epoxy/GRM composites, quantification of the amount of free-standing and protruding GRMs from the abraded particles and acute cytotoxicity of released particles on differentiated THP-1 macrophages. In this study, epoxy resin, which is an important and frequently used polymer, was chosen as polymer matrix to produce the GRM-reinforced composites due to its transparency and ease of manufacturing.

We used human macrophages differentiated from THP-1 cell line for cytotoxicity evaluation because they are important for host defense mechanism and cellular response to foreign particles deposited in the lungs, which signify the acute inhalation toxicity *in vitro*. The results are essential for the hazard and risk evaluation of occupational and consumer exposure and will support the safe development and use of GRM-reinforced polymer composites.

3.2 Material and Methods

3.2.1 Fabrication of Epoxy/GRM Composites

Five types of GRMs were assessed including two types of GNP: GNP-1 (Cheaptubes, USA) and GNP-2 (XG Science, USA), two types of GO: GO-1 (Cheaptubes, USA) and GO-2 and one type of reduced GO (rGO). GO-2 and rGO were provided by Université Paul Sabatier, CNRS, Toulouse, France. The epoxy and hardener used were diglycidyl ether of bisphenol A, DGEBA (Araldite GY 250, Huntsman, USA) and Jeffamine D-230 (Huntsman, USA), respectively. In order to manufacture the epoxy/GRM composites, epoxy resin and 1 wt % GRMs were mixed manually and homogenized using a high speed mixer at 2000 rpm for 5 min. Then GRMs were evenly dispersed in the epoxy matrix using a three-roll-mill (SDY 200, Bühler AG, Switzerland). After addition of hardener, mixing and degassing, the mixture was poured into a metal mold and cured at 80 °C for 12 h and post-cured at 120 °C for 4 h. The fabricated composites were cut to the desired size for an abrasion process.

3.2.2 Characterization of Pristine GRMs and Abraded Particles

Morphology of pristine GRMs and released particles from the composites were characterized using scanning electron microscope (SEM) (Nova NanoSEM 230). SEM equipped with EDX was used to analyze the elemental composition of the materials. Atomic force microscopy was conducted with Solver Nano atomic force microscope (NT-MTD Spectrum Instruments, Moscow, Russia) to analyze the thickness of pristine GRMs. Raman spectra were obtained using a Raman spectrometer (Senterra, Bruker, Billerica, MA). Diffuse reflectance Fourier transform spectroscopy (DRIFTS) was performed using a VECTOR 22 spectrometer (Bruker Optics). X-ray photoelectron spectroscopy was performed with a Scanning XPS Microprobe system (PHI VersaProbe II spectrometer, Physical Electronics) using monochromatic Al Kα radiation (1486.6 eV). Two random spots per sample were analyzed with a microfocused X-ray beam of 100 µm diameter and dual beam charge neutralization. The samples were pressed onto an indium foil producing flat and continuous areas (no indium signal was observed in the spectra). Survey scan spectra (0-1100 eV) were acquired with 0.8 eV energy step width, 187.85 eV pass energy and 200 ms acquisition time per data point. In addition, higher resolution scans over carbon C 1s and oxygen O 1s were measured (0.125 eV energy step width, 29.35 eV pass energy, 2.4 s acquisition time each per data point). More details about the XPS measurements are given in [26]. X-ray diffraction was performed on an X-ray diffractometer with the scan range

between 5 and 80 degrees and scan rate of 0.017. Zeta potential and hydrodynamic size distribution of both pristine GRMs and released particles were characterized using a Zetasizer (model Nano ZS, Malvern Instruments, Worcestershire, UK). For zeta potential measurement, the particles were dispersed in 10% PBS in water. It was not feasible to measure the zeta potential in biological medium since the high ionic strength and the biological constituents in the medium could induce electrode blackening, which could cause errors to the measurement results. The average values of three consecutive measurements were reported. The particle dispersions were prepared in water and complete RPMI-1640 cell culture medium followed by ultra-sonication prior to hydrodynamic size measurement. Due to instability of the particle dispersion, ultra-sonication was performed just before each size measurement. The mean Z average (Z_{ave}) size was obtained from three separate measurements. GRMs were tested for endotoxin contamination with an Endosafe® PTS portable test system (PTS100, Charles River Laboratories; temperature control 37 ± 1°C; photo detectors at 395 nm wavelength) and Endosafe®PTS Cartridges (Charles River Laboratories, Charleston, USA; assay sensitivity 0.01EU/mL) according to the manufacturer's instructions. Further technical details were reported in previous studies [23,26].

3.2.3 Abrasion Process and Particle Collection

The schematic of the experimental set up is depicted in Fig. B1 (adapted from Schlagenhauf *et al.* 2012 [42]). In this study, we used a Taber abraser (Model 5135, Taber, North Tonawanda, NY) equipped with S-42 sandpaper strip wrapped around a CS-0 wheel and an additional weight of 1 kg to simulate the sanding process on the surface of the composites. The released particles from the abrasion were drawn from the abrasion area by a rectangular probe, that was placed next to the abrasive wheel above the composite, with a small suction area of 40 mm^2 to increase the air flow rate near the sample surface, while the suction area used in the study of Schlagenhauf *et al.*, 2012 [42] was 48 mm^2. The samples were analyzed using two instruments including an aerodynamic particle sizer (APS) (Model 3321, TSI) and a scanning mobility particle sizer (SMPS) consisting of a differential mobility analyzer (DMA) (Model 3080, TSI, Shoreview, MN) and a condensation particle counter (CPC) (Model 3775, TSI). These instruments enable online measurement of the particle size distribution of the release particles. After that, the particles were collected on Nuclepore track-etched polycarbonate membranes (Whatman) with a pore size of 0.2 µm. The flow rate was generated by the vacuum line and monitored in the range of 9 to 11 L/min using a mass flow controller (Model GFM37, Aalborg, NY). With our setup, the SMPS analyzed the particles with electrical mobility diameter ranging from 13 to 573 nm, while the APS analyzed the particles with aerodynamic diameter ranging from 0.54 to 19.81 µm. At least three particle size distributions were collected from each sample. The collection of abraded particles for *in vitro* toxicity analysis and for further characterization was performed without the SMPS and the APS to reduce the loss of particles through tubing.

To validate the experimental set up, we also performed experiments with polystyrene latex (PSL) particles with well-defined sizes of 105 nm, 1 µm and 2 µm. A house-made atomizer was employed to generate aerosol particles of PSL dispersions. After the diffusion dryer (silica gel), the aerosol particles entered the instrumentation (either SMPS or APS). The results demonstrated that using a rectangular probe did not affect the particle size distributions of the aerosolized particles (Fig. B2).

The Origin 2018 software (OriginLab Corporation, Northampton, MA) was used to fit the particle size distributions to lognormal distribution (Equation 3.1) (coefficient of determination > 0.99). The parameters in Equation 3.1 are listed as follows: $f(d)$ is the normalized fraction of the measured particle size distributions as a function of particle size, d; n is the number of the fitted modes; y_0 is the baseline of the lognormal distribution; A_i is the area under the graph of each fitted mode; w_i is the standard deviation of each fitted mode; μ_i is the mean of each fitted mode.

$$f(d) = \sum_{i=1}^{n} y_{0,i} + \frac{A_i}{\sqrt{2\pi} w_i d} exp\left(-\frac{(\ln(d)-\mu_i)^2}{2w_i^2}\right) \qquad \text{Equation 3.1}$$

3.2.4 Detection and Quantification of Free-Standing and Protruding GRMs

Raman spectroscopy mapping was employed to differentiate between GRMs from epoxy in the abraded particles. The abraded particles from epoxy/GNP-2 composite were used as representative for Raman spectroscopy mapping. Raman mapping were performed with a WITec Alpha 300 R confocal Raman microscope in backscattering geometry. As excitation a Laser with wavelength of 532 nm and 0.25 – 5 mW power was employed. To focus the light on the sample a 50x Objective (Zeiss, numerical aperture = 0.55) is used. The backscattered light was coupled to a spectrometers: a 300 mm lens-based spectrometer with a grating of 600 g/mm equipped with a thermoelectrically cooled CCD. An area of 35 µm x 35 µm (115 x 115 points) was scanned with an integration time of 2 s per point. The area intensity map was plotted with spatial average size of 2.

The released particles might contain particles with free-standing GRMs, GRMs fully-embedded in polymer matrix, or GRMs partially protruding from the polymer matrix. The GRMs that are not completely covered by epoxy matrix are called exposed GRMs, including the free-standing and the partially protruding forms. To determine the exposed fraction of GRMs in the abraded particles, an indirect quantification approach using lead-labeling techniques combined with inductively coupled plasma - optical emission spectrometry (ICP-OES) was applied [39]. Lead ions adsorbed on the GRMs can be desorbed from the exposed part of the GRMs, whose amount can be correlate to the desorbed lead ions detected. Therefore, this method can quantify the amount of exposed GRMs, but it cannot differentiate between free-standing and protruding

GRMs. It is important to emphasize that the Pb^{2+}-labelled GRMs were only employed for quantification of free-standing and protruding fraction of GRMs by ICP-OES. Other experiments were performed using the Pb^{2+}-free specimen.

Lead-Labeling of GRMs and Determination of Pb^{2+} Adsorption and Release Capacity

Three GRMs, GNP-1, GNP-2 and GO-1, were used as representatives for a wide range of different species of GRMs. Adapting the lead uptake and release approach of Schlagenhauf *et al.*, 2015 [39], master batches of lead-labeled GRMs were produced. Lead ion (Pb^{2+}) was used as the labeling element for GRM detection. Pb^{2+}-loaded GRMs were produced by immersion of 1.5 g of GRMs in 400 mL of Pb^{2+} solution. The Pb^{2+} solution was prepared by dissolving 200 mg of lead (II) acetate trihydrate in 1 L of Millipore water. The GRMs were dispersed in the solution by ultra-sonication for 30 min. After further stirring for 2.5 h, the Pb^{2+}-loaded GRMs were collected by filtration and dried at 50 °C under vacuum for 14 h. The Pb^{2+} uptake capacity was analyzed by immersion of 100 mg Pb^{2+}-loaded GRMs into 5 mL 0.1 M HNO_3 for 1 h. Then the GRMs were filtered out by centrifugal filtration (Amicon Ultra-4 30 kDa, Merck Millipore) at 3000 rpm for 10 min. The filtrate was collected for Pb^{2+} analysis by ICP-OES (Vistra-PRO, Varian Inc., Palo Alto, CA).

Detection of Pb^{2+} by ICP-OES

100 mg of abraded epoxy/Pb^{2+}-loaded GRM particles were immersed in 5 mL of 0.1 M HNO_3 for 1 h. The GRMs were removed by centrifugal filtration and the Pb^{2+} concentration in the filtrate was analyzed by ICP-OES. Three independent measurements of each GRM sample were performed. In addition, two control samples were produced to detect potential leaching of lead ions into the epoxy (control A) and to determine, after adding the hardener, how much lead ions might be released into epoxy matrix and later exposed by abrasion process (control B). For control A, 1 g of epoxy resin was mixed with 0.1 g of lead-coated GRMs and ultra-sonicated for 1 h. Then the GRMs were removed by filtration. The remaining epoxy was dissolved in acetone and 0.1 M HNO_3, consecutively. The solution was analyzed for Pb^{2+} by ICP-OES. For control B, the highest possible amount of Pb^{2+} that could be absorbed and released by GRMs was added into epoxy. Then hardener was added and the mixture was cured at 80 °C for 12 h and post-cured at 120 °C for 4 h. After curing, abrasion process was performed for control B. Control B was assumed as an extreme case when all of the loaded lead ions were released from GRMs into epoxy matrix due to the addition of hardener and tested how much such lead ions could be detected in the abraded particles after abrasion process. The abraded particles were analyzed for Pb^{2+} by ICP-OES as described above.

3.2.5 Cell Culture and Cell Treatment

Human THP-1 monocytes were obtained from European collection of cell cultures (Lot number13 C011,ECOCC, England). After thawing cells were grown in suspensions in T75 cell culture flasks, sub-cultured at least three times prior to experiments and were grown in complete cell culture medium (RPMI-1640 medium, Sigma-Aldrich) supplemented with 10% fetal calf serum (FCS, Sigma-Aldrich), 1% L-glutamine (Sigma-Aldrich) and 1% penicillin–streptomycin–neomycin (PSN, Sigma-Aldrich). Cells were maintained at 37 °C and 5% CO_2 in humidified atmosphere and routinely sub-cultured twice a week at 70–80% confluency. For experiments, THP-1 monocytes were differentiated to macrophages with 200 nM phorbol 12-myristate 13-acetate (PMA; Sigma-Aldrich) for 72 h before particle exposure. THP-1 cells were seeded in well plates with densities of $4x10^4$ cells per well (96 well/ 0.35 cm^2 growth area) in 200 µl medium (MTS, LDH and DCF assay), $2.5x10^5$ cells per well (24 well/ 1.9 cm^2 growth area) in 500 µl medium (for ELISA) or $5x10^5$ cells per well (12 well/ 3.9 cm^2 growth area) in 1000 µl complete cell culture medium (for GSH) and cultivated for 72 h in presence of 200 nM PMA. After differentiation, PMA containing medium was removed and the cells were washed with pre-warmed phosphate buffered saline (PBS) twice before experiments. For all experiments, stock dispersions of the tested materials of 1mg/mL in ultrapure water (GOs, rGO and abraded particles) or sterile filtered (0.22µm pores) 160 ppm Pluronic F-127 (Sigma-Aldrich) in ultra-pure water (GNPs) were prepared by sonication for 10 min (ultrasonic bath, Sonorex Super RK 156 BH, Bandelin) prior to usage and used for maximum one month. Stock dispersions were diluted to the final experimental concentrations in complete cell culture medium, with a percentage of 10% dispersion in medium and suspensions were gently pipetted on top of the cells growing in well plates.

Analysis of Cell Viability and Cytotoxicity (MTS and LDH assay)

Cell viability was assessed after 24 and 48 h of exposure by measurement of the metabolic activity via MTS (3-(4,5-dimethylthiazol-2-yl)-5-(3-cyrboxymethoxy-phenyl)-2-(4-sulfophenyl)-2H-tetrazolium, inner salt) assay obtained as CellTiter96 Aqueous One Solution (Promega). The assay was performed according to the manufacturer's protocol considering the intrinsic GRMs absorbance. Differentiated THP-1 cells were exposed to 200 µL of GRMs or abraded particles diluted in complete cell culture medium at a concentration in the range of 0–40 µg/mL for 24 and 48 h. Cadmium sulphate ($CdSO_4$, Sigma-Aldrich) was applied as the positive control at a concentration of 1000 µM. After exposure, the medium was replaced by 120 µL MTS working solution (20 µL MTS reagent plus 100 µL phenol-red free RPMI-1640). Background absorbance was measured at 490 nm directly after addition of the working solution to consider intrinsic absorbance of residual GRMs. Final absorbance was measured at 490 nm in a microplate reader (Mithras2 Plate reader, Berthold Technologies, Germany) after incubating the cells at standard cell culture conditions for 60 min. Absorbance values were corrected

for intrinsic GRMs absorbance by subtraction of the background values and normalized to untreated samples.

In addition, cytotoxicity was assessed by the lactate-dehydrogenase assay (LDH,CytoTox96® Non-Radioactive Cytotoxicity Assay, Promega) according to the manufacturer's instruction. Differentiated THP-1 cells were exposed to GRMs and abraded particles as mentioned before. 0.2%Triton X-100 (Sigma-Aldrich) served as positive control. After exposure, cell culture medium was collected, centrifuged to remove GRMs and analyzed for LDH release. Assay reagent was added to each well containing the collected cell culture medium and background absorbance was measured at 490 nm right after application to consider the intrinsic absorbance of the GRM in the medium. The 96-well plates were incubated at room temperature for 30 min and final absorbance was measured at 490 nm in the Mithras2 microplate reader. The background absorbance was subtracted from the final values and normalized to untreated samples. Cell free interference assays were performed for pristine GRMs and abraded particles from neat epoxy with the MTS assay at a concentration range of 0–40 µg/mL to exclude potential interference reactions of GRMs with the assay reagents along with possible wrong interpretation (Fig. B12) [43].

Detection of Reactive Oxygen Species and Oxidative Stress (DCF and GSH assay)

The formation of reactive oxygen species (ROS) was detected using a 2′,7′-dichlorofluorescein assay (H_2DCF-DA) [44]. The cell-permeant H_2DCF-DA (2′,7′-dichlorodihydrofluorescein-diacetate; Molecular Probes, Invitrogen) enters the cells and intracellular esterases cleave off the diacetate part. The resulting H_2DCF is ROS sensitive. Its transformation to the fluorescent form DCF serves as a measure of total ROS production. GRMs and abraded particles were diluted in Hank's balanced salt solution (HBSS). Differentiated THP-1 cells were loaded with 50 µM H_2DCF-DA in HBSS per well and incubated in a humidified incubator at standard growth conditions for 60 min. After washing twice with pre-warmed HBSS, cells were exposed to 100 µL of particle dilutions followed by incubation in a humidified incubator at standard growth conditions for 2 h. Positive control was 50 µM 3-morpholinosydnonimine (Sin-1, Sigma-Aldrich). Fluorescence was measured in the Mithras2 microplate reader with excitation at λ=485nm and emission at λ=528 nm. Fluorescence-values were blank-corrected and normalized to untreated controls. To address the possibility of false-positive and false-negative results, we performed cell free interference assays to evaluate the reactivity towards H_2-DCF of the materials alone (Fig. B12) [44].

The intracellular total reduced glutathione (GSH) content of the exposed THP-1 cells was measured using the Glutathione Assay Kit (Cayman Chemical) for deprotonated cell lysates. For cell deproteination, cells were collected by gently scrapping them from the well plate. Cells were then homogenised in 50 mM cold MES buffer (2-(*N*-morpholino)ethanesulphonic acid) and centrifuged (10000 *g* for 15 min at 4 °C). The lysates were deproteinated by the addition of

equal volumes of metaphosphoric acid (MPA) reagent to each sample. After 5 min incubation at RT, samples were centrifuged (2000 *g* for 5 min at 4 °C) and assessed for their GSH content according to the manufacturer's protocol. L-Buthionine-sulfoximine (BSO; 300µM; Sigma-Aldrich) for 24 h was used as a positive control. GSH analysis was performed following GRMs exposure as described above for 24 h and 48 h. Absorbance was measured at 405 nm in the Mithras2 microplate reader. Values are presented as fluorescence percentage relative to the negative control, which was the cells without the treatment with tested materials.

(Pro-) Iinflammatory Cytokine Detection

The (pro-) inflammatory response of differentiated THP-1 macrophages after 24 h and 48 h of exposure to GRMs, and abraded particles was analyzed with enzyme-linked immunosorbent assays (ELISA) for the inflammatory markers interleukin 8 (IL-8), interleukin 6 (IL-6), interleukin 1- beta (IL-1β) and tumor necrosis factor alpha (TNF-α), where the exposure time ranged from 6 h and 24h. Lipopolysaccheride (LPS, from Escherichia coli, 1 mg/mL in complete cell culture medium, Sigma Aldrich) served as the positive control to stimulate inflammatory response. The amount of inflammatory proteins released in the supernatant was quantified by the commercially available uncoated ELISA kits (Invitrogen) according to the manufacturer's protocol. Prior to analysis cell supernatants were centrifuged to remove GRMs. Measured values (Mithras2 Plate reader, Berthold Technologies, Germany) were blank corrected and are shown relative to the negative control. Interference assays for pristine GRMs and abraded particles from neat epoxy were performed as described by Drasler and collegues [23], to exclude false-positive and false-negative results (data not shown).

Cell Morphology

Phase contrast (Axio Imager 10x/20x/40x, Carl Zeiss AG, Switzerland) and fluorescence microscopy (CLSM, LSM780, 60x/1,40 oil, Carl Zeiss AG, Switzerland) analysis of differentiated THP-1 macrophages were conducted after 24 h and 48 h of exposure to GRMs and abraded particles. For fluorescence microscopy, cells were washed 3 times with PBS, fixed in 4% paraformaldehyde (PFA, in PBS, Sigma Aldrich) for 15 min and incubated in 0.1 M Glycine in PBS for 15 min to remove the remaining PFA. Thereupon, cells were permeabilized with 0.2% Triton X-100 (in PBS, Sigma Aldrich). F- actin was stained with Alexa-488 conjugated phalloidin (Life Technologies, Thermo Fisher Scientific, Switzerland), and nuclei were counterstained with DAPI (4′,6-diamidino-2-phenylindole Life Technologies, Thermo Fisher Scientific, Switzerland). DAPI (1:1000) and phalloidin (1:50) were diluted in 0.3% Triton X-100 and 1 g bovine serum albumin in PBS. Staining was performed for 1.5 h at room temperature. Cells were washed 3 times with PBS and mounted with mowiol (Sigma-Aldrich) and kept at 4 °C until microscopic analysis.

3.2.6 Statistical Analysis

Results are expressed as mean ± standard error of mean (StEM) with at least three independent experiments (n ≥ 3). Comparison between groups were evaluated by Student's *t*-test and two-way analysis of variance (ANOVA) using the Graph Pad Prism (GraphPad Software Inc., La Jolla, CA, USA). A statistical significance was defined as $p < 0.05$ compared to the control group.

3.3 Results

3.3.1 Characterization of Pristine GRMs and Abraded Particles from Epoxy/GRM Composites

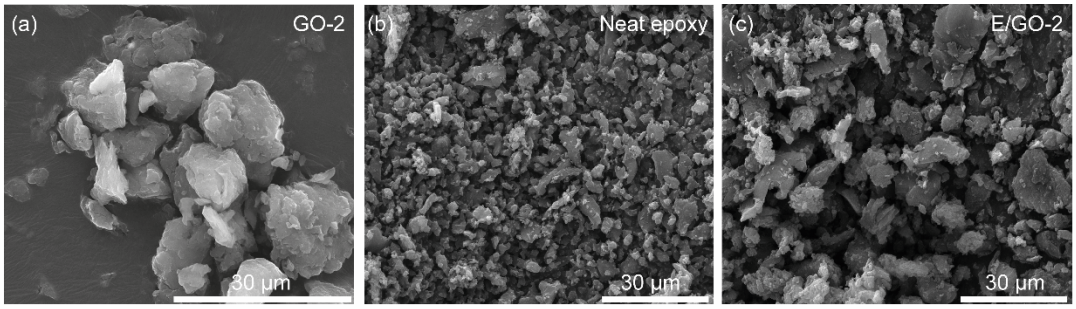

(d) Summary of physicochemical properties of pristine GRMs

Pristine GRMs	GNP-1	GNP-2	GO-1	GO-2	rGO
Lateral dimension (SEM)	1-10 µm	50-150 µm	1-50 µm	1-25 µm	1-25 µm
Number of layers or Thickness	4.56 ± 1.06 nm [b]	6-8 nm [a]/ 239 ± 174 nm [b]	Few to single layer [a]/ 21.6 ± 21.1 nm [b]	~5 layers [a]/ 97.5 ± 46.7 nm [b]	< 4 layers [a]/ 108 ± 85.9 nm [b]
Raman I(D)/I(G) ratio (532 nm)	0.36	1.56	2.33	2.05	2.04
C/O ratio [c]	20.3	33.5	1.8	2.1	4.7
Zeta-Potential in 10%PBS (mV) ± SD	-54.9 ± 3.56	-49.6 ± 3.65	-45.8 ± 2.93	-39.8 ± 1.79	-47.3 ± 2.91

(e) Summary of zeta potential of abraded particles

Abraded particles	Neat epoxy	E/GNP-1	E/GNP-2	E/GO-1	E/GO-2	E/rGO
Zeta-Potential in 10% PBS (mV) ± SD	-19.1 ± 2.76	-19.4 ± 1.76	-16 ± 1.5	-21.2 ± 0.46	-21.8 ± 1.23	-15.5 ± 1.35

[a] Value from manufacturer
[b] Obtained from atomic force microscopy (AFM)
[c] Obtained from X-ray photoelectron spectroscopy (XPS)

Figure 3.1 Characterization of pristine GRMs and abraded particles from epoxy/GRM composites. SEM images of (a) pristine GO-2, (b) abraded particles from neat epoxy, (c) abraded particles from an epoxy/GO-2 composite. (d) Summary of physicochemical properties of pristine GRMs. (e) the zeta potential of abraded particles.

The characterization results of physicochemical properties of pristine GRMs and abraded particles from epoxy/GRM composites are summarized in Fig. 3.1. SEM micrographs of pristine GRMs showed loose agglomerates of micrometer-sized platelet-like (GNP-1, GNP-2, GO-2) or sheet-like structures with some wrinkles (GO-1, rGO) (Fig. 3.1a-c and B3). The abraded samples showed a broad range of differently sized particles with irregular morphologies and rather flat surfaces. The presence of GRMs in the abraded particles could not be detected by SEM imaging. The dispersion stability from zeta potential measurement revealed that pristine GRMs were fairly stable in water (absolute zeta potential > 30 mV), whereas the abraded particles were more likely to agglomerate (Fig. 3.1e).

Raman spectra showed similar absorption peaks of GNP-1 and GNP-2 containing D, G, and 2D bands [45] at around 1355cm^{-1}, 1581 cm^{-1} and 2700 cm^{-1}, respectively (Fig. B4a). For GO-1, GO-2 and rGO, strong D and G bands were observed while the 2D band appeared only weakly. The intensity of the G band relates to the vibration of sp^2 hybridized carbon atoms, whereas that of the D band associates with the vibration of sp^3 hybridized carbon atoms, missing atoms or added atoms of other species than carbon in the carbon structures and the defects in the crystal [46,47]. The intensity ratio I(D)/I(G) of GNP-1 and GNP-2 was clearly lower than that of GO-1, GO-2 and rGO, suggesting that GO-1, GO-2 and rGO accommodated more oxidized carbons with sp^3 hybridization than GNPs did. This is in agreement with XPS results showing higher oxygen content of GOs and rGO than that of GNPs (Fig. 3.1d). Reproducible results were obtained with XPS from the two different measurement points, pointing towards the homogeneity of the investigated samples. Moreover, the fitting of functional groups to the obtained XPS spectra demonstrated that both GNPs were similar in terms of composition and bonding with only low amount of oxygen-containing functional groups. These groups are significantly enhanced in GO-1, GO-2 and rGO samples. Thereby, slight differences in the distribution of C-O, C=O and COO type bonds were found between the GO-1 and GO-2 samples.

Regarding FTIR results (see Fig. B4b), all GRMs showed an absorption peak around 1400 cm^{-1}, which is the vibration peak of the O—H deformation [48]. The peaks between 1635 and 1683 cm^{-1}, which were observed for all GRMs, can be assigned to either the stretching vibration of C=C backbone or to the resonance of the O—H stretching of the absorbed water molecules or hydroxyl groups between 3100-3600 cm^{-1} [49]. The bending of C—OH bond was observed as a sharp peak at 1521 cm^{-1} for GO-1 and a small peak at 1540 cm^{-1} for GO-2 [50], in agreement with the XPS results, where GO-1 contained more C—O than GO-2.

The XRD patterns of GNP-1 and GNP-2 displayed the sharp diffraction at 2-theta 26.7° and 26.9°, which corresponds to the 002 crystal plane with a d-spacing of 3.31 Å and 3.33 Å, respectively (Fig. B4c). The 001 crystal plane of GO-1 and GO-2 was observed at 2-theta 12.3° and 12.2° associated with the d-spacing of 7.2 Å for both GOs. The higher d-spacing in case of GO indicates the presence of oxygen-containing functional groups (epoxy, hydroxyl, carboxyl) on graphene sheets constructing GO [49,51]. The disappearance of the peak around 12° was

observed for rGO, since the reduction of GO to rGO significantly removed the oxygen-containing functional groups from the graphene sheets. This is consistent with the FTIR results showing the disappearance of O—H vibration peaks from rGO.

EDX mapping was employed to analyze the elemental compositions of the abraded particles, specifically to identify whether the abrasive materials could be released from the sanding paper. Since Al_2O_3 was the main component of the abrasive material, we used aluminum as an identification element. The representative SEM/EDX image of abraded particles from neat epoxy showed only small amounts of aluminum (Fig. B5). This indicates that the release of abrasive materials was negligible and is not expected to affect particle size distribution nor toxic effects [42].

3.3.2 Particle Size Distributions of Abraded Particles

The particle size distributions of abraded particles from neat epoxy and epoxy/GRMs composites were analyzed and the results are shown in Fig. 3.2. Particle size distributions fitted with lognormal distribution are presented in Table B3, which includes the particle mode, electrical mobility (d_e) and aerodynamic diameter (d_a), the count median diameter CMD (μm), the geometric standard deviation σ_g, and the area fraction F. During abrasion, the total concentrations measured by SMPS ranged from 0.5×10^4 to 1×10^5 particles/cm^3 with background concentrations between 1000 and 1500 particles/cm^3 (CMD ~100 nm) and those analyzed by APS ranged from 4000 to 6000 particles/cm^3 with background concentrations between 6 and 15 particles/cm^3 (CMD ~0.7 μm).

The abraded particles from neat epoxy and epoxy/GNP composites showed three modes, while those from epoxy/GO and epoxy/rGO composites showed four modes. The first mode was below 500 nm and analyzed by SMPS (Fig. 3.2a), while the other modes were in the micrometer range and measured by APS (Fig. 3.2b).

The first modes of all abraded particles were between 300 nm and 400 nm, and no clear difference in the particle size distributions among all abraded particles was observed. For the other modes, there was no significant difference between the particle size distributions of neat epoxy and those of epoxy/GNP, whereas a notable divergence in the particle size distributions between neat epoxy and epoxy/GO, epoxy/rGO was apparent. For neat epoxy and epoxy/GNP, two modes were detected. Mode 3 that ranged from 2 to 2.5 μm was more dominant than mode 2 at 1 μm. The particle size distributions of epoxy/GO and epoxy/rGO from APS contained 3 modes. Mode 2 at 0.6 μm was the least significant mode. For epoxy/GO, the third mode at 0.8 μm was more prevalent than the fourth mode at 2 μm. For epoxy/rGO, the difference between the fractions of mode 3 at 0.9 μm and mode 4 at 2 μm were not as large as that of epoxy/GO. Considering cumulative fractions, larger amounts of sub-micrometer particles were released from epoxy/GO and epoxy/rGO as compared to neat epoxy and epoxy/GNP composites.

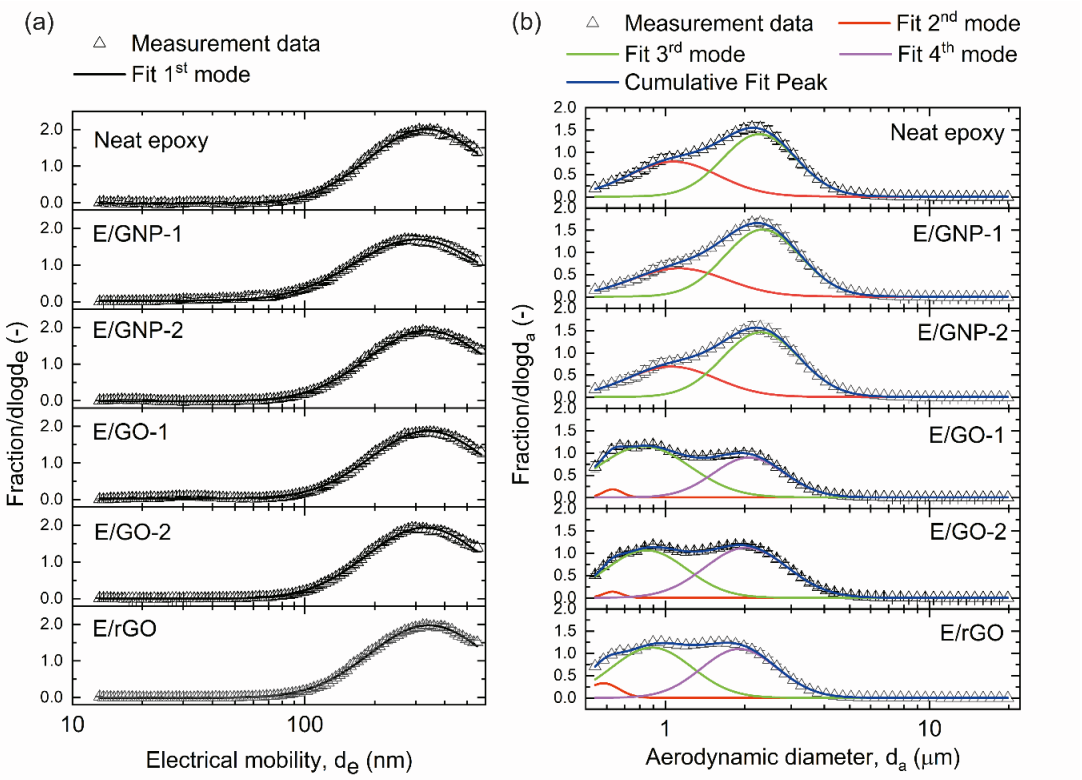

(c) Summary of mode size of the PSD measured by SMPS and the size range measured by APS of abraded particles

Abraded particles	Neat epoxy	E/GNP-1	E/GNP-2	E/GO-1	E/GO-2	E/rGO
Mode size measured by SMPS (μm)	0.333	0.302	0.314	0.338	0.327	0.341
Size range measured by APS (μm)	1-2	1-2	1-2	0.6-2	0.6-2	0.6-2

Figure 3.2 Particle size distributions (PSD) of abraded particles from neat epoxy or epoxy/GRM (E/GRM) composites. (a) Particle size distributions in the sub-micrometer range (13-573 nm) measured by SMPS. (b) Particle size distributions in the micrometer range (0.54–19.81 μm measured by APS. The measurement data were the average of at least three experiments. (c) Summary of mode size of the PSD measured by SMPS and the size range measured by APS of abraded particles.

3.3.3 Detection and Quantification of Free-Standing and Protruding GRMs

Raman spectroscopy mapping was employed to differentiate between GRMs from epoxy in the abraded particles. The abraded particles from epoxy/GNP-2 composite were used as representative for Raman spectroscopy mapping. To quantify the fraction of exposed GRMs from the abraded particles, epoxy/GRM composites were produced using GRMs (GNP-1, GNP-2 and GO-1) that had been pre-labeled with lead ions. Abraded particles were subsequently subjected to acid treatment and ICP-OES analysis to quantify the amount of Pb^{2+} released from protruding and free-standing GRMs [39].

Detection of Free-Standing and Protruding GRMs from the Abraded Particles by Raman Spectroscopy Mapping

Owing to the distinctive Raman spectra of GNP, Raman mapping was performed in order to differentiate GNP from epoxy in the abraded particles obtained from epoxy/GNP-2 composites. The presence of free-standing and protruding GRMs was confirmed by the Raman mapping of a representative area as shown in Fig. 3.3a and b, which qualitatively demonstrated the release of GNP-2 from the abrasion process of the composites. Raman spectrum of reference abraded epoxy particles exhibited the vibration of the epoxy backbone at 1114, 1185, and 1460 cm^{-1}, the vibration of aromatic C=C at 1610 cm^{-1} and the stretching vibration of aliphatic C-H bond at 2800-3000 cm^{-1}. The reference spectrum of GNP-2 shows the typical D band at around 1355 cm^{-1}, G band at 1581 cm^{-1} and 2D band at 2700 cm^{-1}. Fig. 3.3a shows a map of the intensity ratio of the 2D band (center 2700 cm^{-1}, width 200 cm^{-1}) to an epoxy related band (center 3065 cm^{-1}, width 60 cm^{-1}). The non-selected area indicated in gray was mainly the bare substrate not covered by the abraded particles. The color scale indicated the darker color as higher epoxy content and the brighter color as higher GNP content. The fate of GNP in the epoxy composites after abrasion process could possibly be explained by the representative Raman spectra in Fig. 3.3b. GNP might be released from the composite without notable transformation represented by spectrum A, which was almost identical to the GNP reference spectrum. GNP might be transformed and released from the composite during the fabrication or abrasion process resulting in defected structure as evidenced by spectra B and C showing different I(D)/I(G) ratio from the reference GNP-2. GNP might be still embedded in a thin layer of epoxy (spectra C and D) since the spectra show both epoxy signature and GNP peaks. Representative spectra from flat surface and cross-sectional surface of the composite (Fig. B6) always showed epoxy feature because GNP was covered by epoxy, which could represent the GNP in the embedded form. Therefore, we can assume that spectra A and B in Fig. 3.3b were more likely to represent free-standing and/or protruding GNP because the epoxy feature did not appear. With Raman spectroscopy mapping, the presence of free-standing and/or protruding GNP (exposed GNP) can be verified.

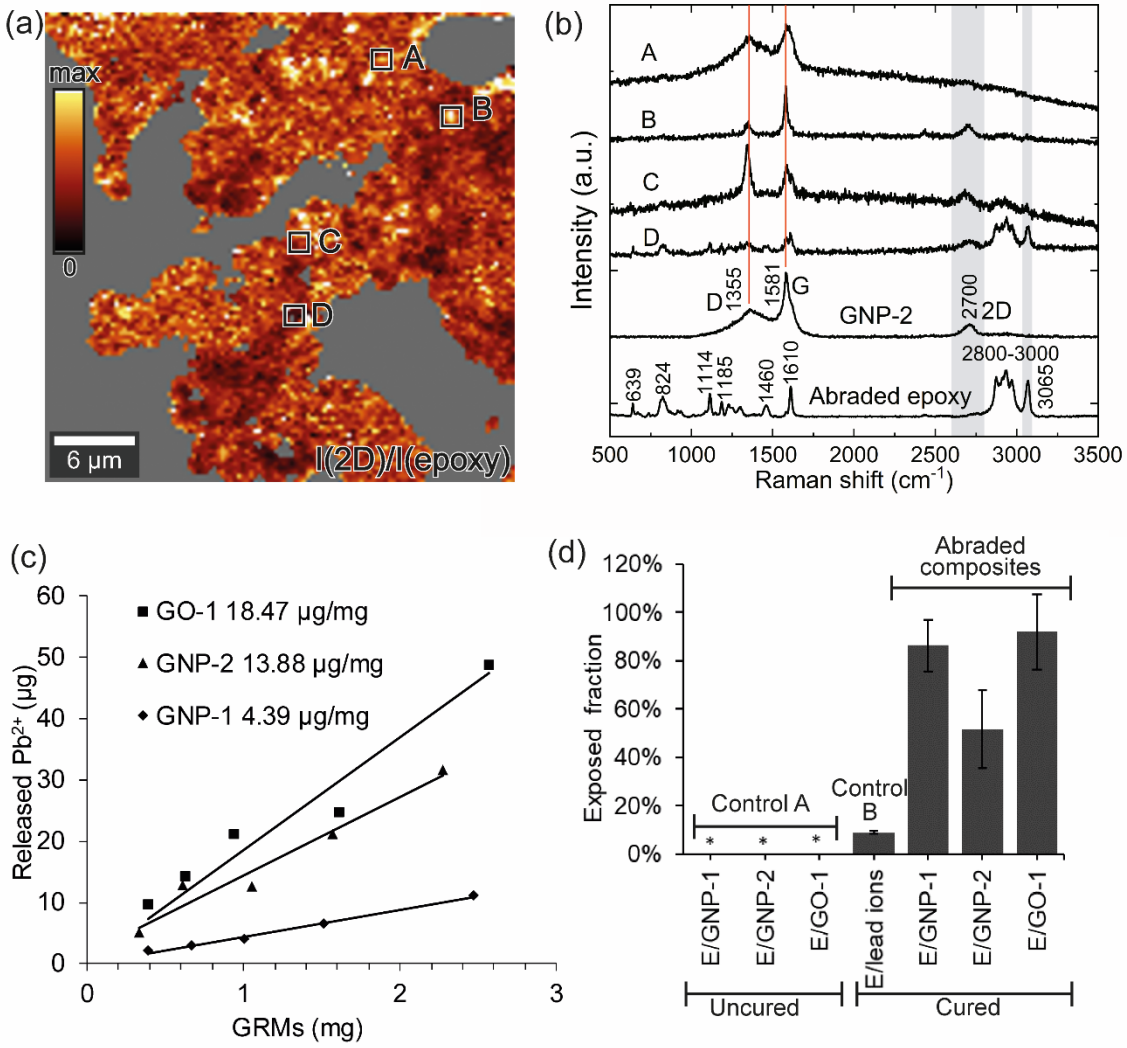

Figure 3.3 Qualitative and quantitative detection of GRMs released from abrasion. Raman spectroscopy mapping of abraded particles from E/GNP-2 showing (a) map of the ratio of the intensity of the 2D band (center at 2700 cm^{-1}) as a marker of GNP-2 to the intensity of an epoxy related Raman band (center at 3065 cm^{-1}). The compared Raman bands are indicated in (b) by gray areas. (b) Representative Raman spectra from different regions in the mapping area as compared to reference GNP-2 and abraded neat epoxy. Red lines are guides to the eye indicating the GNP-2 related Raman bands. (c) Pb^{2+} release capacity of GNP-1, GNP-2, and GO-1 from one representative example of each material. (d) Bar chart of the release fraction of Pb^{2+} from control samples and the exposed fraction of GRMs from three epoxy/GRM composites. Three measurements were performed for each sample. The average mean values are reported with the standard deviations. The concentration of Pb^{2+} in control A (uncured samples) was below the detection limit of 0.1 mg/L, which is marked by *.

Quantification of Free-Standing and Protruding GRMs by Pb^{2+} Labelling Method

Pb^{2+} Adsorption and Release Capacity by GRM

The release of Pb^{2+} per unit mass of GRMs was determined to understand the adsorption and release capacity from lead-loaded GRMs (Fig. 3.3c). GO-1 released the highest amount of Pb^{2+} with a value of 18.47 µg/mg followed by GNP-2 with a value of 13.88 µg/mg. A significant lower concentration of 4.39 µg/mg was detected for the release of Pb^{2+} by GNP-1.

Detection of Exposed GRMs by Lead Ion Release

Two control samples, control A and B, were analyzed to verify that the lead ions measured by ICP-OES were correlated to the amount of GRMs and not due to unspecified leakage of lead ions caused by the manufacturing and/or abrasion process. Control A was evaluated to study whether lead ions can leach from GRM into epoxy matrix. The results showed that the concentrations of leaching Pb^{2+} ions from the control A sample were not detectable by the ICP-OES with a detection limit of 0.1 mg/L. Therefore, prior curing, lead ions did not detach from the GRMs to leach into epoxy. However, Pb^{2+} ions might be released from the GRM by dissolving to the added hardener during the curing process under 80 °C, which means that the detected Pb^{2+} ions from the abraded particles were not correlated to the amount of exposed GRM. It is not possible to confirm whether the lead ions were released or not after adding hardener and/or during the curing process because GRM cannot be removed from the mixture of epoxy, GRM and hardener after curing. Therefore, control B was produced by directly adding the lead ions into epoxy to account for the maximum possible fraction of Pb^{2+} ions leached out from the cured epoxy composite by an abrasion process. The amount of added Pb^{2+} ions was decided based on the worst-case scenario that all Pb^{2+} ions absorbed on the GRM can be released from GRM. Since the Pb^{2+} absorption and release capacity of GO-1 was the highest among the considered GRMs, the corresponding amount of Pb^{2+} that can be absorbed and released by GO-1 was selected as an extreme case assuming that all of the Pb^{2+} from GO-1 could be transferred into the matrix after adding hardener and then released by an abrasion process. The released Pb^{2+} detected from control B was 9.04 ± 0.69% of the total amount of lead ions added to the epoxy, which was the maximum possible fraction of lead ions leached out from the epoxy matrix and the minimum was 0%. This range contributed to the final uncertainty of the GRM release fraction.

Fig. 3.3d displays the amounts of free-standing and protruding GRMs (exposed fraction of GRMs) calculated as the ratio of the free-standing or protruding GRMs divided by the total amount of GRMs embedded in the composite. The fraction of 51% to 92% of the added GRMs in the composites was present as free-standing and protruding GRMs. High exposed fractions were measured for GNP-1 and GO-1 with 86.2 ± 10.8% and 92.0 ± 15.5%, respectively. The fraction of exposed GNP-2 was 51.7 ± 16.3%, lower than the other two GRMs.

3.3.4 Assessing the Cellular Effects of GRMs and Abraded Particles

To understand acute effects of GRMs and abraded particles on lung macrophages *in vitro*, we assessed four endpoints from the oxidative stress paradigm including formation of ROS, depletion of GSH, induction of (pro-) inflammatory responses, and additionally alterations in cell morphology and cell viability/cytotoxicity. Due to the high hydrophobicity of GNP-1 and GNP-2, a biocompatible detergent Pluronic F127 [43] was used to disperse these materials prior to exposure to the cells. Other pristine GRMs and all of the abraded particles were dispersed in endotoxin-free water. Special attention was given to potential interferences of pristine GRMs with the different biological assays by the inclusion of appropriate controls to test for catalytic activity, quenching or intrinsic absorption. Interference was observed only for GO-2 in the DCF assay at concentrations above 10 µg/mL (Fig. B12b). Moreover, all pristine GRM particles quenched the fluorescent signal in immunocytochemical stainings (Fig. B13). Toxic effects from particles released from the abrasion wheel on differentiated THP-1 cells was not expected as confirmed by measurement of the marker element of the wheel and in a previous study using a similar experimental setup [42].

Impact on Oxidative Stress

Changes in ROS and antioxidant glutathione are indicators of oxidative stress, which is frequently observed as a response to nanoparticle exposure caused by an imbalance of the generation of intracellular ROS and a limited antioxidant capacity of cells [52–54]. GSH is an antioxidant peptide that balances the production and destruction of ROS. At high ROS levels, cells initiate a protective response to promote their survival by activating transcription factors and increasing the antioxidant defense (GSH). At high levels of ROS, the protective response is overtaken by inflammation leading to cytotoxicity. Pristine GRMs induced a dose-dependent accumulation in ROS formation after 2 h of exposure in differentiated THP-1 cells (Fig. 3.4a) which was significant for GO-1 at the highest concentration of 40 µg/mL. Only GO-2 showed an initial increase in ROS formation followed by a strong decrease at higher concentrations, which was due to quenching of the fluorescent signal (Fig. B12). No significant formation of ROS was observed for all abraded particles (Fig. 3.4b). GSH levels were slightly decreased for all GRMs, however, a significant dose-dependent reduction of GSH was observed only after exposure to GNP-2 for 24 h (Fig. 3.4c). No significant reduction in glutathione levels was detected after 24 h and 48 h of exposure to abraded particles (Fig. 3.4d).

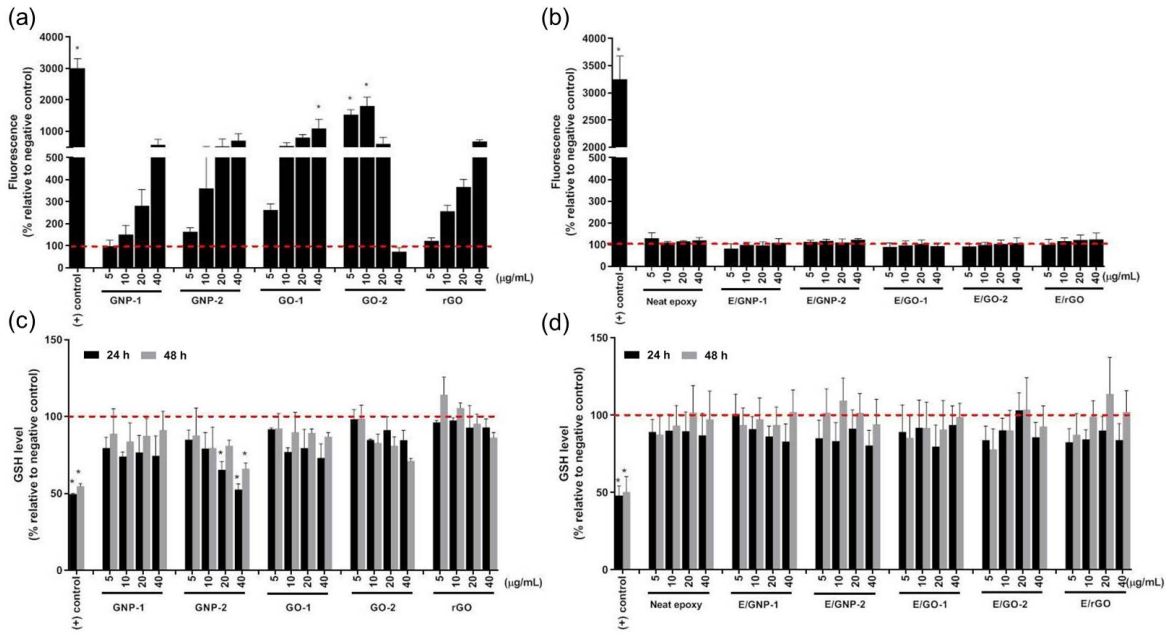

Figure 3.4 Oxidative stress measured by DCF and GSH assay. ROS accumulation was assessed after 2 h of exposure to (a) pristine GRMs or (b) abraded particles. 50 µM Sin-1, a morpholino compound, was used as a positive control. Antioxidant glutathione levels of THP-1 cells were measured after 24 h and 48 h of exposure to (c) GRMs and (d) abraded particles. 300 µM BSO was used as the positive control. The results show the mean ± StEM from at least three independent experiments. The * symbol represents $p< 0.05$ as compared to the negative control (untreated cells).

Impact on (Pro-) Inflammatory Responses

(Pro-) inflammatory cytokines and chemokines, which are endogenous mediators of the immune system, are a group of cytokines or chemokines that are produced in response to inflammatory stimuli to control the inflammatory response. To investigate the cytokine production, we determined the release of four crucial (pro-) inflammatory cytokines i.e. TNF-α, IL-1β, IL-6 and IL-8 in the supernatant. Pristine GRMs did not trigger a significant release of IL6 and TNF-α, but there was a slight trend for a dose-dependent increase of cytokine levels for GNP-1 and GNP-2 (Fig. 3.5). GNP-2 caused a significant increase in IL-1β and IL8, but only at the two highest concentrations (20 µg/mL and 40 µg/mL). Abraded particles from neat epoxy and epoxy/GRM composites did not significantly elevate the level of TNF-α, IL-1β, IL-6, and IL-8 in differentiated THP-1 cells after treatment of 6 h and 24 h for TNF-α and treatment of 24 h and 48 h for the other cytokines (Fig. 3.5).

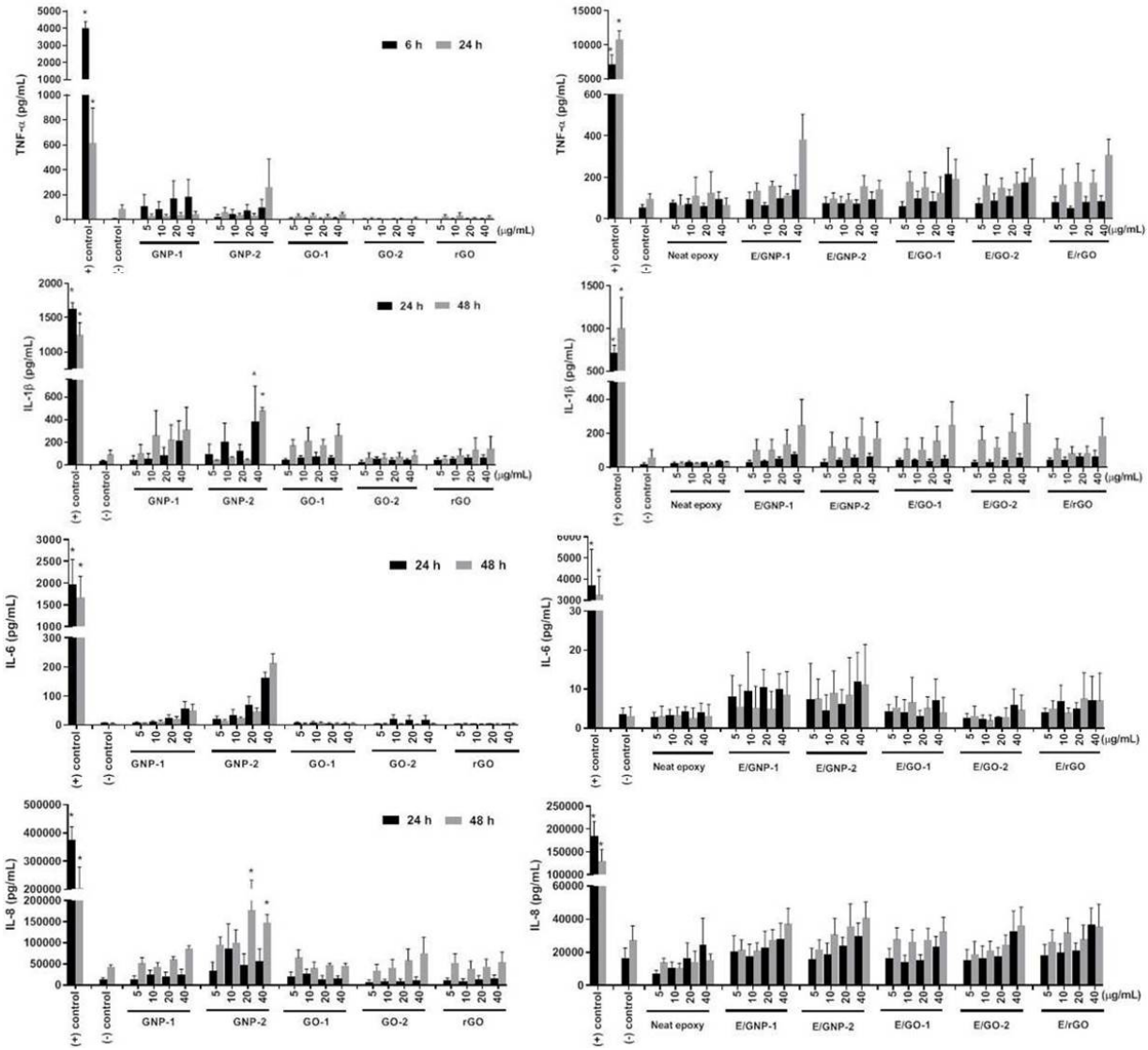

Figure 3.5 (Pro-) inflammatory response of THP-1 macrophages after treatment with GRMs and abraded particles from neat epoxy and epoxy/GRM composites. Concentrations of IL-1β, IL-6 and IL-8 were measured after 24 h and 48 h of exposure while TNF-α release was measured after 6 h and 24 h of exposure. 1 μg/mL LPS was used as the positive control. Results are shown as mean ± StEM from at least three independent experiments. The * symbol represents $p<0.05$ as compared to negative control (untreated cells).

Impact on Cell Viability and Cell Morphology

Cell viability and cytotoxicity were determined using the MTS assay that measures mitochondrial activity of cells and the LDH assay, which determines the levels of released LDH following cell membrane rupture. The pristine GRMs did not reduce mitochondrial activity upon exposure to 40 μg/mL for up to 48 h with the exception of GNP-2, which induced a time- and concentration-dependent decrease in cell viability of differentiated THP-1 cells (Fig. 3.6a) and a subsequent but transient increase in cytotoxicity (Fig. B14). Treatment of THP-1 macrophages

with abraded particles from neat or GRM-reinforced epoxy composites did not induce any decrease in mitochondrial activity (Fig. 3.6b) or increase in the amounts of released LDH (Fig. B14) after 24 h and 48 h of exposure.

No major alterations of cell morphology, i.e. cell nuclei and F-actin cytoskeleton were observed 48 h post-exposure to pristine GRMs or abraded particles (Fig. B13). Some pristine GRMs quenched the fluorescent signal at 488 nm, in particular for GO-1 and GO-2. The deposition of particles on the cells was confirmed from phase contrast images (Fig. B13).

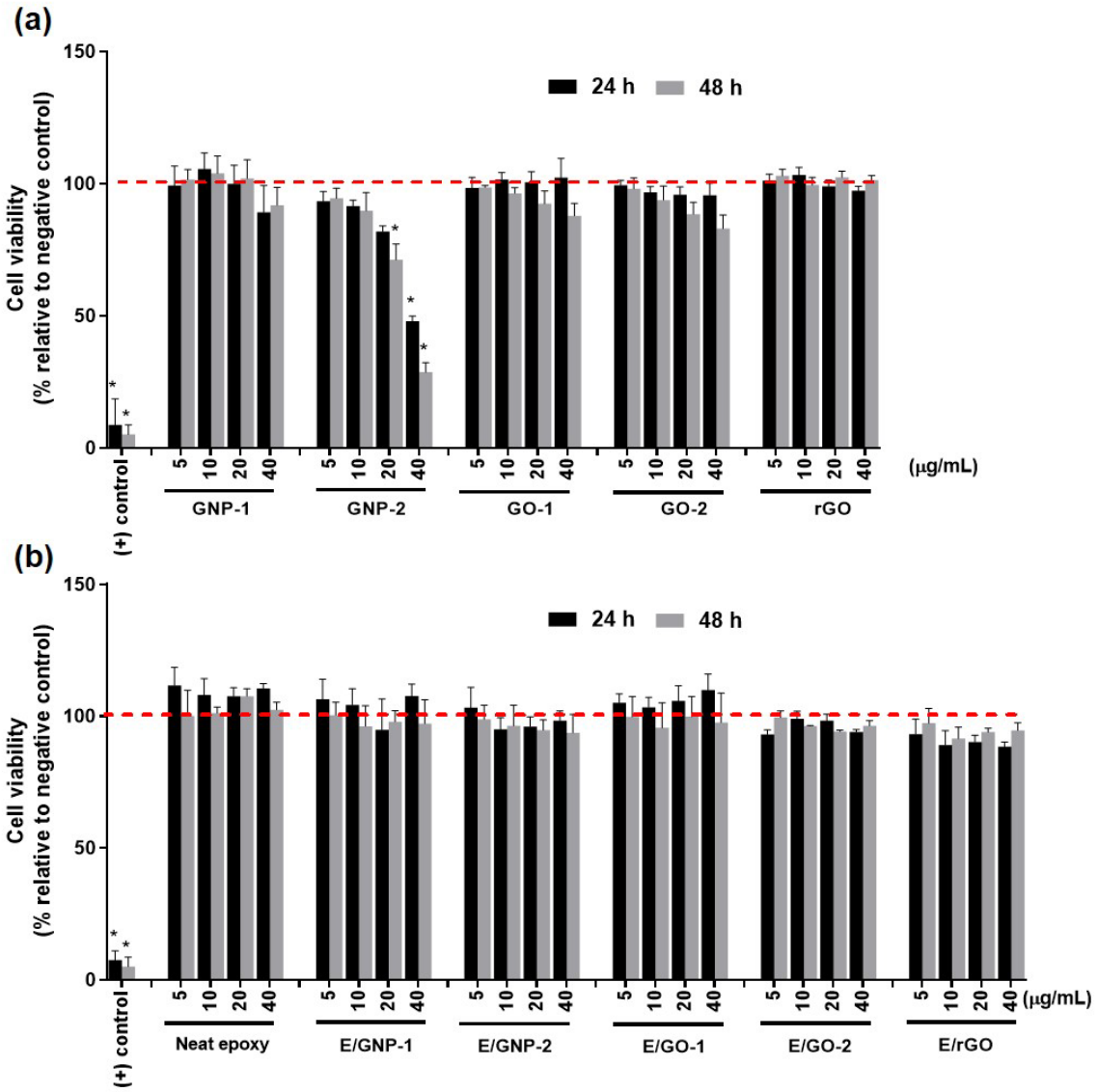

Figure 3.6 Cell viability measured by MTS assay. MTS was performed to evaluate the cell viability of THP-1 macrophages after treatment for 24 h and 48 h with (a) pristine GRMs or (b) abraded particles. 1000 µM $CdSO_4$ was used as a positive control. The results show mean ± StEM from at least three-independent experiments. The * symbol represents $P < 0.05$ as compared to negative controls (untreated cells).

3.4 Discussion

In this study, we focused on the human health risks of GRMs concerning both occupational exposure to pristine GRMs during manufacturing process and consumer exposure to the GRM-containing products. Therefore, we investigated the particles released from GRMs-reinforced epoxy composites by an abrasion process. Moreover, the cytotoxicity of pristine GRMs and the abraded particles were assessed.

3.4.1 Particle Size Distributions

Addition of 1 wt % GO and 1 wt % rGO, enough to improve the material properties of epoxy, induced considerable changes in the particle size distributions of abraded particles in the micrometer size range as compared to particles released from neat epoxy or epoxy/GNP composites. These changes included the presence of an additional mode at 0.6 µm and an increase in the fraction of the particles with aerodynamic diameter around 1 µm. This might be related to the improvement in dispersion of GO in epoxy matrix as compared to the dispersion of GNP in epoxy matrix because of an increase in interfacial adhesion between GO and epoxy due to the presence of carboxylic groups on the GO surface. The better dispersion could result in an enhancement of mechanical properties i.e. tensile strength and toughness of the composites [55]. As reported by Chandrasekaran et al, epoxy/thermally reduced GO composite demonstrated higher fracture toughness than epoxy composite filled with GNP [56]. The increase of toughness could make the composites more difficult to crack [57], leading to delamination of smaller particles. Since the addition of GO and rGO provoked the release of smaller particles as compared to the addition of GNP, this indicated that the released particles can be tuned or controlled via the properties of GRMs. Nevertheless, this will need further investigations and is not the aim of this study.

The PSDs of the abraded particles from all investigated epoxy/GRM composites were in the same range (between 70 nm and 3 µm) as the previously reported PSDs for the epoxy system [42]. Especially, the value of the first mode of abraded particles from neat epoxy (0.333 ± 0.0073 µm) was comparable to the value reported for neat epoxy by Schlagenhauf and coworkers (0.326 ± 0.040 µm) [42]. However, in contrast to our study where we did not observe a noticeable shift of the first mode by adding 1 wt% GRMs, they found that addition of 0.1 wt% and 1 wt% of CNT shifted the first mode of the abraded particles from 326 nm to 392 nm and 415 nm, respectively. CNTs were found to form interconnected structures in the epoxy composites [58], while GRMs could not form such interlinked structures due to their innate 2D morphology. Consequently, the size of abraded particles from composites containing an interconnected particle network might be increased because such structures could reinforce the epoxy matrix. Total concentrations of the abraded particles measured by SMPS in our study were around 5-fold higher than those in Schlagenhauf et al., while the total concentrations measured by APS from both studies were comparable. This suggested that the experimental condition

used in this study could generate higher fraction of smaller particles as compared to Schlagenhauf et al. [42]. The divergence in the PSDs of abraded particles might be due to the use of different abrasive materials (alumina and silica- versus alumina-containing abrasive material) or different abrasion conditions (applied load of 0.5 kg versus 1 kg).

3.4.2 Detection and Quantification of Free-Standing and Protruding GRMs

Pb^{2+} Adsorption and Release Capacity by GRM

Adsorption sites of metal ions include oxygen-containing functional groups and delocalized π electron systems between carbon atoms or sp^2 carbon of graphene sheets [59]. High Pb^{2+} uptake capacity of GO can be ascribed to the presence of oxygen-containing functional groups on the surface of GO, which can be confirmed by Raman intensity ratio I(D)/I(G). The intensities of D and G peaks are an indication of sp^3 carbon and sp^2 carbon, respectively [60]. As sp^2 carbons are the main component of graphene sheets, the existence of sp^3 carbon associates with oxygenated functional groups. These oxygenated groups facilitate the adsorption of metals on the GO surface via three mechanisms, namely electrostatic attraction, ion exchange and surface complexation [61,62]. In our study, the I(D)/I(G) ratio of GO-1 was higher than those of GNP-2 and GNP-1. Therefore, the high release capacity observed for GO can be attributed to its high I(D)/I(G) ratio that correlated to the high amount of oxygenated functional groups. The surface of GNPs contained much lower amounts of oxygen and thus GNPs had a lower capacity for lead ions than GOs. Other studies reported a similar trend for rGO, whose surface consists mainly of non-oxygenated carbons. For example, Li and coworkers found a decrease in the maximum adsorption capacity of rGO (47 mg/g) as compared to GO (299 mg/g) [63].

Detection of Exposed GRMs by Lead Ion Release

The potency of lead labelling method was evaluated using two control samples (control A and B), which could identify the undesired leaching of lead ions from GRMs. The amounts of lead ions leaching from GRMs into epoxy matrix (control A) was below the detection limit. Control B was carried out in the worst-case scenario when all of the lead ions would detach from GRMs after adding hardener to understand how much of the lead ions can be leached out of epoxy after abrasion process. We found substantially higher amounts of lead ions released from Control B (9.04 ± 0.69% as compared to the previous study for epoxy/CNT composites (0.1%) [39]. The difference might originate from the use of 1 kg additional weight for abrasion in our study as compared to 0.5 kg employed by another study [39]. Higher applied weight could result in smaller abraded particles as shown by the higher total concentrations measured by SMPS in our study as compared to another study [42]. Smaller particles, due to their larger surface area, could lead to more leached lead ions. Even in this worst-case scenario, the detached and leached ion fraction (9%) was still substantially lower than the released ion fractions measured from the abraded particles (51% - 92%), which demonstrated that majority of the released ions were

from the exposed GRMs. In addition, we took the detached and leached ion fraction into consideration in assessment of the uncertainty.

We measured the fraction of the GRMs that was presented as free-standing and protruding form in relative to the amount of added GRMs. The results showed a substantially high fraction of protruding and free-standing GRMs in the abraded particles, which was 86.2 ± 10.8%, 51.7 ± 16.3% and 92.0 ± 15.5% for GNP-1, GNP-2 and GO-2, respectively. High exposed fraction of GRMs from abraded particles of epoxy/GRMs composite could be explained by the failure mechanism of the composite, which led to release of GRMs embedded in the epoxy matrix. The failure mechanism of GRM-reinforced epoxy nanocomposites was investigated in previous studies [64–66]. Interfacial debonding between GRM and epoxy molecule or adhesive failure could occur due to weak interaction between GRM and epoxy resin. The cohesive failure inside graphene sheets such as the breakage of graphene layer could simultaneously occur as evidenced in the previous study [64].

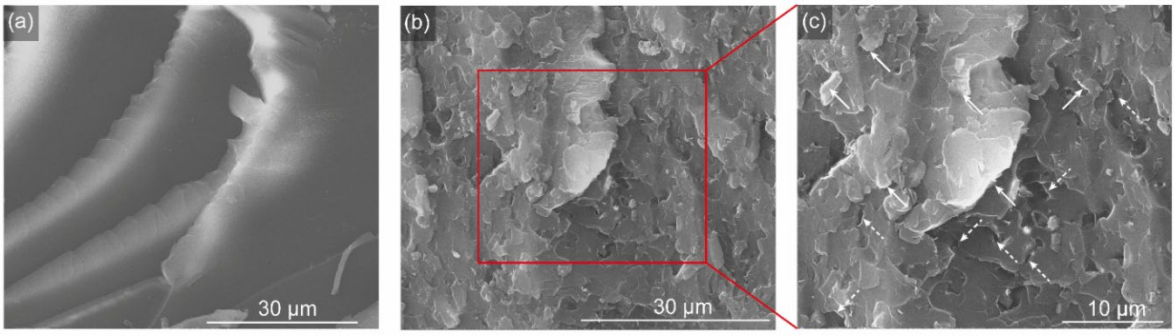

Figure 3.7 SEM images of crack surface of freeze-fractured samples of (a) neat epoxy resin and (b), (c) epoxy/GNP-2 composite. Solid arrows in (c) indicate pulled-out GNPs. Some parts of the pulled-out GNPs, seen as brighter areas when tilted upward from the fractured surface, detached from the epoxy matrix. Dashed arrows in (c) indicate broken GNPs. Broken GNPs were still attached to the epoxy matrix and could be identified from cleavages and voids on the fractured surface.

The failure mechanism of epoxy/GNP composites could be identified from SEM images of fractured surface of the composite [64]. Fig. 3.7 shows SEM images of freeze-fractured surface of neat epoxy resin and epoxy/GNP-2 composite. Fracture morphology of neat epoxy (Fig. 3.7a) shows smooth and mirror-like surface with parallel ridges along the direction of crack propagation. In the presence of GNP-2, the fracture surfaced (Fig. 3.7b and c) is rougher in comparison to neat epoxy resin and shows bulges and fracture structure. This was due to the fact that the mechanical reinforcement effect of GNP-2 could hinder and alter the path of crack propagation [64]. When the crack approached the GNP layer, it could propagate along the interface between GNP and epoxy resin matrix. Since GNPs in our study were not functionalized,

they bound to epoxy resin by Van der Waals force and not by covalent bond. Therefore, interfacial debonding could occur between epoxy matrix and GNP, which could be described by pulled-out GNPs marked by solid arrows in Fig. 3.7c. Since the pulled-out GNPs were partially or entirely detached from the epoxy matrix, they could be identified from the brighter areas implying that the pulled-out GNPs tilted upward from the surface. In abraded particles, the pulled-out GNP from epoxy matrix could be demonstrated by TEM images in Fig. 3.8.

GRM agglomerates could also act as stress concentrator leading to cohesive failure inside the graphene layer since the increasing number of graphene layers could reduce the efficiency of stress transfer between graphene layers [67]. In Fig. 3.7c, ruptured GNPs, which could be identified from cleavages and voids on the fractured surface, were indicated by dashed arrows. Therefore, interfacial debonding between GRM and epoxy matrix as well as the cohesive failure inside graphene sheets can explain the high fraction of freely accessible fraction of GRM in the abraded particles.

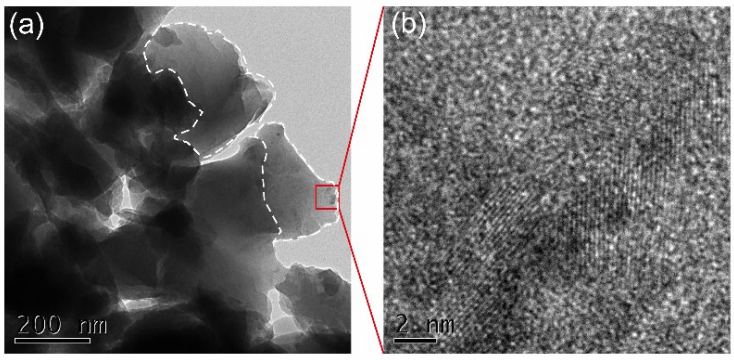

Figure 3.8 (a) TEM image of abraded particles from epoxy/GNP-2 composite showing the protruding GNP-2 (pulled-out GNP-2) from epoxy resin marked with dashed line and (b) layered structure of GNP-2 at higher magnification.

The high released fraction of GRMs is in strong contrast to a previous study [39] on the release of CNTs from epoxy composites, which found only a minor amount of exposed CNTs from abraded particles of 0.4%. This might be explained by the fact that GRMs and CNTs are extremely different in terms of morphology and size. GRMs are two-dimensional material and their agglomerates are still platelet structure, while CNT is one-dimensional material, but CNT agglomerates can be formed by CNTs entwining together. CNTs in Schlagenhauf et al. [39,42] had an outer diameter about 13 nm and a length of 1-10 µm. In epoxy matrix, some CNTs can be coiled into compact structure in the range of 200-300 nm, while some CNTs can be chopped during three-roll milling process resulting in an average tube length of 0.7 ± 0.2 µm [68]. GRMs have lateral size in the range of tens to hundreds of µm. The sizes (projected area equivalent diameter) of pristine GNP-2 from SEM images (Fig. B7) ranged from 10 µm to 150 µm. Optical microscopic images (Fig. B8a-c) showed that after high speed mixing, particles smaller than 10

µm were observed and particles larger than 100 µm were still detected. This implied that agglomerates of GNP-2 could be disintegrated by shear force caused by the high speed mixer. After three-roll milling, the sizes of GNP-2 particles were substantially reduced (Fig. B8d-f) and all particles observed were smaller than 16.5 µm. Similar results after three-roll milling from optical microscopic images were also observed for GNP-1 (Fig. B9) and GO-1 (Fig. B10) as their particle sizes were smaller than 8.5 µm and 11.5 µm, respectively. Detailed analysis of GRMs' sizes during processing was described in the Appendix B. Sizes of the abraded particles ranged from a few hundred nanometer to several micrometer, which could be bigger than the size range of CNT, but smaller than that of pristine GRMs. In other words, GRMs were less likely to be entirely covered in epoxy matrix in comparison to CNTs, which was in agreement with TEM results in Fig. 3.8.

GNP-2 had the least amounts of exposed fraction and the largest lateral dimension. GNP-1 and GO had smaller lateral dimension and higher exposed fraction. If we consider a single particle of GRMs, a smaller particle has less accessible surface and thus weaker interaction between the surface of GRMs and epoxy molecules. Therefore, smaller GRMs could be more easily pulled out from the composites when the abrasive force is applied on the composite's surface. However, further studies are needed to confirm this hypothesis. Nonetheless, this lead-labelling approach provides the necessary quantitative values that are of extreme importance to properly assess the cytotoxicity of the released particles.

3.4.3 Cell Effects

Several studies propose oxidative stress as a key mechanism for cytotoxicity of nanomaterials [44,69] including GRMs [70,71] leading to cell damage and eventually cell death [72,73]. Therefore, we assessed different relevant endpoints of the oxidative stress paradigm including ROS formation, GSH depletion, (pro-) inflammatory cytokines as well as cell viability/cell death in differentiated THP-1 human macrophages. We focused this study on macrophages, since they are phagocytic cells that are an important part of the host defense and play a key role in cellular responses to particles that deposit in the lungs [22,71,74]. Alveolar macrophages are present in the surface-lining layer of the alveoli and in the interstitial space of the lung parenchyma. They respond to and internalize foreign substances and particles and are a major source of cytokine/chemokine production, underlining their importance for acute inhalation toxicity assessment *in vitro* [54,75]. Another important consideration is the use of realistic concentrations. Occupational exposure to GRMs can only be estimated from the existing limits of CNT exposures, where a full working lifetime exposure would results in a alveolar mass retention of 10-50 µg/cm^2 and an acute respiratory exposure (24 h) would be in the range of 1µg/cm^2 [70]. The doses from 5-40 µg/mL used in this study corresponds to 1.3-25 µg/cm^2 in the different plate formats and therefore covers realistic doses at 5 µg/mL and slightly overdose levels at 40 µg/mL.

All GRMs induced ROS after 2h of cell exposure, but we only found a slight decrease in GSH, which indicates some oxidative stress. For GNP-2 the strong drop in GSH level does not necessarily occur due to the induction of oxidative stress by the particles but could be partly a secondary response following the induction of cell death. The slight increase of GSH levels from 24 h to 48 h exposure might indicate that the cells partially adapted with the oxidative stress response by activation of antioxidative responses and enzyme scavenging systems. According to the oxidative stress paradigm, prolonged oxidative stress to cells may result in the activation of inflammatory responses [44]. Studies with different types of immune cells (Jurkat, THP-1, PBMC and RAW 264.7) [21,71,74] showed an induction of cytokine release as a consequence of GRM exposure. Additionally, Schinwald and colleagues confirmed that cytokine release was stimulated by phagocytosis of GRM [21]. However, we did not detect a significant (pro-) inflammatory response although we observed that the cells were in close contact with particles. Only GNP-2 slightly induced the expression of the different (pro-) inflammatory cytokines at the two highest concentrations (20 and 40 μg/mL). As the ultimate and most deleterious outcome of the oxidative stress paradigm, we analyzed if GRM exposure did reduce cell viability and result in cell death. GNP-2 induced a time- and concentration-dependent decrease in the mitochondrial activity of differentiated THP-1 macrophages as measured by MTS assay, while membrane rupture as an indicator of cell death followed a dose-but not time-dependent response. This could suggest a more sustained impact of GNP-2 on mitochondrial enzyme activity that did however not lead to cell death. The decrease in cytotoxicity from the 24 h to 48 h time point may be explained by a partial adaptation of the cells to GNP-2 induced oxidative damage. For the other pristine GRMs, we did not observe any significant acute adverse effects on cell viability or cytotoxicity up to 48 h of exposure. Nevertheless, further studies should address if prolonged exposure to relatively biopersistent GRMs [22] may induce a more pronounced oxidative stress response with oxidative damage to proteins and DNA in the cells and long-term adverse effects. Furthermore, addition of radical scavengers such as N-acetylcystein could help to further corroborate the role of ROS in GNP-2 induced cell death since some of the observed effects may also be secondary due to cell death.

It is well known that there is a strong correlation between the biological activity of nanoparticles and their physicochemical properties [54]. This is also the case for many carbon-based materials, where a complex interaction of several characteristics is defining their toxicity [76]. By choosing five GRMs, we intended to cover a large part of GRM characteristics and to relate their properties to their biological activity. In general the biological activity of particles increases as the particle size decreases [54]. Similar results have been reported for GO, showing a more significant impact on immune cells of smaller GO flakes in comparison to bigger GO flakes [74]. Additionally, it was shown that GRMs with smaller lateral size and increased functional group densities showed a larger impact on epithelial cells [27]. For GNPs, we found a positive correlation between lateral size of the particles and their toxicity while no such effect was apparent for the different GO materials, probably due to the relatively small difference in

their lateral dimensions. Another study from Mendes and co-workers [22] further showed size affected uptake of GO by macrophages with a preferential internalization of larger GO flakes and clusters. However, we could not verify preferential uptake of larger particles since it is technically challenging to quantify internalization of label-free GRMs.

Studies focusing on composites found that the abraded particles from polymer/CNT composites did not cause acute toxic effects [39,77,78], which is comparable to our findings. Wohlleben and colleagues, who investigated *in vitro* toxicity of abraded particles from polyurethane/3% CNT composites on lung tissue, also found no significant increase in toxicity from the addition of CNT to polymer matrix [77]. Similarly, abraded particles from epoxy/1% CNT composites did not show any acute cytotoxic effects i.e. increase in ROS formation, DNA damage, increase in TNF-α and IL-8, and decrease in mitochondrial activity, on A549 human alveolar epithelial cells or THP-1 differentiated macrophages [39]. They reported only a very low release of free-standing or protruding CNTs (0.4%) and that CNTs were mostly embedded in the polymer matrix, which could explain the absence of cytotoxic effects. However, in our study, we found substantial high fractions of exposed (free standing or protruding) GRMs in the abraded particles (86%, 92% and 52% for GNP-1, GO-1 and GNP-2, respectively). While 20 µg/mL GNP-2 were cytotoxic to THP-1 macrophages, even 40 µg/mL of abraded particles from epoxy/GNP-2 composites did not affect any of the investigated endpoints.

Previous studies showed that the neat epoxy or other polymer matrix materials did not induce (pro-) inflammatory responses [38,39,78]. Similarly, this study also confirmed that the abraded particles from neat epoxy do not elicit any inflammatory responses. Therefore, the potential inflammation could only be expected due to the protruding or released GRMs or due to the formation of new materials from the mixing of GRM with epoxy and from the fabrication process of the composite. For the former case, where the toxicity was caused by the released GRMs and assuming no transformation of the GRMs from the processing, we did not expect significant (pro-) inflammatory responses since we did not find any (pro-) inflammatory response for pristine GRMs with the exception of a low response from high concentration of GNP-2 exposures, which was confirmed in our experiments. Moreover, only 1 wt % GRM is added to the epoxy composite and thus, even with a release of 100% of GRMs, the cells would be mostly exposed to epoxy materials. For example, 20 µg/ml exposure to abraded particles would correspond to 0.15 µg/ml exposure to pristine GRMs. For the latter case, where the transformation of the materials could occur during the processing, we showed that the abraded particles did not induce cytokine expression. This indicated that the transformation of the materials did not result in the formation of new particles with immunotoxic properties.

3.5 Conclusions

The release of the particles from the GRM-reinforced epoxy composites is dependent on the GRM type as evidenced by our findings showing that the addition of GO and rGO induced the

release of a new mode at around 0.6 µm of the abraded materials as compared to innate epoxy or epoxy/GNP composites. This reveals the potential to tune the release of the particles. In order to evaluate potential health risks of particles released from GRM-reinforced epoxy composites and pristine GRMs, we assessed the acute toxicity of physicochemically distinct GRMs and epoxy/GRM composites on human macrophages. A significant fraction of the embedded GRMs was released in the free-standing and protruding form in the abraded particles. Pristine GRMs induced some oxidative stress responses and in case of GNP-2 even cell death. However, the abraded particles from epoxy/GRM composites did not reveal any adverse cell responses in human THP-1 macrophages, which was probably due to the low percentage of GRMs used in the composites and limited intrinsic *in vitro* toxicity of the GRMs. Therefore, GRMs with proper size and chemical properties in the appropriate concentration range may be good options as nanofillers with limited human health impact.

Conflicts of interest

There are no conflicts of interest to declare.

Acknowledgement

We thank Dr. Emmanuel Flahaut from Université Paul Sabatier, CNRS, Toulouse, France for kindly providing GO-2 and rGO for this study.

The research leading to these results has received funding from EU Horizon 2020 Framework Graphene Flagship project GrapheneCore1 (Grant Agreement No. 696656), the NanoScreen materials challenge co-sponsored by the Competence Centre for Materials Science and Technology (CCMX) as well as Swiss National Science Foundation (grant number 310030_169207).

3.6 References

1. Mayorov, A.S.; Gorbachev, R. V.; Morozov, S. V.; Britnell, L.; Jalil, R.; Ponomarenko, L.A.; Blake, P.; Novoselov, K.S.; Watanabe, K.; Taniguchi, T.; et al. Micrometer-Scale Ballistic Transport in Encapsulated Graphene at Room Temperature. *Nano Lett.* **2011**, *11*, 2396–2399, doi:10.1021/nl200758b.
2. Lee, C.; Wei, X.; Kysar, J.W.; Hone, J. Measurement of the Elastic Properties and Intrinsic Strength of Monolayer Graphene. *Science (80-.).* **2008**, *321*, 385–388, doi:10.1126/science.1157996.
3. Balandin, A.A.; Ghosh, S.; Bao, W.; Calizo, I.; Teweldebrhan, D.; Miao, F.; Lau, C.N. Superior Thermal Conductivity of Single-Layer Graphene. *Nano Lett.* **2008**, *8*, 902–907, doi:10.1021/nl0731872.
4. Wick, P.; Louw-Gaume, A.E.; Kucki, M.; Krug, H.F.; Kostarelos, K.; Fadeel, B.; Dawson, K.A.; Salvati, A.; Vázquez, E.; Ballerini, L.; et al. Classification framework for graphene-based materials. *Angew. Chemie - Int. Ed.* **2014**, *53*, 7714–7718, doi:10.1002/anie.201403335.
5. Williams, R.J.J.; Giacalone, N. *Epoxy Polymers*; Pascault, J.-P., Williams, R.J.J., Eds.; Wiley: Weinheim, Germany, 2010; ISBN 9783527324804.
6. Garg, A.C.; Mai, Y.-W. Failure mechanisms in toughened epoxy resins—A review. *Compos. Sci. Technol.*

1988, *31*, 179–223, doi:10.1016/0266-3538(88)90009-7.

7. Wajid, A.S.; Ahmed, H.S.T.; Das, S.; Irin, F.; Jankowski, A.F.; Green, M.J. High-Performance Pristine Graphene/Epoxy Composites With Enhanced Mechanical and Electrical Properties. *Macromol. Mater. Eng.* **2013**, *298*, 339–347, doi:10.1002/mame.201200043.
8. Wang, Y.; Yu, J.; Dai, W.; Song, Y.; Wang, D.; Zeng, L.; Jiang, N. Enhanced thermal and electrical properties of epoxy composites reinforced with graphene nanoplatelets. *Polym. Compos.* **2015**, *36*, 556–565, doi:10.1002/pc.22972.
9. Chatterjee, S.; Wang, J.W.; Kuo, W.S.; Tai, N.H.; Salzmann, C.; Li, W.L.; Hollertz, R.; Nüesch, F.A.; Chu, B.T.T. Mechanical reinforcement and thermal conductivity in expanded graphene nanoplatelets reinforced epoxy composites. *Chem. Phys. Lett.* **2012**, *531*, 6–10, doi:10.1016/j.cplett.2012.02.006.
10. Chandrasekaran, S.; Seidel, C.; Schulte, K. Preparation and characterization of graphite nano-platelet (GNP)/epoxy nano-composite: Mechanical, electrical and thermal properties. *Eur. Polym. J.* **2013**, *49*, 3878–3888, doi:10.1016/j.eurpolymj.2013.10.008.
11. Bari, P.; Khan, S.; Njuguna, J.; Mishra, S. Elaboration of properties of graphene oxide reinforced epoxy nanocomposites. *Int. J. Plast. Technol.* **2017**, *21*, 194–208, doi:10.1007/s12588-017-9180-9.
12. Ciardiello, R.; Drzal, L.T.; Belingardi, G. Effects of carbon black and graphene nano-platelet fillers on the mechanical properties of syntactic foam. *Compos. Struct.* **2017**, *178*, 9–19, doi:10.1016/j.compstruct.2017.07.057.
13. Ni, Y.; Chen, L.; Teng, K.; Shi, J.; Qian, X.; Xu, Z.; Tian, X.; Hu, C.; Ma, M. Superior Mechanical Properties of Epoxy Composites Reinforced by 3D Interconnected Graphene Skeleton. *ACS Appl. Mater. Interfaces* **2015**, *7*, 11583–11591, doi:10.1021/acsami.5b02552.
14. Yang, S.; Wang, J.; Huo, S.; Wang, M.; Wang, J.; Zhang, B. Synergistic flame-retardant effect of expandable graphite and phosphorus-containing compounds for epoxy resin: Strong bonding of different carbon residues. *Polym. Degrad. Stab.* **2016**, *128*, 89–98, doi:10.1016/j.polymdegradstab.2016.03.017.
15. Liu, S.; Fang, Z.; Yan, H.; Wang, H. Superior flame retardancy of epoxy resin by the combined addition of graphene nanosheets and DOPO. *RSC Adv.* **2016**, *6*, 5288–5295, doi:10.1039/C5RA25988F.
16. Shi, Y.; Yu, B.; Zheng, Y.; Yang, J.; Duan, Z.; Hu, Y. Design of reduced graphene oxide decorated with DOPO-phosphanomidate for enhanced fire safety of epoxy resin. *J. Colloid Interface Sci.* **2018**, *521*, 160–171, doi:10.1016/j.jcis.2018.02.054.
17. Liu, S.; Yan, H.; Fang, Z.; Wang, H. Effect of graphene nanosheets on morphology, thermal stability and flame retardancy of epoxy resin. *Compos. Sci. Technol.* **2014**, *90*, 40–47, doi:10.1016/j.compscitech.2013.10.012.
18. Sang, B.; Li, Z.; Li, X.; Yu, L.; Zhang, Z. Graphene-based flame retardants: a review. *J. Mater. Sci.* **2016**, *51*, 8271–8295, doi:10.1007/s10853-016-0124-0.
19. Liu, Y.; Luo, Y.; Wu, J.; Wang, Y.; Yang, X.; Yang, R.; Wang, B.; Yang, J.; Zhang, N. Graphene oxide can induce in vitro and in vivo mutagenesis. *Sci. Rep.* **2013**, *3*, 3469, doi:10.1038/srep03469.
20. Akhavan, O.; Ghaderi, E.; Akhavan, A. Size-dependent genotoxicity of graphene nanoplatelets in human stem cells. *Biomaterials* **2012**, *33*, 8017–25, doi:10.1016/j.biomaterials.2012.07.040.
21. Schinwald, A.; Murphy, F.A.; Jones, A.; MacNee, W.; Donaldson, K. Graphene-based nanoplatelets: A new risk to the respiratory system as a consequence of their unusual aerodynamic properties. *ACS Nano* **2012**, *6*, 736–746, doi:10.1021/nn204229f.

22. Mendes, R.G.; Mandarino, A.; Koch, B.; Meyer, A.K.; Bachmatiuk, A.; Hirsch, C.; Gemming, T.; Schmidt, O.G.; Liu, Z.M.; Rümmeli, M.H. Size and time dependent internalization of label-free nano-graphene oxide in human macrophages. *Nano Res.* **2017**, *10*, 1980–1995, doi:10.1007/s12274-016-1385-2.
23. Drasler, B.; Kucki, M.; Delhaes, F.; Buerki-Thurnherr, T.; Vanhecke, D.; Korejwo, D.; Chortarea, S.; Barosova, H.; Hirsch, C.; Petri-Fink, A.; et al. Single exposure to aerosolized graphene oxide and graphene nanoplatelets did not initiate an acute biological response in a 3D human lung model. *Carbon N. Y.* **2018**, *137*, 125–135, doi:10.1016/j.carbon.2018.05.012.
24. Ou, L.; Song, B.; Liang, H.; Liu, J.; Feng, X.; Deng, B.; Sun, T.; Shao, L. Toxicity of graphene-family nanoparticles: a general review of the origins and mechanisms. *Part. Fibre Toxicol.* **2016**, *13*, 57, doi:10.1186/s12989-016-0168-y.
25. Chang, Y.; Yang, S.T.; Liu, J.H.; Dong, E.; Wang, Y.; Cao, A.; Liu, Y.; Wang, H. In vitro toxicity evaluation of graphene oxide on A549 cells. *Toxicol. Lett.* **2011**, *200*, 201–210, doi:10.1016/j.toxlet.2010.11.016.
26. Kucki, M.; Rupper, P.; Sarrieu, C.; Melucci, M.; Treossi, E.; Schwarz, A.; Leon, V.; Kraegeloh, A.; Flahaut, E.; Vazquez, E.; et al. Interaction of graphene-related materials with human intestinal cells: an in vitro approach. *Nanoscale* **2016**, *8*, 8749–8760, doi:10.1039/c6nr00319b.
27. Mittal, S.; Kumar, V.; Dhiman, N.; Chauhan, L.K.S.; Pasricha, R.; Pandey, A.K. Physico-chemical properties based differential toxicity of graphene oxide/reduced graphene oxide in human lung cells mediated through oxidative stress. *Sci. Rep.* **2016**, *6*, 39548, doi:10.1038/srep39548.
28. Yue, H.; Wei, W.; Yue, Z.; Wang, B.; Luo, N.; Gao, Y.; Ma, D.; Ma, G.; Su, Z. The role of the lateral dimension of graphene oxide in the regulation of cellular responses. *Biomaterials* **2012**, *33*, 4013–4021, doi:10.1016/j.biomaterials.2012.02.021.
29. Hu, W.; Peng, C.; Luo, W.; Lv, M.; Li, X.; Li, D.; Huang, Q.; Fan, C. Graphene-Based Antibacterial Paper. *ACS Nano* **2010**, *4*, 4317–4323, doi:10.1021/nn101097v.
30. Hu, W.; Peng, C.; Lv, M.; Li, X.; Zhang, Y.; Chen, N.; Fan, C.; Huang, Q. Protein Corona-Mediated Mitigation of Cytotoxicity of Graphene Oxide. *ACS Nano* **2011**, *5*, 3693–3700, doi:10.1021/nn200021j.
31. Liao, K.-H.; Lin, Y.-S.; Macosko, C.W.; Haynes, C.L. Cytotoxicity of Graphene Oxide and Graphene in Human Erythrocytes and Skin Fibroblasts. *ACS Appl. Mater. Interfaces* **2011**, *3*, 2607–2615, doi:10.1021/am200428v.
32. Froggett, S.J.; Clancy, S.F.; Boverhof, D.R.; Canady, R.A. A review and perspective of existing research on the release of nanomaterials from solid nanocomposites. *Part. Fibre Toxicol.* **2014**, *11*, 17, doi:10.1186/1743-8977-11-17.
33. Duncan, T. V; Pillai, K. Release of Engineered Nanomaterials from Polymer Nanocomposites: Diffusion, Dissolution, and Desorption. *ACS Appl. Mater. Interfaces* **2015**, *7*, 2–19, doi:10.1021/am5062745.
34. European Committee for Standardization (CEN) *Workplace atmospheres-size fraction definitions for measurement of airborne particles*; London, England, 1993;
35. Su, W.-C.; Ku, B.K.; Kulkarni, P.; Cheng, Y.S. Deposition of graphene nanomaterial aerosols in human upper airways. *J. Occup. Environ. Hyg.* **2016**, *13*, 48–59, doi:10.1080/15459624.2015.1076162.
36. Martin, T.R.; Meyer, S.W.; Luchtel, D.R. An evaluation of the toxicity of carbon fiber composites for lung cells in vitro and in vivo. *Environ. Res.* **1989**, *49*, 246–261.

37. Saber, A.T.; Koponen, I.K.; Jensen, K.A.; Jacobsen, N.R.; Mikkelsen, L.; Møller, P.; Loft, S.; Vogel, U.; Wallin, H. Inflammatory and genotoxic effects of sanding dust generated from nanoparticle-containing paints and lacquers. *Nanotoxicology* **2012**, *6*, 776–788, doi:10.3109/17435390.2011.620745.
38. Wohlleben, W.; Brill, S.; Meier, M.W.; Mertler, M.; Cox, G.; Hirth, S.; von Vacano, B.; Strauss, V.; Treumann, S.; Wiench, K.; et al. On the Lifecycle of Nanocomposites: Comparing Released Fragments and their In-Vivo Hazards from Three Release Mechanisms and Four Nanocomposites. *Small* **2011**, *7*, 2384–2395, doi:10.1002/smll.201002054.
39. Schlagenhauf, L.; Buerki-Thurnherr, T.; Kuo, Y.-Y.; Wichser, A.; Nüesch, F.; Wick, P.; Wang, J. Carbon Nanotubes Released from an Epoxy-Based Nanocomposite: Quantification and Particle Toxicity. *Environ. Sci. Technol.* **2015**, *49*, 10616–10623, doi:10.1021/acs.est.5b02750.
40. Pang, C.; Neubauer, N.; Boyles, M.; Brown, D.; Kanase, N.; Hristozov, D.; Fernandes, T.; Stone, V.; Wohlleben, W.; Marcomini, A. Releases from transparent blue automobile coatings containing nanoscale copper phthalocyanine and their effects on J774 A1 macrophages. *NanoImpact* **2017**, *7*, 75–83, doi:10.1016/j.impact.2017.06.002.
41. Han, C.; Zhao, A.; Varughese, E.; Sahle-Demessie, E. Evaluating weathering of food packaging polyethylene-nano-clay composites: Release of nanoparticles and their impacts. *NanoImpact* **2018**, *9*, 61–71, doi:10.1016/j.impact.2017.10.005.
42. Schlagenhauf, L.; Chu, B.T.T.; Buha, J.; Nüesch, F.; Wang, J. Release of Carbon Nanotubes from an Epoxy-Based Nanocomposite during an Abrasion Process. *Environ. Sci. Technol.* **2012**, *46*, 7366–7372, doi:10.1021/es300320y.
43. May, S.; Hirsch, C.; Rippl, A.; Bohmer, N.; Kaiser, J.-P.; Diener, L.; Wichser, A.; Bürkle, A.; Wick, P. Transient DNA damage following exposure to gold nanoparticles. *Nanoscale* **2018**, *10*, 15723–15735, doi:10.1039/C8NR03612H.
44. Roesslein, M.; Hirsch, C.; Kaiser, J.-P.; Krug, H.; Wick, P. Comparability of in Vitro Tests for Bioactive Nanoparticles: A Common Assay to Detect Reactive Oxygen Species as an Example. *Int. J. Mol. Sci.* **2013**, *14*, 24320–24337, doi:10.3390/ijms141224320.
45. Ferrari, A.C.; Basko, D.M. Raman spectroscopy as a versatile tool for studying the properties of graphene. *Nat. Nanotechnol.* **2013**, *8*, 235–246, doi:10.1038/nnano.2013.46.
46. Chen, L.; Hu, X.; Wang, J.; Yu, Y. Impacts of Alternative Fuels on Morphological and Nanostructural Characteristics of Soot Emissions from an Aviation Piston Engine. *Environ. Sci. Technol.* **2019**, *53*, 4667–4674, doi:10.1021/acs.est.9b01059.
47. Eckmann, A.; Felten, A.; Mishchenko, A.; Britnell, L.; Krupke, R.; Novoselov, K.S.; Casiraghi, C. Probing the Nature of Defects in Graphene by Raman Spectroscopy. *Nano Lett.* **2012**, *12*, 3925–3930, doi:10.1021/nl300901a.
48. Stankovich, S.; Piner, R.D.; Nguyen, S.T.; Ruoff, R.S. Synthesis and exfoliation of isocyanate-treated graphene oxide nanoplatelets. *Carbon N. Y.* **2006**, *44*, 3342–3347, doi:10.1016/j.carbon.2006.06.004.
49. Sharma, N.; Sharma, V.; Jain, Y.; Kumari, M.; Gupta, R.; Sharma, S.K.; Sachdev, K. Synthesis and Characterization of Graphene Oxide (GO) and Reduced Graphene Oxide (rGO) for Gas Sensing Application. *Macromol. Symp.* **2017**, *376*, 1700006, doi:10.1002/masy.201700006.
50. Andrijanto, E.; Shoelarta, S.; Subiyanto, G.; Rifki, S. Facile synthesis of graphene from graphite using ascorbic acid as reducing agent. In Proceedings of the AIP Conference Proceedings; 2016; Vol. 1725, p.

020003.

51. Ferreira, F.V.; Cividanes, L.D.S.; Brito, F.S.; de Menezes, B.R.C.; Franceschi, W.; Simonetti, E.A.N.; Thim, G.P. Functionalization of Graphene and Applications. In; 2016; pp. 1–29 ISBN 978-3-319-35109-4.
52. Thurnherr T. Fischer K. , Diener L., Manser P., Maeder-Althaus X., Kaiser J.P., Krug H.F., Rothen-Rutishauser B., Wick P., B.C. A comparison of acute and long-term effects of industrial multiwalled carbon nanotubes on human lung and immune cells in vitro. *Toxicol. Lett.* **2011**, *200*, 176–186, doi:10.1016/j.toxlet.2010.11.012.
53. Thurnherr, T.; Su, D.S.; Diener, L.; Weinberg, G.; Manser, P.; Pfnder, N.; Arrigo, R.; Schuster, M.E.; Wick, P.; Krug, H.F. Comprehensive evaluation of in vitro toxicity of three large-scale produced carbon nanotubes on human Jurkat T cells and a comparison to crocidolite asbestos. *Nanotoxicology* **2009**, *3*, 319–338, doi:10.3109/17435390903276958.
54. Oberdörster, G.; Maynard, A.; Donaldson, K.; Castranova, V.; Fitzpatrick, J.; Ausman, K.; Carter, J.; Karn, B.; Kreyling, W.; Lai, D.; et al. Principles for characterizing the potential human health effects from exposure to nanomaterials: elements of a screening strategy. *Part. Fibre Toxicol.* **2005**, *2*, doi:10.1186/1743-8977-2-8.
55. Park, M.-S.; Lee, S.; Lee, Y.-S. Mechanical properties of epoxy composites reinforced with ammonia-treated graphene oxides. *Carbon Lett.* **2017**, *21*, 1–7, doi:10.5714/CL.2017.21.001.
56. Chandrasekaran, S.; Sato, N.; Tölle, F.; Mülhaupt, R.; Fiedler, B.; Schulte, K. Fracture toughness and failure mechanism of graphene based epoxy composites. *Compos. Sci. Technol.* **2014**, *97*, 90–99, doi:10.1016/j.compscitech.2014.03.014.
57. Zok, F.W.; Miserez, A. Property maps for abrasion resistance of materials. *Acta Mater.* **2007**, *55*, 6365–6371, doi:10.1016/j.actamat.2007.07.042.
58. Hollertz, R.; Chatterjee, S.; Gutmann, H.; Geiger, T.; Nüesch, F. a; Chu, B.T.T. Improvement of toughness and electrical properties of epoxy composites with carbon nanotubes prepared by industrially relevant processes. *Nanotechnology* **2011**, *22*, 125702, doi:10.1088/0957-4484/22/12/125702.
59. Cao, Y.; Li, X. Adsorption of graphene for the removal of inorganic pollutants in water purification: A review. *Adsorption* **2014**, *20*, 713–727, doi:10.1007/s10450-014-9615-y.
60. Ferrari, A.C. Raman spectroscopy of graphene and graphite: Disorder, electron–phonon coupling, doping and nonadiabatic effects. *Solid State Commun.* **2007**, *143*, 47–57, doi:10.1016/j.ssc.2007.03.052.
61. Bian, Y.; Bian, Z.Y.; Zhang, J.X.; Ding, A.Z.; Liu, S.L.; Wang, H. Effect of the oxygen-containing functional group of graphene oxide on the aqueous cadmium ions removal. *Appl. Surf. Sci.* **2015**, *329*, 269–275, doi:10.1016/j.apsusc.2014.12.090.
62. Peng, W.; Li, H.; Liu, Y.; Song, S. A review on heavy metal ions adsorption from water by graphene oxide and its composites. *J. Mol. Liq.* **2017**, *230*, 496–504, doi:10.1016/j.molliq.2017.01.064.
63. Li, Z.; Chen, F.; Yuan, L.; Liu, Y.; Zhao, Y.; Chai, Z.; Shi, W. Uranium(VI) adsorption on graphene oxide nanosheets from aqueous solutions. *Chem. Eng. J.* **2012**, *210*, 539–546, doi:10.1016/j.cej.2012.09.030.
64. Zaman, I.; Kuan, H.-C.; Dai, J.; Kawashima, N.; Michelmore, A.; Sovi, A.; Dong, S.; Luong, L.; Ma, J. From carbon nanotubes and silicate layers to graphene platelets for polymer nanocomposites. *Nanoscale* **2012**, *4*, 4578, doi:10.1039/c2nr30837a.
65. Zheng, W.; Chen, W.G.; zhao, Q.; Ren, S.X.; Fu, Y.Q. Interfacial structures and mechanisms for

strengthening and enhanced conductivity of graphene/epoxy nanocomposites. *Polymer (Guildf).* **2019**, *163*, 171–177, doi:10.1016/j.polymer.2018.12.055.

66. Meng, Q.; Araby, S.; Ma, J. *Toughening mechanisms in epoxy/graphene platelets composites*; 2015; ISBN 9781782422914.
67. Gong, L.; Young, R.J.; Kinloch, I.A.; Riaz, I.; Jalil, R.; Novoselov, K.S. Optimizing the reinforcement of polymer-based nanocomposites by graphene. *ACS Nano* **2012**, *6*, 2086–2095, doi:10.1021/nn203917d.
68. Hollertz, R.; Chatterjee, S.; Gutmann, H.; Geiger, T.; Nüesch, F. a; Chu, B.T.T. Improvement of toughness and electrical properties of epoxy composites with carbon nanotubes prepared by industrially relevant processes. *Nanotechnology* **2011**, *22*, 125702, doi:10.1088/0957-4484/22/12/125702.
69. Donaldson, K.; Tran, L.; Jimenez, L.A.; Duffin, R.; Newby, D.E.; Mills, N.; MacNee, W.; Stone, V. Combustion-derived nanoparticles: A review of their toxicology following inhalation exposure. *Part. Fibre Toxicol.* **2005**, *2*, 10, doi:10.1186/1743-8977-2-10.
70. Gangwal, S.; Brown, J.S.; Wang, A.; Houck, K.A.; Dix, D.J.; Kavlock, R.J.; Hubal, E.A. Informing selection of nanomaterial concentrations for ToxCast in vitro testing based on occupational exposure potential. *Env. Heal. Perspect* **2011**, *119*, 1539–1546, doi:10.1289/ehp.1103750.
71. Horváth, L.; Magrez, A.; Burghard, M.; Kern, K.; Forró, L.; Schwaller, B. Evaluation of the toxicity of graphene derivatives on cells of the lung luminal surface. *Carbon N. Y.* **2013**, *64*, 45–60, doi:http://doi.org/10.1016/j.carbon.2013.07.005.
72. Graham, U.M.; Jacobs, G.; Yokel, R.A.; Davis, B.H.; Dozier, A.K.; Birch, M.E.; Tseng, M.T.; Oberdörster, G.; Elder, A.; DeLouise, L. From Dose to Response: In Vivo Nanoparticle Processing and Potential Toxicity. *Adv. Exp. Med. Biol.* **2017**, *947*, 71–100, doi:10.1007/978-3-319-47754-1_4.
73. Li, N.; Sioutas, C.; Cho, A.; Schmitz, D.; Misra, C.; Sempf, J.; Wang, M.; Oberley, T.; Froines, J.; Nel, A. Ultrafine particulate pollutants induce oxidative stress and mitochondrial damage. *Environ. Health Perspect.* **2003**, *111*, 455–460, doi:10.1289/ehp.6000.
74. Orecchioni, M.; Jasim, D.A.; Pescatori, M.; Manetti, R.; Fozza, C.; Sgarrella, F.; Bedognetti, D.; Bianco, A.; Kostarelos, K.; Delogu, L.G. Molecular and Genomic Impact of Large and Small Lateral Dimension Graphene Oxide Sheets on Human Immune Cells from Healthy Donors. *Adv. Healthc. Mater.* **2016**, *5*, 276–287, doi:10.1002/adhm.201500606.
75. Ochs,Matthias ; Weibel, E.R. Fishman's Pulmonary Diseases and Disorders. In *Chapter 2: Functional Design of the Human Lung for Gas Exchange*; 2015.
76. Ma-Hock, L.; Strauss, V.; Treumann, S.; Küttler, K.; Wohlleben, W.; Hofmann, T.; Gröters, S.; Wiench, K.; van Ravenzwaay, B.; Landsiedel, R. Comparative inhalation toxicity of multi-wall carbon nanotubes, graphene, graphite nanoplatelets and low surface carbon black. *Part. Fibre Toxicol.* **2013**, *10*, 23, doi:10.1186/1743-8977-10-23.
77. Wohlleben, W.; Meier, M.W.; Vogel, S.; Landsiedel, R.; Cox, G.; Hirth, S.; Tomović, Ž. Elastic CNT-polyurethane nanocomposite: synthesis, performance and assessment of fragments released during use. *Nanoscale* **2013**, *5*, 369–80, doi:10.1039/c2nr32711b.
78. Schlagenhauf, L.; Kianfar, B.; Buerki-Thurnherr, T.; Kuo, Y.-Y.; Wichser, A.; Nüesch, F.; Wick, P.; Wang, J. Weathering of a carbon nanotube/epoxy nanocomposite under UV light and in water bath: impact on abraded particles. *Nanoscale* **2015**, *7*, 18524–36, doi:10.1039/c5nr05387k.

Appendix B

Graphical Abstract

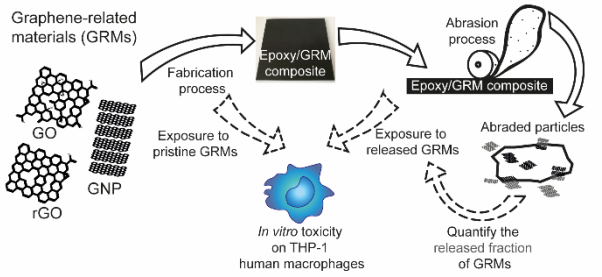

We measured the cytotoxicity of the pristine GRMs and abraded particles from epoxy/GRM composites, which indicated low risks to consumers of such composites.

Abrasion Process and Particle Collection

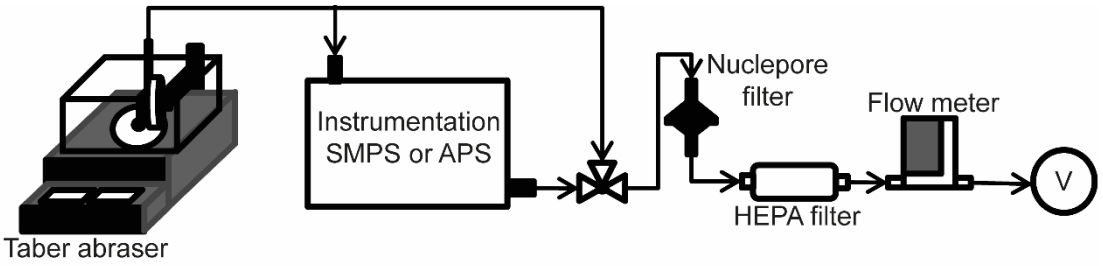

Figure B1 Schematic representation of experimental setup for particle size distribution measurement.

Influence of the Rectangular Probe on Particle Sampling

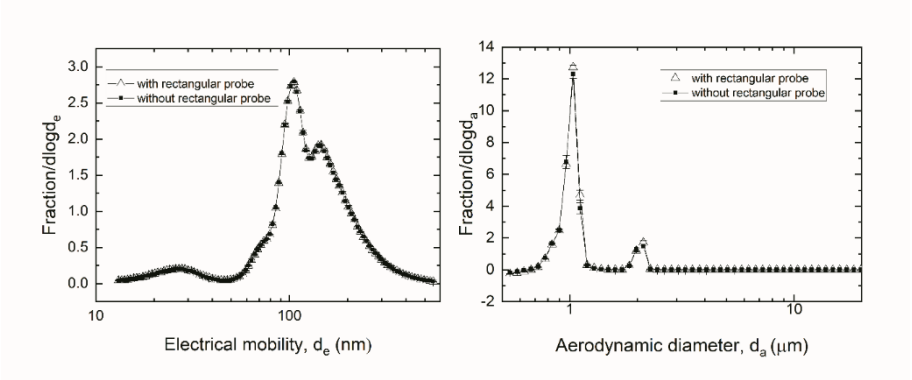

Figure B2 Size distribution of aerosolized PSL particles sampled in presence or absence of a rectangular probe. (a) Samples of aerosolized 105 nm PSL particles measured by SMPS from three independent measurements. (b) Samples of 1 µm and 2 µm PSL particles analyzed by APS from five independent measurements. Data represent mean +/- SD.

Characterization of Pristine GRMs and Abraded Particles

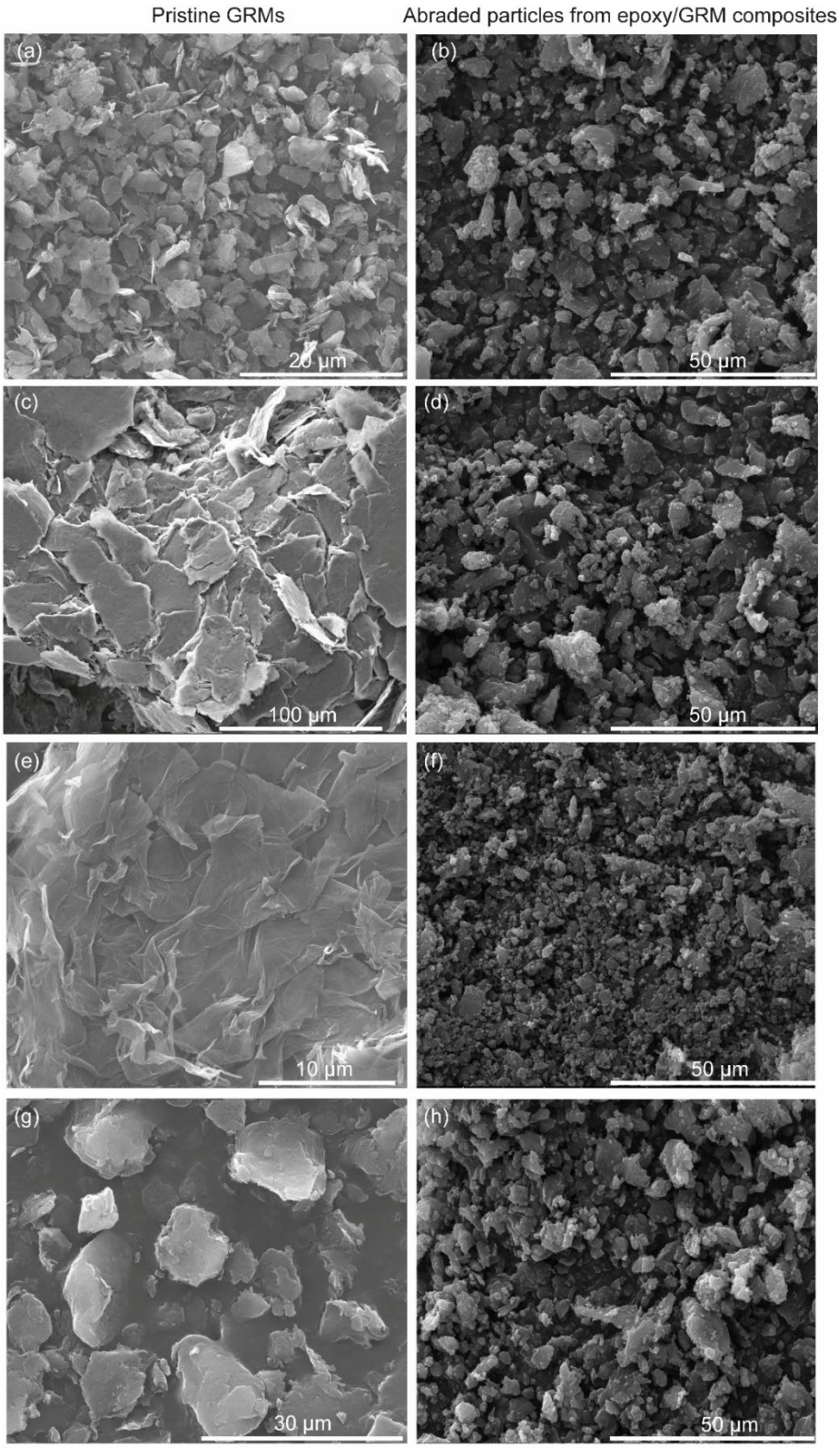

Figure B3 SEM of pristine GRMs and abraded particles from epoxy/GRM composites. Images of pristine and abraded particles from samples of (a,b) GNP-1; (c,d) GNP-2, (e,f) GO-1 and (g,h) rGO.

From SEM images (Fig. B3), in abraded particles from epoxy/GRM composites, GRMs cannot be distinguished from epoxy matrix. Therefore, it is not possible to observe the structural transformation of GRMs from SEM images. We performed Raman spectroscopy, which can be ones of the methods used to explain structural transformation of the GRMs in the composites. As shown in Fig. 3.3b, by comparing the Raman spectrum of the pristine GNP-2 to that of the GNP-2 in the abraded composite, the I(D)/I(G) ratio appeared to have different intensity (spectra B and C). This suggested that GNP might be transformed during the fabrication or abrasion process resulting in defected structure. In addition, the effect of manufacturing process on the sizes of GRMs were studied by analysis of optical microscopic images of GRMs in epoxy matrix, which is demonstrated below.

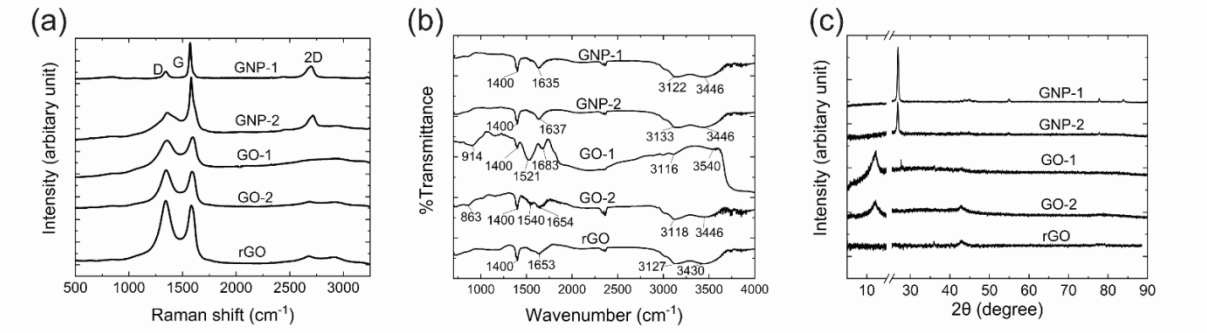

Figure B4 Characterization of pristine GRMs. (a) Raman spectra (b) FTIR spectra and (c) XRD patterns of pristine GRMs.

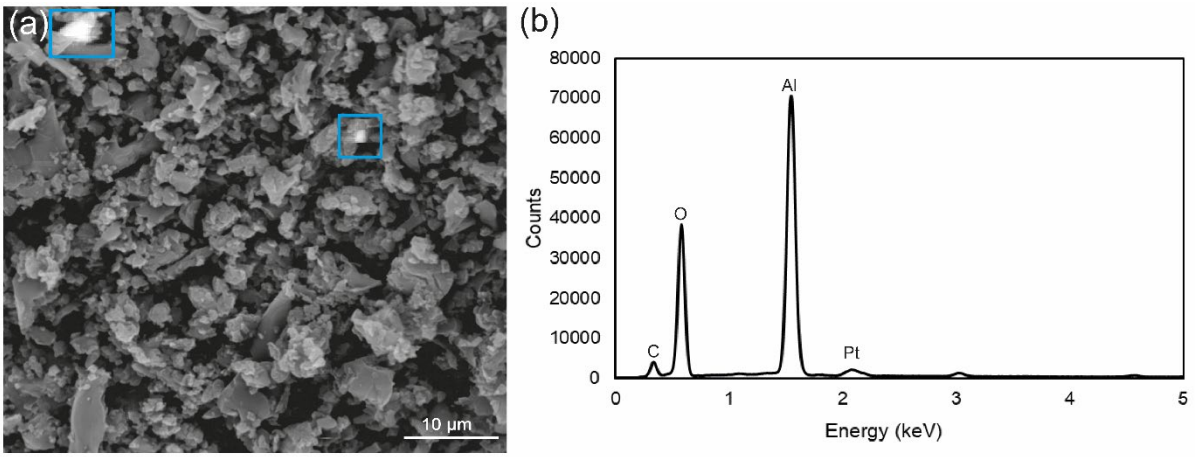

Figure B5 SEM-EDX analysis of abraded particles from neat epoxy. (a) Representative SEM image of abraded particles from neat epoxy. Aluminum appears as white spots, which were marked in blue boxes.(b) EDX spectrum from point analysis of the white spot marked by a rectangle in (a).

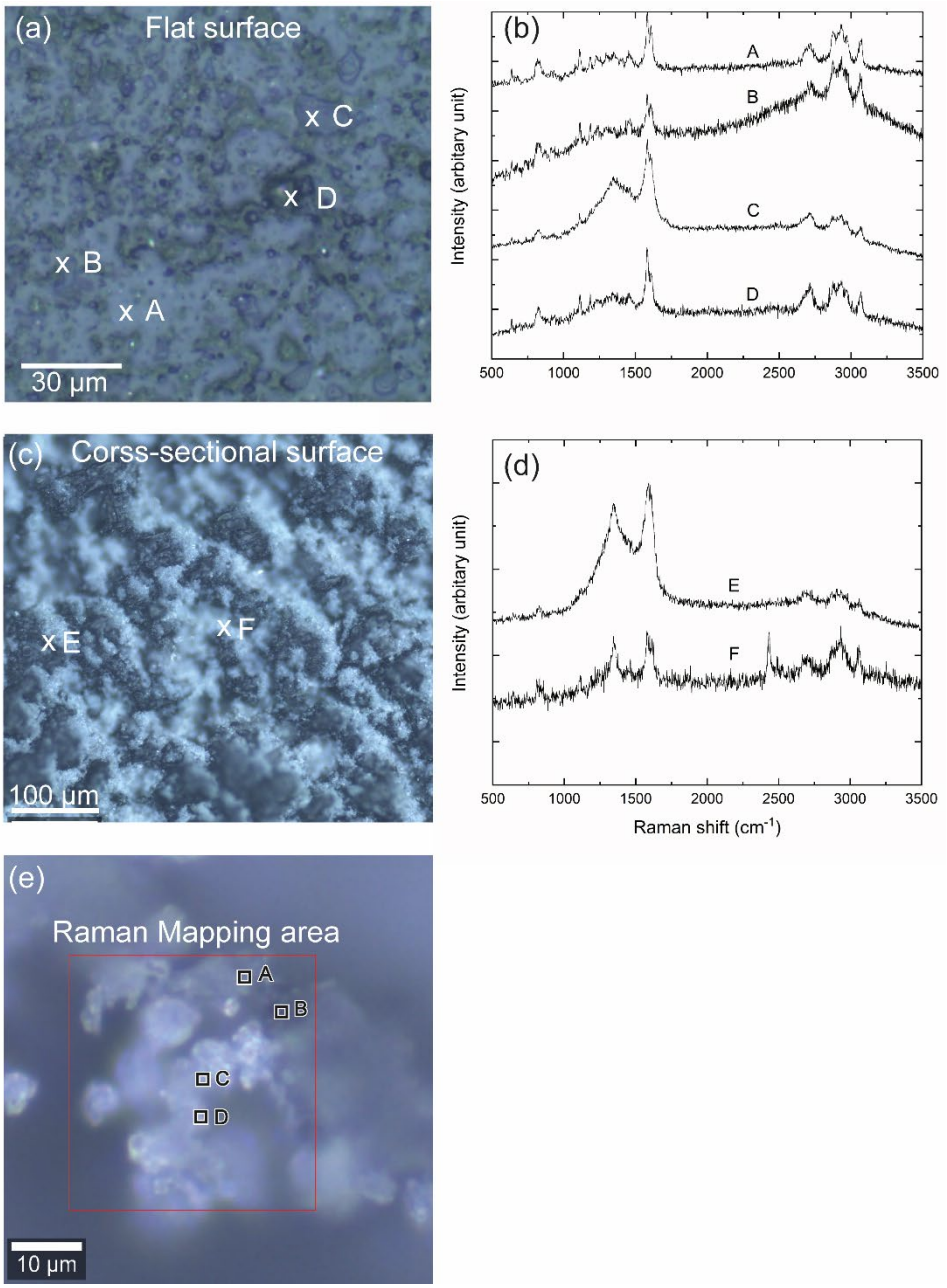

Figure B6 Spots of Raman spectroscopy analysis of (a) flat surface and (c) cross-sectional surface of E/GNP-2 composites and the corresponding spectra on (b) flat surface and (d) cross-sectional surface. (e) Optical image of the abraded particles from E/GNP-2 with Raman mapping area marked by red square and four points (A-D) where the individual spectrum was shown in Fig. 3.3.

Effect of Manufacturing Process on Sizes of GRMs

We analyzed the transformation of GRM size using images from SEM and optical microscopy. ImageJ software was employed to detect the particles and obtain the projected area of the detected particles. SEM images of pristine GNP-2 (Fig. B7) were analyzed by manually drawing the particle edge and the projected area of the identified particles were calculated using ImageJ. Optical microscopic images of GRMs in epoxy matrix were analyzed using ImageJ to detect

GRM particles and then to calculate the corresponding particles' projected area. Since the observed GRM particles have irregular shape, particle size can be referred to projected area equivalent diameter, which is the diameter of a spherical particle having the same projected area as the considered particle.

Since the processing of epoxy/GRM nanocomposites involved high speed mixing, three-roll milling, addition of hardener and curing, we showed the GRM sizes in the epoxy matrix after two important steps before curing i.e. high speed mixing and addition of hardener after three-roll milling. Optical images of GNP-2 particles in epoxy matrix after high speed mixing and after three-roll milling were displayed in Fig. B8a-c and Fig. B8d-f, respectively. Fig. B9 and Fig. B10 show GNP-1 and GO-1 in epoxy matrix after three-roll milling, respectively.

Histograms of the particle sizes of GNP-2 after each step, and GNP-1 and GO-1 after three-roll milling were summarized in Fig. B11. At least three images were analyzed to plot a histogram.

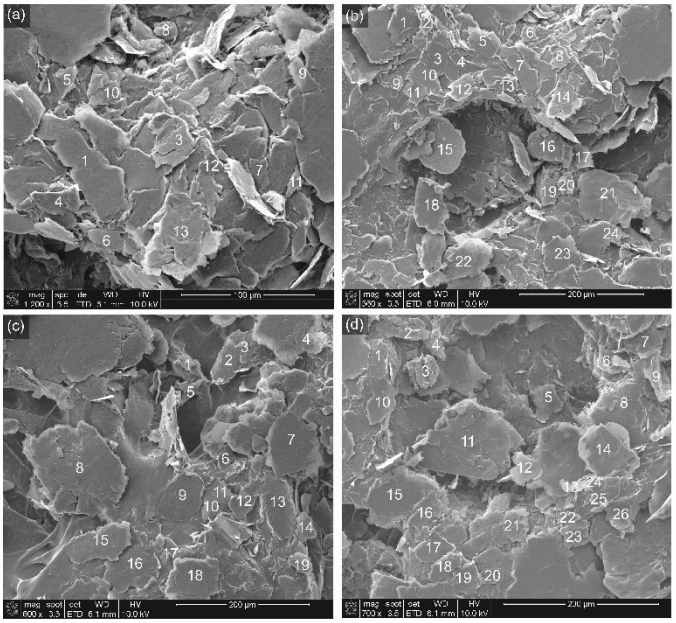

Figure B7 SEM images of pristine GNP-2. Number labelling indicates the particles whose edge could be identified and thus their corresponding projected area could be analyzed by ImageJ.

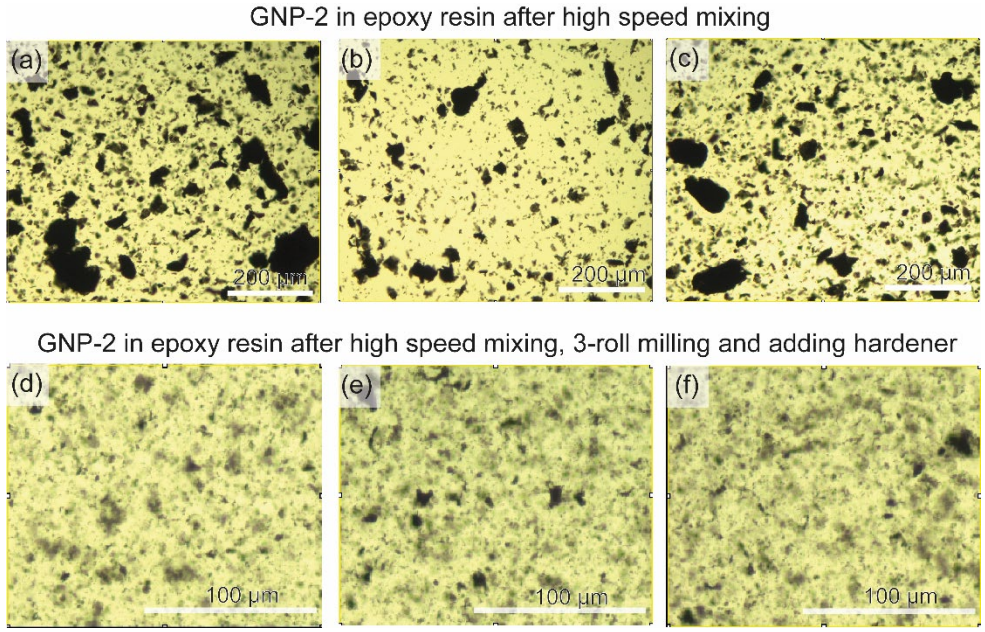

Figure B8 Optical micrographs of GNP-2 in epoxy resin matrix (a)- (c) after high speed mixing and (d) – (f) after high seed mixing, three-roll milling and adding hardener

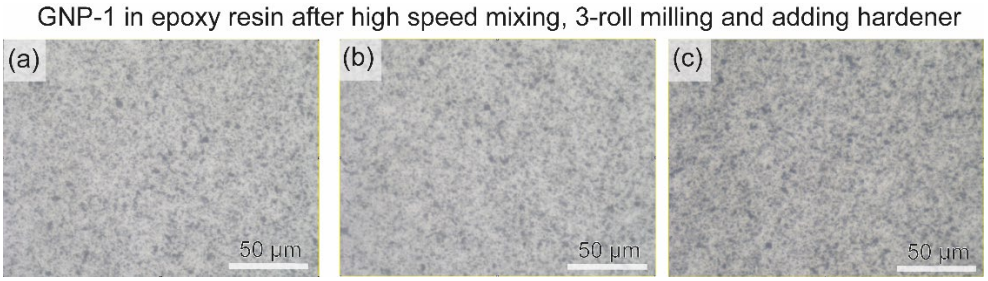

Figure B9 Optical micrographs of GNP-1 in epoxy resin matrix after high speed mixing followed by three-roll milling and adding hardener

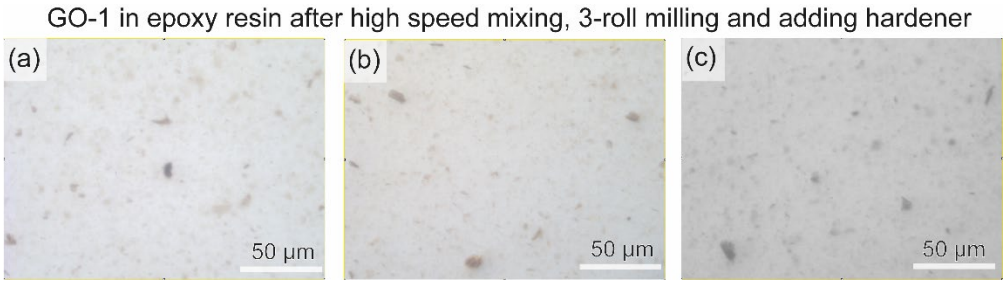

Figure B10 Optical micrographs of GO-1 in epoxy resin matrix after high speed mixing followed by three-roll milling and adding hardener

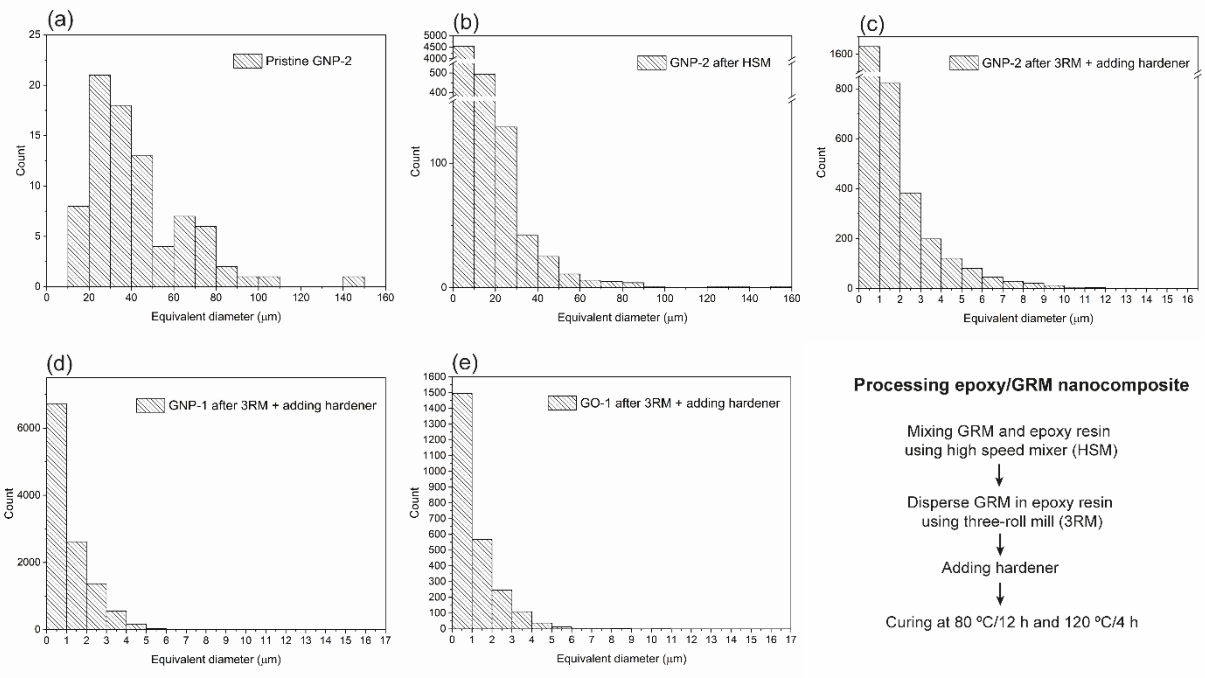

Figure B11 Histograms of GRM size before and during processing of epoxy/GRM nanocomposite. Histogram of (a) pristine GNP-2, (b) GNP-2 in epoxy resin matrix after high speed mixing (HSM), and (c) after three-roll milling (3RM) and adding hardener. Histogram of (d) GNP-1 and (e) GO-1 after three-roll milling and adding hardener.

Exclusion of Interferences of GRMs and Abraded Neat Epoxy Particles in the MTS and DCF Assays

MTS interference was performed regarding the ability of GRMs to reduce MTS without cellular contribution. The treatment of interference control samples and the assay procedure were identical to the protocol described in materials and methods. GRMs and neat epoxy show a certain intrinsic absorbance, which was corrected by subtracting the background, but are not reactive, i.e. do not process MTS (Fig. B12a) when comparing the absorbance to an untreated control (-) including cells. To determine the influence of GRMs and neat epoxy quenching an existing fluorescent signal, particles were incubated with the fluorescent dye DCF as described in the material and methods. Fig. B12b shows the relative fluorescence in percentage to the control samples with no GRMs as 100%, whereas GRM containing samples show the impact on the intensity of the fluorescence.

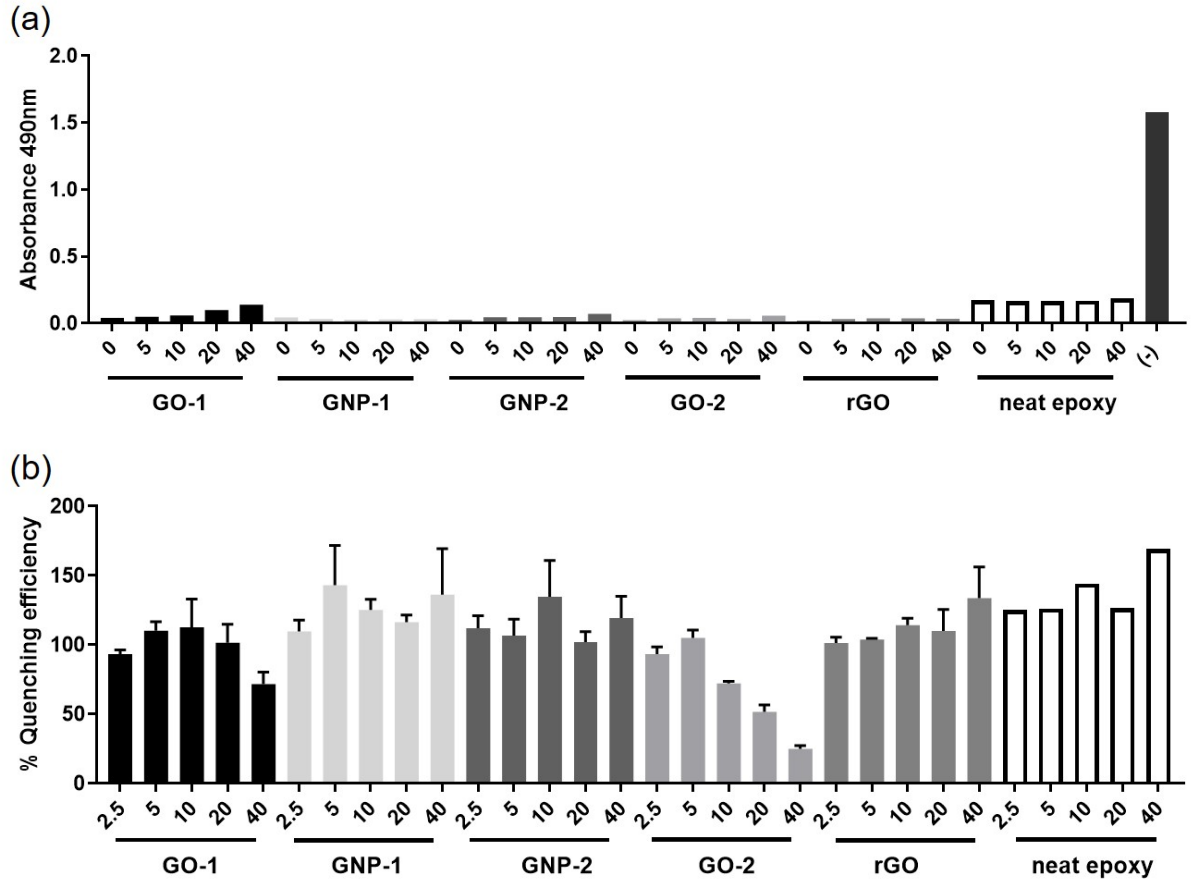

Figure B12 Interference assessment of the pristine GRMs and neat epoxy with the MTS and DCF assay. (a)Pristine GRMs and abraded neat epoxy particles did not interfere with the MTS measurements. (-) is a representative absorbance value of an untreated control measurement with THP-1 cells. Data represent a single experiment (b) Abraded neat epoxy particles did not quench, but GRMs quench an existing DCF signal. % Quenching efficiency displays relative fluorescent values (to untreated control). Mean values and corresponding standard deviations

from three independent experiments are shown for pristine GRMs while one only one experiment was performed for abraded neat epoxy particles.

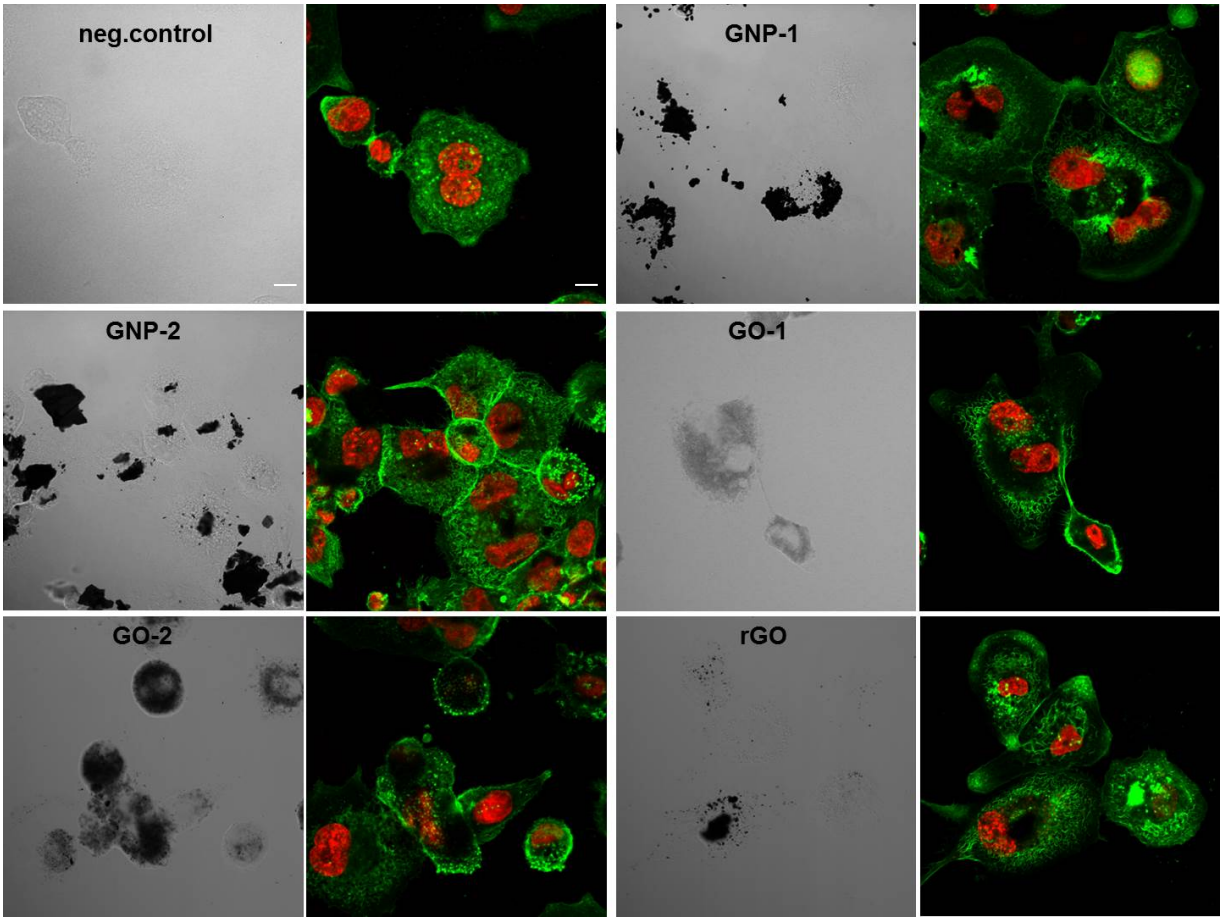

Figure B13 Light microscopy and confocal microscopy images of THP-1 macrophages exposed to 40µg/mL GRM for 48h, Actin cytoskeleton (green), Nuclei (red) and GRMs (black), scale bar =10 µm

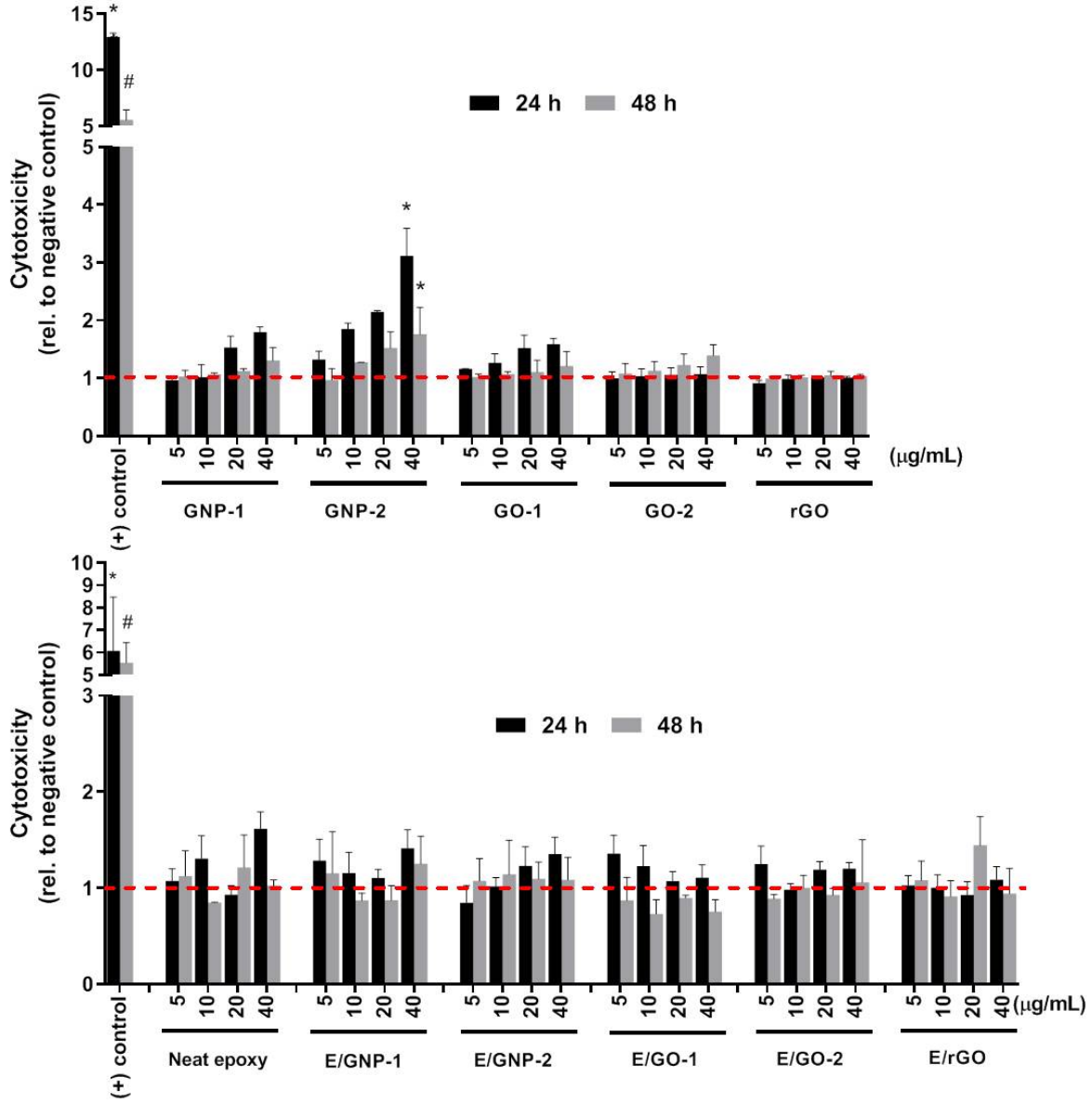

Figure B14 LDH release from THP-1 macrophages after exposure to GRMs and E/GRMs for 24 h and 48 h. Data shown represent the mean ± StEM of at least three independent experiments. The * symbol represents $p<0.05$ as compared to negative control (untreated cells). Incubation of cells for 1h to 0.2% Triton-X served as positive control (+)

Table B1 Hydrodynamic size of pristine GRMs

	Z_{ave} diameter (nm)/ PdI				
GRMs / Dispersant	GNP-1	GNP-2	GO-1	GO-2	rGO
Water	NA	NA	765 ± 17.1/ 0.42 ± 0.03	255 ± 1.68/ 0.18 ± 0.01	243 ± 8.13/ 0.45 ± 0.07
Complete RPMI-1640 medium	NA	NA	940 ± 87.7/ 0.55 ± 0.04	275 ± 16.1/ 0.24 ± 0.04	95.4 ± 24.0/ 0.62 ± 0.14

NA: When polydisperse index (PdI) is larger than 0.7, the data is not valid and the results are marked as NA (Not Applicable). The DLS measurement is not suitable for these particles because GNP-1 and GNP-2are polydisperse and tend to agglomerate.

Table B2 Hydrodynamic size of abraded particles from epoxy/GRM composites

	Z_{ave} diameter (nm)/ PdI					
Abraded particles / Dispersant	Neat epoxy	Epoxy/GNP-1	Epoxy/GNP-2	Epoxy/GO-1	Epoxy/GO-2	Epoxy/rGO
Water	1230 ± 260/ 0.696 ± 0.180	1822 ± 139/ 0.559 ± 0.122	NA	NA	NA	NA
Complete RPMI-1640 medium	NA	NA	NA	NA	NA	NA

NA: When polydisperse index (PdI) is larger than 0.7, the data is not valid and the results are marked as NA (Not Applicable). The DLS measurement is not suitable for most of these particles because they are polydisperse and tend to agglomerate.

Table B3 Summary of the analyzed parameters from the fitted particle size distributions

Sample	Parameter	Mode 1	Mode 2	Mode 3	Mode 4
Neat epoxy	d_e or d_a [(a)]	0.333 ± 0.0073	1.087 ± 0.0826	2.271 ± 0.0565	-
	CMD	0.461 ± 0.011	1.274 ± 0.1220	2.516 ± 0.0548	-
	σ_g	1.76 ± 0.01	1.48 ± 0.04	1.38 ± 0.01	-
	F		0.26 ± 0.01	0.74 ± 0.01	-
E/GNP-1	d_e or d_a [(a)]	0.302 ± 0.0123	1.148 ± 0.0760	2.306 ± 0.0791	-
	CMD	0.445 ± 0.011	1.372 ± 0.1248	2.605 ± 0.0710	-
	σ_g	1.86 ± 0.03	1.52 ± 0.05	1.39 ± 0.01	-
	F		0.22 ± 0.01	0.78 ± 0.01	-
E/GNP-2	d_e or d_a [(a)]	0.314 ± 0.0102	1.075 ± 0.0834	2.300 ± 0.0601	-
	CMD	0.480 ± 0.0212	1.259 ± 0.1323	2.574 ± 0.0416	-
	σ_g	1.81 ± 0.03	1.48 ± 0.05	1.40 ± 0.02	-
	F		0.21 ± 0.01	0.79 ± 0.01	-
E/GO-1	d_e or d_a [(a)]	0.338 ± 0.0159	0.632 ± 0.0072	0.832 ± 0.0159	2.075 ± 0.0249
	CMD	0.465 ± 0.0176	0.637 ± 0.0066	0.974 ± 0.0027	2.286 ± 0.0362
	σ_g	1.76 ± 0.02	1.09 ± 0.00	1.49 ± 0.04	1.36 ± 0.01
	F		0.01 ± 0.00	0.40 ± 0.03	0.59 ± 0.03
E/GO-2	d_e or d_a [(a)]	0.327 ± 0.0143	0.632 ± 0.0072	0.847 ± 0.0078	2.027 ± 0.0273
	CMD	0.460 ± 0.0257	0.636 ± 0.0020	0.959 ± 0.0013	2.303 ± 0.0412
	σ_g	1.77 ± 0.02	1.09 ± 0.00	1.42 ± 0.01	1.43 ± 0.01
	F		0.01 ± 0.00	0.28 ± 0.02	0.71 ± 0.02

E/rGO	d_e or d_a [(a)]	0.341 ± 0.0036	0.582 ± 0.0014	0.891 ± 0.0164	1.902 ± 0.0713
	CMD	0.479 ± 0.0142	0.595 ± 0.0048	1.008 ± 0.0426	2.123 ± 0.0573
	σ_g	1.79 ± 0.03	1.15 ± 0.01	1.42 ± 0.05	1.39 ± 0.02
	F		0.02 ± 0.01	0.33 ± 0.04	0.65 ± 0.03

Mode 1 was obtained from SMPS, whose particle size corresponded to electrical mobility d_e, while mode 2 – 4 were obtained from APS, whose particle size corresponded to aerodynamic diameter d_a.

Chapter 4

Airborne Emissions from Combustion of Graphene Nanoplatelet/Epoxy Composites and Their Cytotoxicity on Lung Cells *via* Air-Liquid Interface Cell Exposure *In Vitro*

Woranan Netkueakul [1,2,3], Savvina Chortarea [3], Hao Li [1,2], Guangyu Qiu [1,2], Milijana Jovic [4], Sabyasachi Gaan [4], Yvette Hannig [3], Tina Buerki-Thurnherr [3], Peter Wick [3]*, Jing Wang [1,2]*

1 Institute of Environmental Engineering, ETH Zurich, 8093, Zurich, Switzerland
2 Laboratory for Advanced Analytical Technologies, Empa, Swiss Federal Laboratories for Materials Science and Technology, 8600, Dübendorf, Switzerland
3 Particles-Biology Interactions Lab, Empa, Swiss Federal Laboratories for Materials Science and Technology, 9014, St. Gallen, Switzerland
4 Additives and Chemistry Group, Advanced Fibers, Empa, Swiss Federal Laboratories for Materials Science and Technology, St. Gallen, 9014, Switzerland

* corresponding authors

Author contributions

W.N. fabricated epoxy composites and characterized the physicochemical properties of GNP and emissions from the combustion. W.N., S.C., and J.W. designed the combustion exposure experiment. W.N. and S.C. performed *in vitro* toxicity assessments and analyzed the toxicity data. W.N and L.H. analyzed PAH data. L.H. proposed PAH formation mechanism. W.N. and G.Q. performed Raman spectroscopy mapping and analyzed the Raman data. W.N., S.C., Y.H., and M.J. performed the combustion and exposure experiments. Y. H. maintained the cell culture. M.J. calibrated the cone calorimeter. S.G. supported with the cone calorimeter and fire behavior analysis. S.C designed and supervised the *in vitro* experiments. T.B.T. and P.W. supervised and supported with the *in vitro* toxicity assessment. P. W. and J.W. initiated the project, conceived the study, and supervised the study. W.N. wrote the manuscript. All of the authors have discussed the results and have given approval to the final version of the manuscript.

This work has been submitted to *Environmental Science and Technology*.

Abstract

Graphene nanoplatelet (GNP) as nanofiller improves the mechanical strength, electrical conductivity, and flame retardancy of the polymers significantly. With an increasing number of GNP-reinforced products, a careful safety assessment is needed to avoid any social and economic drawbacks. However, there has not been any study addressing the effects of combustion-generated emissions from GNP-reinforced products in the lung, the most sensitive exposure route to airborne particles. Therefore, we have studied the influence of GNP as nanofiller on

particle size, polycyclic aromatic hydrocarbon (PAH), and cytotoxicity of the emissions from the combustion of pure epoxy (EP) and GNP-reinforced epoxy (EP-GNP). GNP was not detected in the airborne emissions, but PAH concentration of the particles in airborne fraction was increased for emissions from EP-GNP. A first hazard assessment was performed on human alveolar epithelial cells exposed to airborne emissions at air-liquid interface conditions. Emissions from EP had no acute effects at 24 h and 96 h on cell viability, cell morphology or expression of anti-oxidative stress markers (*HMOX1* and *SOD2* gene*s*), but induced the activation of the aryl hydrocarbon receptor (*CYP1A1* gene) and a transient (pro-) inflammatory response (MCP-1 and GM-CSF). A similar response was observed after exposure to emissions from EP-GNP except an acute transient decrease in mitochondrial activity.

Keywords: graphene nanoplatelet, nanofiller, polymer combustion, air-liquid interface, *in vitro* hazard assessment, alveolar epithelium

Synopsis: Emissions from thermal decomposition of graphene nanoplatelet-reinforced epoxy contain higher amounts of PAH, but do not cause additional acute cytotoxic response compared to the pure epoxy, although further long-term safety investigation is needed.

4.1 Introduction

Graphene nanoplatelet (GNP) is a two-dimensional carbonaceous material consisting of a few to several layers of graphene sheets [1]. GNP has been extensively studied and applied in commercial products as nanofillers to improve the mechanical, electrical, and fire performance of the polymers [2,3]. Due to the improved properties of the composites, an increasing demand of graphene-related materials is predicted [4,5] and will raise the production volume of GNP and GNP-based products [6]. Therefore, a careful assessment about the adverse health effects due to an increasing use of GNP in commercial products are inevitable.

One of the scenarios that can occur at the end-of-life of the GNP-reinforced polymers is the combustion process such as waste incineration, where the process is mostly a complete combustion in the controllable manner, or an accidental fire, which is likely an incomplete combustion that probably generates higher amount of soot. Generally, combustion is a complex process and it is even more challenging to fully understand the combustion of nanomaterial-enabled polymers. The combustion of epoxy (EP) produces a large amount of soot and toxic gases such as CO and HCN [7]. During the combustion, epoxy resin can be degraded by chain scission mechanism and further decomposed to some light combustible gases such as allyl alcohol, acetone, and other hydrocarbons [8]. Rearrangement of the atoms and cyclization of the molecules can occur, which can lead to the char formation. GNP acts as a flame retardant when used as nanofiller in different kinds of polymer [2,9,10]. Addition of GNP slowed down the combustion of epoxy composite due to the barrier effect, which is a migration of GNP to the surface of the

polymer to form a protective layer [2]. GNP could be transformed by thermal oxidation at high temperature during the combustion [11,12]. At a temperature over 850 °C, the defected and basal plane of graphitic layer can be etched leading to hole formation in the layer [11]. Moreover, GNP may be dislocated from the matrix during the combustion process and exist as a part of the char [13] and/or in an airborne fraction, which may pose an additional risk to humans and the environment.

Biological effects of GNP have been reported *in vitro* and *in vivo* in different biological systems [14–19] and are summarized in several reports [20–23]. Due to its distinct platelet-like structure, Schinwald and coworkers showed that GNP with thickness of 100 nm and diameter up to 25 µm have an aerodynamic diameter in the respirable range (smaller than 4 µm) and could be deposited beyond the ciliated airway, in the alveolar structures where macrophages are mainly responsible for clearance process. GNP with a diameter larger than 15 µm could not be entirely phagocytosed by macrophages and thus provoked frustrated phagocytosis, increase in inflammatory cytokines (at 1 – 10 µg/cm^2), and in a later state loss of cellular membrane integrity (only at 5 and 10 µg/cm^2). Our previous study showed that GNP with larger lateral dimension (25 µm) at the delivered doses of 20 and 40 µg/mL induced the release of lactate dehydrogenase due to membrane rupture in THP-1 macrophages, whereas the smaller GNP (5 µm) did not [15]. On the other hand, Drasler *et al*. revealed that GNP with 1-2 µm lateral dimension at 0.3 and 1 µg/cm^2 exposure doses did not cause cytotoxic effects, (pro-) inflammation and oxidative stress towards a 3D alveolar lung cell model [19]. Apart from a variation of the biological models in different studies, the physicochemical characteristics of GNP such as lateral dimensions, thickness, surface area, and surface chemistry could also play a crucial role in the toxicity of GNP [21,22], which may explain the inconsistency in the reported biological responses. Nevertheless, in the context of a combustion event, the toxicity of the pristine GNP may be of limited relevance since the released GNP (if any) likely changed its properties during composite fabrication and thermal decomposition. Moreover, the combination of epoxy and GNP could lead to the formation of new emission particles or gases or induce synergistic effects.

Despite of the growing interest in applying GNP as nanofillers and the increasing number of GNP-filled polymer products on the market, little is known about the effects of GNP on the emissions from the combustion of GNP-containing nanocomposites and the potential hazard of the released particles and gases. Like GNP, carbon nanotube (CNT) is also a carbonaceous material consisting of rolled up graphene sheets. The presence of CNT in the polymer could enhance the concentration of polycyclic aromatic hydrocarbon (PAH) adsorbed to the particles emitted from the combustion of reinforced polyurethane (PU) and polycarbonate (PC) [24]. Watson-Wright *et al.* showed that the particulate emissions from PU-CNT (delivered doses of 0.06, 0.6 and 6 µg/cm^2) caused an increase in reactive oxygen species (ROS) formation and a decrease in mitochondrial membrane potential compared to the emissions from PU in primary

small airway epithelial cells. The emissions from the combustion of the pure polymers (polypropylene (PP) and PC) and the polymer composites (PP-CNT and PC-CNT) induced ROS formation, but they did not observe any difference in the adverse outcomes between the pure polymers and the composites [25]. Coyle and co-workers demonstrated that PC-CNT showed approximately 2-fold more cytotoxicity than PC in human bronchial epithelial cells (BEAS-2B). Moreover, cells exposed to 1.2 μg/cm^2 PC-CNT showed a significant increase in the intracellular ROS formation and DNA damage at 48 h, whereas the cells exposed to PC did not show any cytotoxicity. On the other hand, emission from PU and PU-CNT was not cytotoxic to BEAS-2B [26]. Hufnagel *et al.* investigated the *in vitro* toxicity of combusted CNT, pure polyethylene (PE), and PE-CNT on A549 cells *via* air-liquid interface (ALI) exposure. They found that the combusted PE and PE-CNT induced cytotoxicity at 24 h, while the combusted CNT did not [27]. Despite discrepancy among literature, it is clear that the type of polymer matrix, the physicochemical properties and loading of nanofiller could affect the particles and gases released from the combustion of the nanomaterial-enabled polymer composites and subsequently their potential hazard [24,28,29], which has to be assessed case-by-case.

To our best knowledge, there is currently no information available on the airborne emissions from the combustion of GNP-reinforced polymer and potential human health risks upon inhalation. Therefore, in this study, we have established a new platform to investigate the characteristics and potential hazard of the emissions formed from the combustion of GNP-reinforced polymer. The epoxy and GNP-reinforced epoxy served as a model system of GNP-reinforced polymer, on which we had full transparency of the fabrication process and characterization. The system combines a cone calorimeter (a standard fire analytical instrument), two real-time particle size distribution measurement instruments (aerodynamic particle sizer and fast mobility analyzer), a particle collection system for off-line analysis, and an on-line cell exposure system for *in vitro* cytotoxicity assessment. As a biological model for the lung epithelium, we examined the biological consequences at two time points (24 h and 96 h) of the airborne emissions on differentiated A549 monolayer cultures exposed directly to the emissions at ALI conditions, which more realistically resemble the conditions in the lung. The deposited doses of the emissions were based on the realistic GRM concentrations [30]. This study provides new insights on the characteristics and toxicity of emissions from the combustion of GNP-polymer composites, which is imperative to the safe and sustainable design and use of these promising materials.

4.2 Materials and Method

4.2.1 Epoxy and Epoxy-Graphene Nanoplatelet Composite

Diglycidyl ether of bisphenol A, DGEBA (Araldite GY 250, Huntsman, USA) and an aliphatic polyetheramine (Jeffamine D-230, Huntsman, USA) were used as epoxy and hardener, respectively. GNP (XG Science, Lansing, MI, USA) has lateral dimension of 25 µm according to the manufacturer and the detailed characterization can be found elsewhere [15]. EP and EP-GNP composites were fabricated as described elsewhere [31].

4.2.2 Combustion Experiment and Exposure System

The sample (10 cm width × 10 cm length and 4 mm thickness) was combusted using an FTT cone calorimeter (Fire Testing Technology, West Sussex, United Kingdom) with the heat flux of 50 kW/m^2 (~750 °C). The exhaust pipe of the cone calorimeter was modified for the sampling probe, which was positioned above the flame. The soot from the combustion was sampled to on-line particle characterization instruments, a filter for particle collection, and a cell exposure chamber as shown in Fig. 4.1. Two samples were combusted consecutively for each cell exposure experiment to achieve a deposited dose that was comparable to the realistic GRM concentrations [30]. Three biologically independent experiments were performed for each time point (24 h and 96 h).

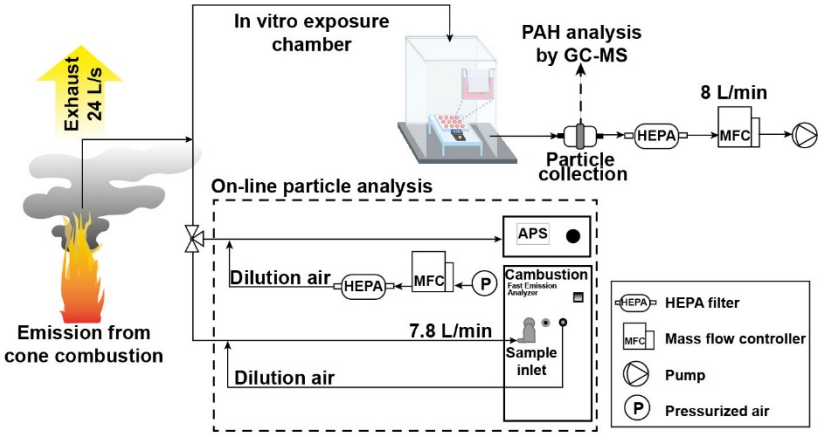

Figure 4.1 Scheme of the set-up of the combustion experiment consisting of cell exposure chamber for *in vitro* toxicity assessment, collection of particles emitted from the combustion for PAH analysis, and on-line aerosol characterization instruments. The drawing of cell exposure chamber was created using Biorender.

The on-line particle size distribution characterization consisted of a fast mobility analyzer (DMS 500, Cambustion, Cambridge, UK) and an aerodynamic particle sizer (APS, Model 3321, TSI, Shoreview, MI, USA). The cell exposure chamber consisted of an inlet on the top where

the emissions enter the chamber. Four outlets at the bottom of four walls of the exposure chamber were connected to a particle filter (AX1720HD, Lydall, Manchester, CT, USA) for particle collection. The flow rate was controlled using a mass flow controller (Aalborg, Orangeburg, NY, USA) and set at 8 L/min. A quartz crystal microbalance (QCM, openQCM wi2, Pompeii, Italy) was placed inside the chamber to monitor the doses of deposited particles. Sauerbrey equation was applied to estimate the mass of the deposited particles based on the frequency change of the quartz crystal [32,33]. Additionally, Si wafer grids were placed in the well plate for scanning electron microscopy (SEM, Nova NanoSEM 230, FEI Company, Hillsboro, OR, USA) analysis of the deposited particles. The number and size of the deposited particles obtained from SEM images in the area of 760 μm^2 were analyzed using ImageJ software.

4.2.3 Off-Line Particle Characterization

Particle morphology and elemental composition of pristine GNP and soot were analyzed using the SEM equipped with an energy dispersive X-ray spectrometer (SEM-EDX, Nova NanoSEM 230). X-ray diffractometer (X'Pert Pro, Malvern Panalytical, Malvern, UK) was employed to determine the X-ray diffraction patterns of the pristine GNP and soot and residual ash from combustion with the scan range between 5 and 80 degrees and a scan speed of 0.02 degree/s. Raman spectroscopy mapping measurements were performed on Senterra Raman spectrometer (Bruker, Billerica, MA, USA). We used an excitation laser with a wavelength of 532 nm and a power of 2 mW and 50x objective lens. Each Raman spectrum was obtained with an integration time of 20 s per point and co-addition of 2 spectra. Particles were sent to a commercial company for the analysis of 16 PAHs (Table C1) using gas chromatography-mass spectrometry. Extraction and analytical methods were compliant with ISO 17025. Details can be found in Appendix C.

4.2.4 Evaluation of Biological Responses

Cell Culture

Human alveolar pulmonary epithelial cell line (A549, American type culture collection CCL-185, Lot number 60120896) was cultivated in complete cell culture medium (Rosewell Park Memorial Institute (RPMI)-1640 medium, Sigma-Aldrich) supplemented with 10% fetal calf serum (Sigma-Aldrich), 1% L-glutamine (Sigma-Aldrich) and 1% penicillin–streptomycin–neomycin (Sigma-Aldrich) in T75 cell culture flasks. Cells were maintained at 37 °C and 5% CO_2 in humidified atmosphere and routinely sub-cultured twice a week. Cells ($5x10^5$ cells per insert) were seeded on the apical side of microporous culture inserts (PET, pore diameter 3 µm, 113.1 mm^2 growth area, Thincerts™, Greiner Bio-One Vacuette Schweiz GmbH, St. Gallen, Switzerland). Cells were cultivated in submerged condition for 96 h, where 1.5 mL complete cell culture medium was added on the basolateral side and 1 mL on the apical side. After 96 h, cells

were transferred to ALI conditions (by removing the apical medium) and kept for 24 h prior to the exposure. For the exposure, cells were transferred to the cell chamber of the platform, without gas composition or temperature control, for 15 min (removal of the lid) during the burning of the composites and then transferred back to the cell culture incubator. After the exposure, cells were incubated for 24 h or 96 h and then analyzed or stored for further analysis. Positive controls for each assays were applied to the cells (100 µL of the indicated controls on apical side) on the day of an exposure experiment unless stated otherwise. Negative control cultures were cells exposed to filtered air (8 L/min) for 15 min.

Cell Morphology

Confocal laser scanning microscope (CLSM, LSM780, 40x objective lens, Carl Zeiss AG, Switzerland) was employed to investigate cell morphology. Cells were fixed in 4% paraformaldehyde (PFA, in PBS, Sigma Aldrich) and permeabilized with Triton X-100 (0.2% v/v in PBS, Sigma Aldrich). Rhodamine phalloidin (Invitrogen; 1:40 in 1% BSA/PBS) was used to stain F-actin and DAPI (4′,6-diamidino-2-phenylindole, Life Technologies, Thermo Fisher Scientific, Switzerland; 1:1000 in 1% BSA/PBS) was used to label the nucleus. After incubation for 2 h without light at room temperature, inserts were washed with PBS, mounted on glass slides using Mowiol (Sigma Aldrich), and stored at 4 °C until the analysis.

Cell Viability

Lactate dehydrogenase (LDH) release from cells is an indicator of cell membrane integrity and the quantification of LDH is used to assess cytotoxicity. Cell culture media at basolateral side were collected and analyzed using CytoTox96® Non-Radioactive Cytotoxicity Assay (Promega Corporation, Madison, Wisconsin, USA) following the manufacturer's protocol with some modification. Cells exposed to 0.5% v/v Triton X-100 (Sigma-Aldrich) in PBS for 1 h were used as positive control. 3-(4,5-di- methylthiazol-2-yl)-5-(3-cyrboxymethoxy-phenyl)-2-(4-sulfophenyl)-2H-tetrazolium, inner salt (MTS) assay, an indicator of mitochondrial activity, was performed using the CellTiter96 Aqueous One solution (Promega). Positive control cultures were treated with 10^4 µM $CdSO_4$ (apically). The Mithras2 microplate reader (Berthold Technologies, Germany) was used for colorimetric measurements. The cell viability was reported relative to the negative control (filtered air exposure). Detailed procedure of LDH and MTS assay can be found in Appendix C.

Cytokine Profiling

The cellular (pro-) inflammatory responses are associated with the amounts of released cytokines and chemokines in cell culture media. Samples were sent to Eve Technologies (Alberta, Canada) for quantification of 15 crucial (pro-) inflammatory cytokines using multiplex technology (Bioplex, Biorad). The cytokine array included the following inflammatory markers:

granulocyte-macrophage colony-stimulating factor (GM-CSF), monocyte chemoattractant protein-1 (MCP-1), tumor necrosis factor alpha (TNF-α), interferon gamma (IFNγ), interleukin 1β (IL-1 β), IL-1ra, IL-5, IL-6, IL-8, IL-12(p70), IL-13, IL-2, IL-4, IL-10, and IL-12(p40). The samples were analyzed in duplicates.

Gene Expression Analysis

At 24 h and 96 h after exposure to the emissions, membranes containing cells were cut from the inserts and preserved in 500 µL of RNA protection buffer (Qiagen AG, Hombrechtikon, Switzerland) until RNA isolation. RNA was isolated using miRNeasy Mini Kit following the manufacturer's protocol (Qiagen). The real-time reverse transcriptase polymerase chain reaction (RT-PCR) was carried out with a 96-well fast reaction PCR system (C1000 Touch™ Thermal Cycler, Bio-Rad Hercules, CA, USA). The complementary DNA (cDNA) was synthesized using the isolated RNA, iScript reaction mix (Bio-Rad Laboratories, Hercules, CA, USA) and iScript reverse transcriptase (Bio-Rad Laboratories). The reverse transcriptase reactions were performed by combining cDNA and iQ SYBR Green Master mix. The relative expression values of the target mRNA was calculated using the $^{\Delta\Delta}$Ct method [34] and glyceraldehyde-3-phosphate dehydrogenase (*GAPDH*) was used as a reference gene. Two anti-oxidative stress markers heme oxygenase 1 (*HMOX1*) and superoxide dismutase 2 (*SOD2*) were assessed. Aryl hydrocarbon receptor (AhR) activation was evaluated using cytochrome P450 1A1 (*CYP1A1*) gene. The primer sequences for all tested genes are reported in Table C2 in Appendix C.

Statistical Analysis

Data were analyzed in three repetitions and all assays were performed at least in duplicates. All results are presented as mean ± standard error of the mean and p values < 0.05 were considered statistically significant. A Turkey post-hoc test was performed using R to compare the means among filtered air control, emissions from EP, and emissions from EP-GNP.

4.3 Results and Discussion

4.3.1 Combustion Characteristics of EP and EP-GNP

In our combustion experiment, we employed the cone calorimeter, a standardized instrument to study the fire behavior of materials according to ISO 5660-1. This allowed us to investigate the effects of nanofillers on the combustion behavior in a controlled manner. The change in combustion profile could affect the physicochemical properties of the emissions and subsequently their potential hazard. The cone calorimetry revealed the fire characteristics of EP and EP-GNP during the combustion and important parameters are summarized in Table C3. The combustion of each sample lasted 5 to 7 min. Plots of heat release rate, which represent the combustion profile of the samples, showed peaks at around 130-140 s (Fig. C1). GNP can slightly delay the

time to ignition of epoxy composite due to the good thermal diffusivity of GNP, which helps to diffuse the heat from material's surface to the bulk [35]. The major effect of adding GNP was a slight reduction in the peak heat release rate (pHRR) and a slight enhancement in CO production, which led to an increase in CO/CO_2 ratio. Complete combustion produces only CO_2 and water, while CO is a result of incomplete combustion. Higher CO/CO_2 ratio of EP-GNP indicated that GNP could contribute to more incomplete combustion compared to pure epoxy. With this, GNP could influence the chemical composition of the emissions.

4.3.2 Particle Characterization

Particle Size Distribution

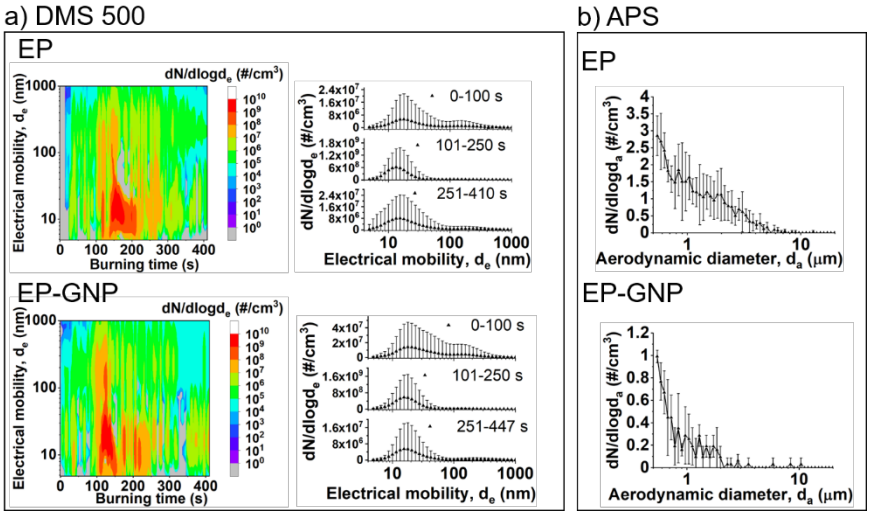

Figure 4.2 Particle size distributions of airborne emissions from the combustion of EP and EP-GNP measured by a) DMS500 and b) APS.

The presence of GNP did not affect the particle number nor the particle size of the emissions. Total concentrations of the emissions from burning EP and EP-GNP measured by DMS500 (Fig. C2) had the peaks in the range of 10^9 particles/cm^3. Fig. 4.2a showed that the particle size distributions had the peak concentrations between 100 s and 200 s of the burning time, which matches well with the time window of peak heat release rate in cone calorimetry. Since the combustion is a dynamic process, different size distributions were observed over the burning period. However, similar characteristics of particle size distributions were detected from the combustion of EP and EP-GNP. Before the peak concentrations (during 0-100 s), average particle size distribution revealed two particle modal sizes at around 20 nm (the dominant mode) and at around 200 nm. At the peak concentrations (101-250 s), the dominant particle mode was at approximately 15 nm and another mode was at around 150 nm, which might not be seen due to its relatively low concentration compared to the first mode. After the peak concentrations (from 251 s), the particle modes were at 15 nm and 200-300 nm. Particles in micrometer range

analyzed by APS showed that particle modes were between 1 to 2 μm (Fig. 4.2b). The results from DMS500 and APS suggested that the sizes of particulate emissions from burning EP and EP-GNP were smaller than 4 μm, which falls into the respirable fraction in the alveolar region of the lung [36].

Raman Spectroscopy Mapping and XRD of the Particulate Emissions

Raman spectroscopy is a useful tool to study graphitic materials because they showed distinctive patterns consisting of D band (1355 cm^{-1}), G band (1581 cm^{-1}) and 2D band (~2700 cm^{-1}). Details can be found in Appendix C. The degree of defects on the graphitic sheets are associated with the shift of the G peak position and the intensity ratio of D band to G band (I(D)/I(G)) [37]. D, G and 2D band positions and I(D)/I(G) were obtained from Raman spectroscopy mapping of pristine GNP, soot and residues from the combustion of EP and EP-GNP (Fig. C3a, Fig. C4, and Table C4). I(D)/I(G) of the soot and residues of EP and EP-GNP was higher than the pristine GNP. Residues of EP and soot of both EP and EP-GNP showed a broad shape of 2D band, whereas residues of EP-GNP showed a broad 2D band ranging from 2300 to 3300 cm^{-1} and a relatively sharp peak around 2703 cm^{-1}. The 2D band of graphene sheet usually appears as a sharp peak and becomes broader with increasing disorder [38]. The shape of the 2D band suggested that the residues from EP-GNP contained amorphous carbon and ordered structure material, which could be an indication of GNP. The 2D band of the EP residues and soot of EP and EP-GNP showed only a broad band indicating the presence of only amorphous carbon [38].

XRD patterns of soot and residues of EP and EP-GNP were compared with that of pristine GNP (Fig. C3b). XRD pattern of GNP had a peak at a 2θ of 26.9°, corresponding to the 002 crystal plane of the ordered hexagonal graphite with an interlayer spacing of 3.33 Å. Residues from EP-GNP showed two peaks at 002 position including a peak at 2θ of 26.9°, an indication of ordered structure carbon, and a broad peak with 2θ ranging from 15° to 30°, an indication of amorphous carbon. The residues of EP and soot of EP and EP-GNP only showed a broad peak at 002 position suggesting the absence of the ordered structure carbon (no GNP). Both Raman and XRD results indicated the presence of GNP in the residual ash, not in the aerosol fraction, which could be due to the ability of GNP to form a network-structured layer during the combustion [2,9,10,31] that made GNP remained in the residues. Kotsilkov and co-workers also found the release of GNP in the residual ash from burning a PLA-GNP film at 850 °C, but there was no information about the release in the airborne fraction [13].

Organic Compounds Analysis by GC-MS

Bar charts in Fig. 4.3 display the value of 16 PAHs and the equivalent benzo(a)pyrene (BaP) PAH concentration. Total amount of PAHs in particulate emissions formed from EP and EP-GNP combustion were 9333 ppm and 15262 ppm, respectively (uncertainty of analysis = 12-

24%), suggesting that GNP embedded in the epoxy composite could amplify the PAH concentration of the particulate aerosol released during the combustion of epoxy composite by around 64% compared to EP. Although combustion of EP-GNP produced higher concentrations of individual PAHs compared to EP, similar composition fractions of individual PAHs within the total amount was observed for EP and EP-GNP. Phenanthrene, fluoranthene and pyrene have the highest concentrations among analyzed PAHs. In terms of toxic potential of the emissions, BaP, benzo(a)anthracene, and dibenzo(a,h)anthracene contributed to the highest fractions of the equivalent BaP concentrations as shown in Fig. 4.3b.

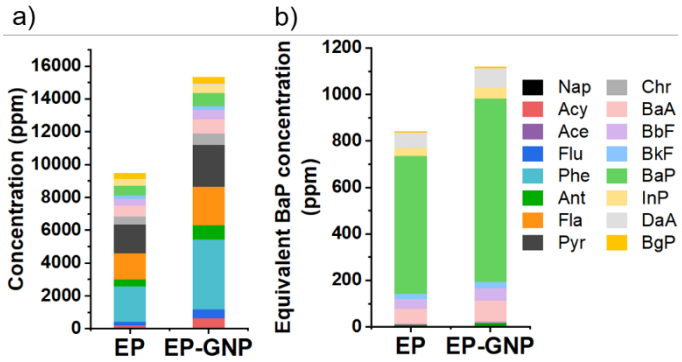

Figure 4.3 a) Comparison between PAH concentrations in ppm (µg PAH per g of particles) of particles emitted from the combustion of EP and EP-GNP and b) corresponding toxic potential of each PAH presented as equivalent benzo(a)pyrene (BaP) concentration [39] (ppm). The analyzed PAHs included naphthalene (Nap), acenaphthylene (Acy), acenaphthene (Ace), fluorene (Flu), phenanthrene (Phe), anthracene (Ant), fluoranthene (Fla), pyrene (Pyr), chrysene (Chr), benzo(a)anthracene (BaA), benzo(b)fluoranthene (BbF), benzo(k)fluoranthene (BkF), benzo(a)pyrene (BaP), indeno(1,2,3-c,d)pyrene (InP), dibenzo(a,h)anthracene (DaA), and benzo(g,h,i)perylene (BgP).

So far, there has not been any studies about the effect of embedded GNP for PAH formation, so we compared our results to CNT and C_{60}, which are also carbonaceous nanomaterials. Singh and co-workers reported the effect of CNT on the enhancement of PAH profile of the particles released from thermal decomposition of thermoplastics [24]. They showed that the degree of enhancement in PAH concentrations varied depending, not only on the type of nanofiller, but also on the type of matrix. For example, PU-CNT had two times higher total PAH concentrations than pristine PU, while PP-CNP and PC-CNT had almost eight times higher total PAH concentrations than their parent matrices. The presence of C_{60} enhanced the formation of some PAH species such as chrysene and phenanthrene by more than 200 and 20 times, respectively, during the waste incineration [40].

Regarding PAH formation mechanism, an increase in PAH concentrations could be caused by metal traces in pristine GNP (Fig. C5), which may exist in the parent graphite used for GNP

synthesis or is introduced during the manufacturing process related to chemical exfoliation [41]. Metal and metal oxides such as Ag, Fe, Pb, Cr, TiO_2, Fe_2O_3, and Al_2O_3 could catalyze the formation of PAH [24,40,42–44]. Metal atoms on soot particles were hypothesized to enhance the formation of PAH by offering active sites where the reactions that catalyzed PAHs could occur [42,43]. Additionally, our cone combustion results suggested that GNP could suppress the combustion process, resulting in an incomplete combustion. According to cone calorimetry results, the higher CO/CO_2 ratio of EP-GNP as compared to EP supported our hypothesis that GNP hindered the combustion process and led to a higher degree of incomplete combustion, which could be a cause for PAH formation.

4.3.3 Evaluation of Biological Responses

We assessed the biological response of alveolar epithelial cells at 24 and 96 h after exposure to the emissions, which allowed us to study acute and chronic cellular effects. The human alveolar epithelial Type II cells (A549) were used in our study because they are polarized and produce surfactant similar to *in vivo* conditions. Moreover, cells were maintained at ALI conditions, which more realistically resembled the *in vivo* situation.

Deposited Dose Determination

The QCM measurements of the filtered air showed no frequency change during the exposure period over 15 min (Fig. C6), indicating that the deposited particles during the filtered air exposure were below the detection limit of QCM (1 ng/cm^2 according to manufacturer). The QCM results and the SEM images showed a reproducible and controlled deposition of combustion particles. Results from QCM (Fig. C7) revealed that the average deposited doses of the emissions from EP and EP-GNP were in the similar range, specifically 0.27 ± 0.08 µg/cm^2 for EP and 0.29 ± 0.08 µg/cm^2 for EP-GNP. Fig. C8 showed the SEM images and the corresponding particle size distributions of the uniformly deposited particles in the well-plate, which were comparable between EP and EP-GNP. The deposited doses in this study were in the same range as those reported in other *in vitro* toxicity studies that performed an air-liquid interface aerosol exposure to carbonaceous materials (CNT, GNP, GO) or emissions from the combustion of polymer nanocomposites (TiO_2 , CuO, or CNT nanofillers) [19,27,45,46]. Only one deposited dose was investigated in this study because our exposure system was not equipped with the controlled humidified atmosphere and CO_2 concentration, which may cause negative impacts to the cells when the exposure period was prolonged to enhance the particle deposition.

Cell Morphology and Viability

Immunocytochemical staining revealed that the cells treated with filtered air, which was used as the negative control, did not show any significant differences in cell morphology and monolayer integrity compared to the untreated cells (Fig. C9). There were no apparent changes in

cell morphology after cell exposure to emissions from EP and EP-GNP as compared to filtered air exposure even at 96 h post-exposure time (Fig. 4.4a). Cell viability was evaluated by the release of LDH (membrane integrity) and MTS assay (mitochondrial activity) (Fig. 4.4b-c). Emissions from the combustion of EP did not affect membrane integrity or mitochondrial activity of the cells up to 96 h post-exposure. For emissions from EP-GNP combustion, a transient decrease in mitochondrial activity (significant at 24 h, $p<0.05$; recovered to negative control levels at 96 h) was observed, but this did not lead to cell death as evidenced by the lack of LDH release at both investigated time points.

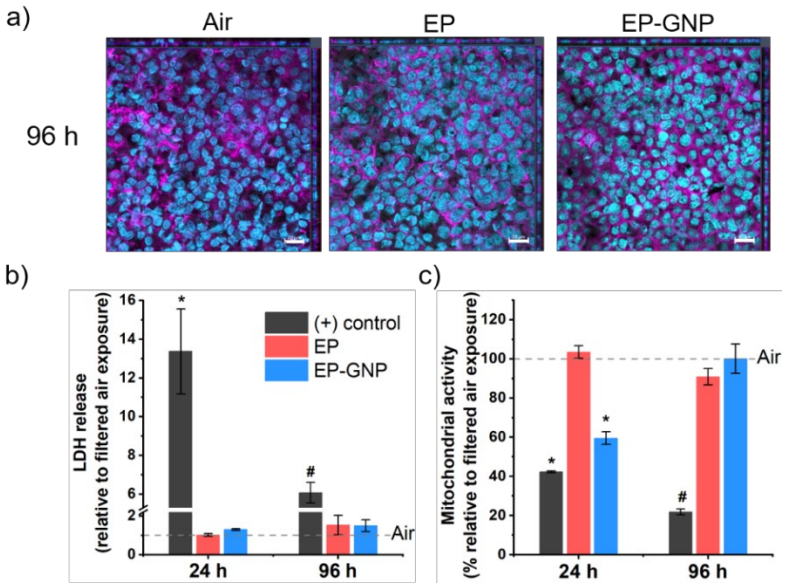

Figure 4.4 a) Cell morphology at 96 h after exposure to filtered air and emissions from combustion of EP and EP-GNP analyzed using confocal laser scanning microscopy. Blue = DAPI; magenta = Rhodamine phalloidin. Scale bar is 20 µm. Cell viability determined by measuring b) the release of lactate dehydrogense (LDH assay) and c) mitrochondrial activity (MTS assay). Triton X-100 (0.5% v/v) and $CdSO_4$ (10^4 µM) were used as (+) controls for LDH and MTS assays, respectively. Bar chart displays average values of three experiments and error bars are standard error of mean. Symbol * and # indicate statistically significantly different from the filtered air exposure ($p<0.05$).

Cytokine profiling

To estimate potential (pro-) inflammatory responses of airborne emissions, we performed a cytokine profiling of 15 cytokines and chemokines. The relative concentration of 10 cytokines, including TNF-a, MCP-1, IL-8, IL-6, IL-5, IL-1Ra, IL-12p70, IL-10, IFNγ and GM-CSF, released into cell culture media compared to filtered air control were displayed in Fig. C10. IL-13, IL-2, IL-4, IL-10, and IL-12(p40) were also included in the Bioplex panel; however, their release levels were below the limit of detection for the experimental set-up. After exposure to

EP and EP-GNP emissions, all cytokines, except MCP-1 and GM-CSF, were at similar levels as cells exposed to filtered air. Both MCP-1 and GM-CSF are associated with (pro-) inflammatory responses and GM-CSF also contributes to the development of autoimmune and inflammatory diseases [47]. We found a significant increase in secreted MCP-1 in cell culture media at 24 h after exposure to emissions from both EP and EP-GNP compared to filtered air exposure, whereas at 96 h the MCP-1 levels in these samples were comparable to filtered air exposure (Fig. 4.5a). EP-GNP further induced a noticeably higher level of the growth factor GM-CSF than filtered air exposure ($p = 0.064$) at 24 h, while EP also induced a slightly higher GM-CSF level at 96 h compared to EP-GNP and filtered air exposure; nevertheless, these increases were not statistically significant (Fig. 4.5b). Since the expressions of the other key cytokines/chemokines in the array were not affected, the increased MCP-1 indicates only a limited (pro-) inflammatory response. The release of MCP-1 and GM-CSF is a cellular protective mechanisms in response to oxidative stress, cytokines or growth factors *via* recruiting monocytes [48] and activating granulocytes and macrophages, respectively [47]. The release of MCP-1 and GM-CSF was previously reported when cells were treated with particles from diesel exhaust or aircraft turbine engine exhaust [49–51].

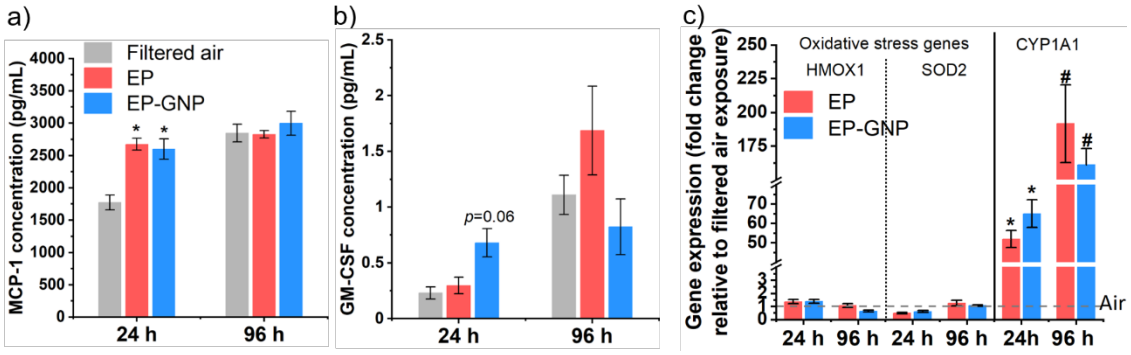

Figure 4.5 Release of two cytokines/chemokine including a) monocyte chemoattractant protein-1 (MCP-1) and b) granulocyte-macrophage colony-stimulating factor (GM-CSF). c) Expression of two oxidative stress genes (*HMOX1* and *SOD2*) and aryl carbon receptor gene *CYP1A1* in comparison to filtered air exposure (negative control). Bar charts present average values from three experiments ± standard error of mean. Symbol * and # indicate statistically significantly different from negative control ($p<0.05$).

Gene Expression Analysis

No significant alteration in expression levels of two oxidative stress-related genes, *HMOX1* and *SOD2*, was detected from exposure to either EP or EP-GNP emissions at 24 h and 96 h time point (Fig. 4.5c). It is well known that oxidative stress is closely related to inflammatory re-

sponses [52]. Although EP and EP-GNP could induce the release of (pro-) inflammatory mediators MCP-1 and GM-CSF, we did not observe any significant deregulation on the expression levels of the oxidative stress related genes *HMOX1* and *SOD2*.

Expression level of *CYP1A1* gene was upregulated by 50-fold at 24 h after exposure to emissions from the combustion of both EP and EP-GNP and further increased by 150-fold at 96 h time-point (Fig. 4.5c). This significant increase in *CYP1A1* expression suggested a strong cellular response to PAHs, which is responsible for metabolism of PAHs *via* the aryl hydrocarbon receptor [53]. Previous studies showed that the presence of PAHs induced an increase in the expression level of *CYP1A1* in A549 cells [54] in a dose-dependent manner [55]. Therefore, elevated PAH concentrations and consequently higher equivalent BaP concentrations of EP-GNP emissions may be one of the contributors to slightly higher *CYP1A1* expression level of EP-GNP at 24 h after exposure compared to EP. Nevertheless, *CYP1A1* expression was similar at 96 h post-exposure for EP and EP-GNP emissions, suggesting that the higher levels of PAHs in EP-GNP emissions did not considerably amplify the cellular response. Overall, despite some differences in the absolute PAH levels, the response in *CYP1A1* activation was rather similar for EP and EP-GNP emissions. However, more genes associated with aryl hydrocarbon receptor should be analyzed to better understand the possible impact of increased PAH concentrations.

Despite a decrease in mitochondrial activity at 24 h after exposure, EP and EP-GNP did not show any significant difference in other cytotoxicity markers. Since we detected that GNP presented only in residual ash, GNP (if any) was not likely to directly contribute to the biological effects of the aerosol emissions found in this study. Even though the combustion of EP-GNP produced higher PAH concentration in the particulate emissions compared to EP, EP-GNP only showed slightly higher, but not significant, expression level of *CYP1A1* gene. Apart from PAHs adsorbed to particles, PAHs and other toxic compounds in the gas phase such as SO_2 and NO_x could be formed during the combustion of epoxy composite. Previous studies reported that some PAHs could inhibit CYP1 family enzymes *i.e.* CYP 1A1, 1A2 and 1B1 and consequently affect the metabolisms of xenobiotics catalyzed by these enzymes [56]. PAHs can induce CYP1 localization to mitochondria, which then leads to mitochondrial respiratory dysfunction [57]. Based on our results, an elevated PAH concentration may account for the decrease in mitochondrial activity caused by EP-GNP with respect to EP. However, the elevated PAH concentration may not be high enough to cause permanent effects as we observed the recovery of the mitochondrial activity of the cells to the level of negative control at 96 h.

The contribution of the soot fraction to the difference in biological effects caused by the emissions from the combustion of EP-GNP compared to those of EP was not likely since the deposited doses in both cases were not statistically different. And the particle size distributions of the emissions from EP and EP-GNP measured by APS and DMS 500 were also in a similar range.

Dilger and co-workers studied the contributions of soot, metals and PAHs, which were the components of the wood smoke particles, to the biological effects of A549 under submerged exposure conditions. The soot and PAHs contributions were mimicked using carbon black and BaP, respectively. They found that PAHs adsorbed to wood smoke particles did induce PAH metabolism by *CYP1A1* to higher extent than the pure BaP. Mitochondrial activity of A549 cells after exposure to carbon black up to 100 µg/mL (31.25 µg/cm^2) was not decreased, but increased, and LDH release was not affected. Carbon black, representing soot fraction, with the delivered doses of 50 and 100 µg/mL and metals could induce ROS formation [58]. In our study, the deposited doses (0.27-0.29 µg/cm^2) were much lower and did not result in an oxidative stress response (as demonstrated by the *HMOX1* and *SOD2* expression). Hufnagel *et al.* also analyzed whether particles and/or gases contributed to the toxic effects of the emissions from the combustion of nanomaterial-enabled polymer by comparing the whole emissions to the particle-filtered emissions. They did not observe any difference in the biological effects on A549 cells after exposure to the whole emissions or the gaseous phase, concluding that the toxic effects were entirely due to the gaseous phase in the emissions such as CO and volatile and semi-volatile organic compounds [27]. Therefore, the reason for the transient reduction in mitochondrial activity caused by EP-GNP but not EP emissions still remains to be identified.

In the present study, we have established and applied a platform to investigate effects of GNP nanofiller in epoxy composite on the aerosol released from the combustion in terms of their particle size and concentration, PAH concentration, and biological effects on lung cells. The concentrations of the released aerosols were in the range of 10^9 particles/cm^3 and their sizes ranged from tens of nanometers to a few micrometers, which is in the respirable size range. The presence of GNP did not alter the particle size distributions of the emissions formed during the combustion of the epoxy. Raman spectroscopy and XRD analysis of the particulates formed in the combustion process confirmed the absence of GNP in the airborne fraction emitted from the combustion of EP-GNP, while GNP were found in the residual ash. Despite its absence in airborne fraction, presence of GNP in EP could enhance PAH concentration of the particles released from the combustion. After exposure to EP and EP-GNP combustion emissions, we did not observe any change in cell morphology, any severe cytotoxicity, release of (pro-) inflammatory factors, nor a change in expression levels of oxidative stress markers, *HMOX1* and *SOD2*, indicating the absence of an acute cytotoxic effect. Emissions from EP and EP-GNP strongly affected the PAH metabolism in the cells (upregulation of *CYP1A1*). The elevated PAH concentration in the particles emitted from EP-GNP combustion may be one of the contributors to the deviation in the toxicological outcome observed in EP-GNP compared to EP. Our results confirm the potential health risks of the aerosol emissions from epoxy composites at their end-of-life *via* a combustion process, at the same time highlights that incorporation of

GNP is not inducing any novel or additive adverse effects on alveolar epithelial cells within 96 h of culture.

Conflicts of interest

There are no conflicts of interest to declare.

Acknowledgement

The research leading to these results has received funding from the European Union (EU) Horizon 2020 Framework Graphene Flagship project GrapheneCore2 and GrapheneCore3 (grant agreement n°785219, 881603), the NanoScreen materials challenge co-sponsored by the Competence Centre for Materials Science and Technology (CCMX) as well as Swiss National Science Foundation (grant number 310030_169207).

4.4 References

1. Wick, P.; Louw-Gaume, A.E.; Kucki, M.; Krug, H.F.; Kostarelos, K.; Fadeel, B.; Dawson, K.A.; Salvati, A.; Vázquez, E.; Ballerini, L.; et al. Classification framework for graphene-based materials. *Angew. Chemie - Int. Ed.* **2014**, *53*, 7714–7718, doi:10.1002/anie.201403335.
2. Zhang, Q.; Wang, Y.C.; Bailey, C.G.; Yuen, R.K.K.; Parkin, J.; Yang, W.; Valles, C. Quantifying effects of graphene nanoplatelets on slowing down combustion of epoxy composites. *Compos. Part B Eng.* **2018**, *146*, 76–87, doi:10.1016/j.compositesb.2018.03.049.
3. Chandrasekaran, S.; Seidel, C.; Schulte, K. Preparation and characterization of graphite nano-platelet (GNP)/epoxy nano-composite: Mechanical, electrical and thermal properties. *Eur. Polym. J.* **2013**, *49*, 3878–3888, doi:10.1016/j.eurpolymj.2013.10.008.
4. Garrington, A. The Graphene Market Will Reach $700m by 2031 Available online: https://www.idtechex.com/en/research-article/idtechex-the-graphene-market-will-reach-700m-by-2031/22414.
5. Reiss, T.; Hjelt, K.; Ferrari, A.C. Graphene is on track to deliver on its promises. *Nat. Nanotechnol.* **2019**, *14*, 907–910, doi:10.1038/s41565-019-0557-0.
6. Kong, W.; Kum, H.; Bae, S.-H.; Shim, J.; Kim, H.; Kong, L.; Meng, Y.; Wang, K.; Kim, C.; Kim, J. Path towards graphene commercialization from lab to market. *Nat. Nanotechnol.* **2019**, *14*, 927–938, doi:10.1038/s41565-019-0555-2.
7. Dao, D.Q.; Rogaume, T.; Luche, J.; Richard, F.; Bustamante Valencia, L.; Ruban, S. Thermal degradation of epoxy resin/carbon fiber composites: Influence of carbon fiber fraction on the fire reaction properties and on the gaseous species release. *Fire Mater.* **2014**, *40*, n/a-n/a, doi:10.1002/fam.2265.
8. Levchik, S. V; Weil, E.D. Thermal decomposition, combustion and flame-retardancy of epoxy resins-a review of the recent literature. *Polym. Int.* **2004**, *53*, 1901–1929, doi:10.1002/pi.1473.
9. Dittrich, B.; Wartig, K.-A.; Hofmann, D.; Mülhaupt, R.; Schartel, B. Flame retardancy through carbon

nanomaterials: Carbon black, multiwall nanotubes, expanded graphite, multi-layer graphene and graphene in polypropylene. *Polym. Degrad. Stab.* **2013**, *98*, 1495–1505, doi:10.1016/j.polymdegradstab.2013.04.009.

10. Liu, S.; Yan, H.; Fang, Z.; Wang, H. Effect of graphene nanosheets on morphology, thermal stability and flame retardancy of epoxy resin. *Compos. Sci. Technol.* **2014**, *90*, 40–47, doi:10.1016/j.compscitech.2013.10.012.
11. Hahn, J.R. Kinetic study of graphite oxidation along two lattice directions. *Carbon N. Y.* **2005**, *43*, 1506–1511, doi:10.1016/j.carbon.2005.01.032.
12. Ermakov, V.A.; Alaferdov, A. V.; Vaz, A.R.; Perim, E.; Autreto, P.A.S.; Paupitz, R.; Galvao, D.S.; Moshkalev, S.A. Burning Graphene Layer-by-Layer. *Sci. Rep.* **2015**, *5*, 11546, doi:10.1038/srep11546.
13. Kotsilkov, S.; Ivanov, E.; Vitanov, N. Release of Graphene and Carbon Nanotubes from Biodegradable Poly(Lactic Acid) Films during Degradation and Combustion: Risk Associated with the End-of-Life of Nanocomposite Food Packaging Materials. *Materials (Basel).* **2018**, *11*, 2346, doi:10.3390/ma11122346.
14. Schinwald, A.; Murphy, F.A.; Jones, A.; MacNee, W.; Donaldson, K. Graphene-based nanoplatelets: A new risk to the respiratory system as a consequence of their unusual aerodynamic properties. *ACS Nano* **2012**, *6*, 736–746, doi:10.1021/nn204229f.
15. Netkueakul, W.; Korejwo, D.; Hammer, T.; Chortarea, S.; Rupper, P.; Braun, O.; Calame, M.; Rothen-Rutishauser, B.; Buerki-Thurnherr, T.; Wick, P.; et al. Release of graphene-related materials from epoxy-based composites: characterization, quantification and hazard assessment in vitro. *Nanoscale* **2020**, *12*, 10703–10722, doi:10.1039/C9NR10245K.
16. Li, Y.; Liu, Y.; Fu, Y.; Wei, T.; Le Guyader, L.; Gao, G.; Liu, R.-S.; Chang, Y.-Z.; Chen, C. The triggering of apoptosis in macrophages by pristine graphene through the MAPK and TGF-beta signaling pathways. *Biomaterials* **2012**, *33*, 402–411, doi:10.1016/j.biomaterials.2011.09.091.
17. Park, E.-J.; Lee, G.-H.; Han, B.S.; Lee, B.-S.; Lee, S.; Cho, M.-H.; Kim, J.-H.; Kim, D.-W. Toxic response of graphene nanoplatelets in vivo and in vitro. *Arch. Toxicol.* **2015**, *89*, 1557–1568, doi:10.1007/s00204-014-1303-x.
18. Park, E.J.; Lee, S.J.; Lee, K.; Choi, Y.C.; Lee, B.S.; Lee, G.H.; Kim, D.W. Pulmonary persistence of graphene nanoplatelets may disturb physiological and immunological homeostasis. *J. Appl. Toxicol.* **2017**, *37*, 296–309, doi:10.1002/jat.3361.
19. Drasler, B..; Kucki, M..; Delhaes, F..; Buerki-Thurnherr D.; Korejwo, D.; Chortarea,S.; Barosova,H.; Hirsch,C.; Petri-Fink,A.; Rothen-Rutishauser,B.; Wick,P., T.. V. Single exposure to aerosolized graphene oxide and graphene nanoplatelets did not initiate an acute biological response in a 3D human lung model. *Carbon N. Y.* **2018**, *137*, 125–135, doi:https://doi.org/10.1016/j.carbon.2018.05.012.
20. Zhang, B.; Wei, P.; Zhou, Z.; Wei, T. Interactions of graphene with mammalian cells: Molecular mechanisms and biomedical insights. *Adv. Drug Deliv. Rev.* **2016**, *105*, 145–162, doi:10.1016/j.addr.2016.08.009.
21. Yang, K.; Li, Y.; Tan, X.; Peng, R.; Liu, Z. Behavior and Toxicity of Graphene and Its Functionalized

Derivatives in Biological Systems. *Small* **2013**, *9*, 1492–1503, doi:10.1002/smll.201201417.

22. Ou, L.; Song, B.; Liang, H.; Liu, J.; Feng, X.; Deng, B.; Sun, T.; Shao, L. Toxicity of graphene-family nanoparticles: a general review of the origins and mechanisms. *Part. Fibre Toxicol.* **2016**, *13*, 57, doi:10.1186/s12989-016-0168-y.

23. Fadeel, B.; Bussy, C.; Merino, S.; Vázquez, E.; Flahaut, E.; Mouchet, F.; Evariste, L.; Gauthier, L.; Koivisto, A.J.; Vogel, U.; et al. Safety Assessment of Graphene-Based Materials: Focus on Human Health and the Environment. *ACS Nano* **2018**, *12*, 10582–10620, doi:10.1021/acsnano.8b04758.

24. Singh, D.; Schifman, L.A.; Watson-Wright, C.; Sotiriou, G.A.; Oyanedel-Craver, V.; Wohlleben, W.; Demokritou, P. Nanofiller Presence Enhances Polycyclic Aromatic Hydrocarbon (PAH) Profile on Nanoparticles Released during Thermal Decomposition of Nano-enabled Thermoplastics: Potential Environmental Health Implications. *Environ. Sci. Technol.* **2017**, *51*, 5222–5232, doi:10.1021/acs.est.6b06448.

25. Watson-Wright, C.; Singh, D.; Demokritou, P. Toxicological implications of released particulate matter during thermal decomposition of nano-enabled thermoplastics. *NanoImpact* **2017**, *5*, 29–40, doi:10.1016/j.impact.2016.12.003.

26. Coyle, J.P.; Derk, R.C.; Kornberg, T.G.; Singh, D.; Jensen, J.; Friend, S.; Mercer, R.; Stueckle, T.A.; Demokritou, P.; Rojanasakul, Y.; et al. Carbon nanotube filler enhances incinerated thermoplastics-induced cytotoxicity and metabolic disruption in vitro. *Part. Fibre Toxicol.* **2020**, *17*, 40, doi:10.1186/s12989-020-00371-1.

27. Hufnagel, M.; May, N.; Wall, J.; Wingert, N.; Garcia-Käufer, M.; Arif, A.; Hübner, C.; Berger, M.; Mülhopt, S.; Baumann, W.; et al. Impact of Nanocomposite Combustion Aerosols on A549 Cells and a 3D Airway Model. *Nanomaterials* **2021**, *11*, 1685, doi:10.3390/nano11071685.

28. Health Hazards of Composites in Fire. In *Fire Properties of Polymer Composite Materials*; Springer Netherlands: Dordrecht, 2006; pp. 359–384 ISBN 978-1-4020-5356-6.

29. Motzkus, C.; Chivas-Joly, C.; Guillaume, E.; Ducourtieux, S.; Saragoza, L.; Lesenechal, D.; Macé, T. Characterization of aerosol emitted by the combustion of nanocomposites. *J. Phys. Conf. Ser.* **2011**, *304*, 012020, doi:10.1088/1742-6596/304/1/012020.

30. Drasler, B.; Kucki, M.; Delhaes, F.; Buerki-Thurnherr, T.; Vanhecke, D.; Korejwo, D.; Chortarea, S.; Barosova, H.; Hirsch, C.; Petri-Fink, A.; et al. Single exposure to aerosolized graphene oxide and graphene nanoplatelets did not initiate an acute biological response in a 3D human lung model. *Carbon N. Y.* **2018**, *137*, 125–135, doi:10.1016/j.carbon.2018.05.012.

31. Netkueakul, W.; Fischer, B.; Walder, C.; Nüesch, F.; Rees, M.; Jovic, M.; Gaan, S.; Jacob, P.; Wang, J. Effects of Combining Graphene Nanoplatelet and Phosphorous Flame Retardant as Additives on Mechanical Properties and Flame Retardancy of Epoxy Nanocomposite. *Polymers (Basel).* **2020**, *12*, 2349, doi:10.3390/polym12102349.

32. Buttry, D.A.; Ward, M.D. Measurement of interfacial processes at electrode surfaces with the electrochemical quartz crystal microbalance. *Chem. Rev.* **1992**, *92*, 1355–1379, doi:10.1021/cr00014a006.

33. Xiao, L.; Zheng, Z.; Irgum, K.; Andersson, P.L. Studies of Emission Processes of Polymer Additives into Water Using Quartz Crystal Microbalance—A Case Study on Organophosphate Esters. *Environ. Sci. Technol.* **2020**, *54*, 4876–4885, doi:10.1021/acs.est.9b07607.

34. Schmittgen, T.D.; Livak, K.J. Analyzing real-time PCR data by the comparative CT method. *Nat. Protoc.* **2008**, *3*, 1101–1108, doi:10.1038/nprot.2008.73.

35. Laachachi, A.; Burger, N.; Apaydin, K.; Sonnier, R.; Ferriol, M. Is expanded graphite acting as flame retardant in epoxy resin? *Polym. Degrad. Stab.* **2015**, *117*, 22–29, doi:10.1016/j.polymdegradstab.2015.03.016.

36. Hofmann, W. Modelling inhaled particle deposition in the human lung—A review. *J. Aerosol Sci.* **2011**, *42*, 693–724, doi:10.1016/j.jaerosci.2011.05.007.

37. Ferrari, A.C.; Robertson, J. Interpretation of Raman spectra of disordered and amorphous carbon. *Phys. Rev. B* **2000**, *61*, 14095–14107, doi:10.1103/PhysRevB.61.14095.

38. Escribano, R.; Sloan, J.J.; Siddique, N.; Sze, N.; Dudev, T. Raman spectroscopy of carbon-containing particles. *Vib. Spectrosc.* **2001**, *26*, 179–186, doi:10.1016/S0924-2031(01)00106-0.

39. Nisbet, I.C.T.; LaGoy, P.K. Toxic equivalency factors (TEFs) for polycyclic aromatic hydrocarbons (PAHs). *Regul. Toxicol. Pharmacol.* **1992**, *16*, 290–300, doi:10.1016/0273-2300(92)90009-X.

40. Vejerano, E.P.; Holder, A.L.; Marr, L.C. Emissions of Polycyclic Aromatic Hydrocarbons, Polychlorinated Dibenzo- p -Dioxins, and Dibenzofurans from Incineration of Nanomaterials. *Environ. Sci. Technol.* **2013**, *47*, 4866–4874, doi:10.1021/es304895z.

41. Wong, C.H.A.; Sofer, Z.; Kube ova, M.; Ku era, J.; Mat jkova, S.; Pumera, M. Synthetic routes contaminate graphene materials with a whole spectrum of unanticipated metallic elements. *Proc. Natl. Acad. Sci.* **2014**, *111*, 13774–13779, doi:10.1073/pnas.1413389111.

42. Wey, M.-Y.; Chao, C.-Y.; Wei, M.-C.; Yu, L.-J.; Liu, Z.-S. The influence of heavy metals on partitioning of PAHs during incineration. *J. Hazard. Mater.* **2000**, *77*, 77–87, doi:10.1016/S0304-3894(00)00254-5.

43. Feitelberg, A.S.; Longwell, J.P.; Sarofim, A.F. Metal enhanced soot and PAH formation. *Combust. Flame* **1993**, *92*, 241–253, doi:10.1016/0010-2180(93)90036-3.

44. Mao, Q.; Luo, K.H. Trace metal assisted polycyclic aromatic hydrocarbons fragmentation, growth and soot nucleation. *Proc. Combust. Inst.* **2019**, *37*, 1023–1030, doi:10.1016/j.proci.2018.06.106.

45. Chortarea, S.; Clift, M.J.D.; Vanhecke, D.; Endes, C.; Wick, P.; Petri-Fink, A.; Rothen-Rutishauser, B. Repeated exposure to carbon nanotube-based aerosols does not affect the functional properties of a 3D human epithelial airway model. *Nanotoxicology* **2015**, *9*, 983–993, doi:10.3109/17435390.2014.993344.

46. Chortarea, S.; Barosova, H.; Clift, M.J.D..; Wick, P..; Petri-Fink, A.;; Rothen-Rutishauser, B.; Human Asthmatic Bronchial Cells Are More Susceptible to Subchronic Repeated Exposures of Aerosolized Carbon Nanotubes At Occupationally Relevant Doses Than Healthy Cells. *ACS Nano* **2017**, *11*, 7615–7625, doi:10.1021/acsnano.7b01992.

47. Shiomi, A.; Usui, T. Pivotal Roles of GM-CSF in Autoimmunity and Inflammation. *Mediators Inflamm.* **2015**, *2015*, 1–13, doi:10.1155/2015/568543.

48. Deshmane, S.L.; Kremlev, S.; Amini, S.; Sawaya, B.E. Monocyte Chemoattractant Protein-1 (MCP-1): An Overview. *J. Interf. Cytokine Res.* **2009**, *29*, 313–326, doi:10.1089/jir.2008.0027.

49. Ohtoshi, T.; Takizawa, H.; Okazaki, H.; Kawasaki, S.; Takeuchi, N.; Ohta, K.; Ito, K. Diesel exhaust particles stimulate human airway epithelial cells to produce cytokines relevant to airway inflammation in vitro. *J. Allergy Clin. Immunol.* **1998**, *101*, 778–785, doi:10.1016/S0091-6749(98)70307-0.

50. Baulig, A.; Sourdeval, M.; Meyer, M.; Marano, F.; Baeza-Squiban, A. Biological effects of atmospheric particles on human bronchial epithelial cells. Comparison with diesel exhaust particles. *Toxicol. Vitr.* **2003**, *17*, 567–573, doi:10.1016/S0887-2333(03)00115-2.

51. Jonsdottir, H.R.; Delaval, M.; Leni, Z.; Keller, A.; Brem, B.T.; Siegerist, F.; Schönenberger, D.; Durdina, L.; Elser, M.; Burtscher, H.; et al. Non-volatile particle emissions from aircraft turbine engines at ground-idle induce oxidative stress in bronchial cells. *Commun. Biol.* **2019**, *2*, 1–11, doi:10.1038/s42003-019-0332-7.

52. Reuter, S.; Gupta, S.C.; Chaturvedi, M.M.; Aggarwal, B.B. Oxidative stress, inflammation, and cancer: How are they linked? *Free Radic. Biol. Med.* **2010**, *49*, 1603–1616, doi:10.1016/j.freeradbiomed.2010.09.006.

53. Shimada, T.; Fujii-Kuriyama, Y. Metabolic activation of polycyclic aromatic hydrocarbons to carcinogens by cytochromes P450 1A1 and1B1. *Cancer Sci.* **2004**, *95*, 1–6, doi:10.1111/j.1349-7006.2004.tb03162.x.

54. Castorena-Torres, F.; de León, M.B.; Cisneros, B.; Zapata-Pérez, O.; Salinas, J.E.; Albores, A. Changes in gene expression induced by polycyclic aromatic hydrocarbons in the human cell lines HepG2 and A549. *Toxicol. Vitr.* **2008**, *22*, 411–421, doi:10.1016/j.tiv.2007.10.009.

55. Genies, C.; Maître, A.; Lefèbvre, E.; Jullien, A.; Chopard-Lallier, M.; Douki, T. The Extreme Variety of Genotoxic Response to Benzo[a]pyrene in Three Different Human Cell Lines from Three Different Organs. *PLoS One* **2013**, *8*, e78356, doi:10.1371/journal.pone.0078356.

56. Shimada, T.; Guengerich, F.P. Inhibition of Human Cytochrome P450 1A1-, 1A2-, and 1B1-Mediated Activation of Procarcinogens to Genotoxic Metabolites by Polycyclic Aromatic Hydrocarbons. *Chem. Res. Toxicol.* **2006**, *19*, 288–294, doi:10.1021/tx050291v.

57. Bansal, S.; Leu, A.N.; Gonzalez, F.J.; Guengerich, F.P.; Chowdhury, A.R.; Anandatheerthavarada, H.K.; Avadhani, N.G. Mitochondrial Targeting of Cytochrome P450 (CYP) 1B1 and Its Role in Polycyclic Aromatic Hydrocarbon-induced Mitochondrial Dysfunction. *J. Biol. Chem.* **2014**, *289*, 9936–9951, doi:10.1074/jbc.M113.525659.

58. Dilger, M.; Orasche, J.; Zimmermann, R.; Paur, H.-R.; Diabaté, S.; Weiss, C. Toxicity of wood smoke particles in human A549 lung epithelial cells: the role of PAHs, soot and zinc. *Arch. Toxicol.* **2016**, *90*, 3029–3044, doi:10.1007/s00204-016-1659-1.

Appendix C

Graphical Abstract

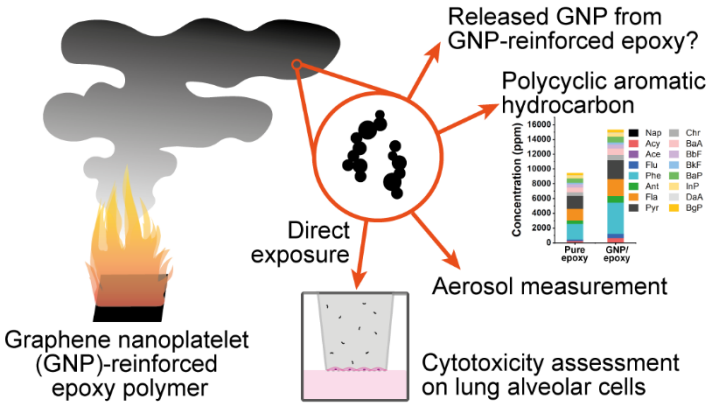

Gas chromatography-mass spectrometry for PAH analysis

The samples are extracted with a mixture of cyclohexane and acetone in an ultrasonic bath. The extract is purified using solid-phase extraction. After purification, the extract was analyzed by gas chromatography-mass spectroscopy (Shimadzu GC-2010 Plus coupled with TQ-8040). For gas chromatography, the column used was Agilent, Select PAH, 30m x 0.25mm x 0.15µm. The oven temperature was programmed in multiple stages with temperature ramping from 70 to 340 °C.

LDH assay

The collected culture media were diluted in complete culture media (1:5 ratio). Triplicates of 50 µL of the diluted samples from each well were transferred to a 96-well plate and50 µL of assay reagent was added. After 30 min incubation at room temperature, stop solution was added and the absorbance was measured at 490 nm.

MTS assay

Cell inserts were transferred to a new 12-well plate and phenol red-free RPMI 1640 medium (500 µL) was added to the basolateral side, while 400 µL of MTS working solution (1:5 dilution of MTS reagent in phenol red-free RPMI 1640) was added to the apical side. After incubation at 37 °C for 1 h, 120 µL of the MTS solution on the apical side of each insert was transferred to a 96-well plate in triplicates and the optical density at 490 nm was measured.

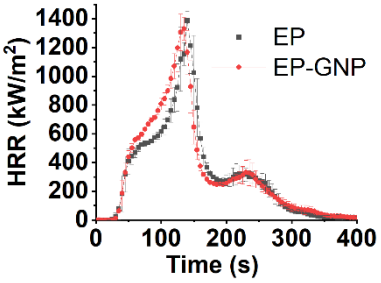

Figure C1 Plots of heat release rate of EP and EP-GNP obtained from cone calorimetry analysis. The data points are average values ± standard deviations from three combustion experiments.

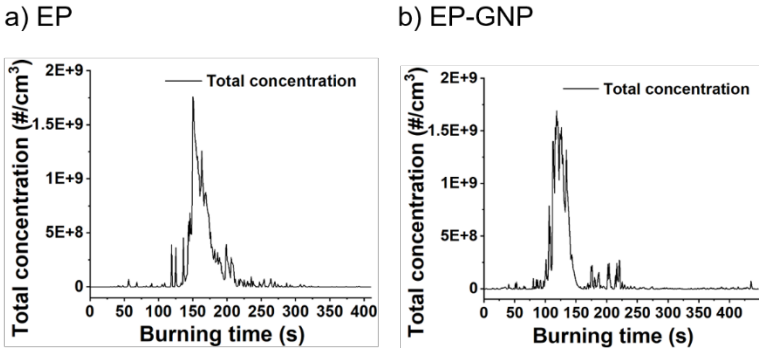

Figure C2 Total concentrations measured by DMS500 of the emissions from combustion of a) EP and b) EP-GNP.

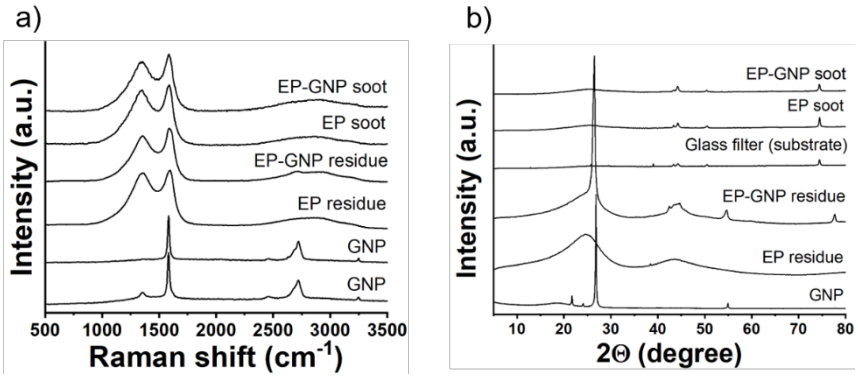

Figure C3 a) Raman mapping results and b) X-ray diffraction patterns of pristine GNP, combustion residues of EP and EP-GNP and soot from combustion of EP and EP-GNP.

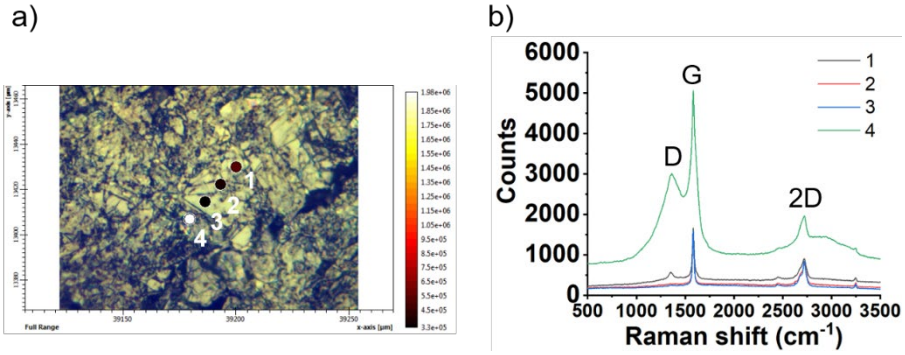

Figure C4 Raman mapping of GNP.

Characteristic Raman shifts of GNP

In general, the D band at 1355 cm^{-1} corresponds to sp^3 vibration (A_{1g} breathing mode) existing when there are defects on graphene sheets. The G band around 1581 cm^{-1} corresponds to sp^2 vibration, which always exists in sp^2 structure such as aromatic compounds, but not only limited to the six-fold rings [37]. The shape and position of the 2D band are associated with the number of graphene layers. Unlike the D band, the 2D band does not represent defects.

Raman spectra of GNP (Fig. S4) showed that the positions and intensities of D band varied depending on the analyzed spots and some spots did not have a D band. The G band and 2D band of GNP appeared as sharp peaks at 1583 cm^{-1} and 2702 cm^{-1}, respectively.

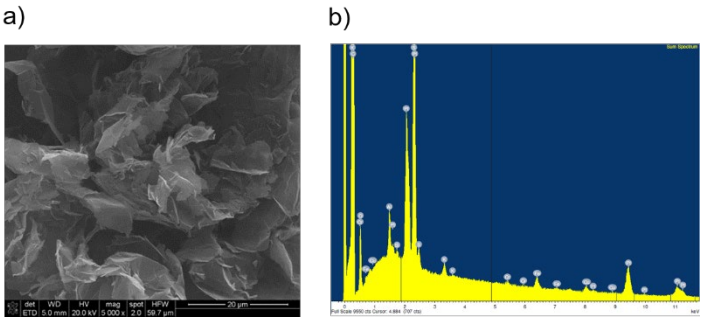

Figure C5 a) Electron microscopy image of GNP and b) elemental compositions of GNP analyzed using EDX.

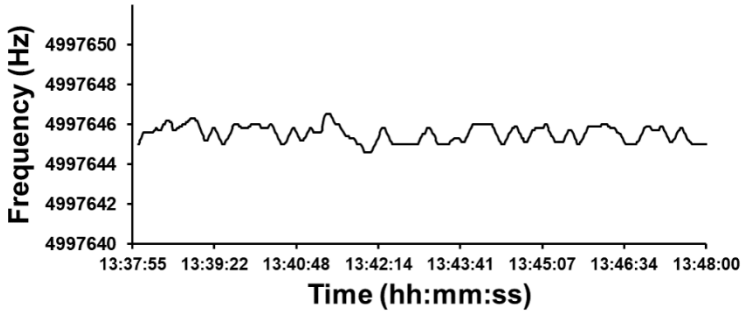

Figure C6 Frequency measured by QCM during the filtered air exposure.

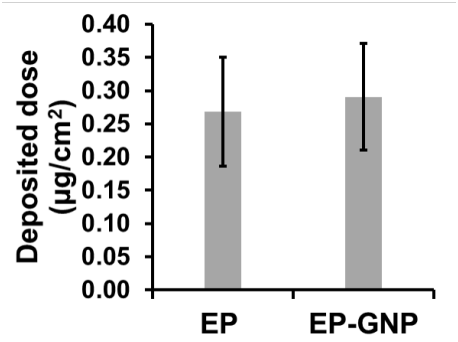

Figure C7 Estimated deposited doses of the particles emitted from the combustion in the cell exposure chamber determined using quartz crystal microbalance (QCM). Bar chart displays average values from at least five experiments and error bars are standard error of mean.

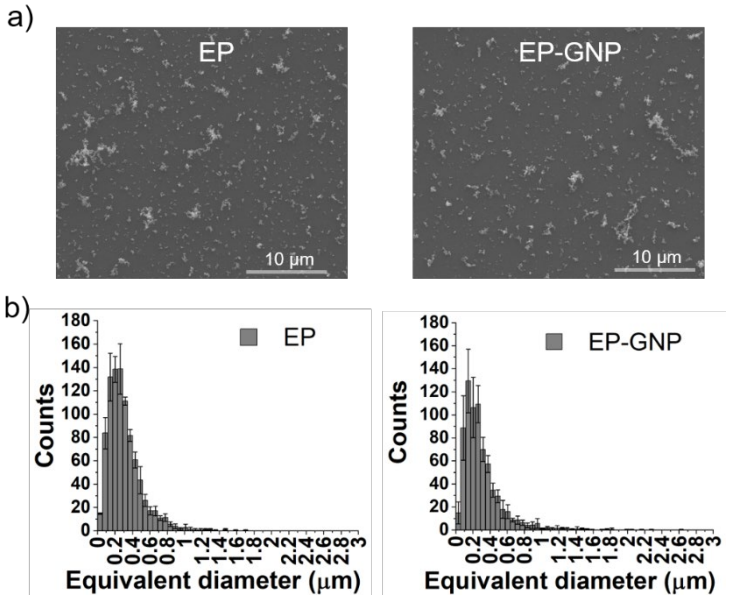

Figure C8 a) Representative electron microscopy images of the deposited aerosols from EP and EP-GNP combustion and b) Number size distributions of the particles deposited on the

bottom of the well-plate. Projected area diameter of particles (equivalent diameter) were determined using ImageJ software. The bar charts show average values ± standard deviation from three electron microscopy images from different areas.

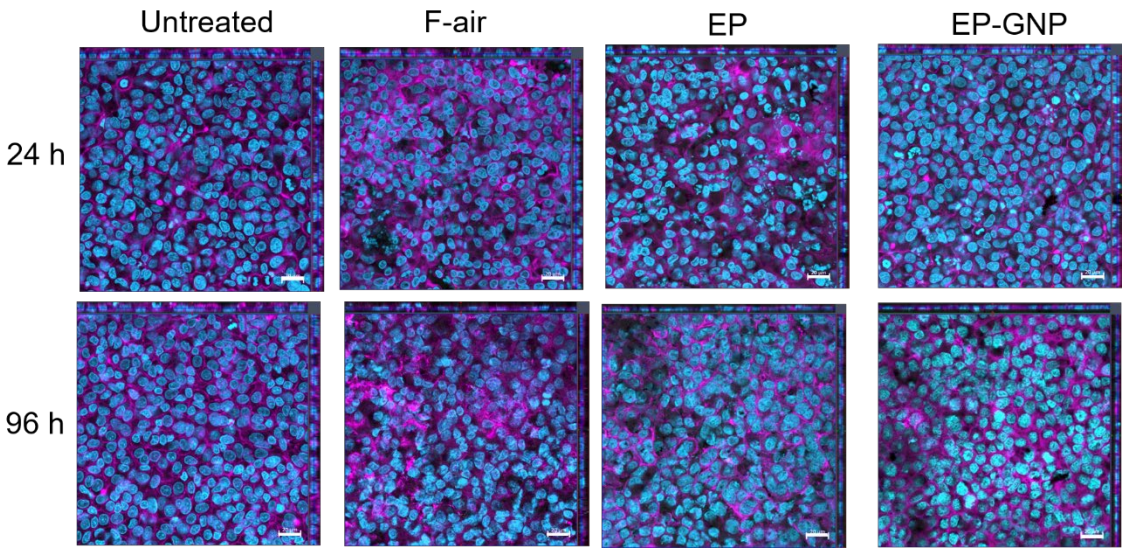

Figure C9 CLSM images of A549 cells under incubator control, filtered air control and exposure to EP and EP-GNP emissions. Scale bars are 20 µm.

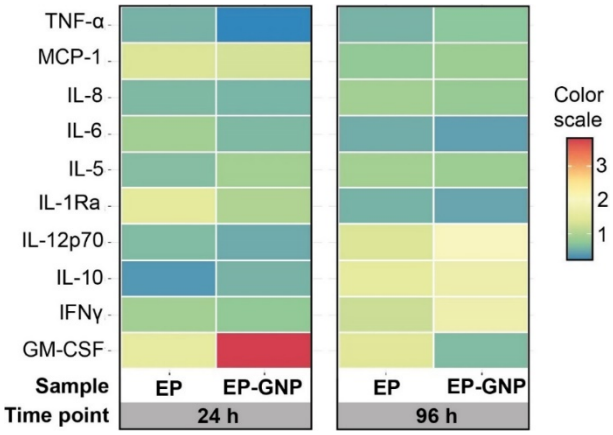

Figure C10 Color map showing relative concentrations of 10 cytokines in cell culture media after 24 h and 96 h post-exposure to emissions from EP and EP-GNP compared to negative control (filtered air exposure). Color bar shows values in folds relative to filtered air exposure.

Table C1 List of PAH analyzed by GC-MS

PAH	Abbreviation
Naphthalene	Nap
Acenaphthylene	Acy
Acenaphthene	Ace
Fluorene	Flu
Phenanthrene	Phe
Anthracene	Ant
Fluoranthene	Fla
Pyrene	Pyr
Chrysene	Chr
Benzo(a)anthracene	BaA
Benzo(b)fluoranthene	BbF
Benzo(k)fluoranthene	BkF
Benzo(a)pyrene	BaP
Indeno(1,2,3-c,d)pyrene	InP
Dibenzo(a,h)anthracene	DaA
Benzo(g,h,i)perylene	BgP

Table C2 Primer sequences for quantitative PCR

Gene	GenBank accession number	Direction	Primer sequence
GAPDH	NC_000012	forward	AAC AGC CTC AAG ATC ATC AGC
		reverse	GGA TGA TGT TCT GGA GAG CC
HMOX1	CP002685	forward	TTC TCC GAT GGG TCC TTA CAC T
		reverse	GGC ATA AAG CCC TAC AGC AAC T
SOD2	NM_000636.2	forward	CTG CTG GGG ATT GAT GTG TGG
		reverse	TGC AAG CCA TGT ATC TTT CAG T
CYP1A1	NM 000499.3	forward	GGC GTT GTG TCT TTG TAA ACC AGT GGC
		reverse	CAG GTA GGA ACT CAG ATG GGT TGA CCC

Table C3 Summary of combustion characteristics of EP and EP-GNP obtained from cone calorimetry

Sample	TTI (s)	peak HRR (kW/m²)	Ave-HRR (300 s) (kW/m²)	EHC (300 s) (MJ/kg)	Total heat release (MJ/m²)	Ave-specific MLR (g/s·m²)	Ave-CO yield (kg/kg)	Ave-CO_2 yield (kg/kg)	CO/CO_2 ratio
EP	24.3±3.1	1426.8±39.9	414.3±8.2	24.0±0.4	126.1±3.0	23.4±1.0	0.054±0.001	1.593±0.003	0.034
EP-GNP	29.3±1.7	1405.6±46.3	430.2±4.8	24.7±0.1	133.2±1.4	23.2±1.5	0.060±0.005	1.588±0.016	0.038

Table C4 Summary of D and G positions and I(D)/I(G) ratios obtained from Raman spectroscopy mapping of pristine GNP, combustion residues of EP and EP-GNP and soot from combustion of EP and EP-GNP

Sample	D position (cm^{-1})	G position (cm^{-1})	I(D)/I(G) ratio area	I(D)/I(G) ratio height	2D position (cm^{-1}), (shape*)
EP-soot	1343.8±4.6	1586.0±2.2	1.85	0.91	2863.2±37.2, (b)
EP-GNP-soot	1346.7±4.5	1586.3±1.0	1.85	0.93	2863.8±23.4, (b)
EP-residues	1353.7±5.2	1593.3±4.5	1.72	0.90	2846.3±27.0, (b)
EP-GNP-residues	1354.0±1.1	1586.7±8.3	1.46	0.74	2703.3±6.5, (b+s)
GNP	1351, 1362	1583	0.14, 0.50	0.14, 0.50	2702.0±0.7, (s)

* (b) – broad peak; (s) – sharp peak

Chapter 5

Summary and Outlook

5.1 Summary

GRMs are new emerging materials that show opportunities in numerous applications. It is important to understand the beneficial properties of GRMs as fillers in the polymer composites and the potential hazard of GRMs as well as of the release aerosols from the GRM-based polymer composites during their use phase and at the end-of-life in order to support the safe and sustainable use and development of GRMs and GRM-based products. However, there is still numerous combinations of GRM and other additives for further property enhancement to be explored and the information about the potential hazards of the GRMs and GRM-containing composites is still limited. This thesis presents the systematic studies to investigate the relationship between the structure-property of GRM-based epoxy composites, the characteristics of the released aerosol particles from two possible scenarios *i.e.* abrasion and combustion, and the corresponding *in vitro* toxicity of the released particles.

The results obtained from this thesis confirmed the hypotheses that the properties of epoxy composite can be largely influenced by the structure of hardener and fillers (DOPO and GNP). Moreover, the hazard of the GRMs as well as the release of the aerosols from the GRM-based composites can be affected by the physicochemical characteristics of the GRMs.

Regarding the structure-property relationship of the epoxy composite, the linear structure of hardener allow the rigidity of DOPO to overshadow the worsen modulus by crosslinking effect. GNP, which is a few layer graphene with the platelet structure, contributes to rigidity effect and enhance the modulus. Even though increasing the loading of DOPO and GNP could enhance the flexural modulus and flame retardancy efficiency of the epoxy composite, the loading of these fillers over some extent could worsen the composites' flexural strength. The improvement in flexural modulus, flexural strength and flame retardancy efficiency could be achieved by balancing the loading amount of the combination of the two fillers.

Another consideration that is needed to be taken into account is the toxicity aspect of the fillers. Since the inhalation is one of the major exposure routes and the most rapid exposure pathway,

toxicity of the pristine GRMs and DOPO from the occupational exposure during the manufacturing and fabrication process is of concern as well as aerosol particles released from the composites during their life cycle should also be considered.

Since DOPO showed no *in vitro* toxic effects towards neural cells, skin cells, lung epithelial cells and macrophages [1] and DOPO is chemically bonded to the epoxy resin, the release of DOPO is of less concern upon the abrasion of the epoxy composites. Hazard assessment of pristine GRMs on human macrophages showed the size- and dose-dependent effect of GRMs. GNP-2, which has larger lateral dimension (25 μm), induced more cytotoxic effect towards human macrophages than GNP-1, which has smaller lateral dimension (5 μm). GO and rGO, with similar lateral dimension to GNP-1, showed no sign of cytotoxicity. However, the effect of surface property on the toxicity cannot be concluded yet from this study.

Release fraction of GRM from an abrasion process could be influenced by the interfacial interaction between the surface of GRM and epoxy molecule, which depends on the platelet structure and the size of the GRM. Comparing among different GRMs, the results from this study showed that GRM with smaller lateral dimension were released with the higher fraction than the larger GRM. Other factors such as C/O ratio, thickness, and interlayer force could also play a role. For example, Hammer *et al*. demonstrated the effect of interlayer bonding of GRMs on the release fraction of GRMs from the epoxy composite via abrasion process. Since GO has stronger interlayer bonding than GNP, the whole GO particles could be released of from the epoxy composite, whereas GNP could be released layer by layer. This could led to higher release fraction of GO than GNP [2]. Therefore, more experiments as well as modelling works are needed to elucidate these points. When compared with another carbonaceous structure CNTs, our results showed significantly high released fraction of GRMs (~50-90%) as compared to the CNTs (<1%). This could be due to the much smaller agglomerates of CNT (in the range of nm) entwining as spherical structure after the manufacturing process compared to the agglomerates of GRM, which were platelet shape with the lateral dimension in tens of micrometer range. The smaller agglomerates of CNT were better embedded in the epoxy composites and more difficult to be released by abrasion of the composites as compared to the agglomerates of GRM. This highlights the fact that even though GRM and CNT are both carbonaceous materials, due to their structural difference, they showed distinct release fractions from the epoxy composite.

For the combustion, normally, the thermal degradation of epoxy produces volatile organic compounds such as acrolein, acetone, and allyl alcohol [3]. When epoxy/DOPO is thermally decomposed, the CO/CO_2 ratio is increased compared to the neat epoxy, which is an indication of the incomplete combustion, suggesting that more volatile organic compounds could be formed in the presence of DOPO. Further studies should characterize the physicochemical properties and investigate the potential toxic effects of the aerosol released from the thermal decomposition of the epoxy/DOPO composites. The results from this thesis revealed that GNP could enhance the PAH formation during the combustion of epoxy/GNP composites as compared to neat epoxy. Although the emissions from the combustion of epoxy and epoxy/GNP composites could induce some biological effects towards lung alveolar epithelial cells (increase in pro-inflammatory response and activation of aryl hydrocarbon receptor, but no effect on LDH release and oxidative stress genes), no significant difference was observed between the emissions from pure epoxy and those form epoxy/GNP, except the transient decrease in mitochondrial activity due to epoxy/GNP emissions. Nevertheless, due to the carcinogenicity of some PAHs, the long-term exposure to the released aerosol from the combustion of epoxy/GNP should be further considered.

Overall, based on their mechanical reinforcement, flame retardancy properties and low *in vitro* toxicity towards lung cells (macrophages and alveolar epithelial cells) shown in this thesis, GRMs show promising opportunities for industrial applications. These results have contributed to an improvement in understanding the structure-property relationship of the GRM-reinforced epoxy composites and hazard assessment information of the pristine GRMs and the GRM-reinforced epoxy composites. These can be useful for the risk assessment of the GRMs and GRM-containing composites, the design of the protection system for people, who are in close contact with the emissions from these composites such as workers, researchers, and firefighters, and the development of the safe and sustainable GRM-reinforced composites.

5.2 Outlook

So far, there is still limited number of studies on the potential hazards of the pristine GRMs and the particles released from the GRM-enabled composites. More experimental data are required to build a more complete dataset for risk assessment, which will allow the safe production and use of the GRMs and GRM-enable products for the environment and human health in the future.

In this study, only limited concentrations of GNP in the epoxy composites were explored *i.e.* up to 5 wt % in the study on the properties of the epoxy composites and 1 wt % in the release

studies. Since GNP concentrations could affect the mechanical reinforcement and flame retardancy properties of the GRM-epoxy composite, the particles released from the abrasion and combustion of the composites containing higher loadings of GRM should be further investigated.

The combustion platform established in this study can be applied to study other nanocomposites. Moreover, FTIR can be implemented to the platform to characterize the toxic gases released during the combustion in real time. Since combustion is a complex process, the effect of nanofillers on the fire behavior and the emissions during the combustion of the polymer composites cannot be generalized. For example, in the context of GRMs, the different loadings of GRMs, the combination of GRMs with other flame retardants, or the types of polymer matrix could affect the characteristics and toxicity of the emissions, which may be different from the outcomes found in this thesis.

In terms of in vitro toxicity models, more complex *in vitro* lung models can be further improved by using the co-culture of epithelial cells and immune cells, which more resemble the real situation. Moreover, primary cells can be employed instead of cell lines, which allow the long-term study and repeated exposure study as well as the study of vulnerable cells obtained from the patients with pulmonary disease asthma and chronic obstructive pulmonary disease (COPD).

5.3 References

1. Hirsch, C.; Striegl, B.; Mathes, S.; Adlhart, C.; Edelmann, M.; Bono, E.; Gaan, S.; Salmeia, K.A.; Hoelting, L.; Krebs, A.; et al. Multiparameter toxicity assessment of novel DOPO-derived organophosphorus flame retardants. *Arch. Toxicol.* **2017**, *91*, 407–425, doi:10.1007/s00204-016-1680-4.

2. Hammer, T.; Netkueakul, W.; Zolliker, P.; Schreiner, C.; Hubeli, J.; Figi, R.; Braun, O.; Calame, M.; Wang, J. Epoxy-graphene-related material composites: Nanostructure characterization and release quantification. *NanoImpact* **2020**, *20*, 100266, doi:10.1016/j.impact.2020.100266.

3. Grassie, N.; Guy, M.I.; Tennent, N.H. Degradation of epoxy polymers: Part 1-Products of thermal degradation of bisphenol-A diglycidyl ether. *Polym. Degrad. Stab.* **1985**, *12*, 65–91, doi:10.1016/0141-3910(85)90057-6.